PHOTOREACTIVE TITANATE NANOMATERIALS FOR WATER PURIFICATION SYSTEMS

By

Ibrahim El Saliby

A thesis submitted in fulfilment of the requirements for the degree of Doctor of Philosophy

Faculty of Engineering and Information Technology

University of Technology, Sydney

AUSTRALIA

2012

CERTIFICATE OF AUTHORSHIP

I certify that the work in this thesis has not previously been submitted for a degree, nor has it been submitted as part of requirements for a degree except as fully acknowledged within the text.

I also certify that this thesis has been written by me. Any help that I have received in my research work on the preparation of the thesis itself has been acknowledged. In addition, I certify that all the information sources and literature used as indicated in the thesis.

Signature of Candidate

……

I dedicate this work to my parents in Lebanon

Jihad & Jamilee El Saliby

ACKNOWLEDGMENTS

I would like to express my deepest gratitude to my supervisor Dr. Ho Kyong Shon for his encouragement, meticulous follow-up and guidance during the completion of my thesis. I will never forget your invaluable efforts to improve the research environment of our group, to intensify our passion to knowledge and to help us achieve our goals. Also, I would like to thank my co-supervisor A/Prof. Jaya Kandasamy for his help and follow up. He has shown serenity and wisdom in dealing with several issues, I thank him for all the help and support during my journey at UTS.

I would like also to acknowledge Dr. Laszlo Erdei for his help in the design, implementation and correction of this research thesis. The help of Prof. Saravanmuthu Vigneswaran, Dr. Robert McLaughlan and A/Prof. Huu Hao Ngo for supporting my research engagement in the CTWW labs is also appreciated.

Warm thanks to all my lab mates and beloved friends, Yousef, Wen, Sherub, Thanh, Mohammad, Johir, Thamer, Dang, Ben, Chinu, Ganesh, Gausul and Javeed for their friendship and help during the last four years.

Special thanks must go to Dr. Andrew McDonagh, Dr. Ric Wuhrer, Mark Berkahn, Katie McBean, Jong Beon Kim and Jong-Ho Kim for training me, sharing their knowledge, and providing valuable help in the characterisation of nanomaterials.

I also would like to thank the University of Technology, Sydney, and the Australian Postgraduate Awards for providing full financial support through scholarships for the completion of this thesis.

TABLE OF CONTENTS

TITLE PAGE i

CERTIFICATE OF AUTHORSHIP ii

ACKNOWLEDGMENTS iv

TABLE OF CONTENTS v

LIST OF FIGURES xiv

LIST OF TABLES xx

ABSTRACT xxi

CHAPTER 1

INTRODUCTION 1-1

1.1. Nanotechnology for Water Remediation 1-2

1.2. Heterogeneous Photocatalysis over TiO_2 1-2

1.3. Visible-light Active Photocatalysts 1-3

1.4. Peroxide Method for Photocatalysts' Synthesis 1-4

1.5. Micro-Assemblies of Nanostructures 1-5

1.6. Research Objectives and Scope 1-6

1.6.1. Objectives 1-6

1.6.2. Scope of the Investigation and Thesis Structure 1-7

CHAPTER 2

LITERATURE REVIEW 2-1

2.1. Nanotechnology in Water and Wastewater Treatment 2-2

2.1.1. History and Overview 2-2

2.1.2. Benefits of Nanotechnology in Water and Wastewater Treatment 2-5

2.1.2.1. Water Treatment 2-5

2.1.2.2. Water Purification 2-6

2.1.3. Application of Nanotechnology in Water and

Wastewater Treatment Processes 2-9
2.1.3.1. Nanomaterials and Membrane Filtration 2-9
2.1.3.2. Metals, Bimetallic Nanoparticles and Mixed Oxides 2-12
2.1.3.3. Modified Photocatalysts 2-15
2.1.4. Nanotechnology and Human Health 2-17

2.2. Heterogeneous Photocatalysis over TiO_2 2-19
2.2.1. Overview 2-19
2.2.2. Fundamentals and Basic Principles 2-20
2.2.3. Photocatalytic Reactors 2-22
2.2.4. Operational Parameters 2-23
2.2.4.1. Photocatalyst Loading 2-23
2.2.4.2. Composition and Characteristics of Photocatalysts 2-24
2.2.4.3. Concentration of Pollutants 2-24
2.2.4.4. Effect of pH 2-25
2.2.4.5. Light Intensity 2-26
2.2.4.6. Dissolved Oxygen 2-27
2.2.4.7. Temperature 2-27
2.2.4.8. Optimisation Methodology 2-28
2.2.4.9. Process Efficiency 2-28
2.2.5. Kinetics of TiO_2 photocatalysis 2-29

2.3. Solar/Visible Light Responsive TiO_2 2-33
2.3.1. Background 2-33
2.3.2. Overview of Visible Light Activity by Doping TiO_2 2-34
2.3.2.1. Nitrogen Doping 2-34
2.3.2.2. Silver Doping 2-36
2.3.3. Doped TiO_2 and Water Reclamation 2-39
2.3.3.1. Nitrogen Doped TiO_2 2-39
2.3.3.1.1. Photodegradation of Dyes 2-39
2.3.3.1.2. Photodegradation of Phenolic Compounds 2-42
2.3.3.1.3. Other Organic Water Contaminants 2-44
2.3.3.2. Silver Doped TiO_2 2-46

2.3.3.2.1. Photodegradation of Dyes 2-46
2.3.3.2.2. Other Prominent Water Contaminants 2-47
2.3.3.3. Co-doping using Metal/non-metal Elements 2-48

2.4. Model Water Pollutants used in this Study 2-51
2.4.1. Humic acid as a Natural Water Pollutant 2-51
2.4.1.1. Characteristics of Humic Acid 2-51
2.4.1.2. Photocatalytic Decomposition of Humic Acids 2-52
2.4.2. Methylene blue 2-54

2.5. Summary 2-57

CHAPTER 3
MATERIALS AND METHODOLOGIES 3-1

3.1. Introduction 3-2

3.2. Materials 3-2
3.2.1. Degussa P25 Photocatalyst 3-2
3.2.2. Chemicals 3-3
3.2.3. Wool 3-3

3.3. Photocatalysts Characterisation Equipments and Methods 3-5
3.3.1. Scanning Electron Microscope / Energy Dispersive X-ray 3-5
3.3.2. Transmission Electron Microscope 3-5
3.3.3. Specific Surface Area and Pore Size Measurements 3-6
3.3.4. X-ray Diffractometer 3-6
3.3.5. X-ray Photoelectron Spectroscope 3-7
3.3.6. Malvern Zetasizer 3-7

3.4. Photocatalytic Reactors 3-8
3.4.1. Photoreactor 1 3-8
3.4.2. Photoreactor 2 3-8

3.4.3. Solar Simulator 3-9

3.5. Auxiliary Laboratory Instruments 3-11

3.6. Analytical Procedures 3-14
3.6.1. UV-vis Spectrophotometry 3-14
3.6.2. Dissolved Organic Carbon Measurement 3-16
3.6.3. Ion Chromatography 3-18

3.7. Data Processing and Plotting 3-19

CHAPTER 4
PEROXIDE METHODS FOR ADVANCED PHOTOCATALYSTS SYNTHESIS 4-1

4.1. Introduction 4-2

4.2. Peroxide Methods for Photocatalysts Synthesis 4-3
4.2.1. Metal Doping of Titania 4-3
4.2.2. Synthesis of Nanomaterials 4-4
4.2.3. Thin Film and Composite Photocatalysts Synthesis 4-7
4.2.4. Nano and Microstructured Photocatalysts 4-9

4.3. Experimental Investigation 4-12
4.3.1. Dissolution of P25 4-12
4.3.1.1. Experiment 1: Sodium Hydroxide Base 4-12
4.3.1.2. Experiment 2: Ammonium Hydroxide Base 4-12
4.3.2. Solution and Powder Characterisation 4-13

4.4. Results and Discussion 4-14
4.4.1. Characteristics of Powder Samples 4-14
4.4.1.1. Solution Characteristics using NaOH Base 4-14
4.4.1.2. Morphology and Composition of Na^{12} and Na^{18} 4-16

4.4.1.3. Solution Characteristics using NH_4OH Base 4-21
4.4.1.4. Morphology and Composition of A^8 and A^{20} 4-24

4.5. Conclusions 4-28

CHAPTER 5
DEVELOPMENT OF VISIBLE LIGHT
SENSITIVE TITANIA PHOTOCATALYSTS
BY COMBINED NITROGEN AND SILVER DOPING 5-1

5.1. Introduction 5-2

5.2. Experimental 5-5
5.2.1. Photocatalysts Synthesis 5-5
5.2.2. Characterisation of Photocatalysts 5-5
5.2.3. Photocatalytic Experiments 5-6
5.2.3.1. Visible Light Source 5-6
5.2.3.2. Simulated Solar Light Source 5-6
5.2.3.3. Data Collection 5-6

5.3. Results and Discussion 5-8
5.3.1. Characteristics of Photocatalysts 5-8
5.3.1.1. SEM/EDX and TEM 5-8
5.3.1.2. Textural Properties 5-12
5.3.1.3. X-ray Diffraction 5-13
5.3.1.4. X-ray Photoelectron Spectroscopy 5-15
5.3.2. Photocatalytic Properties 5-17
5.3.2.1. Visible Light Photocatalysis 5-17
5.3.2.2. Simulated Solar Light Photocatalysis 5-22

5.4. Conclusions 5-25

CHAPTER 6
PREPARATION AND CHARACTERISATION
OF HIGHLY-ADSORBENT AND PHOTOACTIVE
MESOPOROUS NA-TITANATE MICROSPHERES 6-1

6.1. Introduction 6-2

6.2. Experimental Investigation 6-5
6.2.1. Synthesis of Microspheres 6-5
6.2.2. Powder Characterisation 6-5
6.2.3. Adsorption Experiments 6-6
6.2.4. Photocatalytic Properties under UV Light 6-6
6.2.5. Lifetime Cycle of Photocatalysts 6-6
6.2.6. Photocatalyst Separation by Settling 6-7

6.3. Results and Discussion 6-8
6.3.1. Characteristics of Mesoporous Microspheres 6-8
6.3.2. Adsorption of Methylene Blue on Mesoporous Microspheres 6-13
6.3.3. Photocatalytic Decolourisation of Methylene Blue and DOC Removal 6-16
6.3.4. Mineralisation of Methylene Blue 6-18
6.3.5. Photocatalytic Stability 6-19
6.3.6. Supernatant Turbidity 6-22

6.4. Conclusions 6-23

CHAPTER 7
ADSORPTION AND PHOTOCATALYTIC
DECOMPOSITION OF METHYLENE BLUE
OVER H-TITANATE NANOFIBRES 7-1

7.1. Introduction 7-2

7.2. Experimental Investigations 7-4
7.2.1. Synthesis 7-4
7.2.2. HTNF Characterisation 7-4
7.2.3. MB Adsorption Experiments 7-4
7.2.3.1. Effect of HTNF Loading 7-5
7.2.3.2. Effect of MB Concentration 7-5
7.2.3.3. Effect of pH 7-5
7.2.3.4. Effect of Solution Temperature 7-5
7.2.3.5. Adsorption Equilibrium and Isotherms 7-5
7.2.4. Photocatalytic Degradation under Simulated Solar Light 7-6
7.2.5. Photocatalytic Stability 7-7
7.2.6. Photocatalyst Separation by Settling 7-7

7.3. Results and Discussion 7-8
7.3.1. Characteristics of H-titanate Nanofibres 7-8
7.3.2. Effect of Operating Conditions on MB Adsorption 7-10
7.3.2.1. Effect of HTNF Loading 7-10
7.3.2.2. Effect of Initial MB Concentration 7-11
7.3.2.3. Effect of Solution pH 7-12
7.3.2.4. Effect of Solution Temperature 7-13
7.3.2.5. Adsorption Equilibrium and Isotherms 7-14
7.3.3. Photocatalytic Decolourisation and DOC Removal of MB 7-18
7.3.3.1. Effect of Solution pH 7-18
7.3.3.2. Effect of Light Intensity 7-21
7.3.4. Photocatalytic Stability of HTNF 7-23
7.3.5. Settling Characteristic of HTNF 7-26

7.4. Conclusions 7-28

CHAPTER 8
SYNTHESIS, CHARACTERISATION AND SEPARATION OF PHOTOREACTIVE H-TITANATE NANOFIBROUS CHANNEL 8-1

8.1. Introduction 8-2

8.2. Materials and Methods 8-5
8.2.1. Materials and Synthesis of Nanofibrous Channel 8-5
8.2.2. Characterisation of NC-TiO_2 8-6
8.2.3. Study of Photocatalytic Activity 8-7
8.2.4. Sedimentation Experiments 8-8

8.3. Results and Discussion 8-9
8.3.1. NC-TiO_2 Characteristics 8-9
8.3.2. Photocatalytic properties 8-18
8.3.2.1. NC-TiO_2 loading 8-18
8.3.2.2. Effect of Initial HA Concentration 8-20
8.3.2.3. Effect of Process pH 8-22
8.3.3. Lifetime Cycle of NC-TiO_2 8-23
8.3.4. Settleability of NC-TiO_2 8-25

8.4. Conclusions 8-27

CHAPTER 9
CONCLUSIONS AND RECOMMENDATIONS 9-1

9.1. Conclusions 9-2
9.1.1. The Synthesis of Nanomaterials from Peroxo-Titanium Complex 9-2
9.1.2. Nitrogen-doped and Silver Co-doped photocatalysts for Visible and Solar Light Photocatalysis 9-2
9.1.3. Adsorption of Methylene Blue and its Photodecomposition

using Na-Titanate Microspheres under UV Light 9-3
9.1.4. Kinetics of Adsorption of Methylene Blue over Hydrogen-Titanate Nanofibres and its Photodecomposition under Solar Light 9-4
9.1.5. Degradation of Humic Acid over Nanofibrous Channel under UV light 9-5

9.2. Recommendations 9-6

APPENDICES A-1

Appendix A A-2

Appendix B A-4

Appendix C A-5

BIBILOGRAPHY B-1

LIST OF FIGURES

Figure 2.1. TiO_2 nanowire membrane with simultaneous photooxidation potential (Xiao et al. 2008). 2-11

Figure 2.2. Sedimentation of (a) TiO_2 nanoparticles after 30 min and microspheres for (b) 5 min, (c) 15 min and (d) 30 min (Wei et al. 2008). 2-17

Figure 2.3. The proposed HA chemical formula (Schulten 1993). 2-52

Figure 2.4. Chemical structure of MB. 2-55

Figure 2.5. Pathways of MB decomposition (Houas et al. 2001). 2-56

Figure 3.1. SEM image of Degussa P25 TiO_2 particles used in this study. 3-2

Figure 3.2. Zeta potential of 1 g/L Degussa P25 suspension in Milli Q water. 3-3

Figure 3.3. SEM image of a Merino wool fibre. 3-4

Figure 3.4. Photo (left) and a schematic drawing (right) of Photoreactor 1. 3-8

Figure 3.5. Photo (left) and schematic diagram (right) of the annular slurry Photoreactor 2. 3-9

Figure 3.6. Solar simulator outside (left) and inside (right). 3-10

Figure 3.7. SolSim-164 and AM1.5 spectral emission comparison. 3-10

Figure 3.8. Centrifuge (left) and orbital shaker (right). 3-11

Figure 3.9. Hach HI 93414 turbidity and chlorine meter (left) and TPS pH meter (right). 3-12

Figure 3.10. Oven (left) and Labec furnace (right). 3-12

Figure 3.11. Teflon cell used for hydrothermal treatment. 3-13

Figure 3.12. Shimadzu UV-1700 spectrophotometer. 3-15

Figure 3.13. Linear regression of MB concentration versus absorbance at $\lambda = 664$ nm. 3-15

Figure 3.14. Multi N/C 3100 DOC analyser with autosampler. 3-17

Figure 3.15. Standard curve of DOC (mg/L). 3-17

Figure 3.16. Metrohm ion chromatograph. 3-18

Figure 3.17. Linear relationship between peak area (µs/cm.sec) and sulphate concentration (mg/L). 3-19
Figure 4.1. TiO_2 foam produced by Arabatis and Falaras (2003). 4-10
Figure 4.2. Photo-sensitized peroxo species phenomenon described by Shankar et al. (2009). 4-11
Figure 4.3. Absorbance spectrum for PTC solutions of Na^{12}, Na^{18} after 2, 4 and 24 h of reaction time at room temperature. 4-15
Figure 4.4. SEM images of Na^{12} powders at two different magnifications (A) 10 KX and (B) 100 KX. 4-19
Figure 4.5. SEM images of Na^{18} powders at two different magnifications (A) 10 KX and (B) 100 KX. 4-20
Figure 4.6. EDS spectra of Na^{12} (spectrum 4) and Na^{18} (spectrum 5) powders. 4-21
Figure 4.7. Absorbance spectrum for A^8 and A^{20} after 2, 4 and 24 h of reaction time at room temperature. 4-23
Figure 4.8. SEM images of A^8 powders at two different magnifications (A) 10 KX and (B) 100 KX. 4-25
Figure 4.9. SEM images of A^{20} powders at two different magnifications (A) 10 KX and (B) 100 KX. 4-26
Figure 4.10. XPS spectra of (A) A^8 and (B) A^{20} samples. 4-27
Figure 5.1. Zeta potential of TiN and TiNAg. 5-8
Figure 5.2. SEM images of TiO_2-N (a) and TiO_2-N-Ag (b). 5-10
Figure 5.3. TEM images of TiO_2-N (a) and TiO_2-N-Ag (b). 5-11
Figure 5.4. Nitrogen adsorption and desorption in TiO_2-N and TiO_2-N-Ag. 5-14
Figure 5.5. XRD patterns of Degussa P25, TiO_2-N and TiO_2-N-Ag photocatalysts showing anatase (A) and rutile (R) phases. 5-15
Figure 5.6. Decolourisation of MB (a) and DOC removal (b) in the absence of photocatalysts (apparent photolysis) and in the presence of TiO_2-N, TiO_2-N-Ag and Degussa P25 under visible light. 5-18
Figure 5.7. (a) N-doped and (b) N/Ag co-doped TiO_2 photocatalytic mechanism. 5-21

Figure 5.8. Decolourisation of MB (a) and DOC removal (b) in the presence of TiO_2-N, TiO_2-N-Ag and Degussa P25 under simulated solar light. 5-24

Figure 6.1. SEM images of as prepared samples (NT-25 and NT-80) and calcined samples (NTC-25 and NTC-80). 6-9

Figure 6.2. XRD diffraction pattern of NT-80, NT-25 compared to the original Degussa P25 (A) anatase, (R) rutile. 6-11

Figure 6.3. Zeta potential of microspheres prepared at room temperature (powder loading 1 g/L, T = 25 °C). 6-12

Figure 6.4. Zeta potential of microspheres prepared after hydrothermal treatment (powder loading 1 g/L, T = 25 °C). 6-12

Figure 6.5. (A) Decolourisation and (B) DOC removal of MB by adsorption on NT-80, NTC-80, NT-25 and NTC-25 ([MB] = 10 mg/L, pH 7, data collected after 30 min). 6-15

Figure 6.6. Kinetics of (A) decolourisation of MB and (B) DOC photodegradation on NT-80, NTC-80, NT-25 and NTC-25 ([MB] = 10 mg/L, pH 7, photocatalyst loading = 50 mg/L). 6-17

Figure 6.7. Evolution of sulphate ions during the photocatalytic degradation of MB over NT-25, NTC-25, NT-80 and NTC-80 ([MB] = 10 mg/L, pH 7, photocatalyst loading = 50 mg/L). 6-19

Figure 6.8. Lifetime cycles of NT-25, NTC-25 for the decolourisation of MB ([MB] = 10 mg/L, pH 7, photocatalyst loading = 50 mg/L, (A) dark adsorption). 6-20

Figure 6.9. Lifetime cycles of NT-80 and NTC-80 for the decolourisation of MB ([MB] = 10 mg/L, pH 7, photocatalyst loading = 50 mg/L, (A) dark adsorption). 6-21

Figure 6.10. Normalised decrease in supernatant turbidity using NT-25, NTC-25, NT-80, NTC-80 and P-25 (pH 7, photocatalyst loading = 50 mg/L). 6-22

Figure 7.1. Zeta potential of 1 g/L suspension of as-prepared (AP-HTNF) and calcined HTNF (C-HTNF). 7-8

Figure 7.2. SEM images of H titanate nanofibres (A and B). 7-9
Figure 7.3. EDS plot showing the elemental composition of HTNF. 7-10
Figure 7.4. Effect of HTNF loading on the adsorption of MB from solution. (Experimental conditions: MB = 10 mg/L, T = 25 °C, shaking speed = 150 rpm, pH = 9). 7-11
Figure 7.5. Effect of initial MB concentration on the adsorption of MB onto HTNF. (Experimental conditions: HTNF = 0.5 g/L, T = 25 °C, shaking speed = 150 rpm, pH = 9). 7-12
Figure 7.6. Effect of solution pH on the adsorption of MB onto HTNF. (Experimental conditions: HTNF = 0.5 g/L, MB = 20 mg/L, T = 25 °C, shaking speed = 150 rpm). 7-13
Figure 7.7. Effect of solution temperature on the adsorption of MB onto HTNF. (Experimental conditions: HTNF = 0.5 g/L, MB = 20 mg/L, shaking speed = 150 rpm, pH = 9). 7-14
Figure 7.8. (A) Effect of HTNF loading and (B) MB concentration on the amount of dye adsorbed at equilibrium (q_e, mg/g). 7-15
Figure 7.9. (A) Effect of solution's pH and (B) temperature on the amount of dye adsorbed at equilibrium (q_e, mg/g). 7-17
Figure 7.10. (A) Effect of solution pH on the discolouration and (B) DOC removal of MB solution using HTNF. (Experimental conditions: HTNF = 0.5 g/L, MB = 20 mg/L, T = 26 °C, air flow = 0.6 L/min, light intensity = 28 000 lx). 7-20
Figure 7.11. Effect of light intensity on the discolouration (A) and DOC removal (B) of MB solution using HTNF. (Experimental conditions: HTNF = 0.5 g/L, MB = 20 mg/L, T = 26 °C, air flow = 0.6 L/min, pH = 9). 7-22
Figure 7.12. (A) Photocatalytic degradation of MB, (B) desorption of intermediate products and (C) Photocatalytic decomposition of intermediates ("NA" stands for normalised absorbance). 7-25
Figure 7.13. UV-vis spectrum for the photocatalytic degradation of MB showing three stages (stage 1: 0 to 120 min;

stage 2: 121 to 360 min; stage 3: 361 to 480 min). 7-25
Figure 7.14. Photocatalytic stability of HTNF over three degradation cycles. 7-26
Figure 7.15. Normalised turbidity decrease in function of sedimentation time for HTNF and Degussa P25. 7-27
Figure 8.1. A proposed mechanism for NC-TiO_2 synthesis. 8-5
Figure 8.2. NC-TiO_2 synthesis steps. (A) wool fleeces, (B) H-titanate suspension, (C) adsorption of H-titanate on wool fibres, (D) NC-TiO_2 after calcination. 8-6
Figure 8.3. Zeta potential of NC-TiO_2 solution (1g/L). 8-9
Figure 8.4. SEM micrographs of NC-TiO_2 at different magnifications; (A) full size, (B) internal diameter of the channel, (C) maximum wall thickness, (D) nanofibres dimensions. 8-12
Figure 8.5. X-ray diffraction patterns showing NC-TiO_2 and Degussa P25. (A) anatase and (R) rutile. 8-13
Figure 8.6. Nitrogen adsorption results of nanofibrous channels. (A) adsorption-desorption isotherms and (B) pore size distribution curve. 8-15
Figure 8.7. XPS patterns of nanofibrous channels. (A) high-resolution spectra of Ti2p; (B) high-resolution spectra of O1s; (C) high-resolution spectra of S2p and (D) high-resolution spectra of N1s. 8-17
Figure 8.8. Photocatalytic removal of HA over different NC-TiO_2 loads (0.5, 1, 1.5 and 2 g/L) as revealed by absorbance at λ = 254 nm (A) and DOC measurement (B). Experimental conditions: pH 7; Air flow 0.6 L/min; temperature 26 °C; 3x15W UVC lamps. 8-19
Figure 8.9. Photocatalytic removal of HA (5, 10 and 20 mg/L) over NC-TiO_2 as revealed by absorbance at λ = 254 nm. Experimental conditions: pH 7; Air flow 0.6 L/min; temperature 26 °C; 3x15W UVC lamps; NC-TiO_2 = 1g/L. 8-21
Figure 8.10. Photocatalytic removal of HA over NC-TiO_2 in

different pH as revealed by absorbance at λ = 254 nm. Experimental conditions: HA = 10 mg/L, Air flow 0.6 L/min; temperature 26 °C; 3x15W UVC lamps; NC-TiO_2 = 1g/L. 8-22

Figure 8.11. Photocatalytic lifecycle of NC-TiO_2 for the degradation of HA as shown by UV absorbance (A) at λ = 254 nm and DOC (B). Photodegradation reaction conditions: NC-TiO_2 load (1 g/L); pH 7; Air flow 0.6 L/min; temperature 26 °C; 3x15W UVC lamps. 8-24

Figure 8.12. Initial (A, 10 mg/L) and treated (B) HA solutions after the fourth treatment cycle using 1 g/L NC-TiO_2 loading. 8-25

Figure 8.13. Decrease of the supernatant turbidity in function of time at different NC-TiO_2 loads. 8-26

Figure B.1. Adsorption of MB onto TiO_2-N and TiO_2-N-Ag. A-4

Figure C.1. High magnification image of NT-80. A-5

Figure C.2. Adsorption/Desorption isotherms of NT-25 and NT-80. A-6

LIST OF TABLES

Table 2.1. Membrane type and characteristics (Thorsen and Flogstad 2006) 2-5

Table 2.2. Metal compounds and their effect on water and wastewater contaminants 2-13

Table 2.3. Selected methods for the preparation of N doped TiO_2 2-36

Table 2.4. Selected methods for the preparation of Ag doped TiO_2 using $AgNO_3$ as a silver precursor 2-38

Table 2.5. Mecoprop and MCPA degradation rates over several photocatalysts. 2-46

Table 2.6. Recent methods for the preparation of N/metal co-doped TiO_2. 2-49

Table 3.1. List of chemicals 3-4

Table 5.1. Textural parameters of nanocatalysts examined in this study 5-12

Table 5.2. XPS results data for TiO_2-N and TiO_2-N-Ag 5-16

Table 6.1. Textural parameters of microspheres 6-10

Table 7.1. Langmuir isotherm constants for MB adsorption onto HTNF under different operating conditions 7-18

Table 7.2. R_L values for different operational conditions 7-18

Table 7.3. Regression equation and R^2 for MB discolouration against DOC removal 7-21

Table 7.4. Apparent pseudo-first order kinetics for the photocatalytic degradation of MB over HTNF under different operating conditions 7-23

ABSTRACT

Increasing water scarcity and environmental considerations are calling for more effective means to purify industrial and urban wastewaters. Advanced oxidation processes are able to effectively remove many persistent and toxic pollutants from water to enable the use and reuse of impaired quality raw water sources. Among these processes, heterogeneous photocatalysis has some notable inherent advantages, such as relative process simplicity, and the minimal generation of waste streams. Unfortunately, the commercially available photocatalysts show poor efficiency in the utilisation of natural solar radiation and are difficult to separate and recover from treated water, which results in high operational costs. In order to alleviate these recognised problems, this thesis explored an improved method of material synthesis to produce nanomaterials with desirable properties.

The investigation of peroxide method at high pH values showed that this facile approach offers great potential for the fabrication of various nanoparticles, nanostructures, and thin films deposits. The shape, size, structure and surface properties of the resulting photocatalysts were simply controlled through the process pH, the time of reaction, and the chemical composition of the solvent base. Both partial and complete dissolution of the precursors was accomplished to fabricate various, crystalline and amorphous anatase and alkali titanate end products. The use of ammonium hydroxide base was more advantageous, since it provided a very simple means to achieve simultaneous N doping.

Effective N-doping of Degussa P25 commercial photocatalyst was simply achieved using highly concentrated (25%) ammonium hydroxide base in 24 h time at room temperature in an open reactor. The raw product slurries were neutralised with acid, washed with water, and aged until dry at 75 °C. Additional doping (co-doping) with Ag was achieved by adding $AgNO_3$ to the raw slurries. The resulting nanoparticles had elongated rod and needle-like shapes, 2-3 times larger specific surface area (92.9-144.6 m^2g^{-1}) than the precursor P25, and 5.4-6.5 nm mesopore sizes. These photocatalysts were remarkably effective in the photobleaching of Methylene Blue

under visible light, and simulated solar light illuminations. Therefore, this method is suitable to improve the performance of currently available commercial photocatalysts.

Na-titanate microspheres with 700-800 nm diameter were produced at low (25-80 $^{\circ}$C) temperatures using NaOH for base, and P25 precursor in the peroxide method. Both the raw and calcined products showed very high adsorption affinity towards Methylene Blue dye, and were also capable of its degradation under UV light without minimal loss of performance after five complete treatment cycles. The calcined product showed higher catalytic activity, and could be fully recovered from the spent slurry by gravity settling.

Exchanging Na with H in titanates microspheres in HCl solution resulted in the formation of hydrogen-titanate nanofibres, which were transformed into anatase nanofibres after annealing at 550 °C for 6 h. The nanofibres had average specific surface area of 31.5 m^2/g, average pore volume of 0.10 cm^3/g and average pore size of 50 Å. These products also were effective adsorbent of the model pollutant and adsorbents and good photocatalyst under simulated solar light illumination. No reduction in photocatalytic activity was observed over three complete treatment cycles, and the effective separation of nanofibres was achieved by gravity settling resulting in low residual solution turbidity. Such nanofibres may also be used to produce paper-like photoreactive filter materials.

An easily separable fibrous photocatalyst was produced by depositing H-titanate nanofibres on wool fibres serving as bio-template. The calcined end-product showed anatase crystal phase and nanofibrous morphology (about 50 µm length and 9.5 µm diameter), having about 24 m^2/g specific surface area with mesoporous characteristics. These nanofibres were effective in the photocatalytic degradation of humic acid model pollutant solution under UV light irradiation. The performance of this photocatalyst showed only a small decrease after three complete treatment cycles, and the microfibres were easily separated from the treated solution by sedimentation with very low supernatant turbidity.

UNIVERSITY OF TECHNOLOGY, SYDNEY

FACULTY OF ENGINEERING AND INFORMATION TECHNOLOGY

CHAPTER 1

INTRODUCTION

Photocatalysis holds great promise to tackle many of the challenging environmental issues. This thesis presents a limited yet hopefully useful treatment of this subject with a discussion of previous research, grey areas and gaps in knowledge that need further research, a novel method to produce improved photocatalysts, and their use in the practical application of photocatalysis.

1.1. Nanotechnology for Water Remediation

The remediation of contaminated water and air can be described by the group of processes that target removing, reducing or neutralising water contaminants that threaten human health and/or ecosystem productivity and integrity (Theron et al. 2008). This aim is often achieved using a combination of thermal, physico-chemical or biological methods, due to the complexity of water pollutants making their removal by using a single treatment method impossible. Traditional pollutant removal techniques can separate harmful compounds from water into waste streams, or transform undesirable constituents into less harmful or harmless ones. Unfortunately, many substances cannot be effectively removed from water, or rendered innocuous by traditional treatment methods.

During the last decades, advanced oxidation processes (AOPs) have emerged as effective methods of destroying recalcitrant organics and micro-pollutants present in many water sources and sewage effluents (Mills and Lee 2004). These methods rely on free radical reactions that can completely oxidise (mineralise) almost all organic compounds, or following partial treatment, render them amenable to biological treatment. Among AOPs, heterogenous photocatalysis has some unique advantages to attract great research interest.

1.2. Heterogeneous Photocatalysis over TiO_2

The degradation of various organic water pollutants is essential to achieve high water quality. The conventional treatment processes are costly (ion exchange), slow (biological treatment), suffer from fouling (membrane), difficult to handle (activated carbon) and generate a large volume of sludge (flocculation and coagulation). In

contrast, the organic matter degradation by photocatalytic reactions that occur at an interface of a solid/liquid (photocatalyst/dissolved pollutant) is considered a cheap and environmentally friendly technology. The reactions are initiated by the absorbance of photons to drive subsequent redox reactions leading to the decomposition of the surface adsorbed pollutants. The main advantages of photocatalysis for water remediation can be summarised in the following:

- The photocatalyst is not consumed, chemically altered, or transformed.
- There is minimal sludge/waste production.
- No need for costly regeneration.
- Complete mineralisation of pollutants to CO_2, H_2O, and salts can be achieved.

Despite all the benefits associated with the adoption of this technology, there are important shortcomings that need to be resolved, such as the cumbersome separation of nanoparticles from the treated water, and the use of UV light to activate the photocatalyst.

1.3. Visible-light Active Photocatalysts

Solar light is considered a free source of energy which is vastly available during daytimes. The solar spectrum is complex but mainly contains visible light (40%) and a small portion of UV (5%). Therefore, the development of visible-light sensitive photocatalysts remains the main challenge for making photocatalysis a viable technology in the water treatment industry. Visible-light photocatalysts are known as "*second-generation TiO_2 photocatalysts*" which can efficiently harvest visible light from solar energy (Anpo 1997). There is an increasing interest to explore the potential use of these new photocatalysts for treating water pollutants under both visible and solar lights (Malato et al. 2009; Rehman et al. 2009).

The attainment of photocatalytic activity in the visible range has been attributed to several physico-chemical alterations in the lattice structure of TiO_2. These modifications in TiO_2 induce band gap narrowing, resulting in the production of a

narrow band gap visible-light active photocatalyst. Non-metal dopant such as N (Sato et al. 2005; Bianchi et al. 2009) and metal dopant using Ag (Binitha et al. 2009) are few examples of metals and non-metals used to attain photoactivity in the visible spectrum. Moreover, co-doping (or multi-doping) of TiO_2 using a combination of metals/non-metals, metals/metals or non-metals/non-metals is also considered to be an effective means for enhancing the photocatalytic activity of TiO_2 (Ge et al. 2006).

1.4. Peroxide Method for Photocatalysts' Synthesis

The peroxide method can be described by the reaction of a titanium precursor with hydrogen peroxide at any pH (adjusted by acid or base) to produce titania nanomaterials. The reaction result is a dark orange colour solution at low pH (< 3-4) values which changes to dark yellow around pH 7, and to light yellow in the alkaline region. Precipitation can be induced by heating, refluxing, hydrothermal treatment or simply by removing the excess of H_2O_2. The use of high pH solution coupled with hydrothermal treatment has led to the fabrication of nanostructures with interesting morphologies and characteristics. Arabatzis and Falaras (2003) reported TiO_2 foam synthesised by the direct decomposition and reaction of H_2O_2 inside titanium oxide/hexadecylamine slurry. Mao et al. (2006) prepared hollow micrometer aggregates and titanate one-dimensional (1D) nanostructures by a H_2O_2-modified hydrothermal process. Similarly, titanate nanofibers and microspheres were obtained by hydrothermal treatment under high pH using a peroxo-titanium acid as a precursor (Yada et al. 2006). Recently, the use of the peroxo-titanium complex (PTC) solutions also has been exploited for thin films deposition and surface coating (Wang et al. 2009; Lopez et al. 2010). The hydrothermal treatment of PTC produced from the peroxo-titanium reaction typically results in yellow coloured nanostructures, due to the adsorption of peroxo-species. These nanostructures can be manipulated to form different micro-assemblies of titania nanostructures.

1.5. Micro-Assemblies of Nanostructures

Similarly to nanoparticles, the examination of nanofibres under electron microscope reveals that these nanostructures are generally not organised in a uniform manner. However, several researchers have successfully induced the aggregation of nanoparticles on template surfaces, to copy interesting template morphologies (Lakshmi et al. 1997; Xiong et al. 2006). Therefore, the arrangement of nanostructures in desired shapes and forms can also be achieved by following simple procedures, such as the morphology transcription of templates. The thickness of these arrangements can be controlled by contact time, solution pH, and the concentration of the nanostructure solution.

Nature is a rich source of neatly organised macro, micro and nano-templates. The morphology of biological structures is diverse and multidimensional, which have been acquired through adaptation of living organisms, and modified by mutation over long periods of time. The imitation of these structures has been achieved by the production of hierarchical nanomaterials through the morphology transcription of various biospecies. Cotton (Aminian et al. 2007), eggshell (Su et al. 2008), and green-leaf (Li et al. 2009) are few examples of biological morphologies that have been copied using TiO_2.

The morphology transcription using nanostructures may provide an opportunity to minimise the loss of active surface area, an undesirable effect often encountered by using nanoparticles. A relatively inexpensive local product in Australia, wool fleece has interesting microfibrous morphology with a controllable surface charge that can facilitate the adsorption of chemical compounds such as dyes. Moreover, the adsorption of titania nanostructures (having negative surface charge) onto wool surface can also be achieved by simple impregnation methods in a slightly acidic medium.

1.6. Research Objectives and Scope

About a decade ago Rajeshwar et al. (2001) listed the attributes of an ideal photocatalyst for use in heterogeneous photocatalysis systems:

- Stability and sustained photocatalytic activity
- Good overlap of absorption cross-section with solar spectrum
- High conversion efficiency and quantum yield
- Compatibility with a variety of substrates and reaction environments
- Low cost

The commercially available photocatalyst can utilise only UV light energy, and at relatively low quantum yield. It is highly desirable to find novel photocatalysts that are simple to produce, inexpensive, and also able to utilise the visible spectrum of solar radiation.

Experience with pilot and industrial scale systems also revealed that the easy separation and recovery of the photocatalyst particles from the treated water is another important attribute, especially in case of the most effective slurry type reactors. This is a well-recognised and remaining problem that hinders industrial applications of photocatalysis.

This thesis, therefore, is seeking to reduce or eliminate the above shortcomings. The underlying premise of this work is that the peroxide method offers an effective means to produce improved photocatalysts. The main research objectives and scope of this study are outlined as follows.

1.6.1. Objectives

- Synthesis and characterisation of novel titania nanoparticles and nanoassemblies using the peroxo-titanium method.
- Assessing the potential applications of synthesised nanomaterials in water remediation.

1.6.2. Scope of the Investigation and Thesis Structure

This investigation focuses on the development of novel photocatalysts using Degussa P25 as a titanium precursor, hydrogen peroxide as an oxidising agent and ammonium hydroxide or sodium hydroxide for nitrogen doping and nanostructures synthesis, respectively. As a part of nanotechnology, the development of novel photocatalysts (ideal photocatalysts) is of utmost importance to make photocatalytic water treatment an attractive and cost-effective process.

The use of peroxide method for preparing photocatalysts using conventional titania precursors, such as titanium metal and its organic complexes, and $TiCl_4$ etc (Ichinose et al. 1996; Yada et al. 2006) have been presented in the literature. However, the use of titanium dioxide (Degussa P25) as a precursor has hardly been investigated, and relevant research papers were limited to the study of phase separation by the selective dissolution of rutile using weak ammonia or NaOH concentrations (Ohtani et al. 2007). The use of ammonia to produce nitrogen doped TiO_2 at higher (calcination) temperatures is well documented, and so is the use of NaOH to produce nanofibres but there is much less known about using low and near ambient temperature methods. Therefore, the outline of this research project can be summarised in the following:

- Introducing the concept of the research subject and setting research objectives (Chapter 1).
- Compiling a comprehensive literature review on pertinent findings in nanotechnology, the use of heterogeneous photocatalysis in water remediation and the development of visible-light photocatalysts by doping (Chapter 2).
- Selection of characteristic model water contaminants for laboratory experiments.
- Selection of laboratory equipment and instrumentations to achieve the goals set in Chapter 1 (Chapter 3).

- A review of peroxide methods or similar technologies recently used to produce nanomaterials and discuss the findings of a modified method (Chapter 4).
- Investigating the application of novel photocatalysts in water treatment systems, such as for adsorption and photocatalysis (Chapter 5, 6, 7 and 8).
- Summary of major findings and recommendations for future work (Chapter 9).

Nanomaterials and nanoassemblies synthetised through the facile peroxide route have some remarkable intrinsic advantages that can provide better solutions to a range of current and emerging challenges in environmental remediation. These novel materials are easily produced, inexpensive, and offer cost-effective technologies that are robust and relatively simple to use. Therefore, it is hoped that this work incorporates some new ideas, methods, and findings to make a contribution to the growing use of photocatalysis applications for the purification of water, wastewater and air.

UNIVERSITY OF TECHNOLOGY, SYDNEY

FACULTY OF ENGINEERING AND INFORMATION TECHNOLOGY

CHAPTER 2

LITERATURE REVIEW

2.1. Nanotechnology in Water and Wastewater Treatment

2.1.1. History and Overview

"Nano" is derived from the Greek word for dwarf. A nanometer is one billionth of a meter (10^{-9}) and might be represented by the length of ten hydrogen atoms lined up in a row. In nature, nanotechnology first emerged billions of years ago at the point where molecules began to arrange in complex forms and structures that launched life on Earth. Through evolution, mutations and adaptation; plants were able to convert carbon dioxide using the energy from the visible range of sunlight to oxygen through photosynthesis (Roco 1999). This transformation is taking place in tiny structures called "chloroplasts" composed of several nanoscale "thylakoid disks" that contain the green pigment chlorophyll. Another example of a natural nanotechnology is "chemical catalysis" through "catalysts" or in bioscience called "enzymes". Enzymes are biomolecules that catalyse chemical reactions (Smith et al. 1997) and sometimes they are considered as indispensable for the completion of specific reactions.

In 1867, James Clerk Maxwell was the first to mention some of the nano concepts in nanotechnology through a proposed experiment on a tiny entity known as Maxwell's Demon able to handle individual molecules. In the early 20^{th} century, the first observations and size measurements of nanoparticles using an ultramicroscope were made possible in a study of gold sols and other nanomaterials with sizes down to 10 nm and less (Zsigmondy 1914). Zsigmondy, a Hungarian scientist who also discovered microfiltration among other contributions, was the first to characterise particle sizes using the term nanometer, and he developed the first system of classification based on particle size in the nanometer range. Several advances in the field of nanomaterial characterisation were possible after Langmuir and Blodgett (1920s) introduced the monolayer concept, and Derjaguin and Abrikosova (1950s) conducted the first measurement of surface forces (Derjaguin 1954). In 1959, Richard Feynman described a proposed process to manipulate individual atoms and molecules by using one set of precise tools (Gribbin 1997). Since then, many advances were made in the study of nanoscale structures, and the term "nanotechnology" was first defined by Taniguchi (1974) as "Nano-technology mainly consists of the processing of, separation, consolidation, and deformation of

materials by one atom or one molecule".

The tools and methods for nanotechnology involve imaging, measuring, modelling, and manipulating matter at the nanoscale. In the 1980s nanotechnology and nanoscience got a boost with two major developments: the birth of cluster science, and the invention of the Scanning Tunnelling Microscope (STM). Major tools for nanotechnology measurements include equipment such as STM, scanning probe microscopes (SPMs), atomic force microscope (AFM), and molecular beam epitaxy (MBE) (Roco 1999). Diagnosis of particles at the nanoscale level contributed extensively to the production, modification and shaping of structures that are increasingly used in many industrial, health and environmental applications.

Nanostructure science and technology is a broad research area that encompasses the creation of new materials and devices from nanosized building blocks (Hu and Shaw 1998). Building blocks are used to make molecules that are arranged in nanostructures and nanomaterials having dimensions from 1 to 100 nm. This process is known as a "bottom up" approach where building blocks are arranged and then assembled to form larger size material. The formation of powder components (structural composite material) through aerosol techniques is a main example of this approach (Wu et al. 1993). Many other approaches are being used to synthesise and assemble nanostructures but all have their distinct points a) in the control of the size and composition of nanocluster components, and b) in the control of interfaces and the distribution of nanocomponents within the fully formed materials (Hu and Shaw 1998).

At the nanoscale level, materials often show different physical, chemical and biological properties than at their normal size equivalents (Davies 2006). The surface area of particles increases with decreasing particle size, hence nanoscale particles usually exhibit optical, electrical, and magnetic properties that significantly differ from those exhibited by macroscopic particles (Shelley 2005). The often remarkable characteristics of particles at the nanoscale level, therefore, originate from the increase in the number of surface atoms with decreasing particle size.

Nanotechnology can easily merge with other technologies, and modify, endorse or clarify existing scientific concepts; therefore it is called a “platform” technology (Shmidt 2007). The use of nanotechnology in the future is expected to expand into numerous industrial applications. It will help decrease production costs by reducing energy consumption, attenuate environmental pollution, and increase the production efficiencies in developed countries. Moreover, nanotechnology may be a useful tool to address different social problems of developing countries such as the need for clean water and the treatment of epidemic diseases (Fleischer and Grunwald 2008). Nanoscience and nanotechnology may not provide all the solutions for the ever increasing problems of this planet but could help the sustainable development of many social communities.

The potential benefits of nanotechnology have already been identified by many researchers in the environmental and water sector, medicine, and in several industry applications but the future nanotechnology might bring innovations that can answer many existing scientific questions (Theron et al. 2008; Fleischer and Grunwald 2008; Savage et al. 2008). Hence, nanotechnology is going to play an important role in addressing fundamental issues such as health, energy and water (Binks 2007). Major potential environmental benefits of nanotechnology were reported in the draft nanomaterials research strategy by Savage et al. (2008), including:

- Early environmental treatment and remediation
- Stronger and lighter nanomaterials
- Smaller, more accurate and more sensitive sensing and monitoring devices.

Additional benefits lay in the cost-effective use of renewable energy, low energy requirement and low waste generation devices, early disease detectors for preventive treatment, pollution control, and the prevention and remediation using improved systems.

2.1.2. Benefits of Nanotechnology in Water and Wastewater Treatment

2.1.2.1. Water Treatment

Water purification using nanofiltration technology or through adsorption and catalytic degradation processes was made possible by the advances achieved and mysteries revealed in the quantum world. Worldwide, the need for clean water is increasing because of population increase, drought and the contamination of conventional water sources. WHO (2004) reported that 1 billion people are at risk because they do not have access to potable water and another 2.6 billion people lack access to clean water. The innovation of new technologies to increase the availability of clean water commenced 40 years ago (1960s) with the establishment of three membrane separation processes (Table 2.1): reverse osmosis (RO), ultrafiltration (UF) and microfiltration (MF) (Sutherland 2008). During the 1970s and 1980s, nanofiltration membranes (Loose RO) were developed as an intermediate filtration material between ultrafiltration and reverse osmosis (Eriksson 1988). Membrane processes using different types of membrane are becoming increasingly popular for the production of drinking water from seawater, brackish water, wastewater, surface water and groundwater (Ventresque et al. 2000).

Table 2.1. Membrane type and characteristics (Thorsen and Flogstad 2006)

Membrane type	**Pore size (nm)**	**Pressure (bar)**	**Product water**
Reverse osmosis	< 0.6	30 – 70	Pure water (PW)
Nanofiltration	0.6 - 5	10 – 40	(PW) and low molecular solutes
Ultrafiltration	5 - 50	0.5 – 10	All above and macromolecules
Microfiltration	50 - 500	0.5 - 2	All above and colloids

The impact of nanotechnology on the development of tools and techniques for water treatment will be more pronounced in the near future. As scarcity of natural water threatens the advancement and the social security of many communities around the world, it is expected that the solution will emerge from the exploitation of

nanoparticles to make water recycling, seawater desalination and water remediation more efficient and cost effective. For instance, the use of nanofiltration membranes for treating water in rural areas of South Africa to provide drinking water was described by Smith (2006). The advantages of using nanofiltration relied in the direct humanitarian benefit from using nanotechnology and in the promotion of economical viabilities in rural communities. Therefore, the production of nanostructures, nanocomposites and modified nanostrucutres for water remediation will increase because of the need for producing clean water in fast and low energy consumption ways. Nanotechnology should be regarded as the tool to ensure the sustainability of social communities in diverse places and conditions. This is possible through the use of advanced filtration nanomaterials that enable desalination of seawater, recycling of contaminated water and the reuse of wastewater (Theron et al. 2008).

2.1.2.2. Water Purification

Wastewater is any water that has been adversely contaminated by organic pollutants, bacteria and microorganisms, industrial effluent or any compound that deteriorated its initial quality. It can be sub-divided into: i) municipal wastewater (liquid waste discharged by domestic residences and commercial properties), and ii) industrial wastewater (liquid waste discharged by industrial and agricultural activities). Some of the factors that might affect the composition of wastewater are: land uses, groundwater levels, and the degree of separation between stormwater and sanitary wastes. The composition of municipal wastewater is usually less variable than of industrial wastewater, the latter being highly affected by the type of industrial activity involved in the discharge of effluent water. In general, the organic composition of wastewater is estimated to consist of proteins (50%), carbohydrates (40%), fats and oils (10%), and trace amounts (e.g. μg/L or less) of priority pollutants, surfactants, and emerging contaminants. Communal (or municipal) wastewater typically contains 10^5-10^8 colony forming unit (CFU)/mL of coliform organisms, 10^3-10^4 CFU/mL fecal streptococci, 10^1-10^3 protozoan cysts, and 10^1-10^2 virus particles (Ellis 2004).

Treatment of municipal wastewater has to take into consideration all the aspects

related to water contamination, and has to ensure that the product water is free from any substance that might adversely affect the health of humans and the environment. The choice of treatment processes used in wastewater treatment plants is directly related to the composition of the raw (influent) wastewater. Generally, conventional sewage treatment includes the following stages (Crites and Tchobanoglous 1998):

i. Preliminary treatment: to remove coarse and readily settleable inorganic solids with the size range of more than 0.1 mm.
ii. Primary treatment: to remove the bulk of suspended solids including both organic and inorganic matter (0.1 mm to 35 μm).
iii. Secondary biological treatment: to degrade the biodegradable organic matter and nutrients.
iv. Tertiary treatment: to remove a portion of the remaining organic and inorganic solids and pathogenic microorganisms and nutrients. This treatment is normally followed by chemical or physical disinfection before disposal.

Industrial wastewater could be designated as the effluent produced from any industrial activity such as agriculture, food processing, dyeing factories, iron and steel industry, mines and quarries, etc. The composition of industrial effluent will vary according to the activity in question. Therefore, treatment is typically selective to ensure high quality purified water (effluent) at minimal costs. Wastewaters from agricultural activities usually have high organic concentrations originating from animal and vegetable sources, micro-organisms, and various chemicals used for the control of pest and diseases. In contrast, industrial wastewater originating from the metal processing industry, mines or chemical industries might be rich in heavy metals, organic and inorganic compounds as well as chlorinated by-products. Treating industrial wastewater in some cases (i.e readily biodegradable wastewaters) may follow the same stages described for municipal wastewater treatment, but more often involves various physicochemical unit processes (neutralisation, ion exchange etc.) to ensure low concentrations of specific pollutants.

For the purpose of improving the above listed treatment processes, the use of nanomaterials was being researched to fabricate separation and reactive media which

are of high quality in terms of reactivity and performance (Bellona and Drewes 2007). Additionally, the use of nanomaterials and nanoparticles to bio-remediate and disinfect wastewater is gaining popularity (Hu et al. 2005; Mohan and Pittman 2007). For instance, metal oxide nanomaterials such as TiO_2 are among the promising nano-catalysts that were tested successfully for their antimicrobial activity. Moreover, fullerenes (C60) are being used as pollution tracers to provide contaminant-fate information to assist in developing water remediation strategies; magnetic nanoparticles are being developed to adsorb metals and organic compounds; and nanocatalysts are being explored to reduce pollution of oxidised contaminants (Hillie et al. 2006).

For example, metal processing wastewater often contains hexavalent chromium species, Cr(VI), which are toxic, acting as carcinogens, mutagens and teratogens in biological systems (Dupont and Guillon 2003). Metal industries are required to reduce the amount of chromium in their effluent to around 0.1 mg/L (Ayuso et al. 2003) before discharging it into the sewer system. Maghemite nanoparticles were studied by Hu et al. (2005) for their potential in removing and recovering chromium from wastewater. The authors developed a new method by combining the adsorption ability of nanoparticles and the magnetic separation technique. The method was space-saving, cost-effective, simple, and environmentally friendly. Additionally, chromium was successfully removed from the wastewater and the nanoscale maghemite retained its original metal removing capacity after six adsorption-desorption cycles. The adsorption was pH dependent with optimal adsorption at pH 2.5.

The use of nanotechnology to remove contaminants from water is spreading and many advances have already been made. An illustrative summary of recent advances in nanomaterial research for industrial wastewater treatment includes: the nanofiltration of biologically treated effluents from the pulp and paper industry (Manttari et al. 2006); the degradation of organic dyes using manganese–doped ZnO nanoparticles (Ullah and Dutta 2008); the treatment of wastewater from molasses distilleries using nanosize pore membrane (Satyawali and Balakrishnan 2008).

2.1.3. Application of Nanotechnology in Water and Wastewater Treatment Processes

Nanotechnology for water remediation will play a crucial role in water security and consequently the food security of the world. The applications of nanotechnology in the cleanup of contaminated water was summarised by Smith (2006):

- Nanoscale filtration techniques
- The adsorption of pollutants on nanoparticles
- The breakdown of contaminants by nanoparticle catalysts.

These aspects will be briefly discussed below.

2.1.3.1. Nanomaterials and Membrane Filtration

Since sedimentation, flocculation, coagulation and activated carbon each remove a narrow spectrum of water pollutants, membrane filtration (UF, MF, NF and RO) have played a significant role in reducing pollutants and producing high quality pure water (Strathmann 2001). In the last two decades, the development of polymeric and ceramic membranes has positively impacted on the use of membranes. Nevertheless, membrane fouling is a major drawback in the membrane filtration process and poses a serious problem that challenges the viability of the use of membrane.

Nanotechnology is being applied in the production of water purification membranes used in advanced treatment. Recently, Theron et al. (2008) reported the following water filtration membranes are produced from nanomaterials: i) nanostructured membranes made from carbon nanotubes, nanoparticles and dendrimeres, and ii) nanoreactive membranes made from metal nanoparticles and other nanomaterials.

Cohen (2006) reported that a promising approach to improve membrane performance, while mitigating fouling, is to structure the membrane surfaces at the nano- and molecular scale. Porous carbons have a great potential in adsorption and in membrane synthesis for water filtration as they are considered as “molecular sieve

materials". Water filters from carbon nanotubes were synthesised by Srivastava et al. (2004). Those filters were re-usable and showed effective removal of bacterial pathogens (*Escherichia coli* and *Staphylococcus aureus*) and Poliovirus sabin 1 from contaminated water.

The nano-structure manipulation of nanofiltration membranes to produce a surface with salt rejection selectivity was achieved with Linder and Oren (2006). Membranes were prepared having above 70% rejection to NaCl and less than 40% rejection to $CaCl_2$ in single solution. This monovalent/divalent cation selection is very important to minimise membrane fouling by calcium carbonate or sulphate salts and to keep the Na to Ca ratio to a proper level for agricultural purposes. In a similar approach, the nanostructure surface modification of microporous ceramics was achieved by Wegmann et al. (2008) for the aim of efficient virus filtration. The procedure consisted of coating the internal surface area of highly porous elements with a colloidal nano-dispersion of hydrated yttrium oxide. It was then heat treated to obtain an electropositive Y_2O_3 coated surface. Modified nanostructure filters were able to remove about 99.99% of 25 nm diameter MS2 bacteriophages from feed water of pH between 5 and 9.

Water filtration membranes fabricated from nanomaterials are already being promoted by water treatment companies. For instance, Agronide (Pittsburgh) has a product called "*NanoCeram*", which is a purifier that uses 2 nm diameter alumina nanofibres to remove 99.9999% of bacteria, viruses and protozoan cysts from water (Smith 2006).

The use of nanostructured material for improving membrane filters will gain more interest in the near future, because of unlimited benefits that accrue from producing membranes with superior performance in terms of organic and biological contaminants removal, with metal selectivity, that are resistant to fouling, durable and cost-effective. Additionally, nano-reactive material has been used to synthesise membranes for use in water treatment. Nano-reactive membranes were able to decompose pollutants such as 4-nitrophenol (Dotzauer et al. 2006) and bind metal ions (Hollman and Bhattacharyya 2004) in water solution. Polysulfonate

ultrafiltration membranes impregnated with silver nanoparticles were found effective against *E. coli* K12 and *P. mendocina* bacteria strains and showed a significant improvement in virus removal (Zodrow et al. 2009). The nanosilver impregnated membranes (nAg-PSf) were resistant to biofouling mainly because the attachment of bacteria to the membrane surface was prohibited by Ag^{+}.

Recently, TiO_2 nanowire membrane has been successfully fabricated with the capability of filtering organic contaminants from water with simultaneous photocatalytic oxidation (Xiao et al. 2008). Nanowire membrane had uniform thickness, flexible, with nanowires of 20-100 nm in diameter (Figure 2.1). It showed similar photocatalytic activity as Degussa P25 for decomposing humic acid in water and exhibited excellent anti-fouling ability (Zhang et al. 2008).

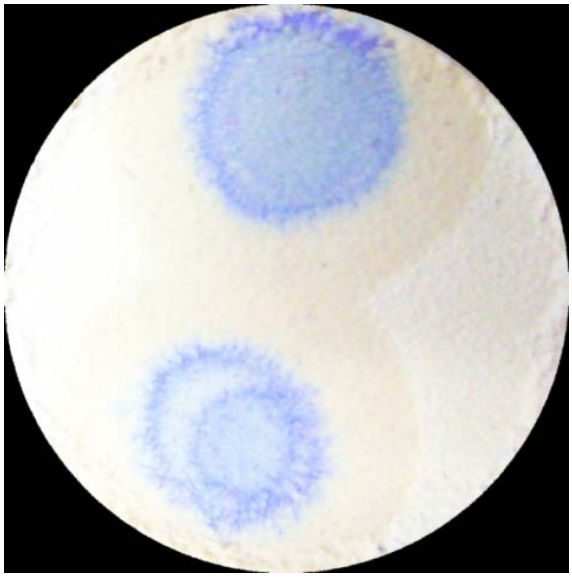

Figure 2.1. TiO_2 nanowire membrane with simultaneous photooxidation potential (Xiao et al. 2008).

Composite photocatalytic membranes, that combine the separation technology provided by the membrane process and the photocatalytic activity of catalysts, were studied by several researchers (Molinari et al. 2000; Zhang et al. 2006; Yang and Li 2008). TiO_2/Al_2O_3 composite membranes fabricated by following the extrusion method and sol–gel/slip casting method effectively decomposed Direct Black168 dye (82% removal) when photocatalysis is coupled with membrane separation

(Zhang et al. 2006). Similarly, Yang and Li (2008) have successfully employed the extrusion method and sol–gel/slip casting method to prepare inside-out tubular TiO_2/Al_2O_3 composite membranes. They reported that the prepared tubular TiO_2/Al_2O_3 composite membranes degraded a great amount of the water pollutant of concern from the target wastewater that had a final permeate turbidity of lower than 0.75 NTU.

2.1.3.2. Metals, Bimetallic Nanoparticles and Mixed Oxides

Adsorption is considered as an effective, efficient and economic method to remove water contaminants (Jiuhui 2008). Effective adsorbents used in the water industry include: i) activated carbon, ii) clay minerals and silicas, iii) zeolites, iv) metal oxides, and v) modified composites (Nouri et al. 2002; Zhang et al. 2005; Theron et al. 2008).

Metals such as iron, copper, gold, aluminium, nickel and silver were used as nanoparticles to improve the quality of several industrial products. Metal nanoparticles can be prepared by chemical (chemical reduction, electrochemical techniques and photochemical reduction) or physical methods (Chen et al. 2001). In water treatment, nanometals were either used in suspensions to degrade contaminants after activating the magnetic behaviour of these metals or by the impregnation into catalysts surfaces to enhance the activity of catalysts such as Au-TiO_2 (Kumar et al. 2008). Iron nanoparticles received considerable attention compared to other metals for its potential applications in water treatment. Zero-valent iron nanoparticles are capable of transforming a wide spectrum of environmental pollutants such as chlorinated organic compounds, heavy metals (As, Pb, Cu, Ni, and Cr), and polychlorinated biphenyls to harmless derivatives (Theron et al. 2008).

Additionally, silver ions have been well known for their toxic effects on bacteria and a wide range of microorganisms (Zhao and Stevens 1998). However, the bactericidal activity of Ag nanoparticles on the bacteria is only partially understood. A brief review of some metal compounds for the treatment of water and wastewater are

presented in Table 2.2.

Bimetallic nanoscale iron particles generated when mixing zero-valent iron (Fe^0) with either palladium (Pd^0) or nickel (Ni^0) were superior in decomposing highly toxic chlorinated organic compounds in wastewater treatment (Cheng and Wu 2001; Hildebrand et al. 2008). Nanoscale bimetallic particles were used extensively for the hydrodechlorination of chlorinated aliphatics and aromatics (Theron et al. 2008). Chlorinated compounds are usually used in the chemical industry and also as agricultural chemicals (Shih et al. 2009). Dechlorination of chlorinated methanes by Pd/Fe nanoparticles was provoked by an expanded bimetallic surface area of particles, enhanced reactivity and low concentration of intermediates (Wang et al. 2009). Palladium-coated gold nanoparticles (Pd/Au) catalytic activity was 70 times more effective than Pd nanoparticles alone, mainly because Au augmented the catalytic ability of palladium (Nutt et al. 2005). The synergetic effect of a Pd on Fe nanoparticles was fully described in a recent study by Shih et al. (2009), who drew two chemical reduction pathways of hexachlorobenzene (HCB) with nanoscale Fe and nanoscale Pd/Fe bimetallic nanoparticles. The Pd/Fe nanoparticles showed faster reduction kinetics of HCB, produced less chloro substituents and resisted oxidation. It is noteworthy to mention that HCB was listed among the dirty dozen persistent organic pollutants (POPs) in the Stockholm Convention.

Table 2.2. Metal compounds and their effect on water and wastewater contaminants

Metal	**Purification effect**	**Reference**
Zero valent iron	Arsenic removal, chlorinated organics, nitroaromatics, nitrate, azo dyes and metal ions deactivation	Morgada et al. 2008 Powell et al. 1995; Deng et al. 2000
Metallic iron	EDTA and synthetic dyes degradation	Pereira and Freire 2006; Gyliene et al. 2008
Silver nanoparticles	Antibacterial and antifungal properties	Lepape 2002

On the other hand, mixed oxides have a good potential as novel adsorbents or catalysts with good photoactivity in water purification (Zhang et al. 2006; Jiuhui 2008). They can be produced through several methods, which are listed below and described in details by Shelley (2005):

- Plasma-arc and flame hydrolysis methods
- Chemical vapour deposition (CVD)
- Electrodeposition techniques
- Sol-gel synthesis
- Mechanical crushing via ball milling
- Use of naturally occurring nanomaterials

Metal oxides such as aluminium oxide, magnesium oxide and titanium dioxide, as well as mixed oxides such as silica-titania have good photocatalytic activity (Shelley 2005). Therefore, they have been used to treat water, to decompose contaminants and to degrade persistent pollutants. The processes of decomposition occur through different routes listed below and were discussed by Jiuhui (2008):

- Adsorption/catalytic oxidation process
- Adsorption/catalytic reduction process
- Adsorption coupled with redox process

Iorio et al. (2008) investigated the sorption of phenanthrene (organic pollutant) by dissolved organic matter (Polymerin) and its complex with Al_2O_3 nanoparticles. The sorption was greatly influenced by the physical state of the complex. Additional findings were promising regarding the use of organic sorbent associated with aluminium oxide nanoparticles to treat water contaminated with hydrophobic organic compounds. Somewhere else, the size of MgO nanoparticles greatly affected its bactericidal activity against *E. coli* and *S. aureus*. The bactericidal activity decreased when MgO nanoparticles size increased from 8 nm to around 11 to 23 nm (Makhluf et al. 2005). Similarly, titanium dioxide nanoparticles are known for their ability (Theron et al. 2008; Jiuhui 2008): i) to adsorb contaminants in water, ii) to decompose water pollutants under UV light irradiation and iii) to kill different strains of bacteria and fungi.

Recently, a complex compound of silica-titania was used to degrade methylene blue as a simulated aqueous organic pollutant in wastewater. The complex of silica-titania arranged in aerogel-like balls (STABs) was prepared by mixing self-made titania sol with commercial silica sol to obtain a silica-titania sol. This was followed by the ball-dropping method and sol-gel process. STABs displayed excellent photocatalytic activity for degrading water contaminants such as methylene blue (Xu et al. 2007).

2.1.3.3. Modified Photocatalysts

The effectiveness of heterogenous photocatalysis has been demonstrated in many scientific studies (Liu and Yang 2003; Cho et al. 2005; Wei et al. 2008; Kumar et al. 2008), and thus its application for the decomposition of recalcitrant and toxic organic compounds is gaining popularity.

TiO_2 based (nano) photocatalysts were used in many environmental applications because titania is cheap, chemically stable, and resistant to corrosion (Dvoranova et al. 2002). The remediation of contaminated water (groundwater and wastewater) using TiO_2 photocatalyst was established for the decomposition of organic matter in water, the degradation of dyes from industrial wastewater and killing bacteria, viruses, fungi and algae in water (Cho et al. 2005; Cho et al. 2005a). The main challenge in this area is to find ways to improve the efficiency of these processes (Cho et al. 2005; Liu et al. 2006). Some of the limitations associated with water treatment by photocatalysis using TiO_2 are:

- Wide band-gap that requires the use of UV light for photocatalytic activation
- Limited surface area in contact with contaminants
- Difficulty of separating TiO_2 nanoparticles from water suspensions

The deposition of nanoparticles on the surface of catalysts is known to provide a larger contact area between the catalyst and the target pollutant, which results in enhanced photocatalytic activity (Schiavello 1998). Sharma et al. (2009) discussed the use of silver nanoparticles to improve the catalytic activity of TiO_2. Ag/TiO_2 surfaces were characterised by advantageous properties, such as activation by visible light, biological compatibility, and antimicrobial activity (Hamal and Klabunde

2007). Loading TiO_2 surface with Au was investigated by Kumar et al. (2008). Au-TiO_2 (8 at. wt % on TiO_2) photocatalysts were prepared by deposition-precipitation method and used for the photocatalytic degradation of an azo dye (Acid Red 88; AR88). The modified catalyst was found to be efficient in degrading Acid Red 88 dye under visible light irradiation, which offered a new perspective for developing visible light responsive catalysts.

Nano-sized TiO_2 and Fe/TiO_2 prepared by a sol–gel method with an anatase dominant crystal structure were used for the photodegradation of 1,2-dichloroethane (1,2-DCE) (Hung et al. 2008). Spherical crystallite particles with sizes of about 10–20 nm were produced. Fe/TiO_2 showed a slight increase in photoactivity in the visible light region with the increase in iron ion doping concentration. The photocatalytic performance of Fe/TiO_2 was better than that of TiO_2 and P25, showing that Fe doping enhanced the catalytic activity of the catalyst and to achieve enhanced 1,2-DCE photodegradation.

The necessary separation and recovery of fine photocatalyst particles from the treated water after photocatalysis is the main disadvantage of the otherwise most effective slurry type reactors. This is a recognised problem that hinders industrial applications. For a promising solution, titania microspheres were synthesised using $TiCl_4$ and $FeCl_3$ as the precursor in the presence of Span-80. The procedure consisted of mixing 5 ml of $TiCl_4$ with 25 ml of 0.3 M $FeCl_3$ and 2 ml of Span-80. The solution was placed in Teflon lined autoclave and was subjected to hydrothermal treatment at 180°C for 48 h. The resulted precipitate was separated from the solution by centrifugation, washed with anhydrous alcohol and water (until pH 7), dried at 60°C and later on calcined at 400°C for 2 h to remove surfactant and organic impurities. The synthesised microspheres were able to degrade 100% of methyl orange (MO) under UV-light irradiation for 3 h and 91% under solar irradiation for 6 h. The most notable achievement was the fast sedimentation of the catalyst after the photocatalytic reaction (Figure 2.2), which facilitated a simple separation from the treated water solution (Wei et al. 2008).

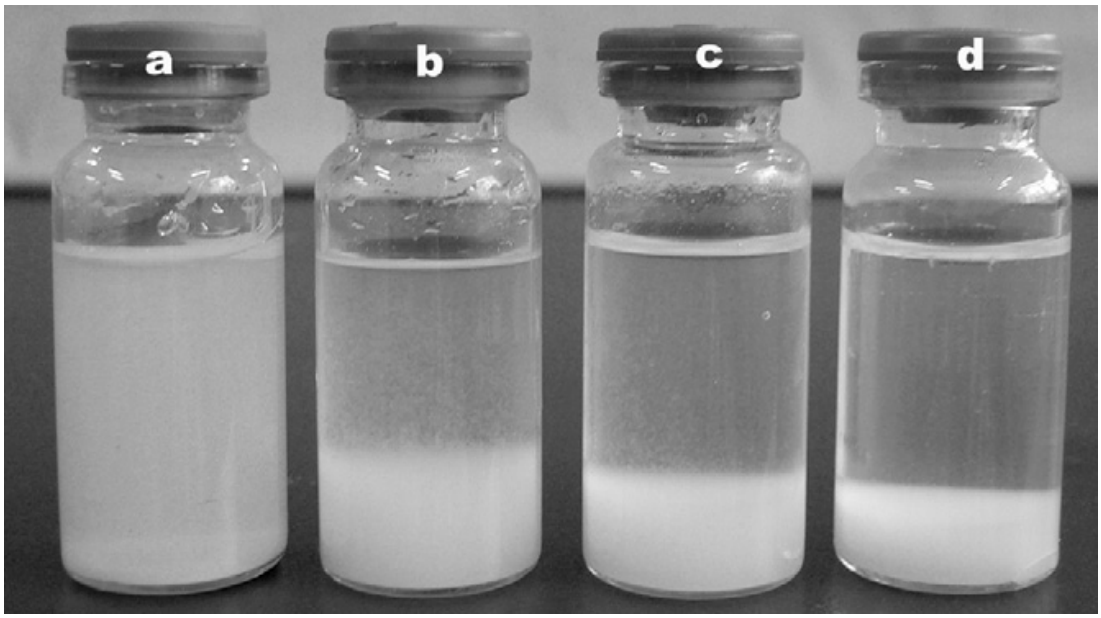

Figure 2.2. Sedimentation of (a) TiO_2 nanoparticles after 30 min and microspheres for (b) 5 min, (c) 15 min and (d) 30 min (Wei et al. 2008).

Similarly, a modified two step sol–gel method (hydrolysis of titanium (IV) butoxide and hetero-coagulation with pretreated kaolinite (K) clay) was used to synthesise a novel titania impregnated kaolinite (TiO_2/K) photocatalyst. The photocatalyst had a rigid porous layer structure, promising nano-size properties and an enhanced adsorption and photocatalytic ability for the removal of Congo red from an aqueous solution. Furthermore, the TiO_2/K photocatalyst was easily separated and recovered from the treated water system by settling (Chong et al. 2009).

2.1.4. Nanotechnology and Human Health

The use of nanomaterials in different applications will increase the risk to human exposure. The populations at risk are mainly researchers and workers in the field of nanotechnology, family members of researchers, consumers of products containing nanomaterials, but increasingly the general public as well (Hoyt and Mason 2008). There is still little information available on the effect of nanotechnology on human health. Generally, nanoparticles can enter the human body through different routes such as skin absorption, ingestion and inhalation (UBA 2006). Skin adsorption occurs after using products such as sunscreens and cosmetics that contain compounds like titanium dioxide. Titanium dioxide enters the skin through the

epidermal layer and it is believed that sunlight exposure might cause deep absorption of nanoparticles. Ingestion of nanoparticles is not a common route but can happen after a hand-to-mouth contamination or as a consequence of inhalation. Ingested nanoparticles traverse the digestive system and might end up in the blood stream, which will carry them to other organs such as kidneys, liver or even the brain. The adverse effect of nanomaterials on the metabolism of organs is not well understood, but their deposition is believed to cause malfunction due to special nanomaterials' characteristics. The most common route of human exposure is inhalation because it can happen easily when nanomaterials dust is present in the workplace. Researchers and workers are the population most at risk when dealing with nanomaterials or nanomaterial products. Nanoparticles enter lungs through the respiratory tract and are deposited in the alveoli. This happens because the small size of nanoparticles prevents their detection by macrophages that usually envelop toxic compounds and remove them from the lungs (Hoyt and Mason 2008). The toxicity of nanoparticles is much more pronounced because they have higher surface area and can react more easily than microparticles. Some studies have reported that carbon nanotubes can damage the lungs if inhaled, while other studies discussed the damage caused to the liver and brain by fullerenes (Shelley 2005). Animal cells are normally not equipped to resist contaminants at the nanoscale level such as nanotubes, therefore their impact is believed to be high as cells will be fully exposed to such nanomaterials.

2.2. Heterogeneous Photocatalysis over TiO_2

2.2.1. Overview

The term “photocatalysis” refers to a chemical transformation or the acceleration of a chemical reaction in the presence of light and a photocatalyst (Kisch, 1989). Various types of photocatalysts are listed in the literature; which can be classified into three groups (Sakata 1989):

1. Dye molecules used as homogeneous photocatalysts
2. Semiconductors used as heterogeneous photocatalysts (HP)
3. A combination of dye and semiconductor species to give dye sensitised photocatalysts

In HP, reactions occur at an interface of a solid/liquid (for aqueous pollutants) or of a solid/gas (for gaseous pollutants). Photocatalytic reactions are initiated by the absorbance of photons to drive subsequent redox reactions on the irradiated (activated) surface of the photocatalyst. The adsorption of pollutants on the photocatalyst is important for their photodegradation, although the photodegradation of pollutants can also occur at a small distance from the irradiated surface due to the migration of reactive species in air and water (Kikuchi et al. 1997; Tatsuma et al. 2001). The photocatalyst is involved in the reactions but is not consumed, chemically altered, or transformed. The most popular semiconductor used in HP is TiO_2 for being relatively inexpensive, chemically stable, and non-toxic.

The use of HP as a green technology in environmental remediation has been well studied to explore the benefits and identify the challenges in this field (Chen et al. 2000; Fujishima et al. 2007). The removal of indoor odours by immobilised TiO_2 films under weak UV illumination (Ohko et al. 1997), the bactericidal effect of TiO_2 under low intensity UV-illumination (Kikuchi et al. 1997), the self-cleaning TiO_2 surfaces (Minabe et al. 2000), and the photocatalytic decomposition of endocrine-disrupter chemicals in water (Ohko et al. 2002) are few examples of using HP in environmental applications.

The growing importance of wastewater reuse and the resulting need to remove recalcitrant pollutants from water has impacted the science and engineering of water treatment, to generate significant research interest in this area (Ollis et al. 1989; Herrmann e al. 1993; Gaya and Abdullah 2008; Chong et al. 2010). Conventional biological methods are unable to fully remove certain pollutants, such as pharmaceuticals, some dyes, personal care products, and pesticides from water. Therefore, new treatment methods, including advanced oxidation processes have gained popularity in order to solve the pollution problems created by emerging pollutants. The application of HP in water treatment has been considered an effective way to eliminate harmful pollutants either by their complete mineralisation or partial degradation that allows successive biological treatment. The major advantages of HP can be summarised as follows:

1. Full degradation (mineralisation) of contaminants even at trace level concentrations
2. Formation of toxic or harmful by-products can be avoided
3. Minimal production of sludge
4. Possibility for the utilisation of sunlight as energy source

Hence, the research and development in the field of HP is growing in order to find suitable photocatalysts for environmental applications and water treatment. The fundamentals of HP using TiO_2, including reactor engineering, the effect of operational parameters, and the kinetics of the photocatalytic reactions will be discussed in the following sections.

2.2.2. Fundamentals and Basic Principles

The band gap (i.e. the gap between the conduction and valence band) of semiconductors can be simply calculated from the formula shown below, where λ is the excitation wavelength of the semiconductor.

E_G (Band gap in eV) = 1240 / λ (nm) (Eq. 2.1)

In general, the photocatalytic properties of semiconductors depend on several factors: i) the position of the energetic level, ii) the mobility and mean lifetime of the photogenerated electrons and holes, iii) the light absorption coefficient and iv) the nature of the interface (Augugliaro et al. 2010).

The continuous UV irradiation of TiO_2 promotes an electron (e^-) from the valence band to the conduction band to leave a positive hole (h^+) in the valence band. The e^- and h^+ charges migrate in random directions to the bulk or surface of the particles. Those elementary charges that reach the surface of the catalyst can react with electron-donors and electron-acceptors species present at the semiconductor/electrolyte interface, or recombine to generate heat (Fujishima et al. 2008). In contrast, the ones trapped in the bulk can only recombine with the release of heat (Linsebigler et al. 1995; Fujishima et al. 2008). The position of the valence band and conduction band edges, as well as the energetic levels of any redox couples are essential parameters to establish if thermodynamics allow the occurrence of oxidation and/or reduction of the species in solution (Chen et al. 2000).

The adsorption of photon by TiO_2 allows the direct transformation of light quanta into chemical energy. After illumination by a UV source the following sequence of events can occur on the surface of TiO_2 (Augugliaro et al. 2010):

$$TiO_2 + h\nu \rightarrow TiO_2(e^-_{(CB)} + h^+_{(VB)}) \quad \text{(Eq. 2.2)}$$

$$OH^- + h^+_{(VB)} \rightarrow {}^\bullet OH \quad \text{(Eq. 2.3)}$$

$$O_2 + e^-_{(CB)} \rightarrow {}^\bullet O_2^- \quad \text{(Eq. 2.4)}$$

$${}^\bullet O_2^- + H^+ \rightarrow {}^\bullet HO_2 \quad \text{(Eq. 2.5)}$$

$$2\,{}^\bullet HO_2 \rightarrow O_2 + H_2O_2 \quad \text{(Eq. 2.6)}$$

$$H_2O_2 + {}^\bullet O_2^- \rightarrow OH^- + {}^\bullet OH + O_2 \quad \text{(Eq. 2.7)}$$

At the solid-liquid interface, and on different zones of the same particle, the redox reactions permit the degradation of many organic and inorganic pollutants by means of formation of very reactive radical species generated in the presence of O_2 and H_2O. The role of oxygen is very important and can be summarised in i) assisting the

charge separation in TiO_2 by capturing TiO_2 electrons, ii) participating in reactions as an actual oxidizer and iii) the generation of active species such as H_2O_2, $^{\bullet}O_2^-$.

2.2.3. Photocatalytic Reactors

There are many factors which have to be considered when designing a photoreactor for water or wastewater treatment. The geometry of the photoreactor, the photocatalysis mode and the energy source (UV lamps or solar light) are the main parameters that impact the final design (Wang et al. 2010).
Based on the geometry, photoreactors could be divided into: i) immersion well, ii) annular, iii) elliptical, iv) multi-lamp, v) film, and vi) fluidised bed classes.

According to the photocatalysis mode, photocatalytic reactors are generally classified into: i) slurry batch photoreactors and ii) fixed-bed photoreactors (Mozia 2010). In the first case, an aqueous suspension of the photocatalyst is mixed with the polluted stream to ensure maximum contact. Even though the efficiency of these systems is high, the separation of the photocatalysts is a main hurdle for industrial up-scaling. In the second type of photoreactors, the photocatalyst is usually immobilised on a solid non-reactive support, such as glass or quartz, to avoid the separation of particles from the solution. Unfortunately, the photocatalytic performance of such systems is typically lacking due to the reduced exposure and activation of photocatalytic surfaces (McCullagh et al. 2011).

The energy source affects the feasibility of any photocatalytic systems. The use of UV lamps requires electrical energy which can negatively impact the cost of the treatment system. In contrast, solar light is free and can be used to activate TiO_2 as its spectrum contains up to 5% of UV light. Solar reactors are divided into concentrated and non-concentrated reactors. Various types have been used for heterogeneous photocatalysis, including i) parabolic trough reactor, ii) compound parabolic collecting reactor, iii) double skin sheet reactor, and iv) thin film fixed bed reactor (Wang et al. 2010).

In the last decade, the photocatalytic degradation of organics was achieved in hybrid photoreactors such as the photocatalytic membrane reactor (Molinari et al. 2000; Choi et al. 2007; Zhang et al. 2009) and the submerged membrane photocatalysis reactor (Ryu et al. 2005; Fu et al. 2006; Rizhi et al. 2009). These studies, which targeted the use of hybrid membrane photocatalytic systems, tried to combine the more effective slurry type photoreactors with membrane modules to ensure an adequate separation of suspended particles.

In a recent publication McCullagh et al. (2011) discussed the latest photoreactor configurations used in environmental remediation. They concluded that the future of photoreactor technology depends on the engineering and design of photoreactors, as well as on the development of more effective photocatalysts, especially in rate-limited systems. For industrial applications the photoreactors need to meet the challenges of capacity, ruggedness, reliability, and ease of operation. In the view of these authors currently only suspension (slurry) type reactors are capable of (with some limitations) meeting such expectations.

2.2.4. Operational parameters

There are several factors (including operational or process parameters) that directly influence the overall photocatalytic process efficiency in a given photoreactor system. The most significant factors include photocatalyst loading, composition and characteristics of the catalyst, contaminant composition and concentration, light intensity, pH of the solution, oxygen supply, and the temperature of reaction. Other engineering parameters such as the detention time and reactor hydraulics are case specific and will not be discussed hereafter.

2.2.4.1. Photocatalyst Loading

The increase of TiO_2 loading increases the rate of the photocatalytic reaction up to some limit, which is due to the increase in the surface area of the photocatalyst available for adsorption and degradation (Mozia et al. 2010). It is necessary to find an optimum mass for a defined application to avoid the decrease of photocatalytic

activity (Gaya and Abdullah 2008). Since the photocatalytic activity is also dependent on the surface absorption of photons by TiO_2 particles, the further increase of TiO_2 loading above the optimum level leads to light screening (shading effect) that results in a decrease in photoefficiency (Chong et al. 2010). Moreover, increased particle collision and agglomeration at high loadings also results in loss of the active surface area (Kaneco et al. 2004).

2.2.4.2. Composition and Characteristics of Photocatalysts

While photocatalysis is sometimes described as being non-selective, this appearance is only due to the extreme reactivity of hydroxyl radicals that react with many compounds. However, the rates still strongly depend on the physicochemical properties of both the photocatalysts and pollutants. Rutile, anatase, mixed photocatalysts i.e. Degussa P25 and doped catalysts have all been tested and photocatalytic differences were reported. The particle size, surface area, porosity and surface charge are the main physical factors affecting photodegradation of certain pollutants. In contrast, metal doped TiO_2 with the presence of impurities and non metal compounds might also significantly affect the photocatalytic reaction. For that reason there is no single “best” photocatalyst that offers a universally high performance (section 2.1.3).

2.2.4.3. Concentration of Pollutants

In HP, organic contaminants can be divided into many and various groups according to their chemical compositions, molecular structure, functional groups, solubility, and their pathways of decomposition. In general, the dark adsorption of organics onto TiO_2 surface precedes photo-oxidation process that occurs during UV irradiation. However, at high pollutant loadings, surface saturation becomes a 'shading' barrier to the absorption of photons by TiO_2 leading to performance degradation by photocatalyst deactivation (Saquib and Muneer 2003; Arana et al. 2004). The determination of an optimal organic loading for a given photoreactor is essential to ensure effective operational conditions. Palmisano et al. (2007) have reported that organic molecules with electron withdrawing group adsorb more

significantly than molecules with electron donating groups. It was also shown that organics with complex molecular formulae (4-chlorophenol, humic acid, etc.) break down to various intermediate products before final mineralisation (Palmisano et al. 2007). In contrast, simple compounds such as oxalic acid have been reported to undergo direct mineralisation to CO_2 and H_2O (Bahnemann 2004). Therefore, the degradation of complex material is best monitored by COD/DOC and/or salt concentration measurements, while HPLC and UV-vis spectroscopy (for measuring a single compound concentration) is quite satisfactory for monitoring the degradation of oxalic acid in order to investigate the kinetics of the photoreaction.

2.2.4.4. Effect of pH

The variation of pH is known to play an important role in the photocatalytic treatment of aqueous organic contaminants. Konstantinou and Albanis (2004) described the effect of pH on the photocatalytic reaction over TiO_2 through: i) changing the ionisation state of TiO_2, ii) modifying the position of the conduction and valence bands, iii) assisting in the agglomeration or dissociation of TiO_2 particles, and iv) interfering in the formation of hydroxyl radicals. Moreover, the process pH (a measure of hydronium ion mol concentration in water) also directly affects the solubility of pollutants, and surface charges.

In general, the isoelectric point or the point of zero charge (PZC) of Degussa P25 TiO_2 lies between pH 6 to 7. In any case, the increase of pH leads to an increase in negative surface charge, while a decrease will result in a more positively charged surface according to the following reactions (Gaya and Abdullah 2008; Chong et al. 2010):

$$\text{At pH} < \text{PZC: } TiOH + H^+ \leftrightarrow TiOH_2^+ \quad \text{(Eq. 2.8)}$$

$$\text{At pH} > \text{PZC: } TiOH + OH^- \leftrightarrow TiO^- + H_2O \quad \text{(Eq. 2.9)}$$

Therefore, the adsorption of charged molecules or species onto TiO_2 is strongly influenced by the pH of the aqueous medium. Negatively charged contaminants are

better adsorbed at lower pH (pH < PZC), while positively charged contaminants are better adsorbed at higher pH (pH > PZC) by electrostatic interaction.

Surface charge neutralisation (pH = PZC) promoted to the formation of larger particle clusters and easier sedimentation (Chong et al. 2010). However, the aggregation of particles could detrimentally reduce the photocatalytic efficiency through the reduction of the exposed surface area and shading effect. The size of agglomerates was found to be highly dependent on the pH difference from the point of PZC (Malato et al. 2009).

The reaction between a hydroxide ion and a positive hole generates a hydroxyl radical (Eq. 2.3). This reaction is favoured under alkaline conditions (more OH^- are available at the TiO_2 surface). The reaction between H^+ ions and e^- also generates reactive radical species (Eq. 2.5), and under acidic conditions, the positive holes might be the major oxidation species (Konstantinou and Albanis 2004). Moreover, hydroxyl radicals can also form through Eq. 2.7. Therefore, it can be seen that the process pH has multiple effects on the photocatalytic reactions; and thus, it is essential to determine the optimal pH for specific applications.

2.2.4.5. Light Intensity

The excitation of TiO_2 surface by a radiant photonic flux ($\lambda < 400$ nm) occurs at very low light intensity. Fujishima et al. (2000) indicated that few photons of energy (as low as 1 $\mu W/cm^2$) are sufficient for the initiation of the photocatalytic reaction. However, the increase of light intensity is essential to ensure that the photocatalyst surface is being appropriately irradiated. The photocatalytic activity of TiO_2 was related to the incident light intensity and the relationship can be summarised as follows (Ollis et al. 1991; Qamar et al. 2006: Mozia et al. 2010): i) at low light intensities (0-20 mW/cm^2) the photocatalytic reaction rate is proportional to the radiant flux, ii) at intermediate light intensities (approx. 25 mW/cm^2) the dependency changes to a square root dependency, and iii) at high light intensities the dependency is reduced to zero.

The increase of reaction rate at low irradiation intensities is due to the formation of electron-hole pairs, with a negligible recombination rate. Above a certain radiant flux the recombination becomes significant and affects the photocatalytic reaction rate. At very high radiant flux intensities the saturated surface coverage results in mass transfer limitations (adsorption and desorption), coupled with another limiting step of the electron transfer from the photocatalyst to the oxygen (Doll and Frimmel 2005).

2.2.4.6. Dissolved Oxygen

The role of oxygen in the photocatalytic reaction was presented in Equations 2.4 and 2.7 that describe the pertinent reactions occurring on TiO_2 surface. Dissolved oxygen (DO) has a primary role in the formation of reactive species, and the stabilisation of intermediates. It was also reported to induce the cleavage mechanism for aromatic rings in organic pollutants (Chong et al. 2010). Previous work found that the concentration of DO can be a limiting factor that sometimes significantly hinders the photomineralisation process in photocatalysis (Wang and Hong 2000). However, increased photocatalytic activity may also occur in the absence of oxygen, attributed to the adsorption of UV photon by dissolved oxygen molecules at $\lambda < 254$ nm. The DO molecules acted as an inner filter and reduced the effective photonic flux on the photocatalyst surface (Shirayama et al. 2001).

2.2.4.7. Temperature

The photocatalytic decomposition of organics usually can proceed without a need for increasing the ambient water temperature. However, an increase in degradation rates was observed with an increase in the temperature range between 20 °C and 80 °C (Malato et al. 2009). Operating the photocatalytic process at low temperatures (near 0 °C) hindered the desorption of the final product from the photocatalyst surface, which caused an increase in the apparent activation energy. In contrast, temperatures above 80 °C disfavoured the adsorption of pollutants and also enhanced the recombination of charge carriers, which were considered the main limiting steps (Gaya and Abdullah 2008; Mozia et al. 2010; Chong et al. 2010).

2.2.4.8. Optimisation Methodology

The optimisation of photoreactor systems is usually undertaken by the conventional one-parameter-at-a-time approach. In other words, the optimisation is achieved by varying one parameter while all the others are kept constant. After determining the optimal condition, based on the decomposition rate of a target pollutant, other parameters are subsequently tested, until all parameters have been optimised. This method is widely accepted and has been used to optimise many operating systems. However, the limitation of this procedure is that the interaction of parameters at different levels cannot be tested. The multivariable optimisation approach is becoming increasingly popular because the optimisation process is more effective, and the interaction among different parameters can be interpreted using the analysis of variance, statistical regression and response surface analysis (Chong et al. 2010).

2.2.4.9. Process Efficiency

The optimisation of a photocatalytic process for a specific reaction (single contaminant) is crucial for the determination of a sound photoreactor/operation parameter configuration. The process efficiency of the system should be assessed based on a standardised method, so the comparison between processes becomes possible. The quantum yield (Φ) was suggested to evaluate the process efficiency in photocatalytic processes (Calvert and Pitts 1966):

Φ = rate of reaction / adsorption rate of radiation (Eq. 2.10)

However, it is very difficult to determine Φ by experimental investigation in many photocatalytic reactors. This is mainly due to the refraction, scattering, transmission and adsorption of light by the suspended particles (Chen et al. 2000).

A relative photonic efficiency (ζ_r) has been proposed to overcome the difficulties encountered by the measurement of Φ (Serpone et al. 1997). The method consisted of measuring the initial disappearance reaction rate of phenol using Degussa P25 as a standard photocatalyst, then measuring the initial disappearance rate of the target

substrate under identical experimental conditions. The ζ_r can then be calculated by the following formula:

ζ_r = initial disappearance rate of substrate / initial disappearance rate of phenol

(Eq. 2.11)

The ζ_r can be used to calculate the quantum yield of the substrate ($\Phi_{substrate}$) relatively to the quantum yield of phenol on Degussa P25 (Φ_{phenol}) by:

$$\Phi_{substrate} = \zeta_r \, \Phi_{phenol} \qquad \text{(Eq. 2.12)}$$

The relative photonic efficiency allowed the comparison of studies performed in different laboratories. Nevertheless, the experimental conditions must be identical, besides that the initial rate does not consider the formation of intermediate compounds and how those might affect the degradation of their parental products. It follows that, the evaluation of photocatalytic processes using a universal reference or indicator is still not possible, since many factors and parameters have interrelated influences on the reaction rate.

2.2.5. Kinetics of TiO_2 Photocatalysis

The kinetics of mineralisation in heterogeneous photocatalysis is often described with the Langmuir-Hinshelwood (L-H) model. This model was originally developed to quantify gaseous–solid reactions (Satterfield, 1970) but can also describe solid–liquid reactions (Ollis, 1985). In the L-H model the *r* rate of reaction is proportional to the θ fraction of surface covered by the substrate (pollutant):

$$r = -\frac{dC}{dt} = k\Theta \qquad \text{(Eq. 2.13)}$$

From Langmuir's equation

$$\Theta = \frac{K \cdot C}{1 + K \cdot C} \qquad \text{(Eq. 2.14)}$$

Therefore

$$r = k \cdot \Theta = k \cdot \frac{K \cdot C}{1 + K \cdot C} \qquad \text{(Eq. 2.15)}$$

with k reaction rate, K constant of adsorption equilibrium, and C substrate concentration at t time.

The integration of Eq. 2.15 between zero and t times gives

$$\ln\left(\frac{C_0}{C_t}\right) + K \cdot \left(C_0 - C_t\right) = k \cdot K \cdot t \qquad \text{(Eq. 2.16)}$$

with C_0 initial and C_t substrate concentration at zero and t irradiation times, respectively.

Solving Eq. 2.16 for k requires the knowledge of K. The θ surface coverage fraction can also be expressed from the number of adsorbed molecules at a given final (equilibrium) concentration:

$$\Theta = \frac{n_{ads}}{n_0} = \frac{K \cdot C}{1 + K \cdot C} \qquad \text{(Eq. 2.17)}$$

$$\frac{1}{n_{ads}} = \frac{1}{n_0} + \frac{1}{n_0 K} \cdot \frac{1}{C} \qquad \text{(Eq. 2.18)}$$

with n_{ads} covered and n_0 total number of available adsorption sites. Noting that Eq. 2.18 is linear, both K and n_0 can be determined from plotting $1/n_{ads}$ versus $1/C$.

It also can be seen from Eq. 2.15 that for relatively high substrate concentrations (and/or *K* values) (KC>> 1) the reaction will be of zero order, while for relatively low substrate concentration and/or *K* values (KC<<1) will be of first order.

In the photocatalytic degradation of MB, Herrmann (1999) reported zero and first order reactions for 5 mmol and 1 mmol initial concentrations, respectively. For the latter case, which is typical in most applications of photocatalysis, the denominator in Eq. 2.15 approaches 1 (one), and thus:

$$r = k \cdot \Theta = k \cdot K \cdot C = k_a \cdot C \qquad \text{(Eq. 2.19)}$$

with k_a apparent (pseudo) rate constant. The integral form of Eq. 2.19 is:

$$C_t = C_0 \cdot e^{-k_a \cdot t} \qquad \text{(Eq. 2.20)}$$

The linearised form of Eq. 2.20

$$\ln\left(\frac{C_0}{C_t}\right) = k_a \cdot t \qquad \text{(Eq. 2.21)}$$

is often used to obtain the k_a apparent reaction rate. However, data linearization also transforms the random (Gaussian) distribution of the error term, which is contrary to the fundamental assumption of random errors used in the derivation of linear regression. Therefore, data linearisation techniques are suitable for only preliminary examinations. The correct values of the reaction rates can be obtained from Eq. 2.20 using nonlinear regression/fitting techniques that are provided by many modern statistical software packages.

It is also emphasised that both the *k* reaction rate constant used in the L-H model and the k_a apparent reaction rate constants used in the first order model are lumped (bulk) parameters. These parameters take into account a number of factors, such as hydraulic conditions and photonic conditions. It follows that the obtained rate values,

that are valid only for the given experimental conditions, cannot be used for the up-scaling of equipment, nor to compare catalyst performances reported elsewhere. Their main use is to quantify and compare the relative performance of a given catalyst, and the effect of various experimental factors.

2.3. Solar/visible Light Responsive TiO_2

2.3.1. Background

Photocatalysis over semiconductors, mainly TiO_2, has been employed and extensively studied over the past few decades (Malato et al. 2009). The so-called "*first generation photocatalysts*" are characterised by that their photoexcitation requires illumination by UV light. Nevertheless, many such photocatalysts showed outstanding performance in decomposing a large number of challenging pollutants of water and air. A number of water pollutants belong to the family of recalcitrant (i.e. non-biodegradable) pollutants which include pharmaceutical and personal care products, industrial wastes, and a large number of pesticides/herbicides. Many of the emerging pollutants are resistant to conventional water treatment processes, noxious to the environment and some are classified as endocrine disrupting agents. The removal of non-biodegradable pollutants from wastewater poses a serious challenge for the water industry. Generally, advanced oxidation processes (AOP), including heterogeneous photocatalysis is well suited to deal with these contaminants. However, the relatively high cost of photocatalysis has always been a disadvantage for its large-scale adoption in treatment processes. The high cost is mainly associated with the energy consumed for the UV light irradiation of the photocatalyst, and to a lesser extent with the energy required for the separation of the photocatalyst's particles from water.

A total of 40% of the solar light reaching the lithosphere is visible light, whereas UV light accounts only for 5% of the total solar radiation. Therefore, the development of new photocatalysts that can effectively harvest visible light is crucial for making this technology viable in the water treatment industry. The use of "*second-generation TiO_2 photocatalysts*" to harvest visible light from solar energy has been reported (Anpo 1997). Most of the research involving the use of second generation TiO_2 photocatalysts has focused on energy conversion and solar cell applications (Yuan et al. 2006), however, there is an increasing interest to explore their potential for treating water pollutants (Chatterjee and Dasgupta 2005; Malato et al. 2009; Rehman et al. 2009).

2.3.2. Overview of Visible Light Activity by Doping TiO_2

Photosensitisers (typically organic dye molecules) have found applications in solar cells since the dye molecules adsorbed on TiO_2 are capable of generating photocurrents from a range of visible wavelengths of light. However, UV light filters are required in such cells to prevent the degradation of the dye under solar radiation. As an alternative to photosensitisation using dyes, titania can be doped with metal and non-metal species. The role of doping, the accumulation of defects (Martyanov et al. 2010) or oxygen vacancies (Ihara et al. 2003; Wang and Doren 2005; Graciani et al. 2008) in the initiation of visible light sensitivity are widely reported and discussed in the literature, therefore only the application of non-metallic dopants (chiefly nitrogen) will be discussed below.

2.3.2.1. Nitrogen Doping

Sato et al. (1986) reported the first visible-light-sensitive nitrogen-doped TiO_2 photocatalyst. N-doped TiO_2 showed better photocatalytic activity than undoped TiO_2 for the decomposition of CO and C_2H_6 under visible-light irradiation. Later, Asahi et al. (2001) prepared N-doped TiO_2 photocatalysts by two different methods. N-TiO_2 films were made by sputtering TiO_2 in N_2/Ar gas mixture, and powders were prepared by treating anatase particles in NH_3/Ar atmosphere at 600 °C. Since then, many articles have proposed, developed, and discussed new methods for preparing N-doped TiO_2 and TiO_2 doped with other non-metal species such as C and S (Chen and Burda 2008; Zaleska 2008).

Photocatalysis is initiated by the adsorption of photon with energy equal or greater than the band gap of TiO_2 (3.0 and 3.2 eV for rutile and anatase, respectively). The narrowing of the band gap enables the adsorption of photon of lower energy level present in the visible light range. The electronic structures of anatase with substitutional N dopant have been investigated by first-principles density functional theory calculations (Wang and Doren 2005). The local density approximation calculations demonstrated that N doping leads to a narrower TiO_2 band gap by introducing some states at the valence band maximum. These findings have been

further validated by the study of Chen and Burda (2008) on the electronic origin of the visible light absorption properties of N-doped TiO_2. Additional electronic states above the valence band edge of pure TiO_2 were identified by x-ray photoelectron spectroscopy (XPS) analysis. The red-shift adsorption of the rutile N-doped TiO_2 was attributed to this additional electron density of states. Graciani et al. (2008) also conducted density-functional calculations on the structural and electronic properties of N doped rutile TiO_2 but came to a different conclusion. They proposed that N doping of rutile TiO_2 does not improve its photocatalytic activity without the presence of oxygen vacancies. They also reported that the presence of oxygen vacancies lowers the implantation energy of nitrogen and stabilises it. The debate over the electronic and structural origins of the visible-light sensitivity of N-TiO_2 is still continuing. New findings using advanced characterisation technologies are expected to clarify this dilemma in the near future.

Selected methods for the preparation of nitrogen doped titanium dioxide are shown in Table 2.3. Generally, nitrogen doped titania nanopowders exhibit yellow colour. Nitrogen doping can be detected by XPS analysis and diffuse reflectance spectroscopy (DRS) measurements (Sato 1986, Asahi et al. 2001). Nevertheless, XPS peak assignment is still a controversial issue, and the shift in the absorbance spectra in DRS cannot guarantee that the powder is photoactive. Therefore, a photocatalytic activity test is always required. Chen and Burda (2004) reported an extended XPS analysis of nitrogen incorporation in TiO_2 nanostructured materials. The binding energy at 401.3 eV for N 1s was attributed to the energy of N atom in the environment of O-Ti-N. This substitutional doping was reported to induce the significant increase in photocatalytic activity in N doped TiO_2 nanoparticles. In a recent study, Asahi and Morikawa (2007) observed that nitrogen doping may result in such species as substitutional N_S or interstitial N_i, substitutional $(NO)_s$, interstitial $(NO)_i$ and substitutional $(NO_2)_s$. The role of band gap modification and the assignment of XPS peaks to N species were discussed in detail by Emeline et al. (2008) and Rehman et al. (2009).

Table 2.3. Selected methods for the preparation of N doped TiO_2

Nitrogen precursors	Method of preparation	Target pollutant	References
Urea, guanidine and ammonium fluoride	Spray pyrolysis	Degradation of acetaldehyde (air pollutant) and trichloroethylene (water pollutant)	Li et al. (2005)
Ammonia solution (28%)	Hydrolysis of $Ti(OCH(CH_3)_2)_4$, TTIP and $TiCl_4$	Photooxidation of CO	Sato et al. (2005)
Urea	Hydrolysis of $Ti(OH)_4$	Photooxidation of KI	Kobayakawa et al. (2005)
Nitrogen gas	RF magnetron sputtering	Not tested	Mardare et al. (2007)
N_2O	Infrared laser pyrolysis technique	Not tested	Alexandrescu et al. (2009)
NH_4Cl	Sol-gel method using TTIP	Not tested	Livraghi et al. (2009)

2.3.2.2. Silver Doping

Metal implantation into TiO_2 was initiated in the late 1970's when the first oil crisis triggered research interest in the production of alternative or synthetic fuels such as H_2. A popular semiconductor material was TiO_2, mainly due to its chemical stability. Gosh and Maruska (1977) studied the photoelectrolysis of water in sunlight with sensitised semiconductor electrodes, and demonstrated that Cr-doped TiO_2 has an extended spectral response into the visible region of the solar spectrum. In 1982, the first visible light active TiO_2 particles were reported by Borgarello et al. (1982). Water cleavage under visible light was successful using the synthesised Cr-doped TiO_2 nanoparticles made by a chemical route. Later, Anpo (1997) presented a new metal-doping approach by ion-implantation. TiO_2 was bombarded by high energy metal ions to dramatically modify its electronic states and induce visible light

response. The same method was successfully employed to produce V, Cr, Ni, Mn and Fe-doped TiO_2 (Yamashita et al. 2002). Recent patents on doped TiO_2 highlighted a number of new techniques to produce visible light active semiconductors by metal doping through chemical routes as well as ion implantation (Zaleska et al. 2008).

Silver metal was used since ancient times by the Indians, Egyptians, and Phoenicians to preserve water, wine and vinegar from spoiling. Silver nanoparticles are used nowadays as antibacterial agents in many products. Because of the low cost and ease of preparation, silver doping may be employed to enhance photocatalytic activity under UV light as well as to promote the visible light response of TiO_2 (Sung-Suh et al. 2004; Chen et al. 2007). The metallic silver particles on TiO_2 surfaces act as electron scavengers and contribute dramatically to the decrease of electron-hole recombination in TiO_2. Thus, Ag-TiO_2 exhibits an overall higher photocatalytic activity in the UV range than undoped TiO_2 (Behnajady et al. 2003; Liu et al. 2003; Rao et al. 2003; Gupta e al. 2006; Chen et al. 2007; Park and Kang 2008; Vinu and Mardas 2009). Moreover, Ag ions cause a blue shift in the adsorption spectrum of synthesised Ag-TiO_2 films suggesting a change in the film nanostructure instead of the introduction of impurity states (Stathatos et al. 2001). Several methods have been employed for the preparation of Ag-doped TiO_2 (Table 2.4). Among these, sol-gel methods are the most popular because they are simple, relatively cheap, and do not require sophisticated equipment.

Ag deposition can enhance the photooxidation power of TiO_2 by the following mechanisms:

1. Ag nanoparticles enhance the electron-hole separation in TiO_2 by trapping the excited electrons after illumination and transferring them to O_2 as an electron acceptor (Herrmann et al. 1986).

Table 2.4. Selected methods for the preparation of Ag doped TiO_2 using $AgNO_3$ as a silver precursor

Method of preparation	Light source	Target pollutant	References
Sol-gel method using titanium tetraisopropoxide (TTIP)	Simulated solar radiation (250 W tungsten halogen lamp)	Photodegradation of Basic Blue 41	Stathatos et al. (2001)
Photodeposition method	Visible light (450 W Xe-arc lamp with a UV cut filter)	Photodegradation of trichloroacetate and carbon tetrachloride	Bae and Choi (2003)
Hydrothermal method using $TiCl_4$	None	Not tested	Liu et al. (2003)
Sol-gel method using TTIP	Visible light (200 W halogen lamp)	Photodegradation of Rhodamine B	Sung-Suh et al. (2004)
Ultrasonic-assisted Sol-gel method using $Ti(O\text{-}Bu)_4$	UVA (8 W medium pressure mercury lamp)	Photodegradation of 2,4,6-trichlorophenol	Rengaraj and Li (2006)
Sol-gel method using Degussa P25	Visible light	Photooxidation of o-Cresol	Chen et al. (2007)
Liquid impregnation and photodeposition methods	UVC (15 W lamp)	Photodegradation of Acid Red 88	Behnajady et al. (2008)
Sol-gel method using $Ti(OC_4H_9)_4$	UVA lamps	Degradation of acetaldehyde (air pollutant)	Yang et al. (2007)
Sol-gel method	UVA (6 x 6W lamps)	Photooxidation of methanol and H_2 production	Park and Kang (2008)
Sol-gel method using metatitanic acid	Direct sunlight	Photodegradation of methyl orange	Binitha et al. (2009)

2. The excitation of the surface electrons and interfacial electron transfer are enabled after the surface plasmon resonance of Ag particles is excited by visible light (λ = 400 nm) (Herrmann et al. 1997; Sung-Suh et al. 2004; Rehman et al. 2009).
3. In the case of dye degradation, Ag-doping also enhances the dye adsorption on TiO_2 and promotes the dye photosensitisation process (Rehman et al. 2009).

Ag doping onto TiO_2 can be detected by XPS analysis, DRS measurements and can be further verified by photocatalytic experiments (Falaras et al. 2003; Vinu and Mardas 2009). Binding energy peaks around 367-368 eV and 373-374 eV indicate the presence of silver in different ionic forms in powders (Lutzenkirchen-Hecht and Strehblow 2009). Generally, the doped Ag ion has an ionic radius greater than that of Ti^{4+}, therefore it is mostly deposited on the surface of TiO_2 and is not readily incorporated at Ti sites in the TiO_2 lattice (Rehman et al. 2009).

2.3.3. Doped TiO_2 and Water Reclamation

A number of N-TiO_2 materials have been assessed for the photodegradation of specific water pollutants, e.g., dyes, phenols and other organic contaminants, although the use of N-doped TiO_2 in large scale water treatment plants currently is still limited.

2.3.3.1. Nitrogen Doped TiO_2

2.3.3.1.1. Photodegradation of Dyes

Dyeing industries generate and discharge significant volumes of contaminated and coloured wastewater. Eutrophication or algal blooms from dye wastewater discharge into rivers and water bodies may result if no or insufficient treatment measures adopted. Unfortunately, the most widely used azo dyes are designed to resist degradation, making their removal difficult in conventional wastewater treatment processes. Moreover, some degradation by-products are of great concern because

they are more toxic, mutagenic or carcinogenic than the original dyes themselves (Oh et al. 1997).

Apart of that some dyes are used as TiO_2 photosensitisers, model dye pollutants are also widely used for testing the photocatalytic activity of nitrogen-doped TiO_2 (Asahi et al. 2001; Liu et al. 2009a). The photocatalytic activity of $TiO_{2-x}N_x$ was evaluated by measuring the decomposition of Methylene Blue (MB) under visible light. Significantly more degradation was observed at an irradiation wavelength of 500 nm compared to the reference TiO_2 (Asahi et al. 2001). Also, no loss in the UV photocatalytic activity was recorded for the N doped photocatalyst over 2 h. Qiu et al. (2007) reported the photodegradation of MB under visible light irradiation ($\lambda >$ 400 nm) for an N-doped TiO_2 photocatalyst prepared by a sol-gel method. The photocatalytic activity of the N-TiO_2 increased with N doping levels (up to 8% N). At 8% N doping, around 85% of MB was removed after 340 min of visible light irradiation. The photocatalytic activity of nitrogen-doped rutile nanostructures was reported for experiments using a Pyrex photoreactor (400 mL) containing 0.16 g TiO_2 and a 20 mg/L MB solution (Yang and Gao 2008). The reactor was irradiated with a 300 W medium pressure lamp equipped with a 400 nm cut-off filter to exclude UV light. Dye degradation was correlated to the shape of the nanomaterial as well as to the percentage of N doping. Complete visible-light photocatalytic degradation of MB was achieved after 7.5 h and 5.5 h using floc-like aggregates and rod-like aggregates of N-doped nanostructures, respectively. No significant reduction in photoactivity under UV irradiation was recorded when comparing the nanostructures with their non-doped homologues. Nitrogen-doped titanate nanotubes (N-TNT) were prepared by using guanidine carbonate to post-treat nanotubes produced by the conventional hydrothermal method (Geng et al. 2009). A simulated solar light photoreactor equipped with 150 W xenon arc lamp was used to decompose 100 mL of 30 mg/L MB solution over 30 mg of N-TNT. The photocatalytic degradation rate of N-TNT was higher than their TNT precursors under solar light irradiation. Calcination at temperatures above 350 °C had a negative effect on the overall performance of N-TNT, mainly because the amount of N decreased with the increase in calcination temperatures. Liu et al. (2010) compared several doped and co-doped photocatalysts for degrading MB under

visible light (14 W lamp, emission at λ = 545 nm). A MB solution (10 mg/L) was mixed with 1 g/L of photocatalyst and irradiated for 6 h to check the rate of photodegradation. The apparent kinetic constant was 0.277 h^{-1}, significantly higher than for Fe doped and Fe-N co-doped TiO_2 catalysts (0.1975 h^{-1} and 0.1694 h^{-1}, respectively). The decrease of photoactivity in the co-doped sample was attributed to the capture of charge carriers.

Recently, Liu et al. (2009a) photocatalytically degraded Rhodamine B (RhB) under visible light (fluorescent lamp, 18 W, glass filter for UV cut off, λ > 420 nm). Nitrogen-doped TiO_2 with different ratios of anatase to rutile were prepared by milling in air and gaseous NH_3 atmospheres. The photocatalytic activity of the samples (100 mg) was assessed in 100 mL of 2 x 10^{-5} M of RhB solution under magnetic stirring, using visible light irradiation after 30 min of dark adsorption. It was concluded that the nitrogen-doped TiO_2 with higher rutile content has a higher photocatalytic activity because of abundant surface water and hydroxyl groups. In the same way, Liu et al. (2009b) reported the photodecomposition of RhB (4 x 10^{-5} M) using the experimental reactor described above over nitrogen-doped mesoporous TiO_2. Substantially higher photocatalytic activity was observed for the N-doped mesoporous TiO_2 compared to the non-doped mesoporous TiO_2 and P25. N-TiO_2 completely decomposed RhB in solution after 4 h of visible light irradiation. The high photocatalytic activity was attributed to the “abundant surface states” in nitrogen doped mesoporous TiO_2.

Acid orange 7 can be degraded under solar light irradiation (12 mW/cm^2) using N-doped TiO_2 as prepared by Liu et al. (2006). Experiments were conducted using Petri dishes (15 ml of Acid orange 7 solution covered with a plastic film to avoid evaporation) containing a solution of 20 mg/L of Acid orange 7 and 10 mg/L of N-TiO_2 at pH of 4.5-5. The degradation followed first order kinetics and full decolourisation was achieved after 4 h of solar irradiation, while only 5% of colour was removed using P25 photocatalyst. Smaller nanoparticles size (10 nm) and high surface hydroxyl group density in N-TiO_2 were reported to cause the increase in photocatalytic activity.

Sun et al. (2008) reported the photocatalytic degradation of Orange G under visible and sunlight irradiation over N-TiO_2. A visible light photoreactor equipped with a 500 W xenon-arc lamp and a UV cut-off filter ($\lambda > 400$ nm) was used to test several photocatalysts under different experimental conditions. Outdoor experiments under direct sunlight were also carried out. The results showed that N-TiO_2 degraded 96.3% of Orange G and P25 degraded 42.6% of the dye under visible light (Xenon arc lamp) in 150 min. The opposite and surprising trend was recorded under solar light irradiation whereby P25 and N-TiO_2 decolourised 90% and 75% of Orange G after 20 min of solar irradiation, respectively.

Gao et al. (2009) synthesised N-doped anatase TiO_2 by a hydrothermal method and photodecomposed Methyl Orange using a quartz cylinder irradiated with a 300 W high pressure mercury lamp. A total of 99% of Methyl Orange was degraded after 20 minutes of irradiation. The photocatalytic degradation was affected by the calcination temperature of the powders, and to a lesser extent by the pH of the solution.

Liu et al. (2008) prepared N-doped TiO_2 films on heated quartz glass substrate. Aqueous Methyl Orange was photodegraded using the prepared film (1 cm^2) under a 15 W daylight lamp equipped with a UV cut-off filter ($\lambda > 400$ nm). The visible light photoactivity of the N-doped films was superior to the undoped films. It was found that N-doping and the high adsorption of Methyl Orange on the surface of the films (causing photosensitisation) contributed to the visible light photocatalytic activity. It is noteworthy to mention that high adsorption azo dyes onto N-TiO_2 was also reported by Janus et al. (2009), but unfortunately, no photocatalytic activity tests have been reported to date investigating any synergetic effects of N-doping and dye photosensitisation.

2.3.3.1.2. Photodegradation of Phenolic Compounds

Wastewater from industries such as resin manufacturing, iron smelting and paper making contains high concentration of phenol and their derivatives (Wang et al. 2005). Phenolic compounds can be toxic, carcinogenic, difficult to degrade and

ubiquitous in natural environments. Many experiments have been conducted to decompose phenolic compounds over N-doped TiO_2 under visible or solar light irradiation (Sun et al. 2008; Huo et al. 2008; Xing et al. 2009; Lee et al. 2010).

Different irradiation sources were used to evaluate the photocatalytic activity of N-doped TiO_2 produced through a sol-gel method followed by calcination of the powder (Wang et al. 2005). A 1000 W xenon lamp (with a UV cut-off filter $\lambda > 400$ nm) irradiated 1 L of 20 ppm phenol solution mixed with 0.5 g of sample powder to conduct visible light photocatalytic tests. Outdoor experiments also were carried out to evaluate the photocatalytic activity under solar irradiation. N-doped TiO_2 calcined at 400 °C decomposed 35.6% of phenol after 2 h of photoreaction under visible light. An increase or decrease in the calcination temperature negatively affected the photocatalytic activity mainly because of the decrease in N content or lower crystallinity, respectively. P25 was more effective than N-doped TiO_2 under solar light illumination and degraded 90% of phenol in 3 h while the N-doped TiO_2 removed only 40% after 7 h.

Lee et al. (2010) studied the influence of nitrogen chemical states on the photocatalytic activity of N-doped TiO_2 nanoparticles under visible light. A 10 ppm phenol solution was used to investigate the photocatalytic activity of the nanoparticles (1 g/L) irradiated with a 200 W halogen lamp equipped with a UV cut-off filter ($\lambda > 420$ nm). They reported different photocatalytic activities with regard to the chemical states of N in the prepared samples. The complete degradation of phenol was not reached before 12, 17 and 24 h for the chemical states expressed at 398.3 eV, both 398.3 eV and 401.6 eV and 401.5 eV alone. The authors attributed the peaks to substitutional (398.3 eV) and interstitial (401.5 eV) N and concluded that the former leads to better photocatalytic activity than the latter.

The degradation of 4-chlorophenol over TiO_2 doped with a series of lower-concentration nitrogen species was reported by Sun et al. (2008). The 6 h photoreaction under visible light (250 W xenon lamp, UV cut-off filter $\lambda > 400$ nm) revealed that the photocatalyst removed 51% of TOC, while undoped TiO_2 failed to decrease the TOC of the phenolic solution. Sun et al. (2009) also carried out similar

experiments with different light sources (visible light: as described above, UV: 250 W high-pressure mercury lamp and natural solar light). N-doped TiO_2 showed higher photoactivity under UV light than P25 (apparent-reaction-rate constants equal 0.163 $min^{-1}$and 0.143 min^{-1} for N-doped TiO_2 and P25, respectively). However, no comparison was reported for visible and solar light between N-doped TiO_2 and P25.
Huo et al. (2008) studied the photodegradation of aqueous *p*-chlorophenol using nitrogen-doped TiO_2 that was prepared under supercritical conditions. The claimed advantage of their method was the obtained crystalline anatase of high specific surface area. Up to 76% of the 10 mg/L *p*-chlorophenol solution was photodegraded after 4 h of irradiation using 50 mg/L of photocatalyst (with the highest N content). The irradiation source was a 500 W xenon lamp topped with a UV cut-off filter ($\lambda >$ 420 nm). This research showed again that the achieved degradation was affected by the percentage of N-doped into TiO_2.

The photocatalysis of other phenolic compounds was studied over several N-doped TiO_2 powders by Xing et al. (2009) and Ananpattarachai et al. (2009). These studies reported very good visible light activity of the N-doped materials, unfortunately, the photocatalysts were not tested for photoactivity under solar light, or compared to the P25. It is expected that a superior N-doped TiO_2 should not only be able to degrade phenolic compounds under visible light for prolonged periods of time, but also should show better overall photocatalytic activity under solar light (40% visible light).

2.3.3.1.3. Other Organic Water Contaminants

The photodegradation of specific pollutants such as benzoic acid and herbicides have been investigated using N-doped TiO_2 (Shifu et al. 2005; Wang et al. 2007; Abramovic et al. 2009). Herbicides are widely used in agriculture, horticulture and landscape activities to kill weeds, and may be transported to the groundwater and runoff by precipitation and irrigation to cause contamination. The photocatalytic oxidation of herbicides in water is an efficient treatment to mineralise them, and cost-effective methods may use solar light.

A photocatalytic treatment of benzoic acid (under simulated solar light (125 W xenon lamp) removed 65% of the initial 25 mg/L concentration after 2 h illumination. The experiments were carried out using a borosilicate photoreactor at 25 °C, and a photocatalyst loading of 0.1 g/L (Wang et al. 2007). The total organic carbon content decreased by 53.4% after 2 h. Single wavelength experiments were conducted to check the performance of the synthesised N-TiO_2, and a non-doped TiO_2 control product obtained by a similar procedure. N-doped TiO_2 showed photocatalytic activity at λ = 334 nm, 365 nm, 500 nm and 600 nm, while the undoped TiO_2 showed activity only in the UV range.

N-doped TiO_2 prepared by ball milling titania in aqueous ammonia solution followed by drying in air at 110°C decomposed monocrotophos (Shifu et al. 2005). Experiments utilised a photochemical quartz reactor equipped with a 375 W medium pressure mercury lamp. The photocatalytic activity of N-doped TiO_2 was assessed using 10^{-4} M monocrotophos solution at a photocatalyst loading of 2 g/L and a pH of 5 over 4 h. With monochromatic light irradiation (λ = 365 nm), TiO_2 (ball milled in water) and N-doped TiO_2 (ball milled in ammonia) showed similar activity with 17.6% and 19.3% degradation after 4 h, respectively. At λ = 405 nm, N-doped TiO_2 (6.1%) showed better photoactivity than TiO_2 (0.97%). N-doping was confirmed by a red-shift in the DRS spectra and two N 1s peaks at 396.5 eV and 402 eV binding energies.

Abramovic et al. (2009) studied the use of N-doped TiO_2 (prepared by a sol-gel method) for the degradation of *RS*-2-(-4-chloro-*o*-tolyloxy)propionic acid (mecoprop) and (4-chloro-2-methylphenoxy)acetic acid (MCPA) herbicides. The photocatalytic degradation was performed in a Pyrex glass cell using 2 g/L of photocatalysts in herbicides' solution (concentration ranged from 1-8 g/L) under different light sources. N-doped TiO_2 showed superior photocatalytic activity under visible light, according to the degradation rates shown in Table 2.5.

Table 2.5. Mecoprop and MCPA degradation rates over several photocatalysts.

	Mecoprop degradation rate (μmol dm^3 min^{-1})		
	Halogen Lamp (50 W)	**Mercury Lamp (125 W)**	**Sunlight**
N-doped TiO_2	1.36*	7.27^	0.05^n
P25	0.86*	9.66^	0.08^n
Direct photolysis	0.22*	0.79^	0.00^n
	MCPA degradation rate (μmol dm^3 min^{-1})		
N-doped TiO_2	1.02*	9.31^	0.05^n
P25	0.74*	9.97^	0.05^n
Direct photolysis	0.18*	1.08^	0.00^n

Degradation rate calculated for time period of *21 days; ^19 h; ^{n}210 min.

2.3.3.2. Silver Doped TiO_2

2.3.3.2.1. Photodegradation of Dyes

An increase in the photocatalytic activity of TiO_2 under UV and visible light can be attained by doping with silver (Sung-Suh et al. 2004; Gupata et al. 2006). The antibacterial properties of silver particles can be incorporated into antibacterial inorganic Ag-TiO_2 complexes (Wu et al. 2010).

Mesoporous titania films can be doped by Ag^+ ions to enhance their photocatalytic activity under visible light (Stathatos et al. 2001). Additionally, the photoreduction of Ag^+ ions (UV light irradiation with a mercury 400 W lamp) in the Ag-doped films increased the rate of photodegradation of Basic Blue 41 solution (illuminated using a 250 W tungsten-halogen spot (0.6 W/m^2) compared to untreated films. The UV treated films showed better photocatalytic activity (full degradation in 20 min) than the untreated films (full degradation in 60 min) due to the creation of metal centres in the film.

Recently, Seery et al. (2007) tested the effect of pre-irradiating Ag-TiO_2 (irradiation was carried out by using a 250 W bulb to photoreduce Ag ions) on its photo-

oxidation activity that was tested under simulated solar and natural sunlight for degrading Rhodamine 6G (R6G, reaction volume = 50 mL, concentration 5 x 10^{-5} M, catalyst loading = 1.2 g/L). The intensity of the natural solar light (0.4-0.68 W/m^2) was generally less than that of the simulated source (0.68 W/m^2), which lowered the rate of degradation in the outdoor experiments. Pre-irradiation of the photocatalyst Ag-TiO_2 reduced the degradation rate from 0.34 min^{-1} to 0.24 min^{-1}. The significant change in rate was assigned to several factors: i) low Ag dispersion, ii) Ag acting as a light adsorption barrier, iii) Ag preventing the adsorption of the organic substrate onto the TiO_2 and iv) Ag acting as an electron-hole recombination centre (Xin et al. 2005; Seery et al. 2007).

Ag deposition onto TiO_2 nanoparticles at 2 at.% was found to be the optimum for the high photocatalytic degradation of Rhodamine B (RhB) under visible light (Sung-Suh et al. 2004). The doped Ag-TiO_2 was prepared by a peptisation method followed by a photocatalytic deposition process. A 100 mL photoreactor was used to degrade 50 mL of RhB solution (10^{-5} M) irradiated by a 200 W halogen lamp as visible light source. The Ag-TiO_2 photocatalyst decomposed 30% more RhB than TiO_2 under visible light, and also showed better photocatalytic activity than P25 and Ag-P25. The high Rhodamine B adsorption on Ag-TiO_2 apparently boosted the photocatalytic degradation due to the photosensitisation mechanism.

Binitha et al. (2009) reported the degradation of Methyl Orange using a nano silver-doped mesoporous TiO_2 under sunlight (between 11:00 and 14:00 h). The photoactivity was studied at a Methyl Orange concentration of 10^{-5} M. After 1 h of solar irradiation using 0.2 g of photocatalyst, the Ag-doped TiO_2 degraded 94% of the Methyl Orange, thus ranking it one of the best among their tested photocatalysts.

2.3.3.2.2. Other Prominent Water Contaminants

Cresols are used in the manufacturing of pesticides, dyes, and PCs, and have been found in drinking and irrigation water. Chen et al. (2007) studied the photodegradation of o-Cresol under visible light over Ag-TiO_2. The maximum

photocatalytic activity was observed for 0.5 wt.% Ag-doping, which was double that of pure TiO_2.

The deactivation of bacteria (*E. coli*) present in wastewater was studied under solar light using Ag-TiO_2 (Ashkarran 2011). The Ag-TiO_2/bacteria suspension was illuminated with a 90 W halogen lamp to conduct the photocatalytic inactivation of bacteria. A significant decrease in the survival rate for the samples treated with Ag-TiO_2 was observed compared with non-doped TiO_2. The results suggested that the antimicrobial properties of Ag were augmented its effect on inducing visible light response in TiO_2, which led to improved disinfection.

2.3.3.3. Co-doping using Metal/non-metal Elements

Co-doping with metal and non-metal elements can further increase the visible light photocatalytic activity of TiO_2. As discussed above, N is a cost-effective non-metal capable of narrowing the band gap of TiO_2. When it is coupled with metal compounds, the co-doped materials may exhibit improved photocatalytic activity. Various metals, such as V, W, Ag, Eu, Ta, Fe and Cd have been used in conjunction with N to boost the photocatalytic activity of TiO_2 (Table 2.6).

Yuan et al. (2010) have co-doped N-TiO_2 with silver nanoparticles to test the photocatalytic activity under fluorescent light for the inactivation of model bacterial cells. The DRS spectra of Ag-N co-doped TiO_2 revealed that the adsorption band shifted towards longer wavelengths into the visible range. The photocatalyst was synthesised by the hydrolysis precipitation method using ammonia and silver nitrate as N and Ag precursors, respectively. Two bacteria (*E. coli* and *B. subtilis*) species were inhibited by irradiating the culture with a fluorescent light in the presence of N-doped TiO_2 and Ag-N-doped TiO_2. The antibacterial property was investigated by the agar hole diffusion-inhibition zone method. Photocatalytic activity was compared by measuring the bacteriostasis circle around the deposition hole (inhibition zone). The 1 at.% Ag co-doping had the highest antibacterial activity showing the widest bacteriostasis circles.

Table 2.6. Recent methods for the preparation of N/metal co-doped TiO_2.

Method of preparation and co-doped metal	**Light source**	**Photoreaction conditions**	**References**
Sol-gel method using tetrabutyl titanate, **Iron (III)**	Visible light (200 W tungsten halogen lamp with a UV cut-off filter)	Photodegradation of RhB (10^{-5} M), 0.1 g TiO_2 in 60 mL solution	Pingxiao et al. (2007)
Precipitation hydrothermal method, **Cadmium**	Visible light (1000 W halogen lamp with a UV cut-off filter)	Photodegradation of RhB (20 mg/L), 1 g/L of photocatalyst	Cong et al. (2007)
Radio frequency magnetron sputtering (film), **Tantalum**	Xenon lamp (Hayashi Tokei, Luminar Ace 251 Xe) with a glass filter	Decomposition of the Oleic acid measured by the contact angle	Obata et al. (2007)
Sol-gel method using tetrabutyl titanate followed by ball milling in urea, **Tungsten**	Visible light (13 W fluorescent lamp with UV cut-off filter)	Photodegradation of sulfosalicylic acid (40 mg/L), 1 g/L TiO_2 Photodegradation of MB (20 mg/L), 0.5 g/L TiO_2	Shen et al. (2008)
Sol-gel method using Ti(O-Bu)$_4$, **Europium**	Visible light (250 W halogen lamp with UV cut-	Photodegradation of reactive red 2 (50 mg/L), 70 mg/L of TiO_2 in	Xu et al. (2008)

	off filter)	200 mL solution	
Wet chemical method using $Ti(O\text{-}Bu)_4$, **Vanadium**	Visible light (400 W xenon lamp with a UV cut-off filter)	Photooxidation of MB (0.005 mM), 40 mg of TiO_2 in 100 mL solution	Gu et al. (2008)
Sol-gel method using TTIP, **Silver**	Visible light (Metal halogen lamp with a UV cut-off filter, 1.6 mW/cm^2)	Photocatalytic inactivation of *E. coli* AN 387 cells	Wu et al. (2010)
Hydrolysis precipitation method using $Ti(OBu)_4$, **Silver**	30 W fluorescent lamp	Photocatalytic inactivation of *E. coli* and *B. subtilis*	Yuan et al. (2010)

Wu et al. (2010) prepared Ag-N-doped TiO_2 by a sol-gel method. They studied the effect of co-doping on the inactivation of *E. coli* AN 387 cells irradiated by a halogen lamp (1.6 mW/cm_2) equipped with a UV cut-off filter. Similarly to the results reported by Yuan et al. (2010), Ag-N-TiO_2 showed the highest photocatalytic activity under visible light. The inactivation was attributed primarily to the production of hydroxyl radicals by photocatalysis rather than to bactericidal effects. The photocatalytic killing mechanism involved oxidative damage to the cell wall and cell membrane, as well as alterations of the internal DNA molecules.

2.4. Model Water Pollutants used in this Study

2.4.1. Humic acid as a Natural Water Pollutant

2.4.1.1. Characteristics of Humic Acid

Natural organic matter is a complex mixture of organic compounds, mainly of humic substances (HS). HS originate from the decay of plant debris (through a process called humification) and are the main cause of the brownish colour of many surface waters. The chemical composition of HS is complex and heterogeneous. The main fractions are customarily being classified as humic acids (HA or HAs), fulvic acids (FA or FAs) and humin (IHSS 2007, Steelink 1999).

Many speculations about the chemical composition of HA have been a source of debate among scientists during the last century. The first empiric formula of HA probably has been suggested by Mulder (1840) as $C_{40}H_{30}O_{15}$. The study of Schulten and Plage (1991) showed that benzenes and alkylbenzenes (with other minor compounds) are major products of the thermo-decomposition of HA. Later on, Schulten (1993) proposed a new "typical" HA formula being as a $C_{308}H_{328}O_{90}N_5$, with a molecular weight of 5540 Da (Figure 2.3). Oxygen was detected in carboxyl, phenolic and alcoholic hydroxyls, carboxylic esters and ethers radical groups. In contrast, N was found in heterocyclic structures.

In general, HS are composed of polydispersed macromolecular assemblies including both hydrophobic domains and hydrophilic functional groups (amphiphilic properties). These properties are responsible for their solubility, surfactant-like character, susceptibility to biodegradation and interaction with a wide variety of organic and inorganic compounds (Stevenson 1994; Sutton and Sposito 2005).

Although being partly biodegradable, HS are considered recalcitrant yet chemically reactive substances (IHSS 2007). They are recognised chelators to bind to metals and heavy metals, and affect the chemistry, cycling and bioavailability of nutritive chemical elements. Also, they play a major role in the formation of disinfection by-products during water treatment (chlorination). The removal of HA from water is required to eliminate the potential hazard from the formation of carcinogenic

trihalomethanes (THMs) and haloacetic acids (EPA 1979; Uyguner and Bekbolet 2011).

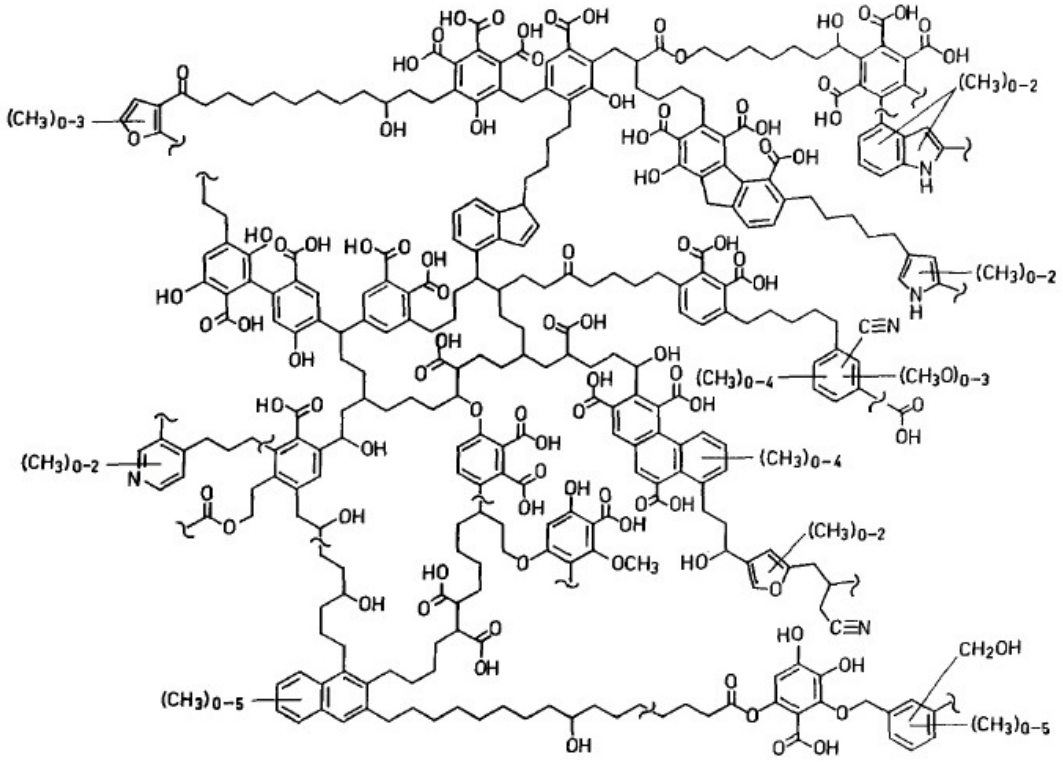

Figure 2.3. The proposed HA chemical formula (Schulten 1993).

2.4.1.2. Photocatalytic Decomposition of Humic Acids

The photocatalytic degradation of HA in aqueous TiO_2 suspension to eliminate the formation of THMs after water chlorination first was reported by Ogawa et al. (1995). The reactor system required 24 h for the complete mineralisation of HA and the chloroform production (after chlorination) was no longer detected. Bekbolet and Ozkosemen (1996) carried out a similar investigation for the decomposition of HA and reported that the removal of HA was correlated to the decrease in the concentration of THMs.

The removal of HS from drinking water using photocatalysis was successfully achieved and reported (Eggins et al. 1997). A 50% removal was obtained after irradiating the suspension for 12 min ([HA] = 100 mg/L, TiO_2 = 1 g/L). In contrast, a

50% mineralisation was only possible after 1 h irradiation. The same research group (Palmer et al. 2002) also studied the kinetics of the photocatalytic degradation of HAs using TiO_2. The heterogeneity of HAs and their high molecular weight significantly affected the kinetics of degradation, which failed to fit commonly used photocatalytic degradation models. The authors investigated the effect of operational parameters at 1 g/L TiO_2 and reported the following:

- The photodegradation at different HAs' concentrations did not fit the L-H model and the photomineralisation showed an apparent zero order kinetics.
- Fluctuating results were obtained when changing the temperature of the reaction.
- Light intensity was proportional to the degradation rate at low intensities; the same was recorded at high intensities until a certain threshold.
- The results of the dissolved oxygen concentration experiments did not follow the L-H kinetics. The authors also reported photodegradation and photomineralisation under nitrogen sparging.
- The maximum mineralisation was obtained at pH 7 and the lowest at pH 9.

In contrast, other studies reported that the L.-H kinetics were adequate to fit the decomposition of HA dissolved in different types of waters (Bekbolet et al. 2002; Al Rasheed and Cardin 2003) and using different photocatalysts (Li et al. 2007). For instance, the operational parameters (high temperature, low pH, high oxygen concentration and a TiO_2 concentration of 2.0-2.5 g/L) have been optimised for the photodegradation of HA in saline water (Al Rasheed and Cardin 2003). However, the authors suggested the use of supported TiO_2 (thin films) because the suspensions were unstable and vigorous agitation was required to avoid settling.

The adsorption and mechanism of HA decomposition was discussed by Wiszniowski et al. (2002). They found that the adsorption of HA onto TiO_2 was promoted by acidic pH (formation of carboxylate surface groups and carboxylic groups on HA) and this played an essential role in the photocatalytic process. The authors also

reported that the photocatalytic process completely mineralised the HA molecules and did not follow the often suggested trend of splitting and/or decomposing high molecular weight molecules into smaller compounds. In contrast, the spectroscopic evaluation of the molecular size profiles during the photocatalytic degradation of HA showed that lower molecular size and high UV absorbing compounds were formed as intermediate products (Uyguner and Bekbolet 2005). Moreover, this was validated by the analysis of the fluorescence spectra which revealed that the peaks shifted to lower wavelengths after photocatalytic degradation of HA. The authors attributed this to the formation of by-products such as alcohols, aldehydes, ketones and carboxylic acids.

Recently, Liu et al. (2008) investigated the photocatalytic removal of HA over TiO_2 by the fractionation and molecular weight characterisation studies. The high performance size exclusion chromatography and rapid fractionation analysis showed that large molecular weight compounds were degraded into lower molecular weight organics. Also, this research found that the decrease in pH (high HA adsorption onto TiO_2) did not improve the photocatalytic activity, therefore indicating the apparent importance of hydroxyl radicals formation.

2.4.2. Methylene Blue

MB is a cationic dye with a molecular formula of $C_{16}H_{18}N_3SCl$, corresponding to a molar mass of 319.85 g/mol (Figure 2.4). It is used in many industrial processes such as textile dyeing, chemical manufacturing, as well in medicine. Similar to other dyes, MB is characterised by high molecular weight, high chemical stability and high water solubility. In general, textile dyeing processes use large amount of water therefore discharge of a significant amount of coloured wastewater that contains toxic wastes, namely suspended solid, un-reacted dyestuffs and auxiliary chemicals (Zhang et al. 2002).

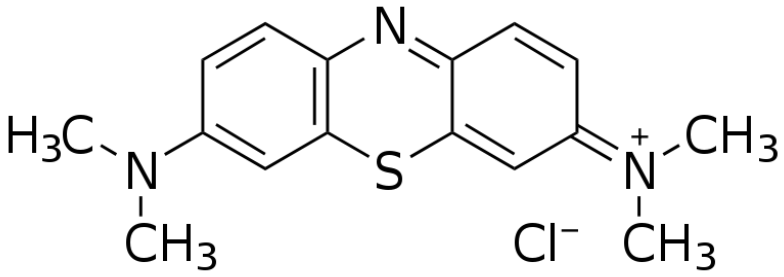

Figure 2.4. Chemical structure of MB.

MB is considered recalcitrant, relatively difficult to remove from water by conventional water treatment processes and a substance that can cause damage to natural ecosystems. Therefore, several advanced oxidation processes were investigated as means to bleach the imparted colour and mineralise MB into essentially harmless salts. Among these processes, HP has been extensively studied in the past few decades, and will also be addressed in the next section (Matthews 1989; Lachheb et al. 2002; Shimizu et al. 2007).

The photocatalytic degradation of MB was experimentally achieved over an illuminated suspension or deposited thin films of TiO_2 under both UV and solar light (Matthews 1991; Lakshmi et al. 1995; Houas et al. 2001; Khalyavka et al. 2001; Zhang et al. 2002; Shimizu et al. 2007). The kinetics of MB photodegradation was found to fit well the L-H model. The total mineralisation of MB and evolution of resulting ions such as sulphate, nitrate, ammonium and CO_2 gas is described by the following generic reaction (Matthews 1989; Houas et al. 2001):

$$C_{16}H_{18}N_3SCl + 25.5O_2 \rightarrow 16CO_2 + 6H_2O + 3HNO_3 + H_2SO_4 + HCl$$

Matthews (1989) found that the rate of CO_2 evolution was four times slower than the rate of MB disappearance. This was attributed to the formation of intermediate products during the photocatalytic degradation. The pathways of MB decomposition and the formation of intermediate products were described in detail by *Herrmann's research group* (Houas et al. 2001). The aromatic metabolites were detected by Gas chromatography/Mass spectrometry (GC/MS) and liquid chromatography/Mass spectrometry (LC/MS) and are presented in Figure 2.5. To describe the

mineralisation, two schemes were presented one for sulphur and another for nitrogen-containing groups. In the first case, the degradation of MB was initiated by the cleavage of the bonds of the $C–S^{+}=C$ functional group by the attack of an $OH^{\bullet}$ radical to form a sulfoxide (R–S(=O)–R'). A second attack resulted in the formation of a sulfone, a third attack gave sulfonic acid and the final or fourth attack was found enough for the total mineralisation and the formation of SO_4^{2-} anion. In the second case, two pathways were described through the progressive attacks of $OH^{\bullet}$ producing phenolic compounds and alcohols/aldehydes before the formation of ammonium and nitrate ions.

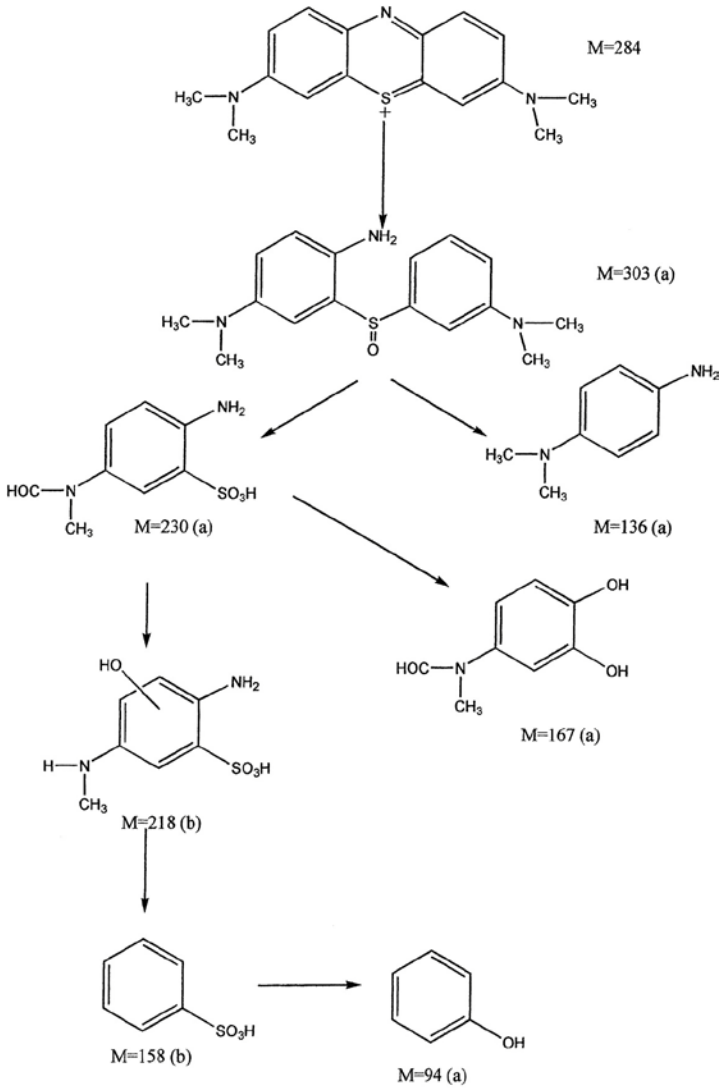

Figure 2.5. Pathways of MB decomposition (Houas et al. 2001).

2.5. Summary

Heterogeneous photocatalysis processes that decompose aqueous contaminants are highly dependent on the reaction conditions and the photocatalytic reactor setup. The adoption of a "standardised" reactor system to allow the comparison between different classes and types of photocatalysts is highly recommended. Even though, the use of “quantum yield” may partially resolve the problem by minimising the effect of reaction parameter, it is by itself dependent on the experimental conditions used.

New classes of visible-light responsive photocatalysts are becoming attractive to enable the more effective utilisation of solar energy. Doping and co-doping of titania is a effective approach to obtain improved visible light active photocatalyst. However, many of the reported doping processes require expensive equipment and/or complicated procedures that are unfeasible for industrial-scale production.

The production of nanostructures that can be easily separated from water is also a great concern for the water treatment industry. Therefore, this thesis will explore and examine novel methods to produce improved photocatalysts with high efficiency, synthesised by environmentally friendly processes and which can be easily separated by settling.

UNIVERSITY OF TECHNOLOGY, SYDNEY

FACULTY OF ENGINEERING AND INFORMATION TECHNOLOGY

CHAPTER 3

MATERIALS AND METHODOLOGIES

3.1. Introduction

This chapter describes the materials, experimental setups, instruments and analytical methods used to achieve the objectives listed in Chapter 1.

3.2. Materials

3.2.1. Degussa P25 Photocatalyst

Degussa P25 TiO_2 powder is a complex mixture of rutile, anatase and amorphous structures (Figure 3.1). The mean particles size is around 30 nm and the specific surface area ranges from 47 to 52 m^2/g. The surface charge of P25 is negative at pH values above 5.8 and positive at lower pH (Figure 3.2). The crystalline powder was used as a titanium precursor in Chapters 4, 5, 6, 7 and 8.

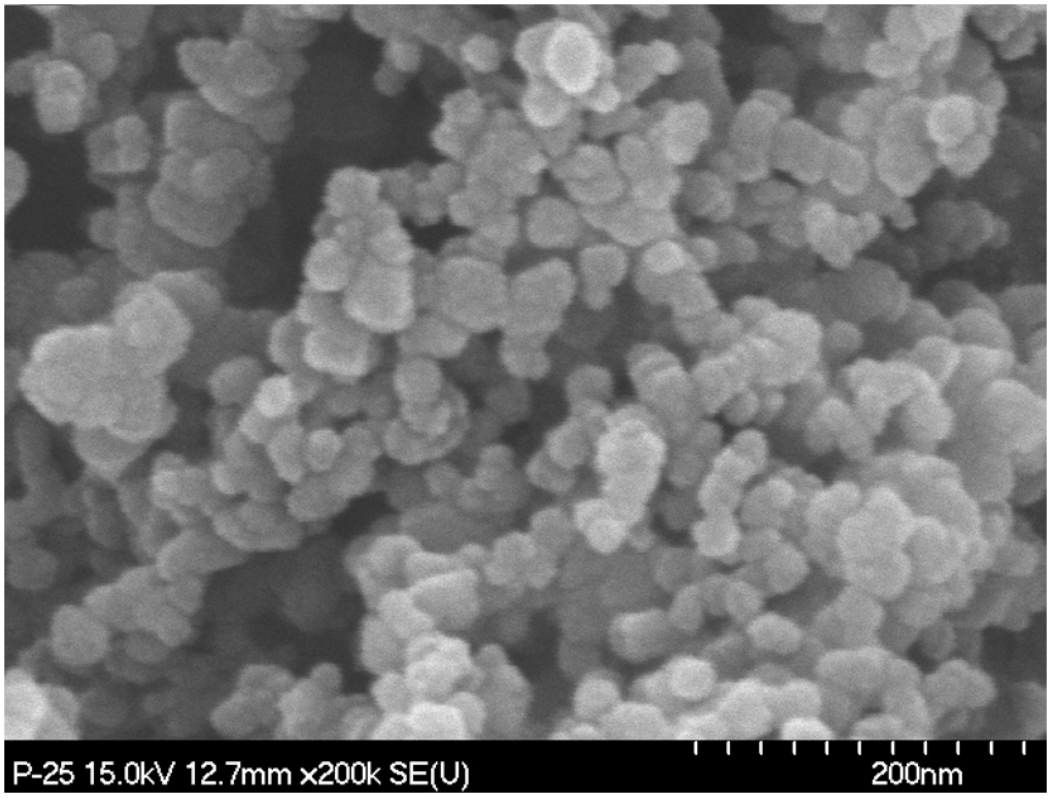

Figure 3.1. SEM image of Degussa P25 TiO_2 particles used in this study.

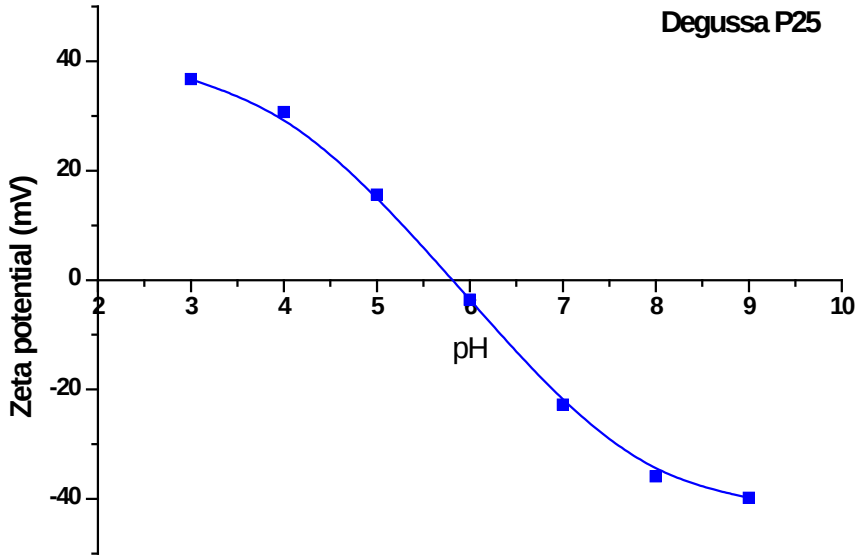

Figure 3.2. Zeta potential of 1 g/L Degussa P25 suspension in Milli Q water.

3.2.2. Chemicals

The list of chemicals used in this study for the preparation of solutions and reagents is presented in Table 3.1.

3.2.3. Wool

Merino wool clean fleeces were purchased from Virginia farm woolworks (Annangrove, NSW, Australia). Morphology characterisation of fibres showed ultrafine fibres of approx. 15.1 µm in diameter. The fibres were not treated and used as received in Chapter 8 (Figure 3.3).

Generally, wool is a natural protein fibre composed of keratin-type protein. Chemically, these proteins contain five elements: carbon, hydrogen, oxygen, nitrogen and sulphur (Bradley et al. 1997). These elements are combined into 19 amino acids linked together in ladder-like polypeptide chains.

Table 3.1. List of chemicals

Generic name	Purity (%)	Supplier	Code
Ammonium hydroxide	28-30	Sigma Aldrich	221228-2.5L-P-A
Hydrochloric acid	37	ANALAR, VWR	20252-420
Hydrogen peroxide	50	ACR	0868
Humic acid (HA)	-	Sigma Aldrich	53680-10G
Methylene blue (MB)	98	Chem Supply	ML045
Nitric acid	69.5	Scharlau chemie S.A.	AC16002500
Sodium carbonate	99.9	UNIVAR	D3247
Sodium hydrogen carbonate	99.7	Chem Supply	SA001
Sodium hydroxide	97	Chem Supply	SA178

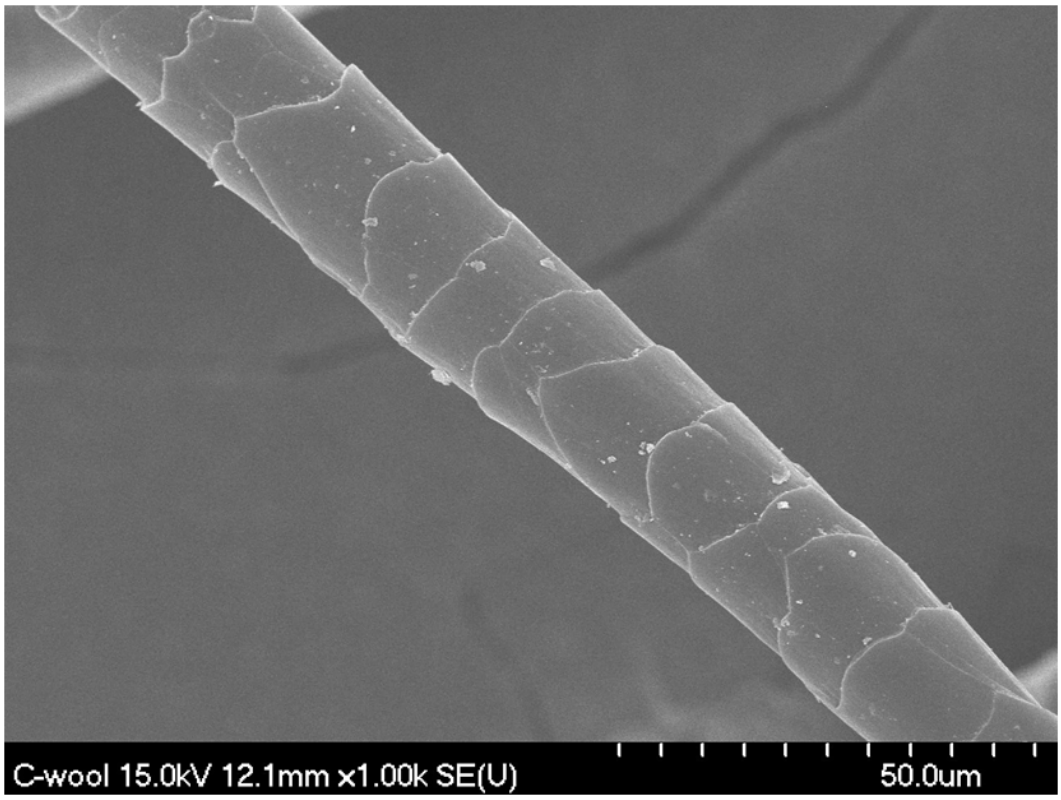

Figure 3.3. SEM image of a Merino wool fibre.

3.3. Photocatalysts Characterisation Equipments and Methods

3.3.1. Scanning Electron Microscope / Energy Dispersive X-ray

The scanning electron microscope/energy dispersive spectroscope (SEM/EDS, Rigaku, Japan) operating at an EHT voltage of 15 kV was used to obtain images of photocatalysts in Chapter 5. In contrast, the photocatalysts prepared in Chapters 4, 6, 7 and 8 were imaged using a Zeiss Supra 55VP SEM operating at 15-20 kV and equipped with an Oxford EDS system for elemental characterisation. The magnification was adjusted between 2 KX and 100 KX to obtain clear morphology images of powders.

Prior to imaging, powder samples were dried in oven at 100 °C for 3 h to remove moisture. The powders were then sprinkled on a carbon tape and the excess was removed by air blowing to get a uniform dispersion of particles. Finally, the samples were placed in the vacuum chamber of the SEM and images were taken using a computer imaging software. The chemical composition of powders was also investigated using an EDS detector. The procedure consisted of pointing the cursor shown on the screen to randomly selected points on the powder and analysing the composition using different software. Elemental composition was generated in terms of percentage.

3.3.2. Transmission Electron Microscope

A Philips CM200 (Netherlands) transmission electron microscope (TEM) operating at 200 kV was used to investigate changes in morphology of samples prepared in Chapter 5.

First, powder samples were ultrasonically dispersed in isopropanol (to avoid forming agglomerations) for 10 minutes. Then, two drops of the suspension were put on a carbon-coated copper grid; this was followed by the evaporation of alcohol at ambient temperature. Samples were then imaged using TEM and images were obtained at different magnifications.

3.3.3. Specific Surface Area and Pore Size Measurements

The specific surface area of photocatalysts was calculated using the Brunauer, Emmet and Teller (BET) method on an automated Micromeritics Gemini surface area analyser (Model 2360, USA). Analysis was undertaken by the multipoint BET surface area measurement with different adsorption pressures. The mesoporosity of samples was estimated from the N_2 desorption data by using the Barrett-Joyner-Halenda (BJH) method (Barrett et al. 1951). The BET surface area was calculated from the physical adsorption of gas molecules on a solid surface using the following equations by using the *nanoporosity view* software:

$$S_{total} = \frac{(v_m N_A S)}{M} \tag{3.1}$$

$$S_{BET} = \frac{S_{total}}{a} \tag{3.2}$$

with N_A Avogadro's number, S molecular cross-sectional area, M molecular weight of adsorbate, and a weight of powder sample.

Sample powders were first placed in a glass cell and purged in N_2 flow for 5 h to remove impurities. The S_{BET} of samples was determined by N_2 adsorption at 77 K using the instrument described before.

3.3.4. X-ray Diffractometer

X-ray diffraction (XRD) patterns were generated using MDI Jade 5.0 (Materials Data Inc., USA). It is a non-destructive technique that reveals detailed information about the crystallographic, chemical and physical properties of materials. The scattered intensity of an X-ray beam was assessed as a function of the wavelength of the incident beam, the incident and scattered angle using the computer software provided by the instrument manufacturer.

Powder samples (0.1 - 0.5 g) were placed in plastic holders and inserted in a shelve-like auto-sampler. The diffraction angles (2θ) were measured between 0 and 90° to detect peaks of anatase and rutile in the synthesised photocatalysts samples.

3.3.5. X-ray Photoelectron Spectroscope

X-ray photoelectron spectra were performed on a Multilab2000 (VG, UK) XPS instrument with a non-monochromatic MgKα radiation and a charge neutraliser at a residual gas pressure of below 10^{-9} Pa. All the binding energies were referenced to the C1s peak at 285 eV of carbon. Instrument control and data processing were performed using the *Avantage* software program provided by the equipment manufacturer.

Dry powders were dispersed on an adhesive carbon tape attached to the sample holder. The loose powders were removed by air blowing or by inverting the sample holder. The holder was then placed in the instrument for measurement.

3.3.6. Malvern Zetasizer

The zeta potential of various powders was determined by Malvern nano series (Nano-zs, Malvern Instruments Limited, UK) analyser. The measurement of zeta potential is achieved by a combination of laser Doppler velocimetry and phase analysis light scattering (PALS) in Malvern's patented M3-PALS technique. The instrument is a combination of an optical measurement unit and a computer that controls the measurement and allows data analysis and presentation.

Samples were prepared by suspending particles in Milli Q water at defined pH values, and injected into a folded capillary cell surrounded by thermal contact plates to minimise the effect of temperature. A blank (Milli Q water) was run before the samples for instrument calibration. The zeta potential was measured within a range of -50 mV and + 50 mV. The reported values are means calculated from 20 measurements. In all experiments, the pH of the suspension was adjusted by acid and base solutions and plotted against the corresponding mean zeta potential value.

3.4. Photocatalytic Reactors

3.4.1. Photoreactor 1

The decomposition of MB under visible light (Chapter 5) was performed in Photoreactor 1. The reactor consisted of a quartz cylinder (40 cm x 7 cm), a submerged cooling device (water cooling) and a quartz cover (Figure 3.4). The assembly was equipped with an air sparging device for supplying dissolved oxygen, a magnetic stirrer and 10 W white light fluorescent lamps (FL 10 D, P.N. Lighting, China) with UV cut-off filter ($\lambda \geq 420$ nm).

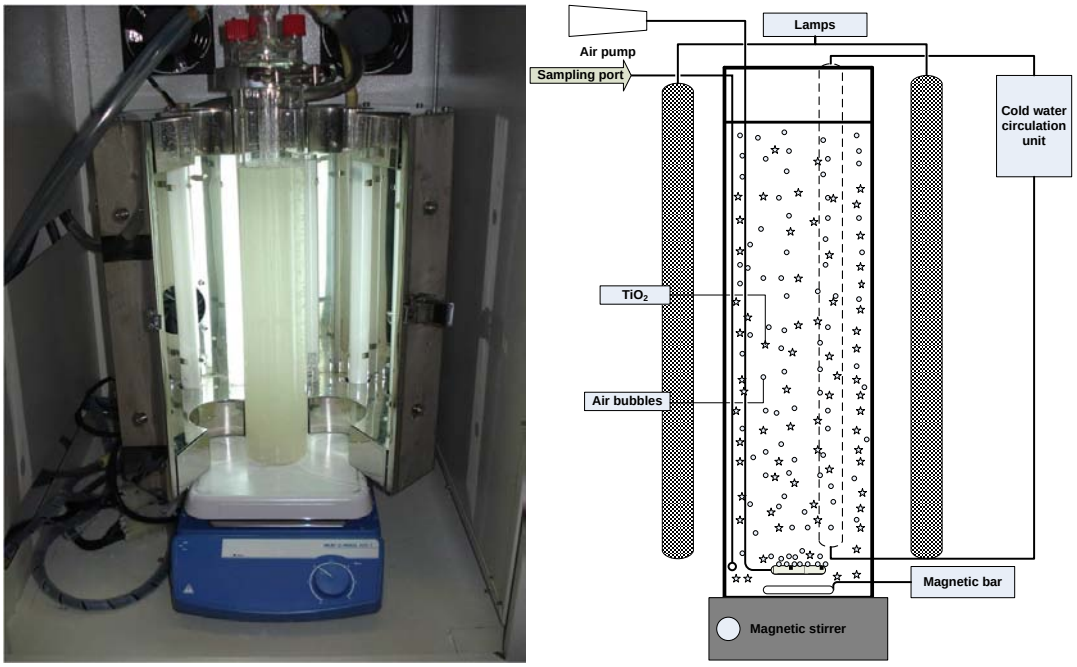

Figure 3.4. Photo (left) and a schematic drawing (right) of Photoreactor 1.

3.4.2. Photoreactor 2

The removal of MB and HA (Chapters 6 and 8, respectively) was carried out in Photoreactor 2 (Figure 3.5). The assembly consisted of a glass cylinder (40 cm x 10 cm), a submerged cooling device (water cooling) and a plexiglass cover. The UVC light lamps (3 x 15 W, Perkin Elmer) were enclosed in quartz sleeves and submerged in the solution during photocatalysis. The oxygen supply and the uniformity of the suspension were maintained by air sparging at 0.6 ml/min and magnetic stirring at 450 rpm, respectively.

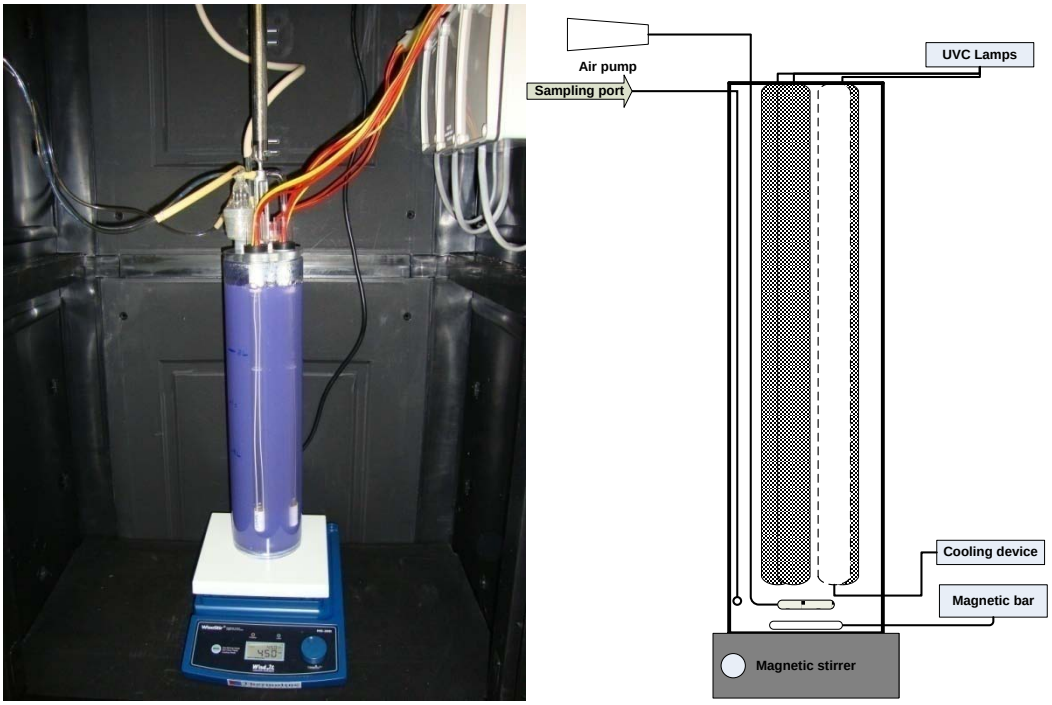

Figure 3.5. Photo (left) and schematic diagram (right) of the annular slurry Photoreactor 2.

3.4.3. Solar Simulator

The Luzchem Research SolSim Xenon photoreactor (solar simulator, Figure 3.6) featured an enclosed exposure chamber, an exhaust system and thermostatic control to maintain the chamber temperature close to ambient temperature. The principal light source was a Xenon lamp (300 W) and a complex filter system ensured emission to closely match the AM1.5 spectrum (Figure 3.7). The total irradiance of the system (280-800 nm) is equal to 590 000 W/m^2 at power meter reading of 238 (x 100 lx).

The photocatalytic degradation of MB (Chapters 5 and 7) under solar light was carried out in a 200 mL glass beaker. The solution was placed in the solar simulator, magnetically stirred and air sparged at a temperature of 26 °C.

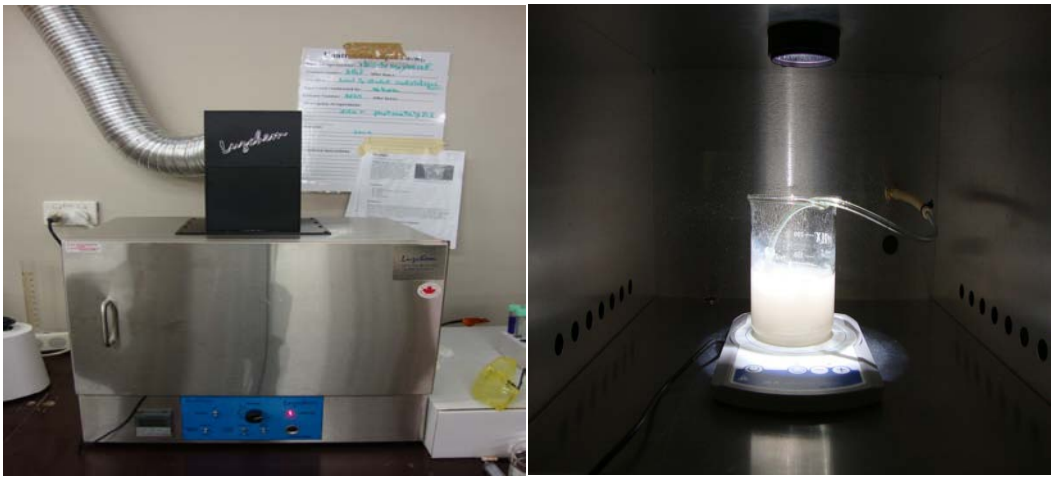

Figure 3.6. Solar simulator outside (left) and inside (right).

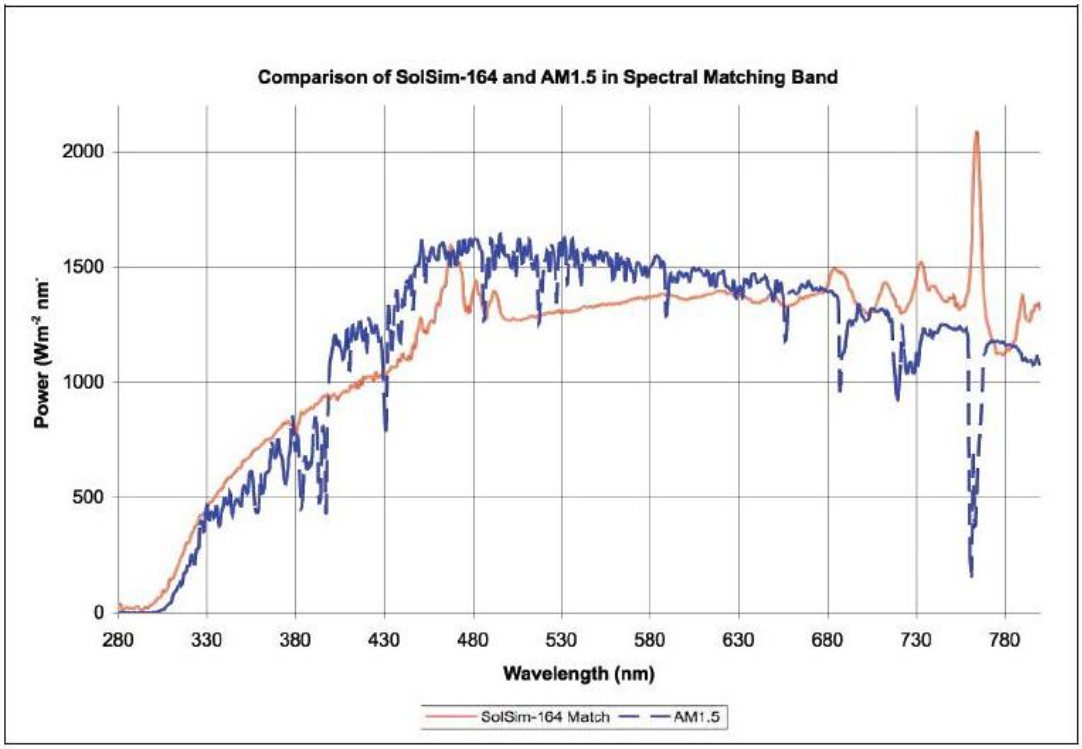

Figure 3.7. SolSim-164 and AM1.5 spectral emission comparison.

3.5. Auxiliary Laboratory Instruments

The separation of the photocatalysts from the solutions (Chapters 4, 5, 6, 7 and 8) was achieved by centrifugation (Centurion Sci., 2040). The suspensions were placed in 50 mL conical bottom centrifuge tubes (Axygen, SCT-50ML-R-S) and the centrifugation was carried out at 3000 rpm for 5 min (Figure 3.8).

The dark adsorption experiments (Chapters 6 and 7) were performed in 250 mL conical glass Erlenmeyer flasks. The homogeneity of suspensions was maintained by placing the flasks in an orbital shaking incubator (Thermoline, TU400) at a set temperature of 25 °C unless otherwise stated (Figure 3.8).

Figure 3.8. Centrifuge (left) and orbital shaker (right).

The turbidity of samples (Chapters 6, 7 and 8) was determined using a combined Hach HI 93414 turbidity and chlorine meter. The obtained data was plotted against time to evaluate the settling of suspended particles.

The pH of solutions was monitored using a TPS 90FL pH meter (TPS Pty Ltd, Brisbane, Australia). Two pH buffer solutions were used to calibrate the instrument (pH = 6.88, TPS 121380 and pH = 4, TPS 121382 solutions) (Figure 3.9).

Figure 3.9. Hach HI 93414 turbidity and chlorine meter (left) and TPS pH meter (right).

Powder drying and calcination was accomplished in a *Labmaster* oven (temperature range RT-200 °C) and a muffle furnace (*Labec*, CE-MLS), respectively (Figure 3.10). The samples were placed in porcelain crucibles and allowed to dry at temperatures between 75 °C and 100 °C. This was followed by homogenising the samples using a mortar and pestle, and sample calcination at 550 °C (Chapter 6 and 7) temperature. The samples were stored in sealed glass tubes until usage.

Figure 3.10. Oven (left) and Labec furnace (right).

Figure 3.11 shows the Teflon cell used in the hydrothermal treatment of photocatalysts (Chapters 5, 6, 7 and 8). The solution was placed in the cell and topped with a Teflon cover before placed in the oven at the desired temperature.

Figure 3.11. Teflon cell used for hydrothermal treatment.

3.6. Analytical Procedures

3.6.1. UV-vis Spectrophotometry

A Shimadzu UV-1700 spectrophotometer (Figure 3.12) was used in this study to detect the formation of peroxo-titanium complex (Chapter 4), measure MB degradation (Chapters 5, 6 and 7), and HA degradation (Chapter 8). The data was generated using computer software provided by Shimadzu Scientific Instruments Pty Ltd.

The formation of PTC complex was monitored for absorbance peak at λ = 410 nm. The photocatalytic decolouration (or bleaching) of MB was monitored by measuring the decrease of absorbance peak at λ = 664 nm. The absorbance data was converted to MB concentration using a Beer- Lambert standard curve. The relationship between MB concentration and absorbance data is shown in Figure 3.13. The absorbance data was used to plot the decrease in concentration using the following formula:

$$PR = \frac{Abs_t}{Abs_0} \qquad (3.3)$$

PR: photocatalytic removal. Abs_t: absorbance at elapsed time *t*. Abs_0: initial absorbance at $t = 0$.

In Chapter 8, the HA photocatalytic removal was assessed by measuring the absorbance at λ = 254 nm.

The spectrophotometer was calibrated using Milli-Q water. Then, samples were placed in standard square 1 cm quartz cuvette, which was inserted in the cuvette holder of the spectrophotometer. Spectral data was saved for processing following a scan in the range of 200 - 700 nm.

Figure 3.12. Shimadzu UV-1700 spectrophotometer.

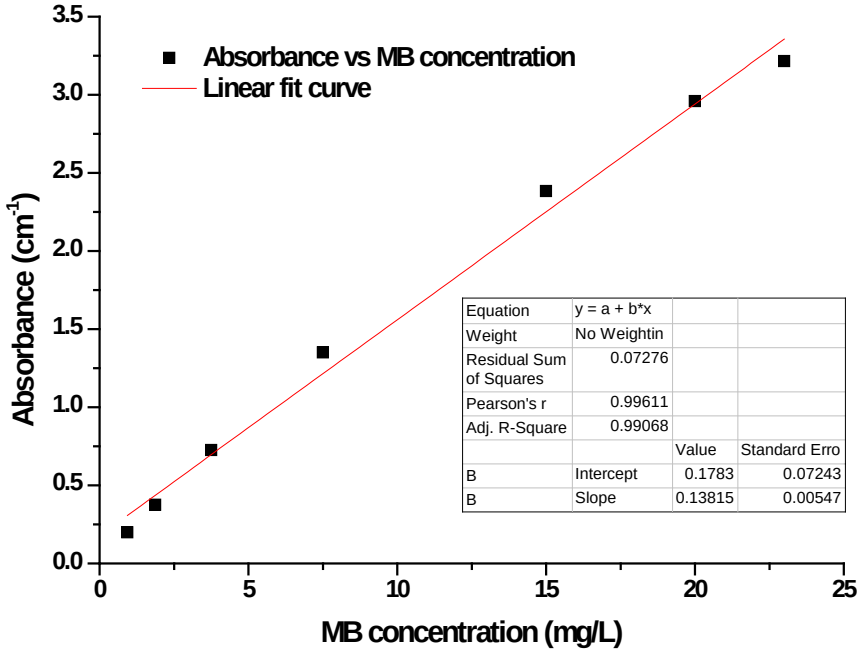

Figure 3.13. Linear regression of MB concentration versus absorbance at λ = 664 nm.

3.6.2. Dissolved Organic Carbon Measurement

A *multi N/C 3100* analyser (Analytic Jena AG, Germany) was used for determining the total carbon content of aqueous samples (Figure 3.14). All samples were filtered through 0.45 µm syringe filters; hence the obtained values represent dissolved organic carbon (DOC). The equipment uses thermocatalytic decomposition in the presence of a special catalyst, with synthetic air used as a carrier gas. The measurement and data processing was controlled by the Multiwin software package provided by the manufacturer of the instrument. Standard DOC solutions were used to calibrate the instrument and the obtained plot is presented in Figure 3.15.

For determinations at least 10 mL of liquid samples were placed in 30 mL glass tubes and loaded in the auto-sampler (APG-64). The injection volume was adjusted to 500 µL by running the selected TOC measurement method. The sample aliquot was then metered directly into the combustion tube, pyrolysed and oxidised in the carrier gas flow (the carrier gas also acts as the oxidising agent) with the aid of the catalyst. The formed test gas CO_2 was fed to the NDIR detector and the generated signal sequence was used to obtain a time integral. The integral was proportional to the carbon concentration in the test solution. A previously determined calibration function was then used to calculate the carbon content of the sample (manufacturer manual).

Figure 3.14. Multi N/C 3100 DOC analyser with autosampler.

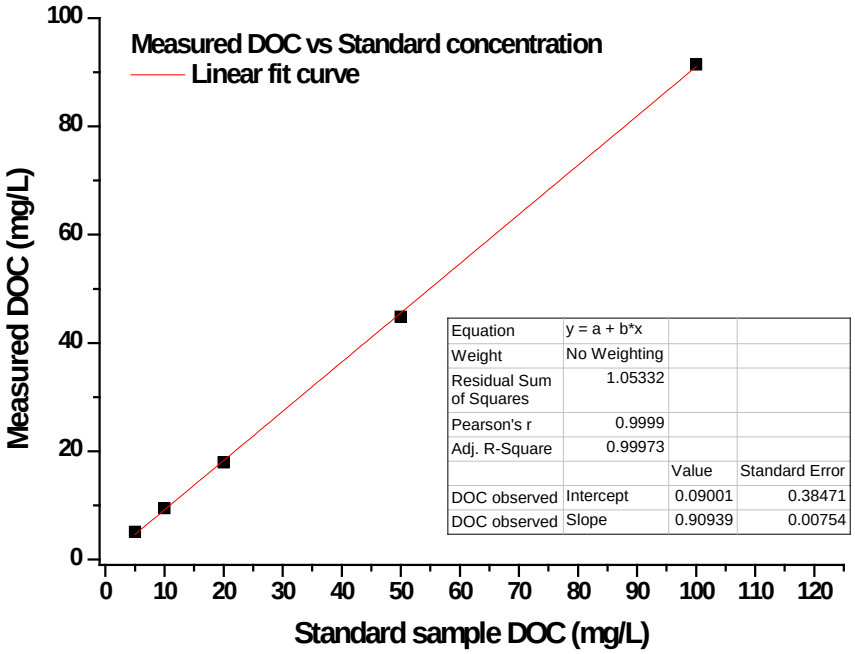

Figure 3.15. Standard curve of DOC (mg/L).

3.6.3. Ion Chromatography

The mineralisation of MB (Chapter 6 and 7) was measured by sulphate determination using a Metrohm ion chromatograph (790 IC) equipped with a Metrosep A Supp 5-150 (150 x 4.0 mm, 5 µm) column (Figure 3.16). The eluent consisted of 1 mmol/L of sodium hydrogen carbonate and 3.2 mmol/L of sodium carbonate dissolved in MilliQ water. The total injection volume was 5 mL (1 mL used for data generation while 4 mL used for rinsing) and the run time was 22 min. The evolution of sulphate was assessed from the peak area that was converted to sulphate concentration using the standard curve shown in Figure 3.17.

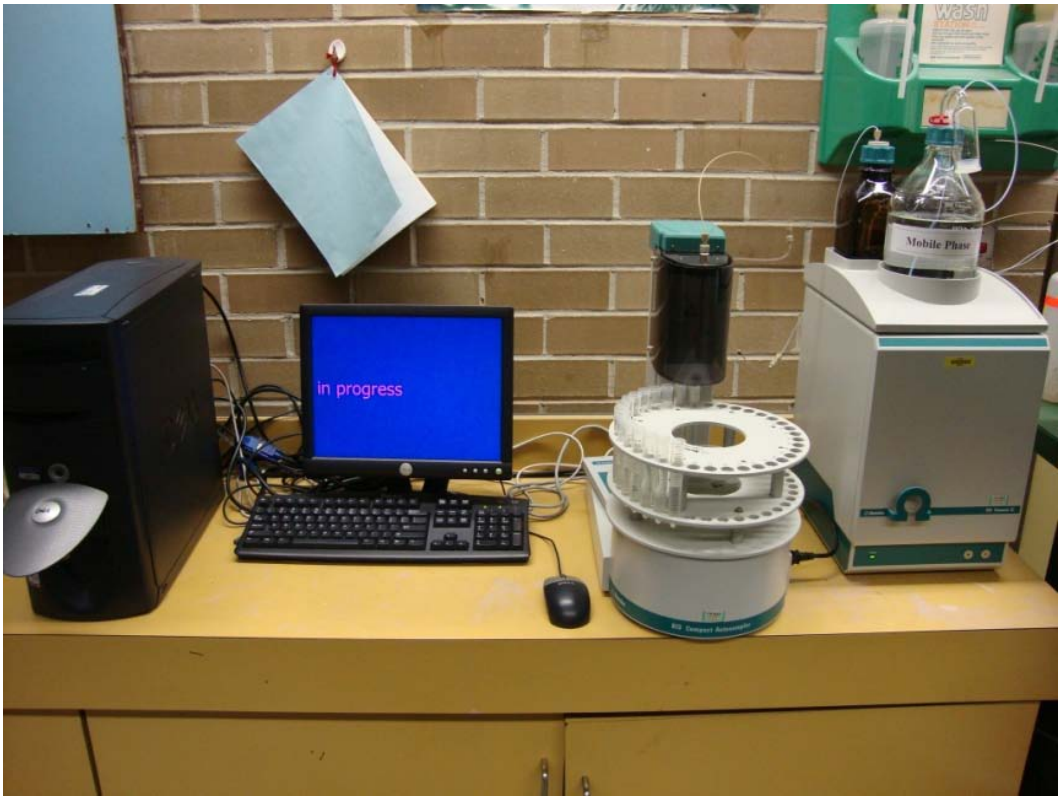

Figure 3.16. Metrohm ion chromatograph.

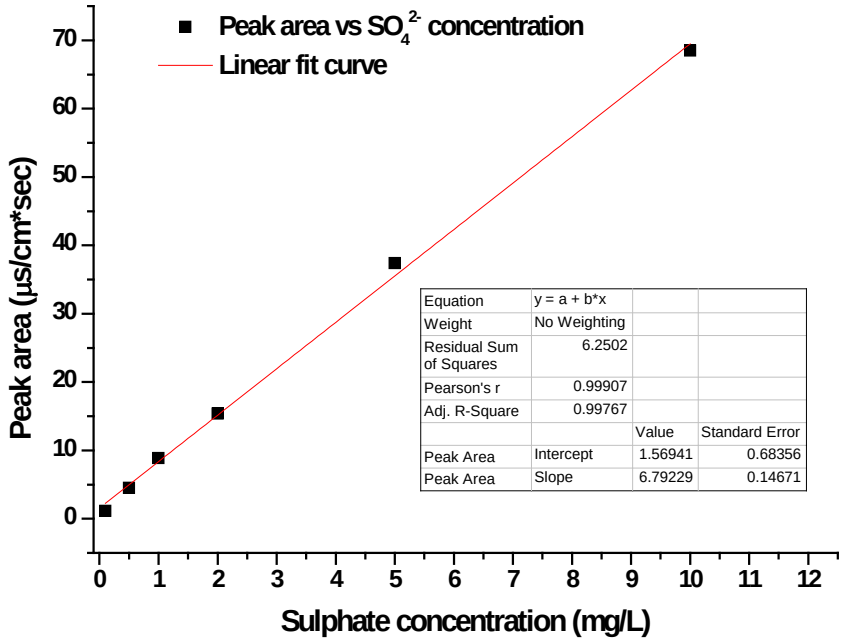

Figure 3.17. Linear relationship between peak area (µs/cm.sec) and sulphate concentration (mg/L).

3.7. Data Processing and Plotting

All data were processed using OriginPro Academic version 8.5.0 SR0 b130 (OriginLab Corporation).

UNIVERSITY OF TECHNOLOGY, SYDNEY

FACULTY OF ENGINEERING AND INFORMATION TECHNOLOGY

CHAPTER 4

SYNTHESYS OF NANOMATERIALS FROM PEROXO-TITANIUM COMPLEXES

4.1. Introduction

Over 140 years ago, Schonn (1870) found that the addition of hydrogen peroxide to an acidic solution of Ti(IV) can turn the solution colour to intense orange. The numerous speculations about the reason behind this change in colour have triggered research and investigation over several aspects and experimental conditions. Not only peroxo-titanium complexes (PTC) became an important tool of analytical chemistry, but eventually provided a cost effective and environmentally friendly route to produce novel nanomaterials.

Muhlebach et al. (1970) studied the chemistry of the peroxo complex of titanium by starting from pure $TiCl_4$ and concentrated H_2O_2 base materials. The procedure consisted of adding drop-wise $TiCl_4$ to H_2O_2 at a temperature of -30 °C to prevent the evolution of O_2. They suggested that hydrogen ions are liberated in high acidic conditions according to the following reaction:

$$Ti.aq^{4+} + H_2O_2 \rightarrow Ti(O_2)(OH)_{n-2}{}^{4-n+} + nH^+ \qquad \text{(Eq. 4.1)}$$

The value *n* denotes the number of hydrogen ions which are liberated when the peroxo complex is synthesised. The authors reported that the increase in pH turns the colour of the solution from intense orange to yellow, and to colourless upon neutralisation.

The effect of pH on the optical properties of PTC was studied by Cai et al. (2005). PTC was prepared by adding H_2O_2 to titanium hydroxide cake. At pH 2.2 a clear orange colour was observed, which on storage changed to light orange (pH 3.9) and to pale yellow colours between pH 5.8 and 10.77. This finding is clearly in disagreement with the earlier report of Muhlebach (1970), who reported colourless appearance in the alkaline region (colourless), probably due to precipitation during the experiments (Cai et al. 2005).

PTC has been employed for the synthesis of titanate nanostructures, thin film deposits, and doping with metals and non-metals species, due the fact that many

metals are soluble in the slightly acidic H_2O_2 (Kudo 1984; Qian et al. 1993; Wang et al. 2009a). The main advantages of using PTC in the fabrication of titania nanomaterials are:

- Cheap and non-hazardous
- Environmentally friendly compound
- The dissolution of titanium precursors can be controlled
- Many metals are soluble in H_2O_2 which facilitates simple metal doping over TiO_2

This chapter presents the published methods used in the synthesis of TiO_2 nanomaterials by employing a peroxo-titanium route. The effect of H_2O_2/base (ammonium and sodium hydroxides) mixtures on the morphology of nanomaterials in alkaline conditions using P25 as a titanium precursor is also briefly discussed.

4.2. Peroxide Methods for Photocatalysts Synthesis

4.2.1. Metal Doping of Titania

The dissolution of some metal ions in H_2O_2 is possible in order to obtain a peroxo-metal complex. The dissolution of molybdenum (Kurusu 1981), tungsten (Murau 1961; Kudo 1984), niobium and vanadium (Ichinose et al. 2003), niobium and tantalum (Stengl et al. 2010) was reported. The preparation of a chemically stable mixture of peroxo titanium aqueous solution and transition metal ions is of significant importance to synthetise metal-doped TiO_2.

Ichinose et al. (2003) prepared an anatase sol from a PTC solution containing niobium and vanadium. In the method, 0.01 mol of titanium powder was dissolved in a mixture of 15 mL of ammonia water (3 mol/dm^3) and 65 mL of H_2O_2 (30%) to prepare the undoped titania. The excess of ammonia and H_2O_2 was removed by ion exchange using resin (H^+-type cation-exchange) and subsequent ultrasonication. The solution was heated at 100 °C for 8 h in an air tight container in order to yield the anatase sol. Niobium and vanadium-doped anatase sols were prepared by the same way, but the residual ammonia concentration was kept at 0.01 mol/dm^3 to ensure the formation of doped anatase sol. The undoped anatase powder exhibited spindle-like

and arrowhead-like crystals, which became cubic at 10 mol% niobium doping. The UV-visible light reflectance spectra of the samples showed clear shift towards the visible range after vanadium doping, but no change was recorded using niobium dopant. The authors concluded that niobium formed interstitial solid solution in anatase, while V^{5+} substituted the Ti^{4+} ion.

In a similar study, the thermal hydrolysis of a PTC solution (containing niobium or tantalum peroxo-complexes) at 100 °C for 3 days resulted in the formation of niobium or tantalum doped anatase TiO_2 (Stengl et al. 2010). The changes of morphology were also studied, and it was reported that niobium doping changed the morphology of TiO_2 from spindle-like to rectangular or square cross section.

4.2.2. Synthesis of Nanomaterials

The synthesis of peroxo-modified anatase sol from peroxo-titanic acid (PTA) solution was achieved using $TiCl_4$ as a titanium precursor (Ichinose et al. 1996). Ammonia solution was added to $TiCl_4$ in a ratio of 1:9 to form a titanic acid gel (pH 7 after precipitation). After washing with water to remove Cl^- ions, H_2O_2 (30%) was mixed with the titanic acidic gel to obtain a yellow transparent solution, which was autoclaved at 100 °C for 6 h to produce the peroxo-modified anatase sol (PA). TEM images showed ultrafine round particles (less than 20 nm in size) that were morphed into cubic shapes with increasing treatment temperature. The PA sols autoclaved at different temperatures were comprised of crystalline anatase according to XRD diffraction patterns. Autoclaving above 120 °C resulted in the decomposition of the peroxo groups, leading to change in colour (from yellow to milky white) and the aggregation of the anatase sol.

A few years later Ichinose et al. (2001) studied the properties of PTA solution and PA derived from peroxo-titanium hydrate. The synthesis involved precipitating the peroxo-titanium hydrate by adding ammonia to a PTC (obtained by mixing $TiCl_4$ and H_2O_2) solution to reach a final solution pH of 10. The hydrate was further treated with H_2O_2 to obtain a PTA solution. The effect of several hydrothermal treatment times (2, 4, 6, 8, 12 and 20 h at 100 °C) was investigated using PTA and the hydrate

for the synthesis of PA. The hydrothermal treatment showed a direct effect on the transformation to crystal anatase from an amorphous peroxotitanium hydrate powder, requiring minimum 2 h for the crystallisation to start. The PA consisted of fine arrowhead-like anatase crystals with less than 20 nm in size, which increased with increasing heating time up to 6 h. The photocatalytic activity of films prepared with peroxo-modified anatase sol was found to be as high as that of the films coated with P25 powder.

Tetraisopropylorthotitanate (TIPT) was slowly mixed with a basic solution of H_2O_2 (pH 9, adjusted by adding NH_4OH) under magnetic stirring at 5 °C to produce a yellow solution of PTC (Bessekhouad et al. 2003). The obtained powder had poor crystallinity as was shown by XRD analyses. The photocatalytic activity of the end product was tested for the degradation of benzamide under Xenon lamp (300 nm < λ < 800 nm). A relatively low degradation rate was recorded that was attributed to the amorphous characteristic and the resulting high concentrations of defects (recombination centres).

Gao et al. (2004) prepared TiO_2 nanoparticles using an aqueous peroxotitanate solution. H_2TiO_3 was dissolved in the presence of H_2O_2 and ammonia in appropriate quantities to obtain a PTC. The PTC solution was diluted with water and acidified by HNO_3 to pH 2.4 to cause precipitation. The precipitate was collected, rinsed with water and dried. The obtained raw powders showed amorphous structure, which changed to crystalline anatase after calcination at temperatures between 300 °C and 800 °C. Crystalline rutile was also observed at temperatures above 850 °C. TEM images revealed that samples prepared at 10 °C had a whisker-shaped morphology, while those prepared at room temperature were particulates. Nanosized rutile TiO_2 was synthesised from an aqueous peroxotitanate solution (Seok et al. 2006). Titanium tetraisopropoxide (TTIP) was added drop-wise to H_2O_2 in different molar ratios. The resulted reddish-yellow colour solution was refluxed at 100 °C for 1-12 h until a colloidal solution was obtained. The separated particles were air-dried and characterised for physical changes. It was found that the molar ratio of TTIP/H_2O_2 (greater than 0.03) was crucial in the formation of rutile phase. The authors concluded that the air-dried samples (no hydrothermal treatment) were amorphous,

and began to crystallise after 3 h of hydrothermal treatment. TEM images showed rod-like crystalline particles with an average size around 100 nm in the elongated direction.

The isolation of anatase crystallites from Degussa P25 was recently reported by Ohtani and co-workers (2007). They used an ice-cooled mixture of H_2O_2 (50 mL, 30%) and aqueous ammonia (2.5%, 5 mL) to selectively dissolve rutile from Degussa P25 powder. They observed that mixing H_2O_2 alone with P25 only slightly affected the crystal composition of the powder. However, the addition of ammonia or NaOH increased the dissolution rate of rutile from Degussa P25. The authors suggested that the dissolution follows these steps:

1. The formation of peroxo complex (reaction between H_2O_2 and Ti^{4+}).
2. The extraction of Ti^{4+} may proceed at high pH (around 7.8).
3. The addition of NH_3 or NaOH increases the pH, and thus promotes the dissolution.

XRD patterns revealed that a characteristic rutile peak at 2θ = 27.4° almost disappeared after treating P25 for 12 h in H_2O_2/NH_4OH at a pH of 7.8. However, the dissolution of rutile was not possible when NH_4OH was replaced with NaOH at the same solution pH. The isolated anatase nanoparticles were round in shape with sizes between 20 and 40 nm.

A facile sol-gel process using a PTC solution was employed to fabricate nanosized anatase and rutile TiO_2 with different shapes, phases and sizes (Chang et al. 2009). The influence of acetic acid on the morphological and phase evolution of TiO_2 nanocrystals was studied. Different precursor solutions (mixtures of H_2O_2 or H_2O/acetic acid/TTIP) were subjected to hydrothermal treatment for 4 h. It was found that the addition of acetic acid to TTIP followed by H_2O_2 lead predominantly to anatase particles, while the addition of TTIP to H_2O_2 followed by acetic acid, yielded equal quantities of rutile and anatase. Rod-like rutile and rice-shaped anatase were detected by TEM in samples prepared by the addition of H_2O_2, while spherical particles were observed in the samples prepared by the addition of H_2O. Recently, Qi

et al. (2010) reported the synthesis of a phase-pure rutile TiO_2 sol by using an aqueous inorganic peroxotitanate solution as a precursor in the presence of $SnCl_2$. The solution was refluxed at 100 °C for 4-12 h to ensure crystallisation. It was found that in the absence of SnO_2 (results from the reaction of $SnCl_2$ and H_2O_2) only anatase particles were observed, while rutile nucleation occurred in the presence of SnO_2. The authors described the mechanisms of synthesis in the following:

1. The phase transition from amorphous-to-rutile happened by the reduction of surface energy requirements for rutile crystallisation in the presence SnO_2.
2. In the absence of SnO_2, anatase nucleation dominated by the thermal decomposition of the precursors.

A thin film coating was prepared on a glass substrate by using the dip coating method. The coated glass was reported to have good UV-shielding ability and was expected to have promising environmental applications.

4.2.3. Thin Film and Composite Photocatalysts Synthesis

Thin films of TiO_2 can offer important means for solar energy conversion and high efficiency photocatalysis (Bach et al. 1998), due to their high permittivity, high refractive index, and transmittance in the visible region. Such films are usually synthesised by vapour-phase deposition techniques, which require sophisticated and expensive equipment, and have high energy consumption (Hitchman and Alexandrov 2001). Recently, there is an increasing interest in the use of PTC solutions for thin films deposition and surface coating (Ge et al. 2006; Jensen and Fuierer 2006; Wang et al. 2009a; Lopez et al. 2010).

Since Kudo (1984) reported a new technique for preparing metal oxides from peroxopolymetallic acid, many researchers have adopted his technique for the preparation of peroxo-metal complexes for synthesising thin film deposits. Aoki and Nogami (1996) made peroxo-polytitanic acid by dissolving Ti powder in H_2O_2 for 24 h; and filtering the yellow solution to suit film deposition. Thin films were prepared by spray pyrolysis of the solution on SnO_2 glass substrate. After annealing,

anatase films were obtained at temperatures below 450 °C, while a mixed phase anatase/rutile films appeared at 550 °C. By following a different approach for the preparation of the peroxo-polytitanic acid (mixing $Ti(OBu^n)_4$ with H_2O_2), Wang and Hu (1999) produced TiO_2 films on glass substrates. Film thickness was controlled by either adjusting the concentration of the coating solution or the repetition of the coating procedure. Amorphous and anatase films were obtained after annealing at 150 °C and 450 °C, respectively. In contrast, Lee et al. (2004a) reported the synthesis of anatase thin films after annealing the coated substrates at 280 °C. Rutile films could only be fabricated after annealing at 990 °C for 2 h. The titanium precursor was $TiCl_3$ whereas ammonia and H_2O_2 were used for the preparation of the PTA solution.

Thin anatase films deposited on glass substrate were used to treat contaminated water under UV light irradiation. It was found that films prepared after the deposition of titania sols obtained by refluxing a PTA solution at 100 °C for 2, 6 and 10 h are highly photoactive (Ge et al. 2006). The crystal size of anatase depended on the refluxing time, and significantly affected the photocatalytic activity of films annealed at 500 °C. A total of 99% decolouration of methyl orange solution was possible after 160 min of photocatalysis. The direct deposition of TiO_2 thin films from a PTC solution under alkaline conditions were first reported by Gao et al. (2003). H_2TiO_3 was dissolved in an ice-cooled mixture of ammonia and H_2O_2 (pH > 10). The as-obtained yellow colour PTC solution was diluted with water and used for the thin film deposition. A glass substrate was floated in the dilute solution for 12 h before being washed with water and dried by air. Amorphous films comprising nanometer sized grains were obtained, and the grains were transformed to anatase crystals after annealing at temperatures above 500 °C.

The photocatalytic activity of TiO_2/activated carbon composites was assessed for the degradation of methyl orange (50 mg/L) under UV light (Wang et al. 2009a). The composite photocatalyst was prepared by dip hydrothermal method using an inorganic peroxo-titanate solution ($H_2TiO_3 + H_2O_2 + NH_4OH$) as precursor. Anatase crystals were detected by XRD after annealing the composite at temperatures above

180 °C. No rutile peaks were detected even after the annealing temperature was increased to 800 °C.

4.2.4. Nano and Microstructured Photocatalysts

Since the work of Kasuga (1998) on the fabrication of TiO_2 nanotubes by a hydrothermal method in high pH using polycrystalline TiO_2 powder, titanate nanostructures have been synthesised through a variety of technologies (Lu et al. 2006; Kuchibhatla 2007). However, the hydrothermal method is still considered an attractive way because of its simplicity and reproducibility (Byrappa and Adschiri 2007). During the last decade, the preparation of PTC at high pH has initiated the production of interesting structures using low-temperature hydrothermal methods.

TiO_2 foam (Figure 4.1) was obtained from the direct decomposition and reaction of H_2O_2 inside titanium oxide/hexadecylamine slurry (Arabatzis and Falaras 2003). Hexadecylamine was first dissolved in a boiling acetone solution and then TiO_2 was added to the mixture (while the solution was still hot) followed by H_2O_2. The oxygen bubbles (resulting from the decomposition of H_2O_2) were trapped in the hexadecylamine-TiO_2 framework and yielding foam titania material. The self-assembly of the amine moieties between TiO_2 nanoparticles was stipulated to cause the complex structure of the foam. The foam structure was weak and could be lost under mechanical crush. However, UV light irradiation (24 h) had no effect on the morphological and structural characteristics of the foam.

Hollow micrometer-sized aggregates and titanate one-dimensional (1D) nanostructures were synthesised by a H_2O_2-modified hydrothermal method (Mao et al. 2006). NaOH and KOH were used as bases and titanium foil as a titanium precursor. The produced aggregates were identified as sodium/hydrogen and potassium/hydrogen titanates. The photocatalytic activity of the prepared materials was tested, and impressive activity was reported for the decomposition of Procion Red dye under UV light illumination. In another study, PTA was used for making titanate nanofibers and microspheres by hydrothermal treatment under high pH (Yada et al. 2006). A mixture of PTA and NaOH (1-15 M) was autoclaved at 100-

120 °C for 5-72 h. High NaOH concentrations led to the development of fibrous structures. Autoclaving time affected the structure and the morphology of the nanofibers, thicker and longer ones were produced after longer periods. Remarkably, the agitation of the mixture during hydrothermal treatment led to the formation of nanofibrous microspheres.

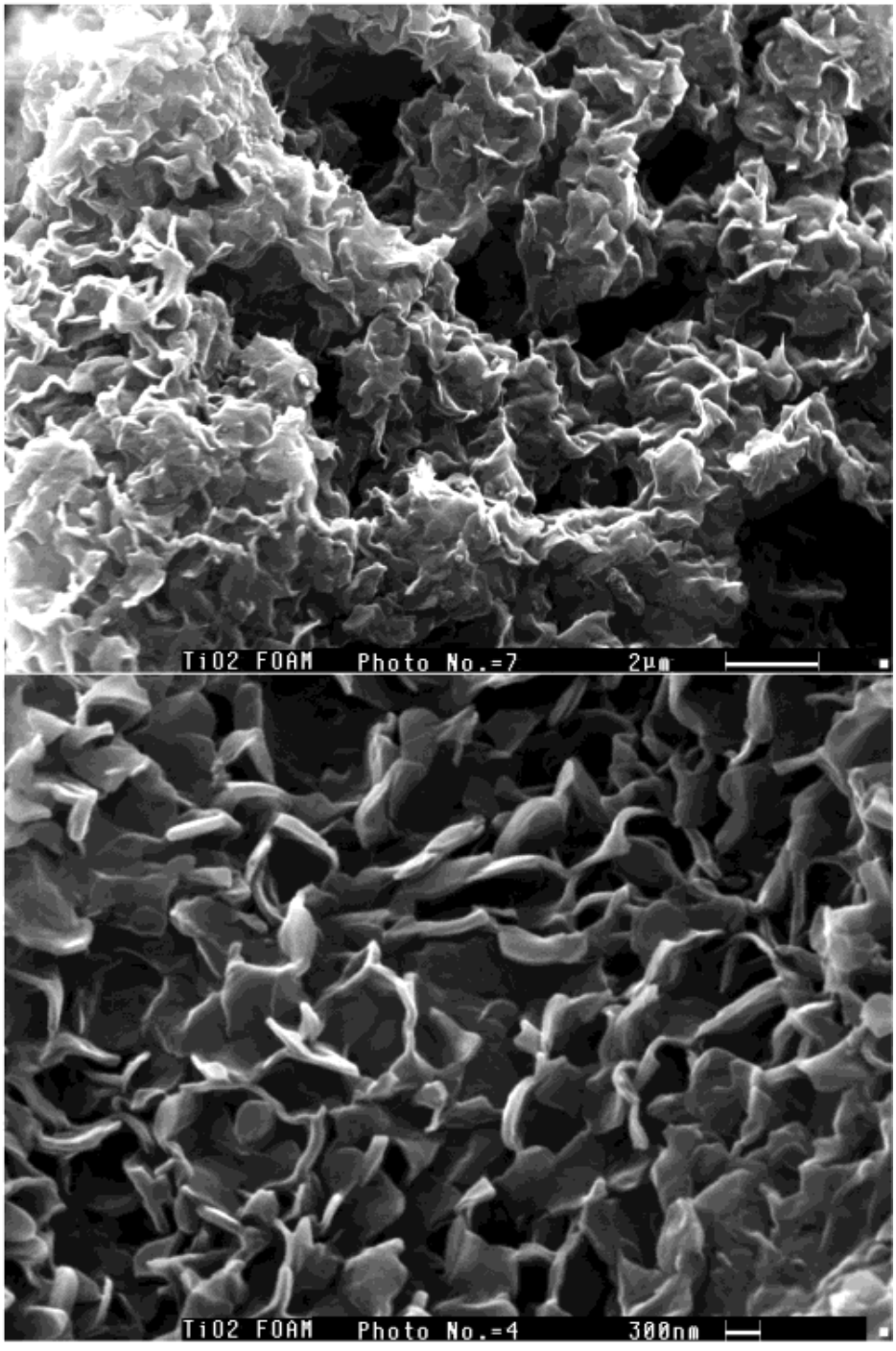

Figure 4.1. TiO_2 foam produced by Arabatis and Falaras (2003).

Recently, the synthesis of titanium oxides from peroxotitanate solution (H_2TiO_3 dissolved in H_2O_2) was reported by studying the effect of different amine group-containing organics (Ryu et al. 2007) and basic additive (Ryu et al. 2008). A hydrothermal treatment was performed followed by sol recovery and calcination of powders. The nature of amine group-containing organics used affected the size of the nanoparticles and their photocatalytic activity (Ryu et al. 2007). Ryu et al. (2008) concluded that the pH of the hydrothermally treated solution (adjusted by NH_4OH) did not affect the XRD pattern of the produced materials. Anatase structure was detected with solution pH values from 2 to 12. However, the nanoparticles' size and photocatalytic activity decreased with the increase of pH. Shankar et al. (2009) used a one-step sol gel method to introduce peroxo species on the TiO_2 surface, using alkaline TiO_2 slurry. The beneficial role of NH^{4+} cation compared to Na^+ was revealed in terms of the concentration of peroxo species attached on TiO_2 surface. These species were found responsible of the visible-light photocatalytic activity of the powder. The mechanism was described as similar to dye-sensitization and is shown in Figure 4.2. The Ti(IV)-OOH complex, adsorbed onto TiO_2, is excited under visible light. This excitation allows the charge migration of e^- to the conduction band of TiO_2 and this triggering the photocatalytic activity. This phenomenon was described by the "photo-sensitized peroxo species".

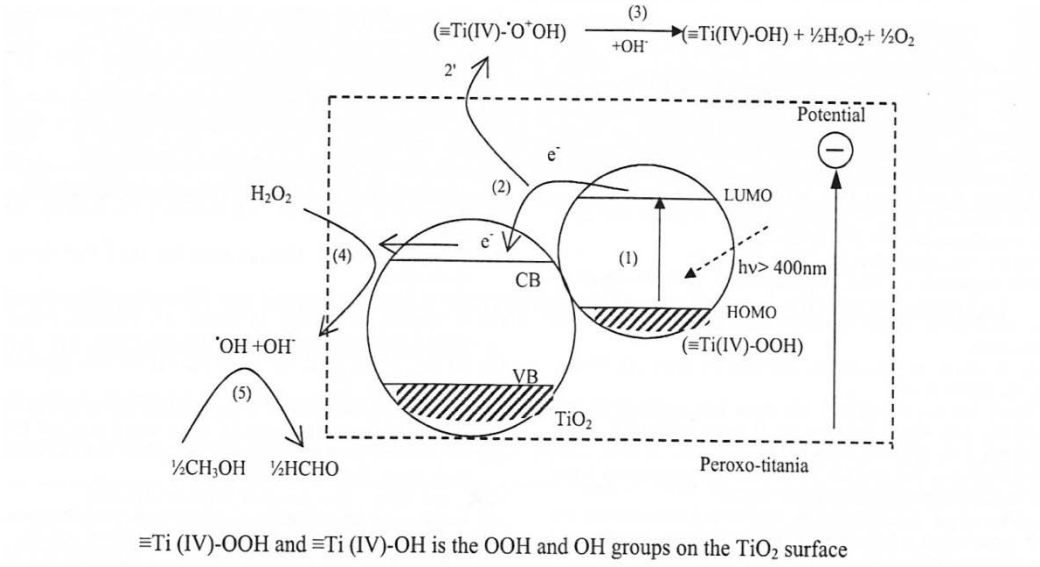

Figure 4.2. Photo-sensitized peroxo species phenomenon described by Shankar et al. (2009).

4.3. Experimental Investigation

4.3.1. Dissolution of P25

The controlled dissolution of Degussa P25 at room temperature (T = 20-22 °C) was investigated in a 250 mL glass Erlenmeyer flask under alkaline conditions. One advantage of using a high alkaline medium lies in the formation of desirable nanostructures when hydrothermal treatment is applied (Chapters 6, 7 and 8).

4.3.1.1. Experiment 1: Sodium Hydroxide Base

In this experiment, 2 g quantities of TiO_2 powders were placed in glass flasks containing 4 g of NaOH pellets. Different H_2O_2 (50%) volumes (12 and 18 mL) were added drop-wise to this mixture to study the dissolution of the titania powder and the formation of PTC. The initial reaction is exothermic, therefore the flasks were topped with a glass slide, and placed in a water bath to minimise evaporation and prevent any overflow of the effervescent solutions. The mixtures were magnetically stirred for 5 min at 300 rpm and left to stand for 24 h. Then the solutions were neutralised by 2 N HCl until pH 7 and left to stand until full precipitation (almost 24 h). The precipitates were collected, washed with MQ water and dried at 100 °C for 12 h. The obtained samples are labelled hereafter as Na^x where x is equal to the volume of H_2O_2 added (12 and 18 mL).

4.3.1.2. Experiment 2: Ammonium Hydroxide Base

In this experiment 2 g quantities of TiO_2 were first dispersed in NH_4OH (8 mL and 20 mL), then 40 mL of H_2O_2 (50%) volumes were added dropwise under magnetic stirring, resulting in exothermic reactions. The mixtures were left to stand at room temperature for 24 h and neutralised with 1 N HNO_3 until pH 7. The powders were obtained after drying the precipitates in oven at 100 °C for 12 h. The obtained samples are designated as A^x where x is equal to the volume of H_2O_2 added (8 and 20).

4.3.2. Solution and Powder Characterisation

The dissolution of P25 was monitored by recording the changes in solution colour over 24 h using a UV-vis 1700 spectrophotometer. Samples were collected and filtered through a 0.45 μm PTFE syringe filter prior to analysis. The absorbance spectrum was assessed and the peak at $\lambda = 410$ nm was assigned to peroxo-titanium complex or dissolved titanium (IV) (Leone 1973; Myers et al. 2004).

Morphology and elemental composition of the powders were analysed after obtaining images of the samples using the SEM/EDS instrument described in Chapter 3. Data on the size of particles and/or structures was calculated by averaging the diameter of 20 measured particles using the software of the supplier. X-ray diffraction (XRD) patterns were generated on a MDI Jade 5.0 (MaterialsData Inc., USA) instrument to verify the crystalline or amorphous structure of the powders. The elemental composition of A^8 and A^{20} samples were studied by XPS analysis using the Multilab2000 (VG, UK) XPS instrument.

4.4. Results and Discussion

4.4.1. Characteristics of Powder Samples

4.4.1.1. Solution Characteristics using NaOH Base

The controlled dissolution of Degussa P25 was achieved by using a hot mixture of H_2O_2 and NaOH at high pH. Two different volumes of H_2O_2 (12 mL and 18 mL) were selected, based on preliminary laboratory experiments not detailed here. The addition of more H_2O_2 (up to 24 mL in volume) to the mixture increased the rate of dissolution (formation of PTC) and reduced the rate of re-precipitation. After adding 12 mL of H_2O_2 to the flask (final solution pH of 13), an exothermic reaction took place due to the decompostion of H_2O_2 over NaOH pellets. After a few minutes the solution became light yellow in colour and foamy in appearance. This foamy appearance lasted almost for 2 days, and was caused by the generation of O_2 gas from the decomposed H_2O_2. In contrast, when increasing the volume of H_2O_2 to 18 mL (final solution pH of 12.5), full dissolution of the titania was achieved, and a yellow colour solution was formed indicating the formation of a PTC solution. This solution was stable at room temperature for several days before the precipitation of a yellow-colour amorphous TiO_2 took place. However, the decrease in solution pH to 7 (by adding HCl) induced the precipitation after 2 h. It has also been found that further decrease in pH to 5 could trigger instant precipitation.

The UV-vis spectrum of the solution was measured to monitor the changes of absorbance at λ = 410 nm (Figure 4.3). The absorbance increased with time to a maximum after 24 h of dissolution for both Na^{12} (3.17 cm^{-1}) and Na^{18} (3.76 cm^{-1}). However, Na^{18} showed higher final absorbance indicating that the dissolution of more TiO_2 particles occurred. After precipitation, the absorbance decreased to 0.11 cm^{-1} and 0.10 cm^{-1} for Na^{12} and Na^{18}, respectively. These results indicated that some of the PTC remained in solution even after precipitation. In previous studies, Leone (1973) and Myers at al. (2004) have studied new analytical methods for the rapid analysis of TiO_2 concentrations in digesta samples. They suggested that the 410 nm peak can give a clear indication of the concentration of TiO_2 in samples in acidic medium (in their study H_2SO_4 was used for sample digestion).

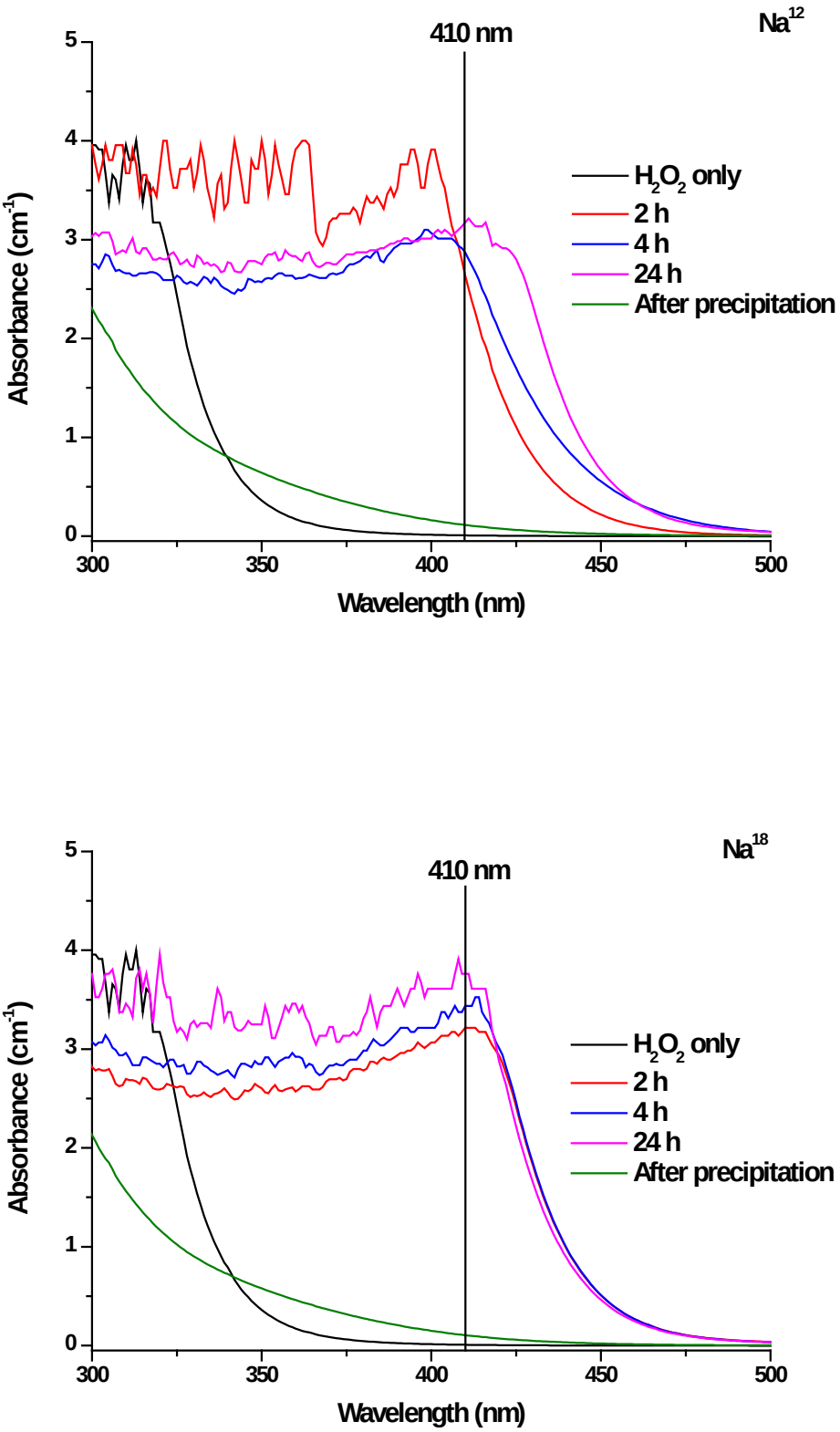

Figure 4.3. Absorbance spectrum for PTC solutions of Na^{12}, Na^{18} after 2, 4 and 24 h of reaction time at room temperature.

Moreover, the procedure validation carried out by Myers et al. (2004) revealed that a strong relationship exists between the concentration of TiO_2 in the tested samples and the absorbance at 410 nm (R^2 = 0.999). Recently, Cai et al. (2005) reported the pH effect on the optical properties of PTC. These authors did not report any peaks at 410 nm, suggesting that this peak was due to the complex formed between H_2SO_4 and PTC rather than PTC alone. In this study, it has been demonstrated that the 410 nm is due to the formation of PTC complex alone, with no other compound involved. H_2O_2 (50%) showed an adsorption band rising at 325 nm, while the diluted H_2O_2 solutions (down to 1.5%) showed a band shift to approximately 300 nm. Therefore, it can be assumed that no overlapping of these bands occurred after the decomposition of H_2O_2 in solution. Furthermore, the reaction took place at high pH and in this study no H_2SO_4 was used for pH adjustment. The decrease of absorbance after precipitation can also be a good indicator of the decrease in PTC concentration in solution.

4.4.1.2. Morphology and Composition of Na^{12} and Na^{18}

After neutralisation by HCl, the suspensions were left undisturbed until full precipitation. The precipitate was collected by centrifugation, washed with pure water and dried in oven. Powder samples were used without further treatment to study changes in morphology.

P25 is a mixed phase nanomaterial with an average particle size of about 30 nm. Figures 4.4 and 4.5 show the micrographs of Na^{12} and Na^{18} samples as obtained by the SEM. Spherical aggregations of a countless number of nanoparticles in the micrometer size range were observed in both conditions. Microspheres with an average diameter of 700 nm for Na^{12} and 1048 nm for Na^{18} were recorded. XRD analyses showed that Na^{12} had an anatase structure while Na^{18} was amorphous. It has been discussed earlier that nanomaterials produced from PTC solutions are usually amorphous in nature (Gao et al. 2003; Ohtani et al. 2007). In this study, the full dissolution and precipitation of P25 resulted in amorphous Na-TiO_2 microspheres, while the partial dissolution yielded anatase Na-TiO_2 microspheres. Ohtani et al. (2007) were the only researchers to report on the dissolution of P25 using a mixture

of H_2O_2 and a base. Their main objective was the isolation of anatase crystals by the selective dissolution of rutile phases. They have reported that the full dissolution of rutile was not possible at a pH of 7.8 using NaOH as a base. It can be inferred from our results that the increase in the amount of H_2O_2 at a relatively similar solution pH promoted the dissolution of both rutile and anatase. The decrease of H_2O_2 volume to 12 mL showed that most of the rutile crystals were dissolved, together with some part of anatase. The further reduction in H_2O_2 was not possible in the current studies due to equipment limitations in ensuring homogeneous mixtures under the experimental setups used.

In previous reports, the aggregation of titanate nanostructures into micrometer-scale spherical assemblies has been discussed (Mao et al. 2006; Yada et al. 2006; Tang et al. 2010). The growth mechanism of the hollow micrometer-scale spheres of titanate 1D nanostructures was described in details by Mao et al. (2006). The mechanism was initiated by titanium oxidation through an H_2O_2-assisted oxidation process in NaOH aqueous solution, which was followed by the increase of titanium concentration in solution, Ti foil formation, nanosheets and nanotubes growth by hydrothermal treatment. The authors ascribed the self-assembly of nanostructures into microspheres (after 120-180 min of hydrothermal treatment) to several factors, such as interfacial tension, van der Waals attractive forces, and the postulated hydrophobicity of adjacent titanate surfaces. In contrast, Yada et al. (2006) concluded that the self-assembly of nanostructures into microspheres aggregates can only be achieved in the absence of mechanical agitation. The effect of solution agitation was found to directly affect the homogenous distribution of chemical species in solution, such as titanium oxyhydroxide and hydroxide ion, resulting in the localised self-organisation of titanate species that triggered the spherical aggregation. Recently, H_2O_2 was found to affect the final morphology of microspheres prepared by the hydrothermal treatment of spherical TiO_2 particles in 0.1 N NaOH solution. Titanate nanotubes were formed in the presence of H_2O_2, while titanate nanosheets were observed in the presence of H_2O (Tang et al. 2010). The presence of the “side-on” peroxo complex (generated by the reversible rupture of Ti-O-Ti bridge) was found to cause the rolling of titanate layer into tubes under mild alkaline conditions.

In this study, except the initial exothermic reaction, the reaction proceeded at room temperature for 24 h. The formation of microspheres was not affected by the degree of rupture of Ti-O-Ti bridge because Na^{12} (partial dissolution) and Na^{18} (full dissolution) showed similar morphologies with a small difference in the diameter of microspheres. Moreover, the solutions were only mixed for a short period of time to ensure homogeneity and then left to stand without any mechanical mixing. Therefore, the formation of micro-assemblies of nanoparticles was due to the following:

- The formation of surface titania-peroxo complex (species of O_2^-, OH^-);
- Na^+ ion bind to the peroxo complex creating heterogeneous surface charges;
- The slow decomposition of H_2O_2 and the release of oxygen enhanced the driving force for the self-aggregation of nanoparticles.

The elemental composition of the Na^{12} and Na^{18} powders is shown in Figure 4.6. The EDS measurements revealed that the Na^{12} and Na^{18} microspheres were composed of Ti, O and Na elements. The Ti and O originated from P25 while the sodium came from sodium hydroxide. Chlorine was not detected (even though HCl was used for neutralisation) indicating that washing the powders with MilliQ water successfully removed this element.

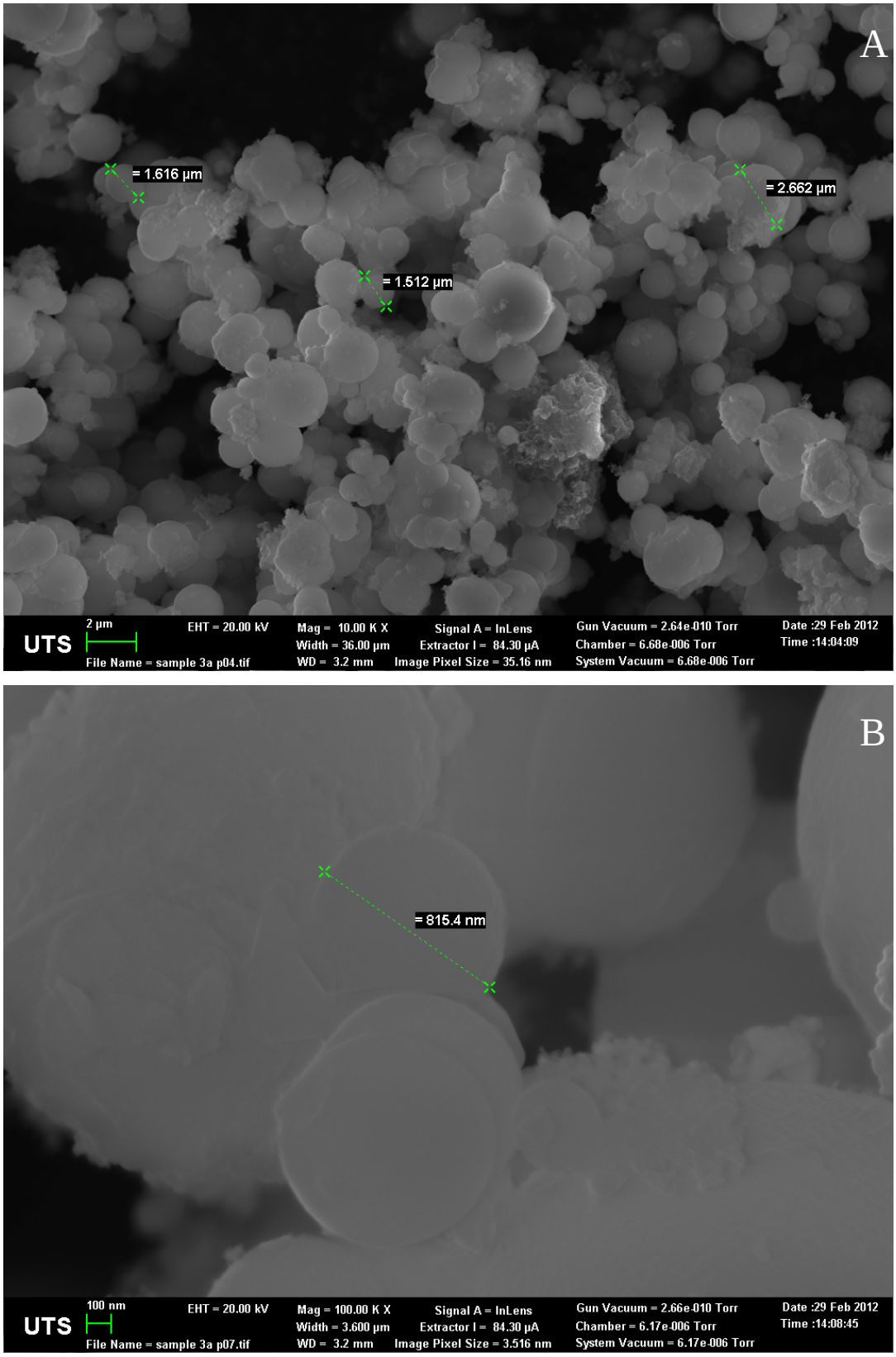

Figure 4.4. SEM images of Na^{12} powders at two different magnifications (A) 10 KX and (B) 100 KX.

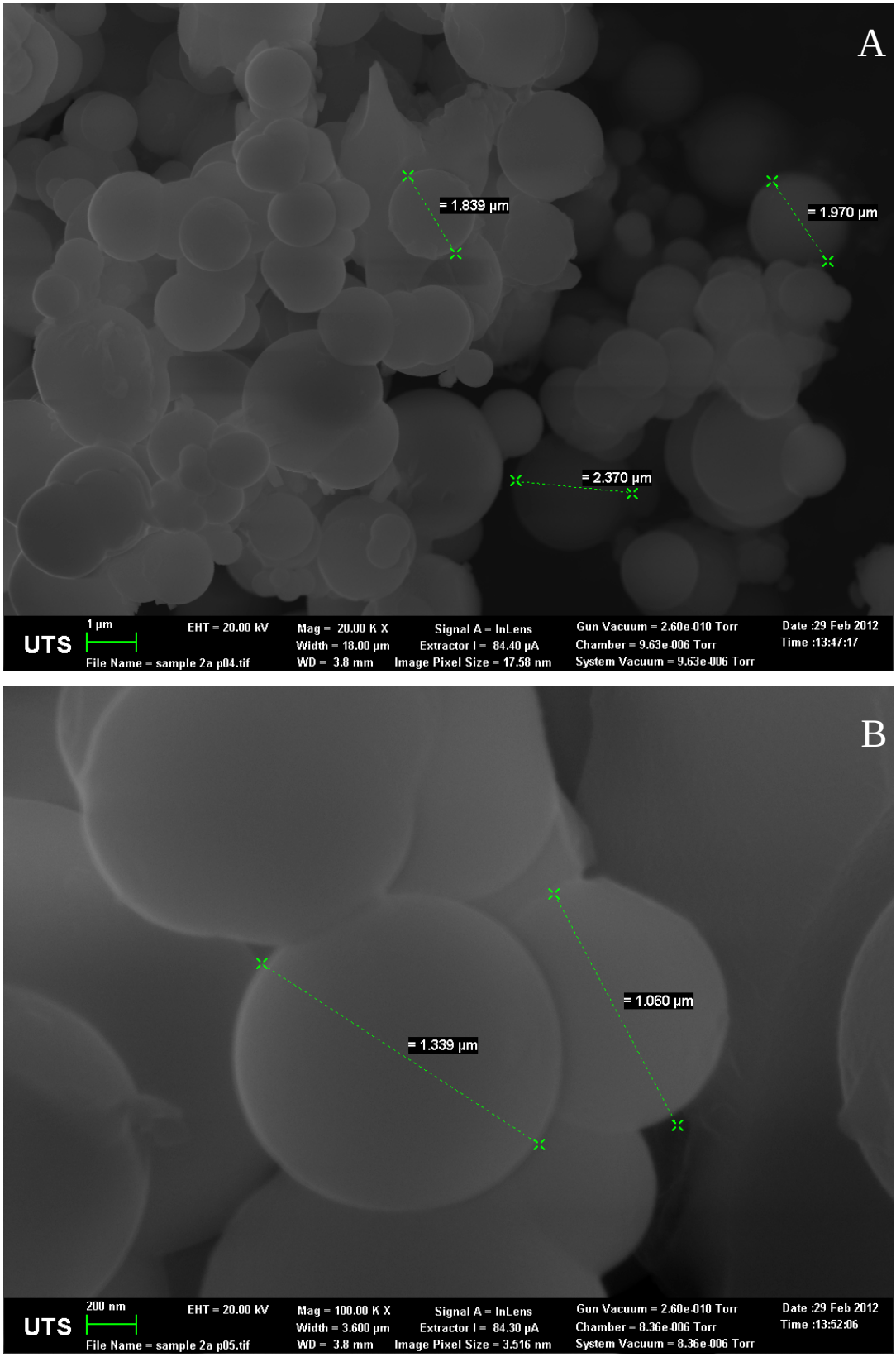

Figure 4.5. SEM images of Na^{18} powders at two different magnifications (A) 10 KX and (B) 100 KX.

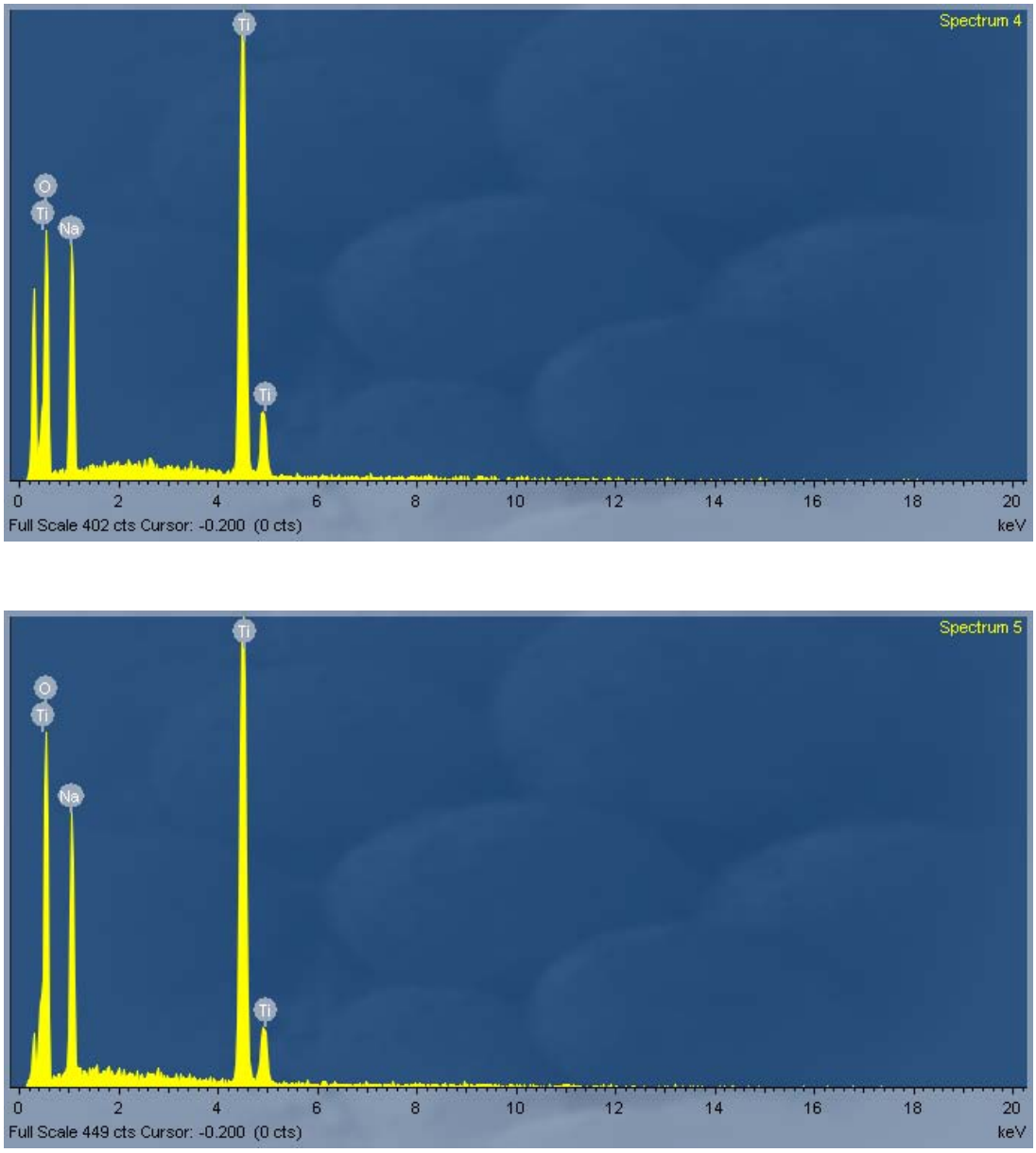

Figure 4.6. EDS spectra of Na^{12} (spectrum 4) and Na^{18} (spectrum 5) powders.

4.4.1.3. Solution Characteristics using NH_4OH Base

Degussa P25 could also be dissolved in a mixture of H_2O_2 and NH_4OH at high pH (10.5). The addition of 40 mL of H_2O_2 to Degussa P25 dispersed in NH_4OH (8 mL and 20 mL) was slowly carried out at room temperature to avoid possible overflow due the the effervescent reaction. The final pH of the solutions was equal to 10.2 and 10.7 after the addition of 8 mL and 20 mL of NH_4OH, respectively. The variation of H_2O_2 volume was preliminary studied between 0 and 40 mL (results not shown here). In the absence of H_2O_2, no dissolution occurred and the final powders showed

physical morphologies similar to that of P25. However, after the addition of H_2O_2, the dissolution of P25 was possible, and faster dissolution (formation of PTC solution) was observed with increasing H_2O_2 volumes. After adding H_2O_2 to the flasks, the solutions were homogenised by magnetic strirring for few minutes until they turned to yellow in colour (indicating PTC formation) and gas bubbles were observed indicating the decompsotion of H_2O_2 to gaseous O_2. The solutions were left undisturbed at room temperature for 24 h. After 24 h of reaction time, the A^8 solution and A^{20} solutions showed a clear yellow colour. Similarly to the solution obtained by adding NaOH, these solutions were also stable at room temperature for one day before precipitation of a yellow-coloured amorphous TiO_2 took place. Also, the decrease in solution pH to 7 (by adding HNO_3) was found to induce the precipitation in abound 1 h, manifested in an exothermic reaction with gas formation.

The UV-vis spectrum of the solution was measured to monitor the changes of absorbance at λ = 410 nm (Figure 4.7). The absorbance increased with time to a maximum after 24 h of dissolution for both A^8 and A^{20} (3.37 cm^{-1}). Although full dissolution was attained, Na^{18} showed higher final absorbance (3.76 cm^{-1}) higher than both A^8 and A^{20},which could be attributed to the use of larger volume of aqueous ammonia and H_2O_2 (dilution effect). After precipitation, the absorbance decreased to 0.10 cm^{-1} and 0.43 cm^{-1} for A^8 and A^{20}, respectively. This result indicated that the addition of higher ammonia volume stabilised the PTC and retarded the precipitation (Ichinose et al. 2003).

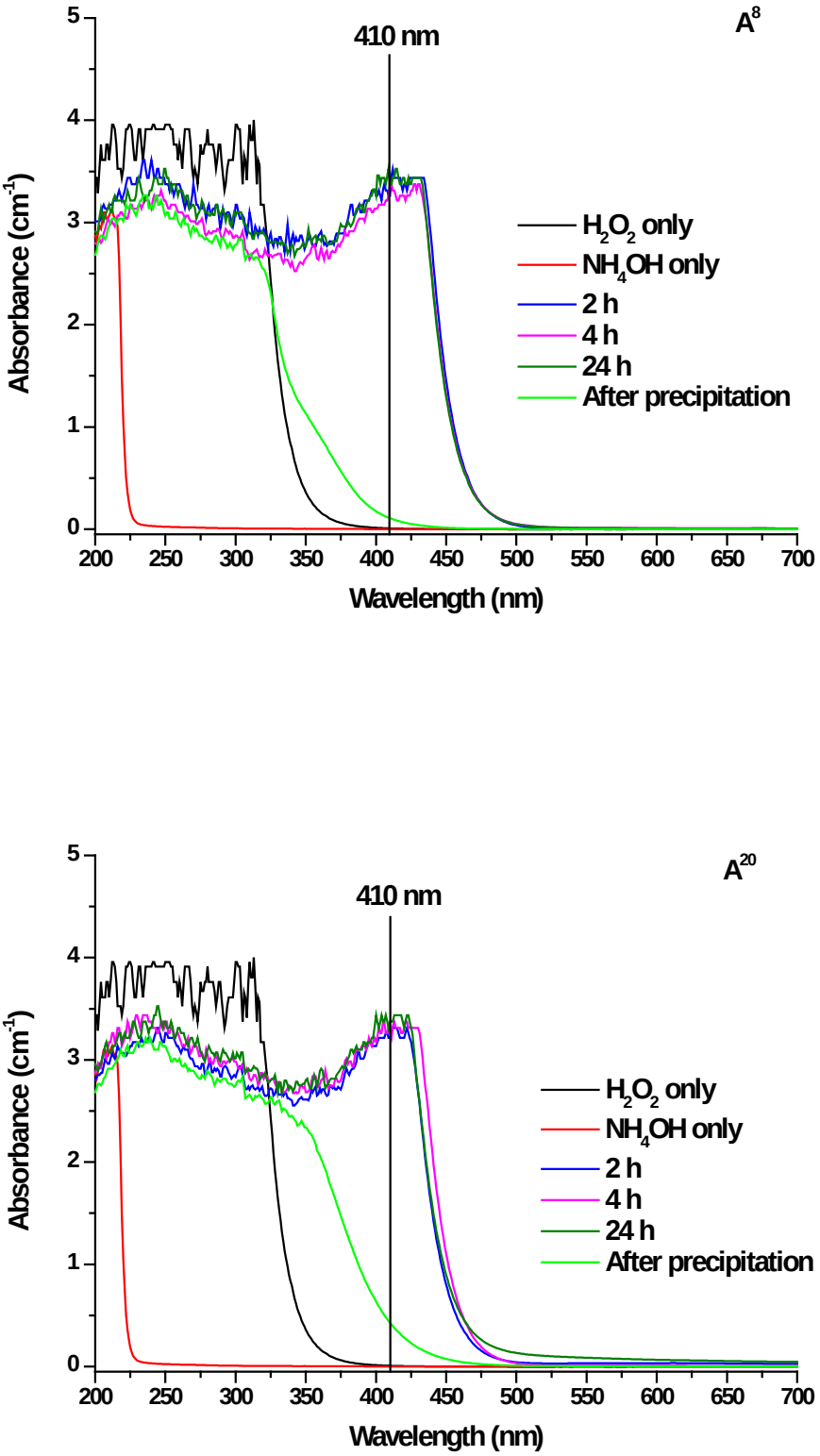

Figure 4.7. Absorbance spectrum for A^8 and A^{20} after 2, 4 and 24 h of reaction time at room temperature.

4.4.1.4. Morphology and Composition of A^8 and A^{20}

A fast precipitation was achieved after neutralising the PTC solution using HNO_3. However, slower precipitation could also be achieved without any pH adjustment by simply leaving the samples undisturbed. Powders for analyses were prepared the same way as described earlier for Na^{12} and Na^{18}.

Figures 4.8 and 4.9 show the SEM micrographs of A^8 and A^{20} samples. The study of powder morphology by SEM revealed that microspheres were present in both samples. The microspheres had average diameters of 1216 nm and 1540 nm for A^8 and A^{20}, respectively. The diffraction pattern of the powders proved that both samples had an amorphous structure, thereby indicating the full dissolution of crystalline anatase and rutile from P25 (Ohtani et al. 2007).

The dissolution of P25 in the presence of ammonia can be utilised in the production of nitrogen doped photocatalysts. The currently available methods for synthesising nitrogen doped TiO_2 were discussed in Chapter 2 (section 2.3.2.1). Accordingly, XPS analysis was carried out to study the elemental composition of amorphous microspheres. The composition of A^8 and A^{20} is shown in Figure 4.10. The samples showed relatively similar composition of Ti, O, N and C (from the carbon adhesive used in the determination). The XPS results were normalised by omitting the C percentage value. The nitrogen atomic percentage was found to be 3.68 at.% (atomic percentage) and 5.87 at.% for A^8 and A^{20}, respectively. The morphology and composition of the samples after calcination at 400 °C for 4 h was also checked, and the results showed that a large percentage of nitrogen was lost (results not shown). The nitrogen content of A^8 decreased to 0.34 at.%, while the A^{20} samples 1.48 at.% of nitrogen residual. The negative effect of calcination on the percentage of nitrogen doped in TiO_2 has also been discussed in section 2.3.3.1. The increase in calcination temperatures was found to negatively affect the percentage of N doped (Geng et al. 2009). In contrast, no changes in morphology were recorded despite some reduction in the average diameter of microspheres.

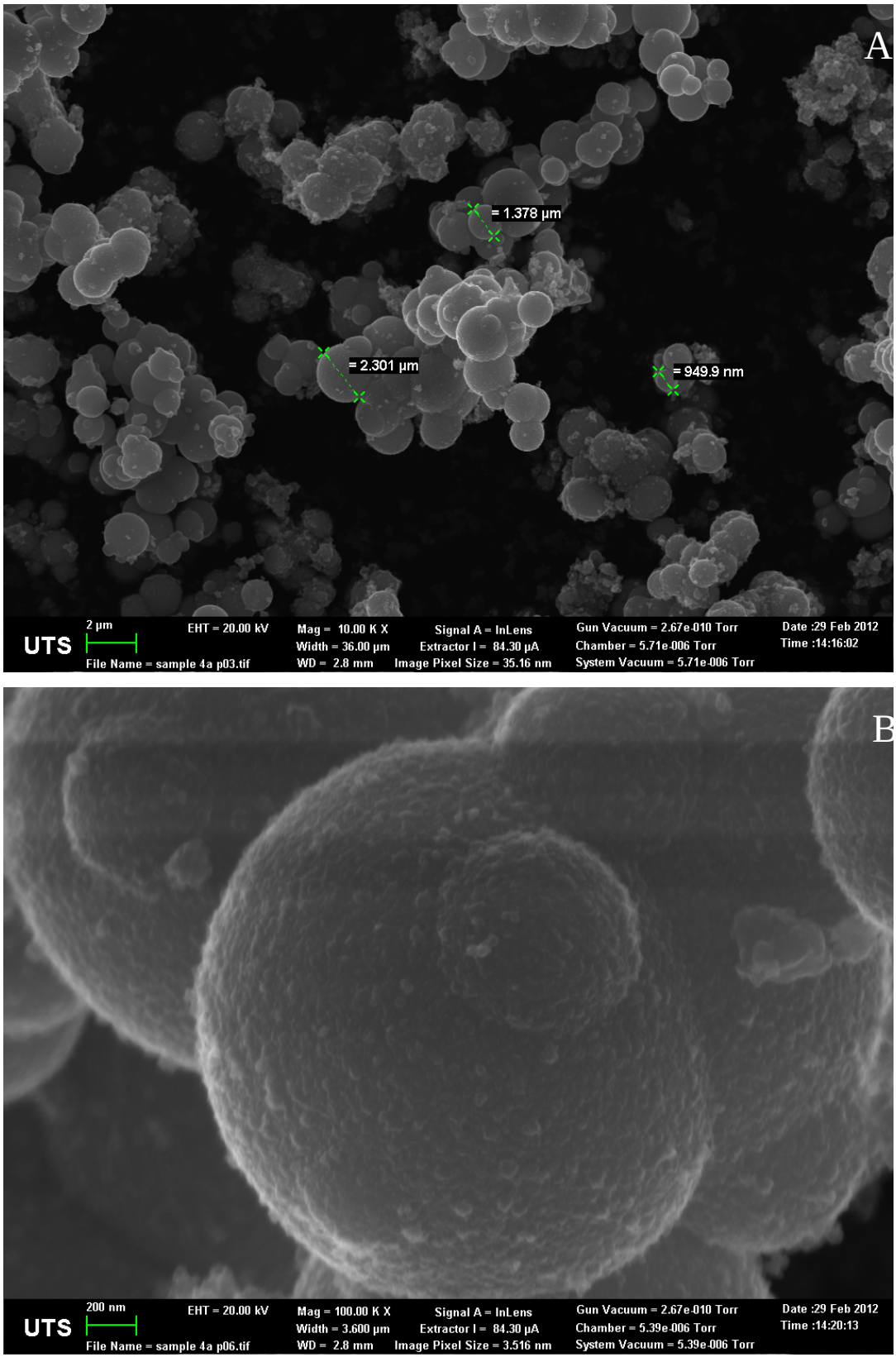

Figure 4.8. SEM images of A^8 powders at two different magnifications (A) 10 KX and (B) 100 KX.

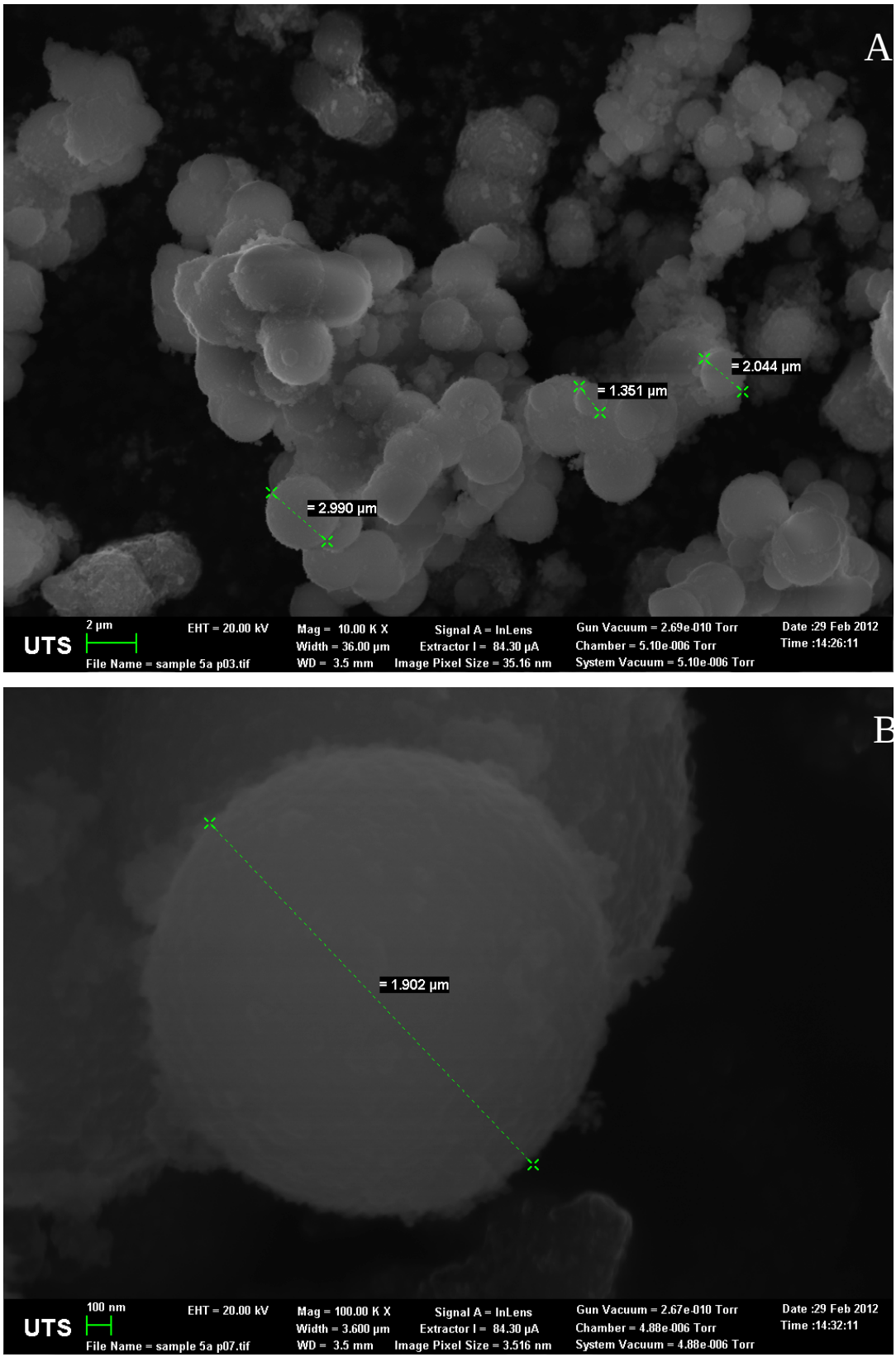

Figure 4.9. SEM images of A^{20} powders at two different magnifications (A) 10 KX and (B) 100 KX.

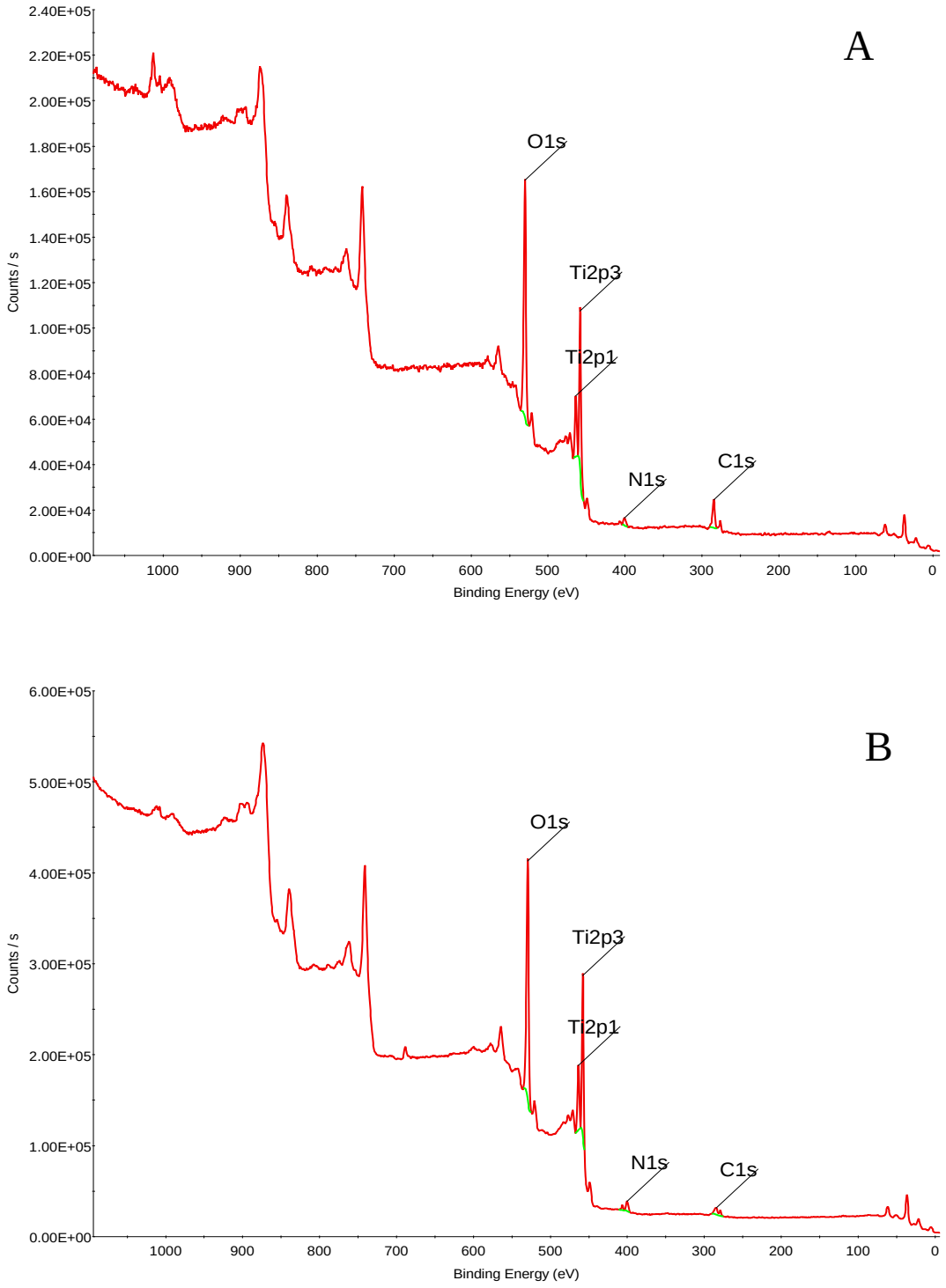

Figure 4.10. XPS spectra of (A) A^{8} and (B) A^{20} samples.

4.5. Conclusions

In this study, the use of PTC for advanced titanate nanomaterials synthesis has been reviewed and investigated. PTC can be obtained by several methods, at different pH and from different titanium precursors. Earlier research found that PTC is a versatile compound with great potentials for the fabrication of nanoparticles, nanostructures and thin films deposits.

The dissolution of P25 was also studied in alkaline media using H_2O_2 solvent. NaOH and NH_4OH were selected for studying the effect of base selection on the final morphology of nanomaterials. The dissolution was monitored by measuring the absorbance at 410 nm and it was found that both partial and full dissolution can be attained at very high pH. The dissolution was not affected by the type of base but the rate increased with the amount of H_2O_2 added in case of NaOH.

Spherical aggregations of a countless number of nanoparticles in the micrometer size range were observed in both conditions. XRD analyses revealed that Na^{12} has an anatase structure while Na^{18}, A^{8}, and A^{20} were amorphous (data not shown). The elemental composition of powders indicated that sodium-titanates can be produced by using NaOH base while nitrogen doped photocatalysts can be synthesised through the same method by using ammonium hydroxide base.

UNIVERSITY OF TECHNOLOGY, SYDNEY

FACULTY OF ENGINEERING AND INFORMATION TECHNOLOGY

CHAPTER 5

DEVELOPMENT OF VISIBLE LIGHT SENSITIVE TITANIA PHOTOCATALYSTS BY COMBINED NITROGEN AND SILVER DOPING

5.1. Introduction

Heterogeneous photocatalysis using TiO_2 catalyst is gaining more attention due to its effectiveness to partially or fully mineralise recalcitrant pollutants (Yang et al. 2008a). TiO_2 has three distinct crystal phases, namely anatase, rutile and brookite (Fujishima and Honda 1972; Asashi et al 2001; Thompson and Yates 2006). The anatase form is the most widely used in photocatalysis, and often considered to be more effective than rutile (Tsai and Cheng 1997). This is because rutile has larger crystal size and thus smaller specific surface area than anatase, which is an important factor in determining the overall activity of photocatalysts (Linsebigler et al. 1995). In general, TiO_2 is the choice photocatalyst for being inexpensive, non-toxic, and chemically resistant. Unfortunately, it cannot efficiently utilise solar radiation, due to the large band gaps of anatase (3.2 eV) and rutile (3.0 eV). These band gaps render the photocatalyst active only in the UV excitation range ($\lambda < 387$ nm for anatase), which represents less than 5% of the solar spectrum at the lithosphere (McAleer and Peter 1980; Livraghi et al. 2009). Therefore, sustained research efforts have been aimed at reducing the band gap of TiO_2 to harness the visible range of sunlight spectrum, and thus reduce the cost of photocatalysis.

Non-metal dopants, such as N (Wang and Doren 2005, Sato et al. 2005; Michalow et al. 2009, Bianchi et al. 2009) and metal dopants using Ag (Yang et al. 2007; Yang et al. 2008a; Binitha et al. 2009) have been successfully used to attain photoactivity in the visible spectrum. Michalow et al. (2009) synthesised a nitrogen doped photocatalyst by ammonolysis of titania nanoparticles. The N 1s position at 395.9 eV detected by their XPS analysis was attributed to nitrogen incorporation in TiO_2 lattice by substitution. The attribution of the XPS N 1s peak components to specific structures (O-Ti-N, N-O-Ti-O or O-N-Ti-O, etc,) is still a debated issue. Related peaks in the range of 396-404 eV were observed by several researchers (Emiline et al. 2008; Bianchi et al. 2009). However, this explanation, and the origin of the visible-light sensitisation of TiO_2 is being questioned by many authors. For example, Asahi et al. (2001) made theoretical densities-of-states calculations for the substitution of oxygen in TiO_2 lattice with several anionic materials. They inferred that the formation of Ti-N bonds is responsible for the visible-light sensitisation of

TiO_2. Wang and Doren (2005) presented first-principle calculations on TiO_2 doped by N. Using the local density approximation, the results showed that N doping narrows the band gap of TiO_2 by providing some states at the valence band maximum, while oxygen vacancies introduce some states close to the conduction band minimum, which then act as shallow donors. In another study, Ihara et al. (2001) produced visible-light active TiO_2 without doping, and attributed this characteristic to oxygen vacancies in the crystal lattice. Later, they studied nitrogen doping of TiO_2 and concluded that N doping acts through retarding the re-oxidation of oxygen deficient TiO_2 (Ihara et al. 2003).

The presence of transition metals on TiO_2 can both increase photoactivity under UV (Behnajady et al. 2008; Nasr-Esfahani and Habibi 2008) and change the surface properties to achieve sensitivity to visible light (Anpo 1997; Binitha et al. 2009). Yang et al. (2007) studied the influence of silver doping on the photoactivity of TiO_2. Increased photoactivity was observed; and a shift in the anatase diffraction peak (101), which indicates that Ag^+ entered the lattice in the form of substitutional impurity. On the other hand, Li et al. (2008) synthesised an Ag-doped mesoporous TiO_2 using silver nitrate and Tyzor LA solution (ammonium titanium lactate solution). This mesoporous silver doped TiO_2 showed unstable structure after calcination. Therefore, the authors suggested that doping with Ag metal should be done after calcination because the presence of Ag in the matrix weakens the structure, which tends to collapse during calcination. Recently, Binitha et al. (2009) prepared Ag doped mesoporous TiO_2 by using silver nitrate and metatitanic acid with subsequent calcination at 250 °C for 12 h. The silver doping was successful and the photocatalyst showed high photocatalytic activity. These examples show that the effects of silver doping on the properties of titania photocatalysts depend on the method of synthesis and the titanium precursor used.

Moreover, co-doping (or multi-doping) of TiO_2 using different compounds is regarded to be more effective for enhancing the photocatalytic activity (Ge et al. 2006a). Li et al. (2005) prepared visible-light-driven nitrogen doped TiO_2 photocatalysts. They found that photocatalysts co-doped with N and F atoms were significantly more active under visible light than products doped with a single

element. This finding was attributed to unique surface characteristics due to synergistic effects of dual dopants. In later studies, Yang et al. (2008a) and Liu et al. (2008) synthesised silver/indium oxide and nitrogen/cerium co-doped TiO_2 photocatalyst, respectively. They both reported enhanced photocatalytic activity compared to single-element doping.

Among various dopants, silver (having electron trapping ability) as a metal and nitrogen (having band gap narrowing ability) as a non-metal offer a promising combination to produce effective visible-light photocatalysts. This Chapter presents results obtained with visible light sensitive TiO_2 photocatalysts incorporating single (N) and dual (N-Ag) dopants prepared by a modified peroxo-titanate method.

5.2. Experimental

5.2.1. Photocatalysts Synthesis

Degussa P25 commercial photocatalyst was used in this study as titanium precursor for synthesising nitrogen doped and silver co-doped photocatalysts. The modified peroxo method described in Chapter 4 was employed to produce nitrogen doped and silver co-doped titanate nanomaterial. Nitrogen doping was attained using ammonium hydroxide base (25% w/w, Fluka, Sigma-Aldrich, Germany) as source of nitrogen, while silver nitrate (99.5%, Fluka, Sigma-Aldrich, UK) provided silver for co-doping. In a typical nitrogen doping synthesis, first 2 g of TiO_2 powder was dispersed in 40 ml H_2O_2 solution (50%, ACR laboratory reagent, Australian Scientific) at room temperature (T = 22 °C), then 8 ml NH_4OH was added to the dispersion. The addition of ammonia caused an exothermic reaction that lasted for few seconds with release of O_2. The combined slurry was further homogenised by mixing, and left to stand for 24 h. After that, the slurry was neutralised with 2 N HNO_3 and aged in oven at 75 °C for 24 h. Similar procedure was followed for the co-doping with silver, except that 0.2 g of $AgNO_3$ also was added to the combined dispersion. The dry solids were washed thoroughly with pure water before drying them at 100 °C for 12 h. The produced nanomaterials are named hereafter P25 (reference photocatalyst), TiO_2-N (nitrogen doped), and TiO_2-N-Ag (nitrogen and silver co-doped) photocatalysts.

5.2.2. Characterisation of Photocatalysts

Characterisation of powder samples was carried out by following the methods described in Chapter 3. The morphology and elemental composition were checked using TEM and SEM/EDS; crystal phase using XRD patterns; BET surface area and porosity using an automated surface area analyser; and doping of elements using XPS instrument. The Zeta potential of the aqueous powder suspensions (1 g/L in MQ water) was measured using a Malvern zetasizer.

5.2.3. Photocatalytic Experiments

5.2.3.1. Visible Light Source

In each experiment, 0.25 g of photocatalyst was suspended in 0.5 L of 23 mg/L methylene blue (MB) solution (pH 7). The suspension was placed in Photoreactor 1 (refer to Chapter 3) under magnetic stirring (450 rpm) for 1 hour to achieve dark adsorption equilibrium, and then visible light photocatalysis was performed for 2 h. The air sparging was 0.5 l/min and the temperature of the reaction was kept at 26 °C by means of water cooling. Slurry samples were collected at fixed time intervals, and filtered through 0.45 μm Millipore syringe discs to remove the photocatalysts particles.

5.2.3.2. Simulated Solar Light Source

In these experiments the photocatalysts were tested for their ability to degrade MB under simulated solar light. 200 mL of MB solution (23 mg/L) were placed in a borosilicate glass beaker, mixed with 0.1 g of TiO_2 powder and stirred in dark for 1 h to reach adsorption equilibrium. Photocatalytic treatment was carried out in a solar simulator (refer to Chapter 3) equipped with a magnetic stirrer, air sparger and temperature controller by means of air cooling. The light source was a 300 W Xe lamp system emitting artificial solar light that was calibrated against the AM 1.5 global tilt standard. Photocatalytic treatment was carried out for 2 h, and samples were collected at fixed time intervals for filtration and analysis.

5.2.3.3. Data collection

The filtered samples were analysed for the change of MB concentration, measured with the UV-Vis 1700 spectrophotometer at 664 nm. A standard calibration curve was obtained for different MB concentration, and served to convert absorbance to concentration (mg/L) units (Figure 3.13). The decolourising ratio (DR) is defined by the formula:

$$DR\ (\%) = (ABS_i - ABS_t) / ABS_i \times 100 \qquad \text{(Eq. 5.1)}$$

where ABS_i and ABS_t represent absorbances of the initial (untreated) and of treated samples, respectively. Thus, the $(ABS_i - ABS_t)$ difference is the net decrease of absorbance, and the fraction is a relative measure of treatment.

DOC analysis was carried out on a Multi N/C 3100 (Analytik Jena) DOC analyser and data was recorded for the reduction in DOC in function of irradiation time.

5.3. Results and Discussion

5.3.1. Characteristics of photocatalysts

5.3.1.1. SEM/EDX and TEM

Yellowish powders were obtained after 24 h treatment, neutralisation with acid, washing with water and drying. The silver co-doped catalyst had a pale yellow that changed to grey when exposed to ambient light for a few days, while the nitrogen doped product had a stable dark yellow colour. The zeta potential of photocatalysts' suspensions is shown in Figure 5.1. A clear decrease in the isoelectric point (point of zero charge, PZC) was found due to the adsorption of peroxo complexes on the surface of the photocatalysts. This required more protons for the neutralisation of surface charges. The measured PZC were around 3.6 and 4.2 for TiO_2-N and TiO_2-N-Ag, respectively. The higher PZC of TiO_2-N-Ag could be due to the presence of ionic silver, which was possibly attached to some peroxo complexes.

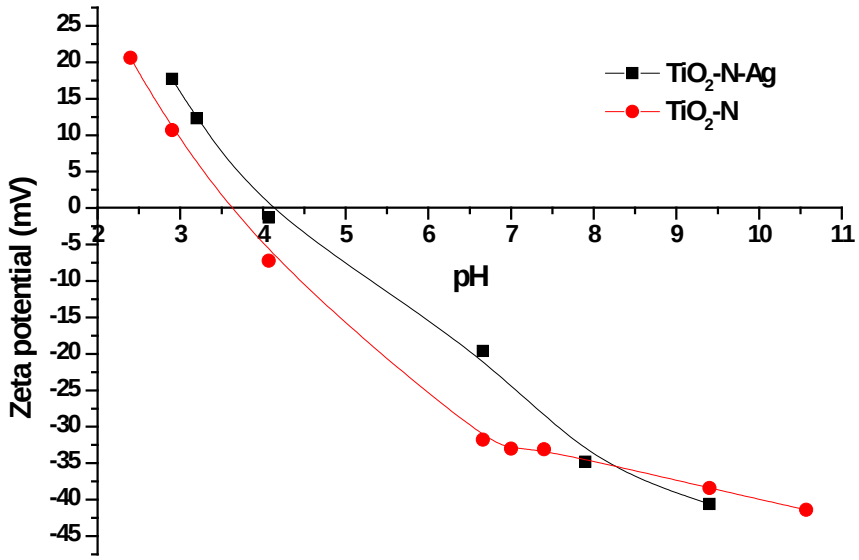

Figure 5.1. Zeta potential of TiN and TiNAg.

SEM pictures of TiO_2-N and TiO_2-N-Ag samples are shown in Figure 5.2. Degussa P25 consisted of round-shaped nanoparticles of 15-30 nm size. The TiO_2-N nanocatalysts had rod shapes with sharp edges (Figure 5.2a). In contrast, the TiO_2-N-Ag samples showed a planar structure of undefined shapes (Figure 5.2b). EDS analyses revealed that Ag content was about 0.5 wt.%, suggesting that 0.2 wt.% was leached out by the washing procedure.

TEM photographs of TiO_2-N showed sharply edged, needle-like nano-assemblies with dimensions of 5-10 nm in diameter and 50-100 nm in length (Figure 5.3a). These nanostructures had no uniform shape, showed structural defects, and particle interconnections were observed at certain sites. TEM analyses also revealed that the Ag nanoparticles were dispersed, though also formed larger clusters at some locations (Figure 5.3b). The presence of Ag clusters also modified the nanostructure of nearby TiO_2-N assemblies. These findings suggest that Ag doping has an important influence on the final structure of hybrid catalysts. The presence of Ag clusters tends to prohibit the formation of long needle-like nano-assemblies in their vicinity, which results in smaller co-doped particles.

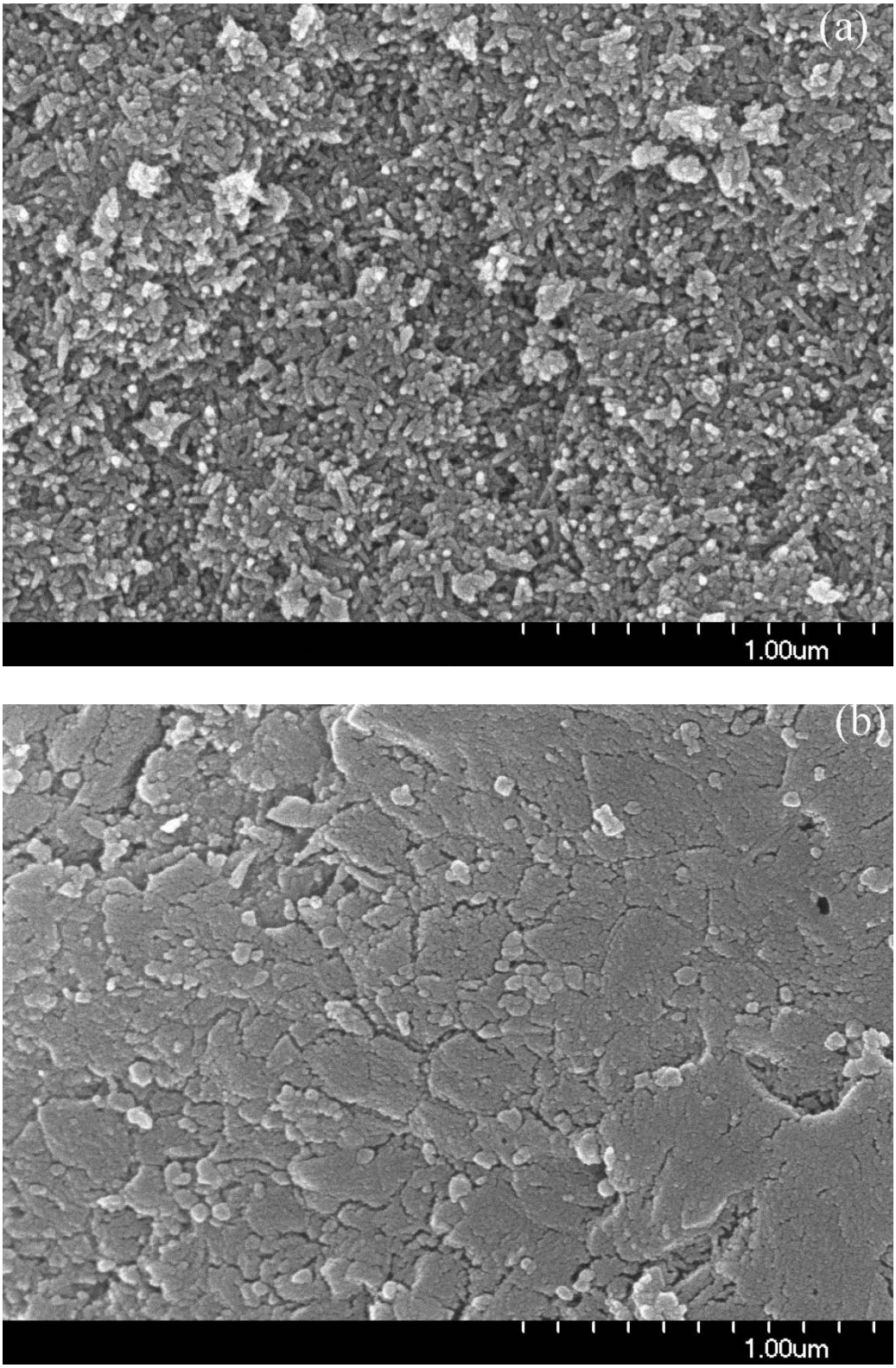

Figure 5.2. SEM images of TiO_2-N (a) and TiO_2-N-Ag (b).

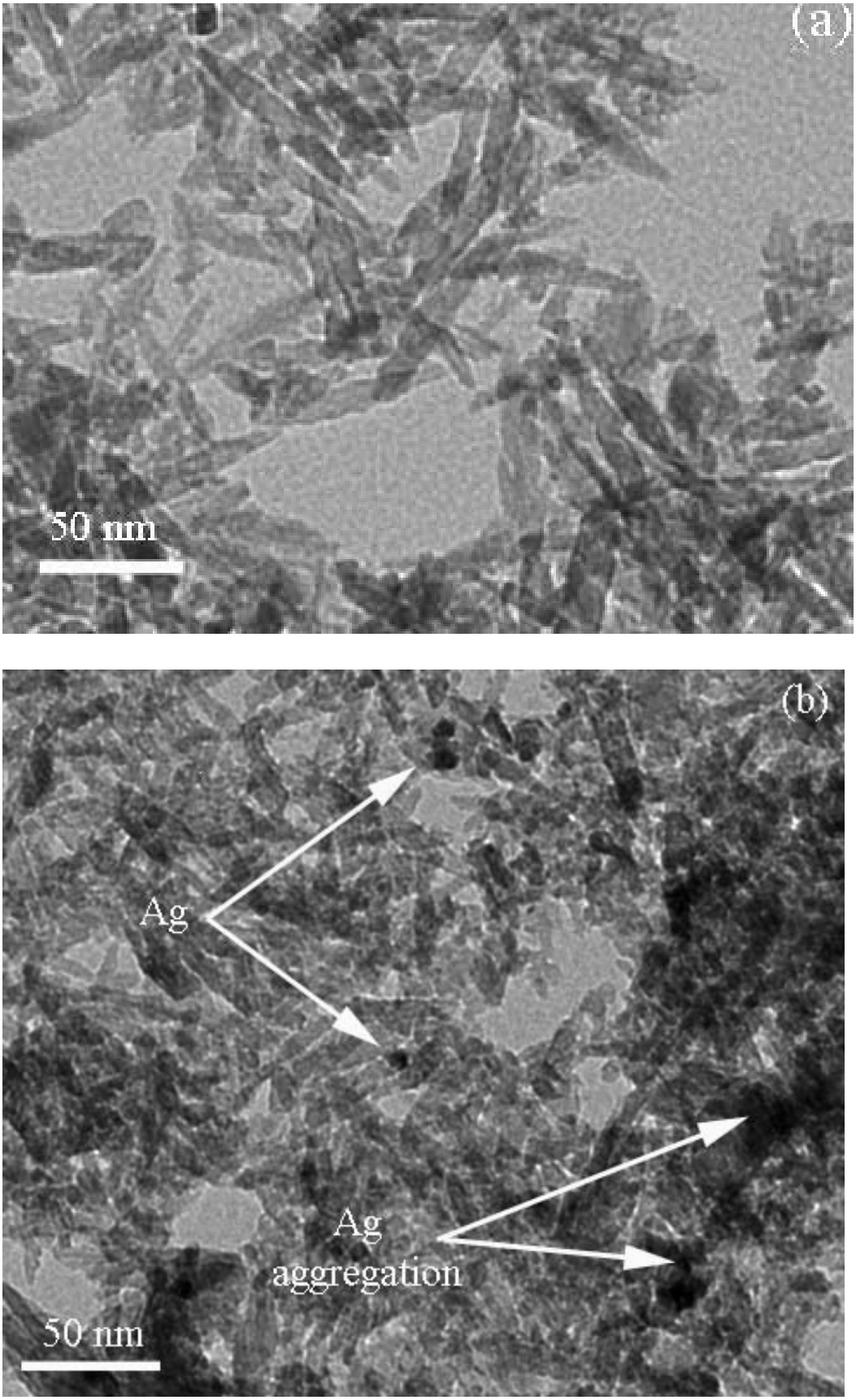

Figure 5.3. TEM images of TiO_2-N (a) and TiO_2-N-Ag (b).

5.3.1.2. Textural Properties

Results of the surface textural properties of TiO_2-N and TiO_2-N-Ag were studied by nitrogen adsorption analysis and are summarised in Table 5.1. Nitrogen doped photocatalysts had larger BET surface area (average 144.6 m^2g^{-1}) than TiO_2-N-Ag (92.9 m^2g^{-1}). Similarly, TiO_2-N showed a higher pore volume of 0.496 cm^3 g^{-1} and a larger mean pore diameter of 65.51 Å. Silver co-doping significantly decreased both the pore volume and pore diameter (0.268 cm^3g^{-1} and 54.3 Å, respectively). This finding is in agreement with previous research. Silver doped nanocatalyst exhibited a significant decrease in surface area compared to their non-doped homologues (Yang et al. 2008a). Similarly, Li et al. (2008) found that the surface area of their catalysts negatively correlated with the doping Ag concentration.

Table 5.1. Textural parameters of nanocatalysts examined in this study

Nanocatalyst	S_{BET}[a] (m^2 g^{-1})	V_p[b] (cm^3 g^{-1})	D_p[c] (Å)
TiO_2-N	144.6	0.496	65.5
TiO_2-N-Ag	92.9	0.268	54.3

[a] BET surface area
[b] Total pore volume (P/P_0 = 0.99)
[c] Mean pore diameter as estimated from nitrogen desorption isotherms using the Barrett-Joyner-Halenda (BJH) model

In general, the pore classification of catalysts is made according to pore width (diameter of a cylindrical pore). Pores are classified into several groups: macropores (> 50 nm), mesopores (2 to 50 nm) and micropores (< 2 nm). Further, micropores can be subdivided into supermicropores (0.7 to 2 nm) and narrow micropores or ultramicropores (< 0.7 nm) (Everett 1972; Zdavkov et al. 2007). N- doped samples had a wide pore size distribution in the mesoporous range of 2.9 to 59.1 nm with few macropores, and silver co-doping resulted in a narrower pore size distribution between 2 to 42 nm (mesopores). Similarly, Binitha et al. (2009) also reported that silver-doped nanotitania had a narrower pore size distribution than their precursor TiO_2.

Figure 5.4 shows the N_2-sorption hysteresis of TiO_2-N and TiO_2-N-Ag, which are in agreement with their mesoporous nature. The isotherm curves show two inflection points located about i) P/P_0 = 0 to 0.05 and ii) P/P_0 = 0.1 to 0.9. The first inflection is due to the formation of a monolayer of gaseous adsorbate, and the second one signals gas filling and capillary condensation in mesopores followed by nitrogen condensation in the macropores (Ruiz and Airoldi 2005). Nitrogen condensation that shows type IV isotherms with H2 hysteresis loop is an indicator of mesopores with cage-like or ink-bottle shape (Dubinin 1960; Everett 1972).

5.3.1.3. X-ray Diffraction

Figure 5.5 shows XRD patterns of TiO_2-N and TiO_2-N-Ag photocatalyst samples. Diffraction peaks for 2θ diffraction angles were recorded between 5° and 90°. Five primary peaks at 25.2°, 38°, 48.2°, 55°, and 62.5° were attributed to different diffraction planes of anatase TiO_2, while the main rutile peak disappeared (Ohtani et al. 2007) and small peaks at 54° and 69° could be attributed to rutile.

Pure Ag shows cubic phase with peaks at 38.21°, 44.47°, 64.47° and 77.48° (Yang et al. 2008a). Silver was not detected by XRD in TiO_2-N-Ag samples due to the homogenous dispersion of Ag, the low Ag concentration and the masking of peaks by those of TiO_2. Binitha et al. (2009) reasoned that the absence of distinct peaks by Ag metal and its oxides is an indication of efficient dispersion of such nanoparticles present in low concentrations. Li et al. (2008) could detect Ag metal in their XRD analysis but they used a very high doping ratio (≈15% Ag). They also found that the dopant was randomly distributed on the grain boundaries of TiO_2, and noted that local Ag clusters were more frequently observed in the more porous regions.

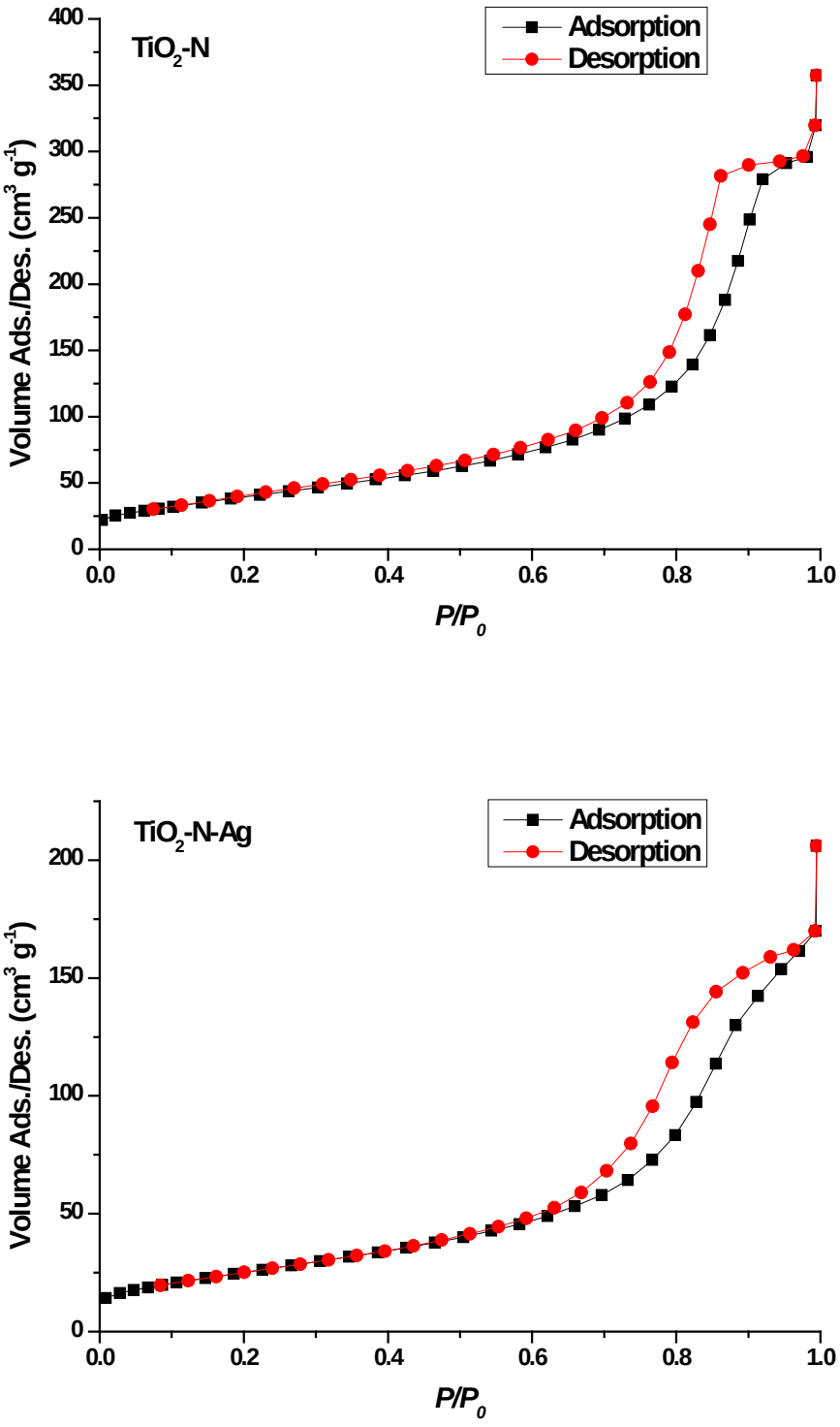

Figure 5.4. Nitrogen adsorption and desorption in TiO_2-N and TiO_2-N-Ag.

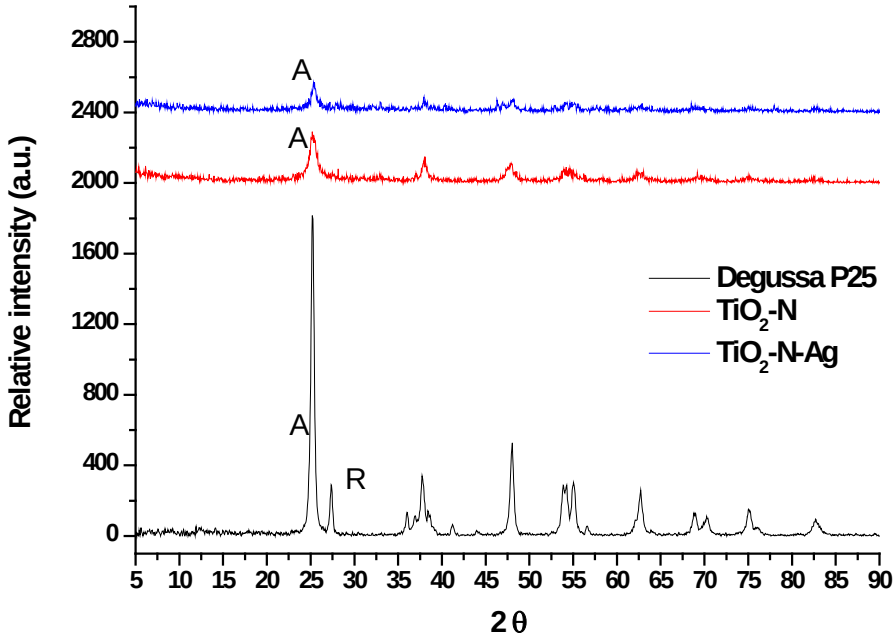

Figure 5.5. XRD patterns of Degussa P25, TiO_2-N and TiO_2-N-Ag photocatalysts showing anatase (A) and rutile (R) phases.

5.3.1.4.X-ray Photoelectron Spectroscopy

The chemical states of titanium (Ti 2*p*), oxygen (O 1*s*) nitrogen (N 1*s*) and silver (Ag 3*d*) dopants were investigated using the XPS technique with results presented in Table 5.2. Oxygen binding energies of 529.64 eV, 530.86 eV and 532.04 eV were attributed to oxygen in the crystalline chemical state, surface-adsorbed oxygen atoms and hydroxyl oxygen atoms, respectively (Li et al. 2004; Liu et al. 2008a). In this study, oxygen state corresponds to crystalline (529.89 eV) and as incorporated in OH group (531.75 eV). Nitrogen content of TiO_2-N-Ag (1.3%) catalysts was significantly larger than that of TiO_2-N (0.8%). The state of nitrogen dopant in TiO_2 matrices is still debated (Burda et al. 2003; Chen and Burda 2008; Graciani et al. 2008; Huo et al. 2008), although two nitrogen species are commonly observed. The first one is detected at a binding energy around 396 eV to assumedly represent Ti–N bond (Asashi et al. 2001). The second one has a binding energy around 400 eV, and is thought to represent O–Ti–N bonds at binding energies of 401.3 eV (Chen and Burda 2004) or 398.2 eV (Sathish et al. 2005). In a recent study, Cong et al. (2007)

reported two kinds of N species with binding energies at 399.2 and 401.3 eV, which were ascribed to O–Ti–N and Ti–O–N forms, respectively.

Table 5.2. XPS results data for TiO_2-N and TiO_2-N-Ag

Sample	Chemical state[a]	Element	BE[b] (eV)	FWHM[c] (eV)
TiO_2-N	Crystalline	O 1*s*	529.89	2.32
	OH group	O 1*s*	531.75	2.18
	Ion	N 1*s*	400.14	3.4
	Ti^{3+}	Ti 2*p*	457.9	1.41
TiO_2-N-Ag	Crystalline	O 1*s*	529.53	2.34
	OH group	O 1*s*	531.95	2.71
	Ion	N 1*s*	400.3	2.05
	Ti^{3+}	Ti 2*p*	457.72	1.81
	AgO	Ag $3d_{5/2}$	366.23	1.53
	AgO	Ag $3d_{3/2}$	372.2	1.52

[a]Adapted from Liu et al. (2008), Park and Kang (2008) and Crist (1999)
[b]BE: binding energy
[c]FWHM: full width at half-maximum of peaks

The present results showed that the binding energies of N 1*s* for TiO_2-N and TiO_2-N-Ag were 400.14 and 400.3 eV, respectively. Thus, it can be assume that N dopant in these photocatalysts existed in the form of O–Ti–N bonds. The Ti 2*p* binding energies of 457.9 eV (TiO_2-N) and 457.72 (TiO_2-N-Ag) correspond to Ti^{3+} (≈ 457.86 eV) (Liu et al. 2008a), implying that Ti^{4+} was reduced to Ti^{3+} under the reaction conditions. Ti^{3+} is known to have greater photoactivity than Ti^{4+} (Park and Kang 2008), and increases the efficiency of the photocatalyst. The measured FWHM is useful to assess the oxidation state of metals. In general, higher FWHM values represent more reduced species (Park and Kang 2008). The FWHM of Ti 2*p* peak was larger in TiO_2-N-Ag than in TiO_2-N that signifies the relative abundance of Ti^{3+} forms. The binding energy of silver was shifted towards lower energy states, which indicated the ionisation of the compound. Ag^{+}, Ag^{2+} and Ag^{3+} have binding energies of 367.9, 367.6 and 367.3 eV, respectively; while Ag^{0} has a binding energy of 368.2 eV (Chen et al. 2007; Lutzenkirchen-Hecht and Strehblow 2009). Although the cited binding energy of Ag^{3+} is higher than in this study, the spin energy separation between the Ag $3d_{5/2}$ and Ag $3d_{3/2}$ states remained 6 eV to verify the accuracy of the analysis. The unusual shift towards smaller binding energies with increasing valence

of silver has also been observed by Lutzenkirchen-Hecht and Strehblow (2009), and was attributed to multiple causes such as ionic charge shifts, lattice potential and extra-atomic relaxation. In this case, it may be concluded that the Ag/TiO_2 surface layer mainly consisted of AgO or Ag^{3+} ionic silver species.

5.3.2. Photocatalytic Properties

5.3.2.1.Visible Light Photocatalysis

The synthesised photocatalysts showed enhanced photocatalytic activities compared with Degussa P25 in the degradation of MB under visible light irradiation (Figure 5.6). The dark adsorption and the photocatalytic treatment were carried out at a pH of 7 and a temperature of 26 °C. The kinetics of MB adsorption onto TiO_2 is regarded to be of Langmuirian type, and equilibrium is reached in less than 1 h (Houas et al. 2001; Herrmann 1999).

Figure 5.6a shows the decolourisation of MB by photolysis to emphasise a point that erroneously appeared in a several publications. Photolysis normally follows a first order reaction, with a small rate constant for MB at UV irradiation (Herrmann 1999), and some authors suggested that the pertinent values should be taken into account (deducted) for the results obtained in heterogeneous photocatalysis process. In the view of the author, the mathematical nonlinearity (1^{st} order reaction of photolysis) by definition does not allow any such simple deduction, regardless of the reaction order of HP. Moreover, in this case any assumed effect of apparent photolysis is certainly negligible, as shown in the flat curve of P25. This finding suggests that photolysis is hindered and negligible as a concurrent process with HP (If photolysis would work as effectively as in the absence of catalyst then the P25 curve should have been as steep or steeper as of photolysis but it's not).

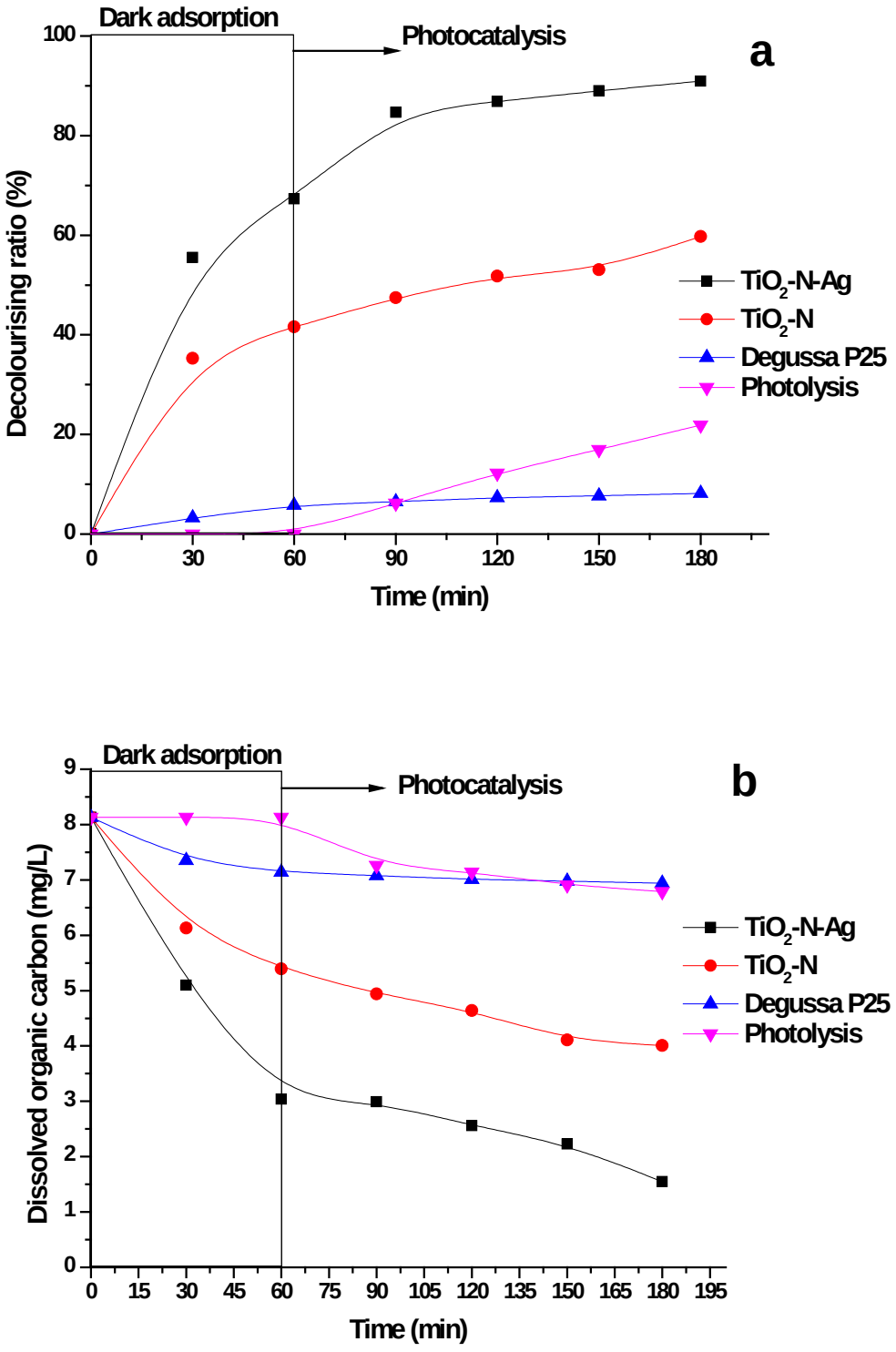

Figure 5.6. Decolourisation of MB (a) and DOC removal (b) in the absence of photocatalysts (apparent photolysis) and in the presence of TiO_2-N, TiO_2-N-Ag and Degussa P25 under visible light.

In these experiments both TiO_2-N and TiO_2-N-Ag exhibited high dark adsorption rates of MB with equilibrium reached after 1 h (Appendix B, Figure B.1). The PZC of TiO_2-N and TiO_2-N-Ag were at pH 3.6 and 4.2, respectively. Therefore, the observed high adsorption between the negatively charged photocatalysts surface and MB (cationic dye) at pH 7 was expected. However, TiO_2-N even though had a larger BET surface area than TiO_2-N-Ag still showed less affinity for adsorption. For the latter, this initial removal rate is a remarkable 67% within one hour of contact. In Chapter 2 (section 2.3.2.2), it was discussed that silver co-doping can significantly affect the photo-oxidative capability of semi-conductors. Moreover, Rehman et al. (2009) reported that the dye adsorption onto TiO_2 particles was boosted by Ag doping, which consequently promoted the dye photosensitisation process. The present results clearly showed that the adsorption of MB molecules was enhanced by silver co-doping despite the reduced surface area.

Following the dark adsorption period, the photo-oxidation of MB was monitored for 2 h under visible irradiation. Figures 5.6a and 5.6b show that Degussa P25 photocatalyst had almost negligible photocatalytic activity under visible light irradiation. In contrast, and in agreement with previous reports, N-doping of titania ensured photo-oxidation under visible light illumination, leading to additional 18% MB colour and 16% DOC removal. An enhanced photocatalytic activity was recorded for TiO_2-N-Ag, which showed an increased extra 23% MB colour removal and 18% DOC decrease.

The mechanism of visible light photoexitation process for nitrogen doped photocatalysts is shown in Figure 5.7a. The presence of N reduces the band gap energy between the CB and VB in TiO_2 according to Chapter 2 (section 2.3.2.1), thereby the energy of visible light photon is sufficient to cause charge separation and migration. The improved efficiency of N/Ag co-doped photocatalyst under visible light illumination could be ascribed to several reasons. Since the Fermi-level of Ag is lower than that of TiO_2, silver serves as an electron sink, and photogenerated electrons can transfer to the Ag particles present in the surface layer of TiO_2 (Zhang et al. 2007). Thus, the silver dopant traps electrons, which results in the improved

separation of the electrons and holes. Consequently, more O^{2-} species and $OH^{\bullet}$ radicals can take part in the removal of MB from solution (Yang et al. 2008a). Moreover, a dye molecule could absorb visible light photons and transfer the energy in the form of e^- to the CB of the photocatalyst. This also will initiate the redox reactions described in Chapter 2 (section 2.2.1). The proposed N/Ag TiO_2 photocatalytic mechanism is illustrated in Figure 5.7b. MB molecules were decomposed to intermediate products before mineralisation took place to generate CO_2, sulphate, ammonia and nitrate (Houas et al. 2001).

The photo-sensitised peroxo-species might have also contributed to the photocatalysis under visible light. The mechanism was shown in Figure 4.4 of Chapter 4, and is similar to the dye photosensitisation. It has been proposed by Shankar et al. (2009) that the excitation of Ti(IV)OOH (PTC) by a visible light photon causes the transfer of e^- to the CB of TiO_2. The electron transfer is followed by the decomposition of adsorbed organics through redox reactions.

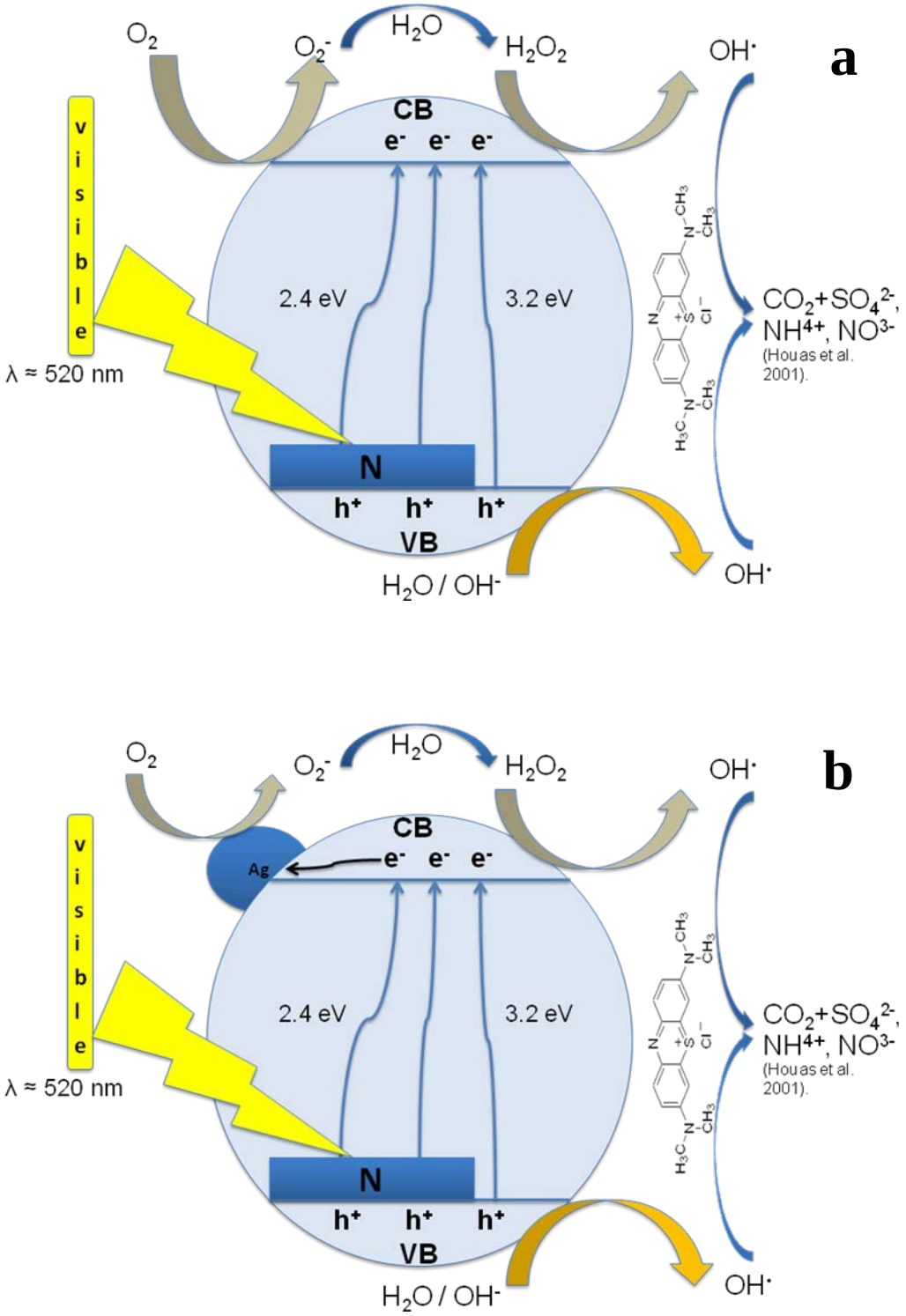

Figure 5.7. (a) N-doped and (b) N/Ag co-doped TiO_2 photocatalytic mechanism.

5.3.2.2.Simulated Solar Light Photocatalysis

Figure 5.8 shows the photodegradation of MB over TiO_2-N and TiO_2-N-Ag under simulated solar light. In these experiments, only 200 mL of MB solution (23 mg/L) but identical 0.5 g/L of photocatalyst loading at a pH of 7, and a temperature of 26 °C were used. The simulator equipment was purchased after the visible light experiments and could not accommodate the 0.5 L volume reactor used previously. Moreover, light intensity and illumination paths are significantly different in Photoreactor 1 and the solar simulator. Therefore the present results and those of the previous section cannot be directly compared with each other.

According to Figure 5.8, both doped photocatalysts showed high adsorption for MB due to surface charge difference, which resulted in a removal of ≈ 63% and 48% for TiO_2-N-Ag and TiO_2-N, respectively. Almost complete decolourisation was obtained for both photocatalysts after 2 h irradiation, with 33% and 50% of MB colour removal for TiO_2-N-Ag and TiO_2-N, respectively. TiO_2-N-Ag also showed better DOC removal than TiO_2-N over the same irradiation period. The benchmarking Degussa P25 photocatalyst also showed good performance in the experimental conditions but exhibited different kinetics. P25 caused only about 10% MB peak reduction by dark adsorption but a high pseudo photo-oxidative rate. This is in agreement with the overall pseudo first order reaction, which is often observed in HP. In contrast, the progress of mineralisation (as indicated by DOC) is fairly linear for the doped photocatalyst (similar to, and consistent with the previous section) to show pseudo zero order reactions. Again, this finding can be explained in the terms of the L-H model as discussed in Chapter 2 Section 2.2.5. (Eq. 2.15 is show here for convenience):

$$r = k \cdot \Theta = k \cdot \frac{K \cdot C}{1 + K \cdot C}$$

For relatively high MB concentrations (or more precisely, at large excess and/or a high value of the adsorption equilibrium K) the reaction would proceed at some maximum rate to reduce the concentration at equal amounts over time. In this case

the initial MB concentration is certainly modest instead of large excess in solution, but its local concentration (on the catalyst surface) is greatly increased due to the dark adsorption by the commencement of photocatalysis. The efficient MB dark adsorption, however, also indicates a high value of the adsorption equilibrium constant K. For these reasons the resulting K*C product value is high, which is manifested in pseudo zero order reactions for the doped photocatalyst.

P25 had excellent photoactivity in the UV range, especially that the simulated solar spectra provided slightly higher radiation intensities (up to 400 nm wavelength) than solar light according to Chapter 3 Figure 3.7. Doped titania adsorbs over a wider spectra but at the cost of lower intrinsic photocatalytic activity, because dopants also act as recombination centres. In any case, all photocatalysts provided near complete decolourisation after 2 h illumination, and TiO_2-N-Ag also matched the performance of P25 to achieve effective mineralisation.

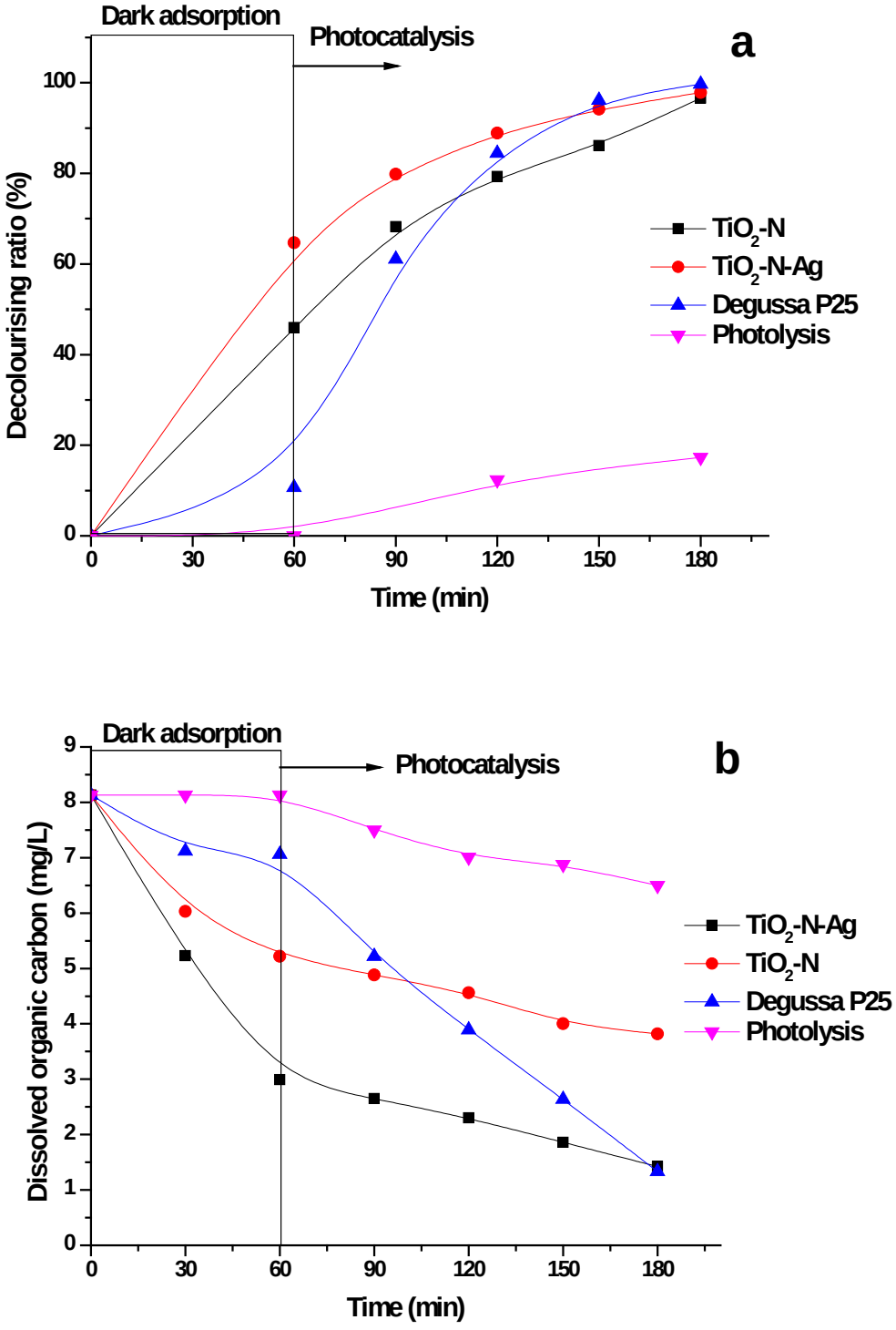

Figure 5.8. Decolourisation of MB (a) and DOC removal (b) in the presence of TiO_2-N, TiO_2-N-Ag and Degussa P25 under simulated solar light.

5.4. Conclusions

This chapter investigated nitrogen-doped and silver co-doped photocatalysts synthetised with a facile peroxide method. The obtained nanomaterials are characterised by relatively high BET surface areas, 144.6 and 92.9 m^2g^{-1} for TiO_2-N and TiO_2-N-Ag, respectively. SEM and TEM photographs revealed structural changes regarding the shapes and sizes of nano-assemblies, typically of elongated rod and needle-like forms. The doped photocatalysts are characterised by mean mesopore sizes of 6.5 nm and 5.4 nm for TiO_2-N-Ag and TiO_2-N, respectively. XRD analysis identified mainly anatase phase, but peaks of Ag were not observed. However, nitrogen doping and nitrogen-silver co-doping were successfully detected by XPS. According to binding energy results, these photocatalysts have O–Ti–N bonds and silver in ionic state.

The photoactivity of catalysts was assessed in batch experiments under visible light irradiation using MB as a model pollutant. The visible light responsive photocatalysts were effective in the photobleaching of MB. The better performance of the co-doped product was mainly attributed to Ag that acted as electron sink to promote photo-oxidation.

The photocatalysts were also tested under simulated solar light spectra. Both photocatalysts fully decolourised MB within 2 h irradiation, and the co-doped product matched the performance of P25 in terms of demineralisation.

UNIVERSITY OF TECHNOLOGY, SYDNEY

FACULTY OF ENGINEERING AND INFORMATION TECHNOLOGY

CHAPTER 6

PREPARATION AND CHARACTERISATION OF HIGHLY-ADSORBENT AND PHOTOACTIVE MESOPOROUS NA-TITANATE MICROSPHERES

6.1. Introduction

In the last decade, the synthesis of various titanate nanostructures such as nanowires, nanospheres and nanofibres has attracted much attention due to their potential uses in different applications, mainly photocatalysis. Titanate nanospheres can be obtained by several processes (Kim et al. 2006; Zhu et al. 2007; Deorsola and Vallauri 2009; Zhou et al. 2009; Tian et al. 2009). Template-based synthesis of hollow titania nanospheres was successfully achieved using a cationic colloidal template as reported by Kim et al. (2006). In that method negatively charged titania precursors were hydrolysed onto cationic colloidal particles, which were subsequently removed by heating at 450 °C to obtain hollow titania nanospheres. Zhu et al. (2007) reported that the fabrication of TiO_2 nanospheres is possible through diffuse coplanar surface discharge-induced plasma chemical vapour deposition process at room temperature and under atmospheric pressure. The resulting crystalline, uniform-sized and photoactive TiO_2 nanosphere films reduced the concentration of formaldehyde from 2.90 mg/L to 2.43 mg/L after 2 h of UV light irradiation (Zhu et al. 2007). Reactive microemulsion synthesis is considered another powerful method for obtaining nanospheres with controlled shape and size. The shape and size control is achieved by using microemulsions (water, oil and surfactant), which are considered as chemical microreactors (Deorsola and Vallauri 2009). Similarly, spray-hydrolytic synthesis (Zhou et al. 2009) and laser ablation (Tian et al. 2009) have been employed to synthesise titanate nanospheres. The fabrication of large titania microspheres can also be achieved by spray coating process (Lee et al. 2008; Zhang et al. 2009a), template (Kartsonakis et al. 2008) and H_2O_2-assisted hydrothermal route (Yada et al. 2006; Jiang et al. 2009). The adoption of environmentally friendly processes to produce nanostructures is essential for both the sustainability of the production and the protection of the environment. Hydrogen peroxide is an environmentally friendly solvent and oxidant. It has been widely employed to synthesise inorganic materials under hydrothermal conditions (Li et al. 2006). Jiang et al. (2009) synthesised hollow anatase TiO_2 microspheres by dissolving commercial titanium (metal) powder in a mixture of H_2O_2, water and hydrofluoric acid. The pH of the mixture was adjusted using ammonia before being exposed to a hydrothermal treatment at 180 ºC for 24 h. The microspheres had an average diameter of 750 nm, a wall

thickness of 80-140 nm, a hollow interior and composed of anatase nanoparticles with diameters of 20-40 nm. In contrast, hollow rutile microspheres were obtained when $TiCl_3$ was used as a source of titanium in the same process, indicating the important role that titanium precursor plays in the morphology and characteristics of the end product (Jiang et al. 2009).

Yada et al. (2006) synthesised layered sodium titanate nanofibres and microspheres from a peroxotitanic acid (PTA) solution. PTA was mixed with NaOH and treated hydrothermally at 100-120 ºC for 5-72 h. The Na-titanates obtained from PTA partially included peroxo group in the titanium oxyhydroxide framework had larger amount of Na^+ ions and had more ion exchange sites. These authors also reported that anatase type nanofibres and microspheres were obtained by the protonation of the nanostructured sodium titanate and the subsequent calcination (Yada et al. 2006) Such nanostructured titanates are gaining popularity in photocatalytic processes for water treatment because of their remarkable photocatalytic activity and their ease of separation from the treated water (Lee et al. 2008).

Dye pollutants resulting from various industrial processes are a recognised source of eutrophication, water colouration and ecosystem perturbation (Houas et al. 2001; Vautier et al. 2001; Senthilkumaar et al. 2006). Photocatalysis is capable of decomposing organic pollutants into harmless compounds (CO_2 and H_2O) without heating, using high pressure oxygen or requiring chemical reactants and additives (Houas et al. 2001). Methylene blue (MB) is a cationic dye and a frequently used model pollutant in bench-scale studies of photocatalysts. Therefore, the pathways of reactions, and the effect of operational parameters (process pH, MB and catalyst concentration, and photonic flux) on reaction kinetics are well established (Houas et al. 2001; Lachheb et al. 2002; Moriguchi et al. 2004; Shimizu et al. 2007; Ogino et al. 2008).

The present chapter presents a novel approach to synthesise titanate microspheres by using simple and commonly available compounds, and relatively low temperature hydrothermal conditions. A modified peroxo-titanate synthesis route, employing sodium hydroxide as a strong base for nanostructure fabrication, was examined in

this process. Microspheres were characterised and tested for the adsorption and photocatalytic activity using MB as a model water pollutant.

6.2. Experimental Investigation

6.2.1. Synthesis of Micropsheres

In a typical synthesis of Na-titanates a modification of the peroxotitanate method (Mao et al. 2006; Yada et al. 2006; Ohtani et al. 2007) was adopted, which involved the mixing of 2 g of Degussa P25 TiO_2 powder with 12 mL of 50% H_2O_2 and 4 g of NaOH so the final pH of the mixture was about 13. The mixture was homogenised using a magnetic stirrer and placed in a Teflon container at two different temperatures (25 and 80 °C) for 24 h. After the hydrothermal treatment, the solids were recovered by centrifugation (Centurion Sci., 2040) at 3000 rpm for 5 min, washed with 1 N HCl solution and Milli Q water until a stable pH of 7, and then dried in oven at 75 °C for 24 h. The obtained products are denoted hereafter NT-xx, where xx indicates the hydrothermal temperature of the synthesis. Some samples were also calcined in a furnace (Labec, CE-MLS) at 550 ºC for 4 h and thus are designated as NTC-xx.

6.2.2. Powder Characterisation

Morphology and elemental composition analyses were carried out using a scanning electron microscope, equipped with an energy dispersive X-ray detector (Zeiss Supra 55VP SEM, Germany) operating at 20 kV. X-ray diffraction (XRD) patterns were generated on a MDI Jade 5.0 (MaterialsData Inc., USA) X-ray diffractometer with Cu Kα radiation source. Data were measured within the range of scattering angle 2θ of 5º-90º. The powders of the specimens were used without further treatment. Brunauer, Emmet and Teller (BET) surface area analyses were performed on an automated surface area analyser (Micromeritics Gemini 2360, USA) by means of nitrogen adsorption-desorption. BET surface areas were determined by a multipoint BET method using the adsorption data in the relative pressure (P/P_0) range of 0.05-0.18. Mean pore diameter and total pore volumes of samples were determined from the desorption isotherms via the Barret-Joyner-Halender (BJH) model. The zeta potential of photocatalyst microspheres (1 g/L in MilliQ water) was measured using a Malvern zetasizer (Malvern Instruments Ltd, Nano-ZS, ZEN3600, UK). The pH of

solutions was adjusted using 0.1 N NaOH and 0.1 N HCl and monitored on a TPS pH meter (Model 90FL, TPS Pty Ltd, Australia).

6.2.3. Adsorption Experiments

MB powder was dissolved in pure water to prepare a stock solution of 10 mg/L concentration, and the pH of the solution was adjusted to 7 using 0.1 N NaOH. TiO_2 loadings of 0.05, 0.1, 0.2 and 0.5 g/L were selected to study the effect of loading on the adsorption of dye molecules. Dye adsorption experiments were carried out in an orbital shaking incubator (TU-400, Thermoline Sci.) operating at 150 rpm and 25 ºC for 30 min to reach adsorption equilibrium. Samples were collected and filtered through 0.45 μm syringe filters (Whatman, regenerated cellulose) before analyses.

6.2.4. Photocatalytic Properties under UV Light

The photocatalytic activity of the mesoporous microspheres was assessed in batch experiments using a 2 L volume of stock MB solution. After the addition of 0.05 g/L photocatalyst, the slurry was mixed with a magnetic stirrer at 450 rpm for 30 min (dark adsorption). The cylindrical reactor (Photoreactor 2, chapter 3) vessel had three (15 W each) immersed UVC lamps (Perkin Elmer), a temperature controlling device and an air sparger (0.6 L/min) to provide dissolved oxygen. Photocatalysis was carried out for 90 min at a stable temperature of 26 ºC. Slurry samples were collected at 15 min intervals and analysed for MB decomposition at λ = 664 nm using a Shimadzu UV-Vis 1700 spectrophotometer. Dissolved organic carbon (DOC) concentrations were monitored using Multi N/C 3100 (Analytik Jena) DOC analyser. Mineralisation of MB was assessed by sulphate determination in collected samples using a Metrohm ion chromatograph (790 IC) equipped with a Metrosep A Supp 5-150 (150 x 4.0 mm, 5 μm) column.

6.2.5. Lifetime Cycle of Photocatalysts

The photocatalytic stability of photocatalysts was studied by running the photodegradation experiments for 5 times under the same experimental conditions

described in section 6.2.4. The repeated degradation was monitored by collecting samples at t = 0 (after 30 min adsorption), 30, 60 and 90 min of photoreaction and analysed for the decrease of absorbance at λ = 664 nm. After each degradation cycle, the supernatant was poured out from the reactor vessel and the photocatalyst was recovered by centrifugation at 3000 rpm for 5 min. The recovered powder was washed with 0.1 N HCl, pure ethanol and MilliQ water to remove any residual by-products resulting from the photodegradation of MB. After each wash, the powder was separated by centrifugation and finally dried at 80 °C for the next degradation cycle.

6.2.6. Photocatalyst Separation by Settling

The separation of catalysts was studied by monitoring the turbidity of the supernatant as a function of time. The experiment was carried out at 22 °C and neutral pH (6.8-7.2) in the cylindrical reactor described in section 6.2.4. A total of 100 mg of catalyst were mixed with 2 L of MilliQ water; the suspension was stirred for 5 min then left at static conditions for 2 h to monitor particle settling. Samples were collected at specific time intervals (0, 15, 30, 60 and 120 min) from a depth of 10 cm and were checked for changes in turbidity. Turbidity was measured using a combined turbidity and chlorine meter (HI 93414, Hanna instruments, USA), which was calibrated using standard turbidity solutions.

6.3. Results and Discussion

6.3.1. Characteristics of Mesoporous Microspheres

The as-prepared titanate powders had pale yellow (NT-80) and yellow colour (NT-25), whereas calcined samples had a white colour. SEM pictures of these products are shown in Figure 6.1. The yellowish colour of NT-25 and NT-80 materials is due to titanium oxyhydroxide containing peroxo group. After calcination, the peroxo group was lost under the effect of temperature, resulting in white coloured powders (Yada et al. 2006).

Microspheres of an average 2.5 μm diameter were observed in NT-80 samples, whereas fused/interconnected and independent microspheres (700 nm average in diameter) were found in NT-25 samples. The smooth external surface of NT-25 microspheres suggests that they were formed by the self-assembly and aggregation of countless number of small nanoparticles (Yu et al. 2008). In contrast, fibrous microspheres were produced by treatment at 80 °C (NT-80, Figure 6.1). High magnification micrographs of the surface of microspheres indicated the presence of fibres of few hundred nanometres in length and a diameter in the range of 40-70 nm (Appendix C, Figure C.1). After calcination, the microspheres maintained their shape but the calcination resulted in shrinkages and the average diameter was reduced to 500 nm for smooth surface microspheres, and to 1.9 μm for fibrous ones. This decrease in the average size of microspheres is due to the collapse of smaller pores and the evaporation of physically adsorbed water. (Zhou et al. 2009). Moreover, the smooth surface of microspheres became rough in calcined samples, indicating that the crystalline size is significantly increased.

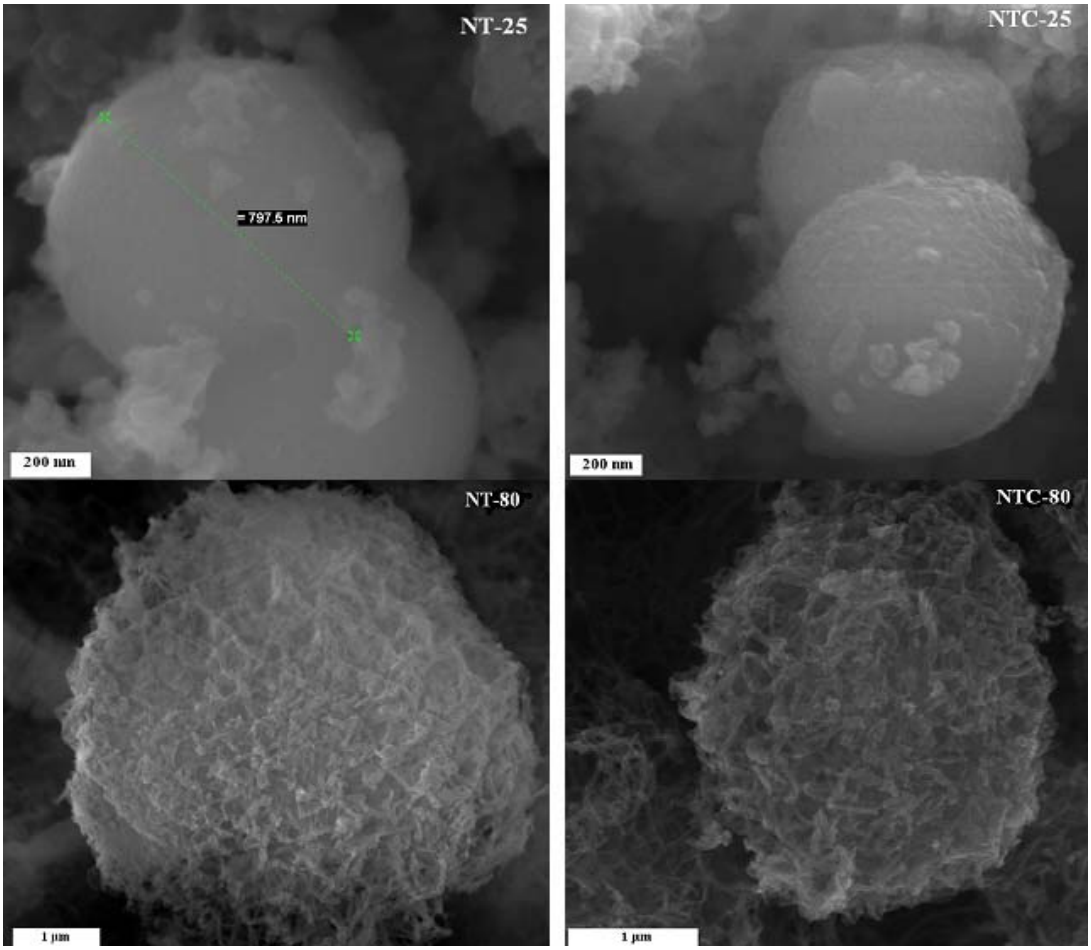

Figure 6.1. SEM images of as prepared samples (NT-25 and NT-80) and calcined samples (NTC-25 and NTC-80).

The N_2 adsorption-desorption measurements were employed to investigate the BET surface area, pore structure and pore volume of microspheres. The isotherms of both samples are of type III with two distinct regions (Appendix C, Figure C.2). The isotherms exhibit a hysteresis loop of type H3, indicating the presence of mesopores (Bordère et al. 1998; Zhou et al. 2009). The shape of these isotherms also indicates the presence and dominance of slit-shaped pores (Rouquerol et al. 1994; Bordère et al. 1998). After calcination, the isotherms of microspheres were similar to uncalcined samples. The only difference was that the adsorbed volume of N_2 decreased by 30 cm^3/g due to the collapse of some mesopores. The BET specific surface area, the total pore volume and the mean pore diameter of microspheres are presented in Table 6.1. The increase in surface area in NT-80 could be attributed to the morphology transfer from nanoparticles to nanostructures (Yuan et al. 2004; Wu et al. 2006). The samples showed an expected decrease in BET surface areas and total

pore volume but an increase in average pore diameter after calcination. The total pore volume decrease is due to the collapse of small pores during the calcination process (Zhou et al. 2009).

Table 6.1. Textural parameters of microspheres

Nanocatalyst	S_{BET}[a] (m^2 g^{-1})	V_p[b] (cm^3 g^{-1})	D_p[c] (Å)
NT-25	24.4	0.16	75.2
NT-80	64.8	0.25	59.9
NTC-25	20.2	0.12	103.2
NTC-80	24.0	0.21	97.0

[a] BET surface area

[b] Total pore volume (P/P_0 = 0.99)

[c] Mean pore diameter as estimated from nitrogen desorption isotherms using the Barrett-Joyner-Halenda (BJH) model

The XRD diffraction peaks of NT-80 and NT-25 for 2θ diffraction angles were recorded between 5° and 90°. Primary peaks of anatase phase at 25.2°, 38°, 48.2° and 55° were observed, while very small diffraction peaks at 54° and 69° indicated the rutile phase (Figure 6.2). The precursor (Degussa P25) is a mixed phase catalyst showing anatase peaks at 25.2°, 38°, 48.2° and 55° and a prominent rutile peak (110) at 2θ = 27.45°. This peak disappeared in NT-25 and NT-80 samples, suggesting that a major portion of rutile crystals was dissolved under the experimental conditions (Ohtani et al. 2007). As expected, anatase phase crystals were obtained after calcining NT-25 and NT-80 at 550 °C for 4 h. EDS measurements revealed that the Na to Ti atomic ratio was equal to 0.38 for NT-25, and 0.22 for NT-80 samples. This difference might be due to the binding of Na^+ ions to the negatively charged peroxo group $(Ti_2O_5)_q(OH)_y^{(y-2q)-}$ that are present more abundantly on NT-25 than on NT-80 (Yada et al. 2006).

The zeta potential of photocatalysts is shown in Figures 6.3 and 6.4. The point of zero charge (PZC) has shifted to lower pH values compared to the original P25 TiO_2. This is mainly due to the adsorption of negatively charged species (OH^-) on the surface of TiO_2 during the synthesis process. The hydrothermal treatment at 80 °C

has not impacted the PZC as it can be seen from the results of NT-25 and NT-80. However, the calcination of powder resulted in an increase of PZC due to the release of peroxo complexes adsorbed on the photocatalysts surface.

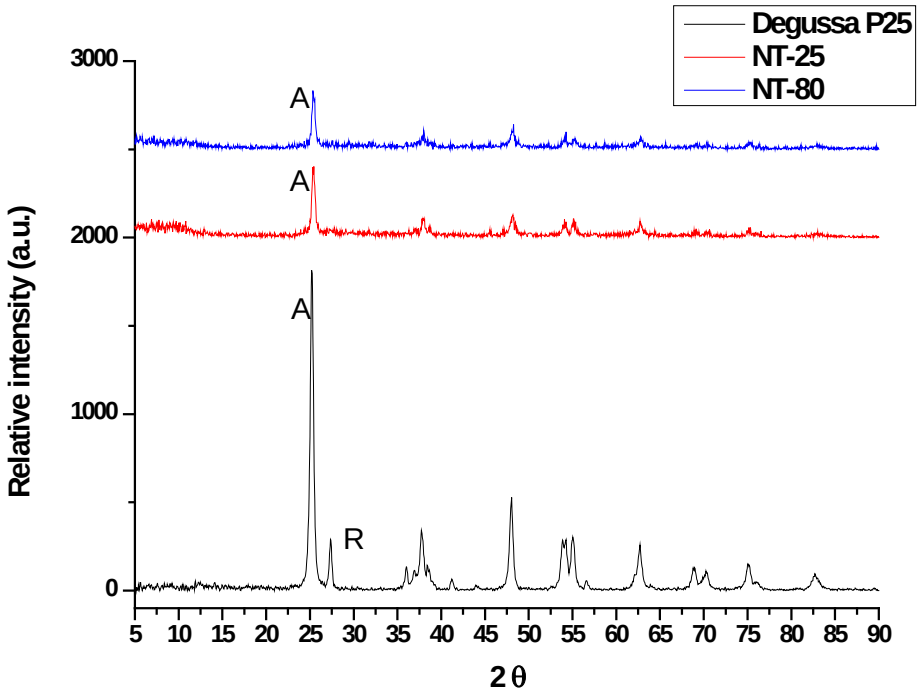

Figure 6.2. XRD diffraction pattern of NT-80, NT-25 compared to the original Degussa P25. (A) anatase, (R) rutile.

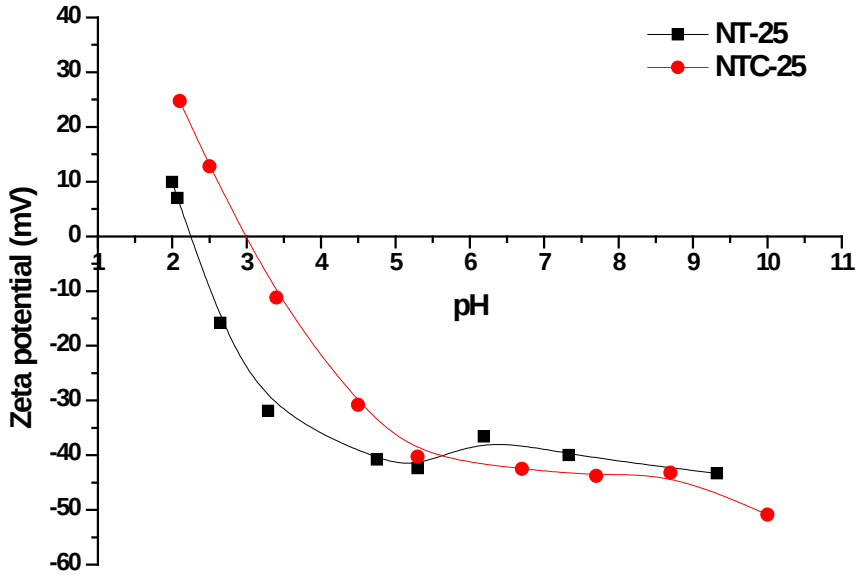

Figure 6.3. Zeta potential of microspheres prepared at room temperature (powder loading 1 g/L, T = 25 °C)

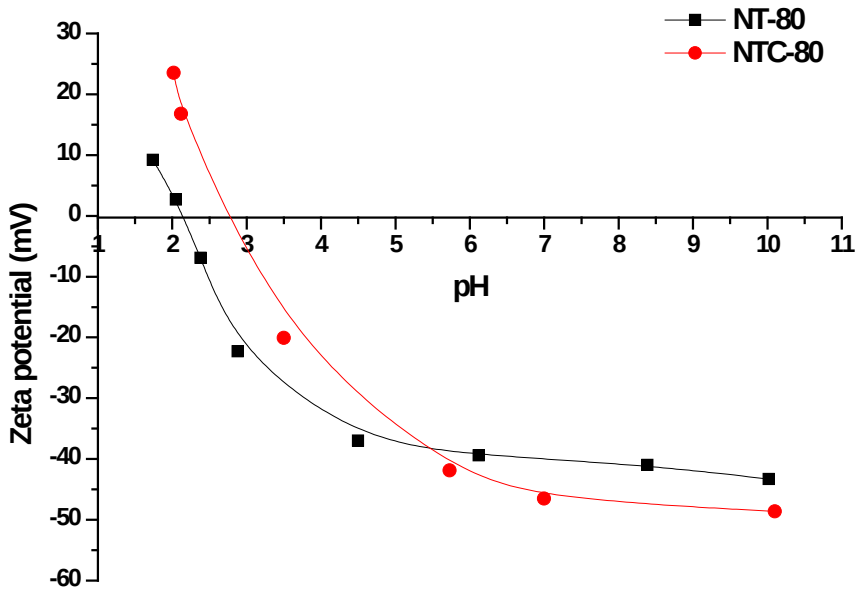

Figure 6.4. Zeta potential of microspheres prepared after hydrothermal treatment (powder loading 1 g/L, T = 25 °C)

6.3.2. Adsorption of Methylene Blue on Mesoporous Microspheres

The adsorption of MB on the surface of the photocatalysts was studied experimentally at pH 7 (Figures 6.5A and 6.5B). The colour adsorption capacity and the DOC removal of NT-80 and NTC-80 were larger than those of NT-25 and NTC-25. In general, NT-80 showed the highest capacity for MB adsorption followed by NTC-80 > NT-25 > NTC-25. The dispersed powders were coloured dark blue after mixing them with MB stock solution, indicating that the removal of MB was due to the adsorption of MB molecules on the mesoporous microspheres. After 30 min adsorption time practically complete decolourisation was reached for NT-80 and NTC-80 at 0.5 g/L catalyst loading. NT-80 had higher surface area (64.8 m^2/g), bigger pore volume (0.25 cm^3/g) and lower mean pore diameter (59.9 Å) than NT-25 (24.4 m^2/g, 0.16 cm^3/g, 75.2 Å). Similarly, NTC-80 had higher surface area (24.0 m^2/g), bigger pore volume (0.21 cm^3/g) and lower mean pore diameter (97.0 Å) than NTC-25 (20.2 m^2/g, 0.12 cm^3/g, 103.2 Å). Calcination had little negative effect on the adsorption capacity of the fibrous microspheres at low catalyst loading (0.05 g/L, 0.1 g/L and 0.2 g/L) but no effect at high loading (0.5 g/L). These results can be explained by the decrease in surface area, pore volume and the increase of PZC and mean pore diameter. The effect of surface area of the catalysts on MB adsorption revealed that microspheres of nanofibrous-assemblies are more effective adsorbent of MB than microspheres composed of the aggregation of nanoparticles. NT-80 had the biggest surface area and showed the highest MB adsorption, whilst NTC-25 (20.16 m^2/g) showed the lowest overall adsorption.

MB adsorption can also be affected by the cation exchange capacity of Na-titanate nanostructures, which showed high affinity towards basic and acid dyes (Lee et al. 2007). The authors reported that the adsorption capacity may be decreased by exchanging Na^+ with H^+ using washing of the Na-titanate in acidic solution. MB as a cationic dye can be exchanged with Na^+ ions, which are incorporated in the crystal matrix of TiO_2 or Na-titanate. EDX results (section 6.3.1) revealed that the amount of sodium present in NT-25 is larger than that in NT-80. However, the adsorption of the sodium cations on the negatively charged peroxo group reduced their availability for exchange. Here as well, the negatively charged peroxo groups $(Ti_2O_5)_q(OH)_y^{(y-2q)-}$

were saturated due to the strong binding to Na^+ ions, which made them also unavailable as a possible boost for adsorption (Yada et al. 2006; Lee et al. 2007). Hence, NT-25 had less-available peroxo groups and Na^+ ready for exchange was less efficient in adsorbing MB than NT-80. After the hydrothermal reaction at 80 °C, this binding was lost, resulting in a decreased number in peroxo groups. The loss of peroxo groups was evidenced by colour change of the catalyst, which turned into pale yellow. Consequently, Na^+ was leached by washing of the powders with pure water, which explained the decrease of Na^+ concentration in NT-80.

Photocatalysts loading of 50 mg/L was adopted in the rest of the study to minimise the effect of adsorption on photocatalysis results.

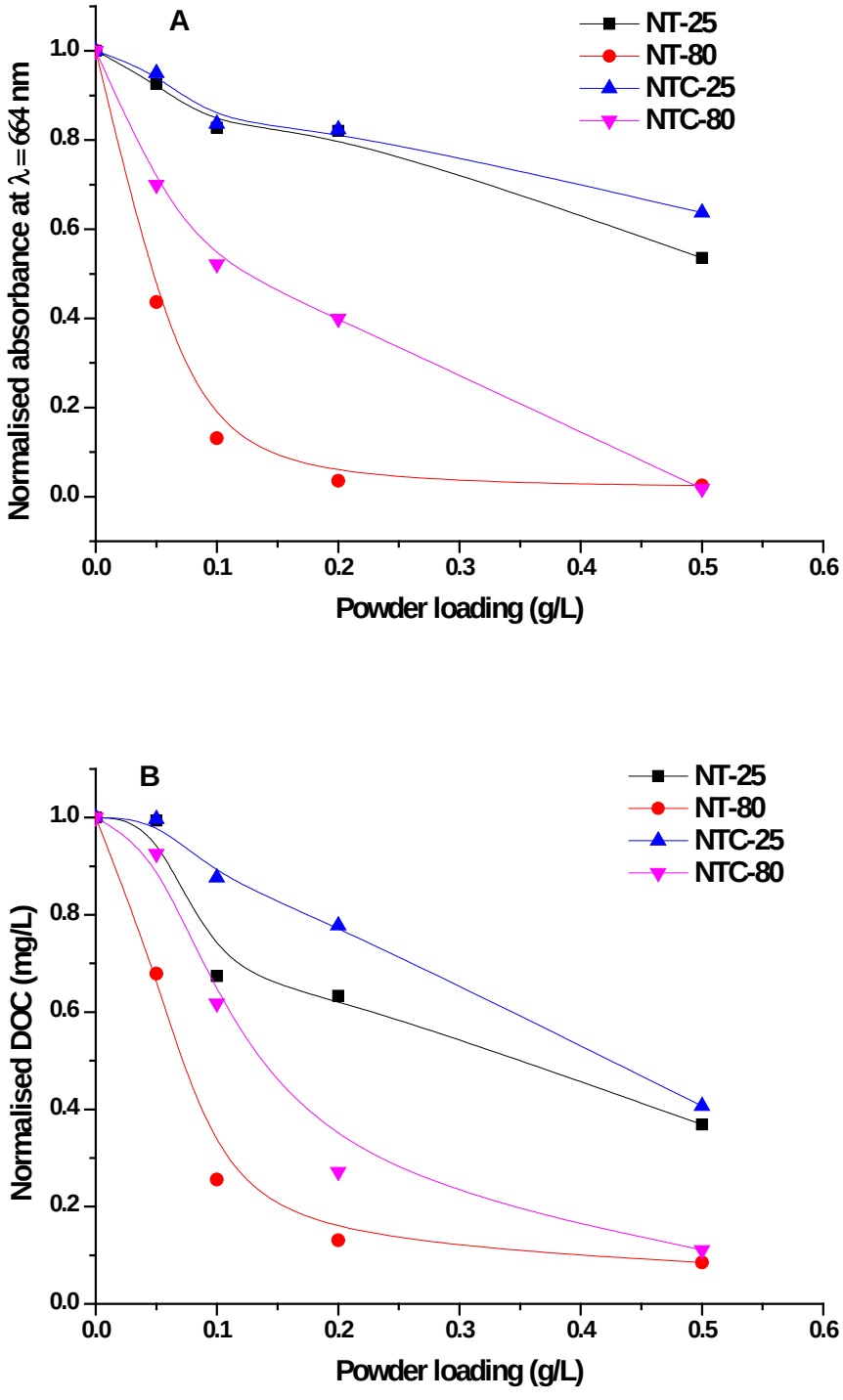

Figure 6.5. (A) Decolourisation and (B) DOC removal of MB by adsorption on NT-80, NTC-80, NT-25 and NTC-25 ([MB] = 10 mg/L, pH 7, data collected after 30 min).

6.3.3. Photocatalytic decolourisation of methylene blue and DOC removal

Figures 6.6A and 6.6B show the photocatalytic degradation of MB under UV light. MB was adsorbed onto the catalysts surface for 30 min in dark conditions before the UV lamps were turned on. The decolourisation of NT-80 slurry was complete after 90 min illumination, and reached about 85% for the other materials (NTC-80, NT-25, and NTC-25). Low correlations between the decolourisation and the decrease of DOC suggested the limited use of the absorbance data to measure organic matter removal for this pollutant. In the present work, baseline experiments showed that UV illumination alone (i.e. in the absence of catalyst) for 90 min reduced the characteristic adsorption peak at 664 nm by 17%. Redox potential measurements and DOC reduction by 11% confirmed that the decolourisation was due to chemical degradation rather than temporary and reversible colour change.

Heterogenous photocatalysis over TiO_2 follows a well defined mechanism. The process is initiated by the adsorption of photons by titania, and is maintained through a series of reactions that involve the production of positives holes (h^+) and hydroxyl radicals ($OH^\bullet$) (Houaas et al. 2001; Herrmann 1993). The photooxidation of organic compounds is thus reached via successive attacks by $OH^\bullet$. In the present study, MB removal was assessed through the decrease in the absorbance at 664 nm and the decrease in DOC. The results showed that NT-80 was the best photocatalyst in terms of MB decolourisation and DOC removal. Relative absorbance was reduced by 50% and the DOC was reduced by 30% after 45 min of UV irradiation. The removal of MB using mesoporous microspheres decreased in the order NT-80 > NTC-80 > NT-25 > NTC-25. The calcination of the powders did not increase the photoactivity of the catalysts, which can be ascribed to the changes in textural parameters. Microspheres had lower BET surface area and pore volume after calcination, which negatively affected their photocatalytic activity. Degussa P25 was used as a reference photocatalyst and showed 95% decolourisation of MB solution and 85% DOC removal after 1 h of UV-irradiation at 50 mg/L load.

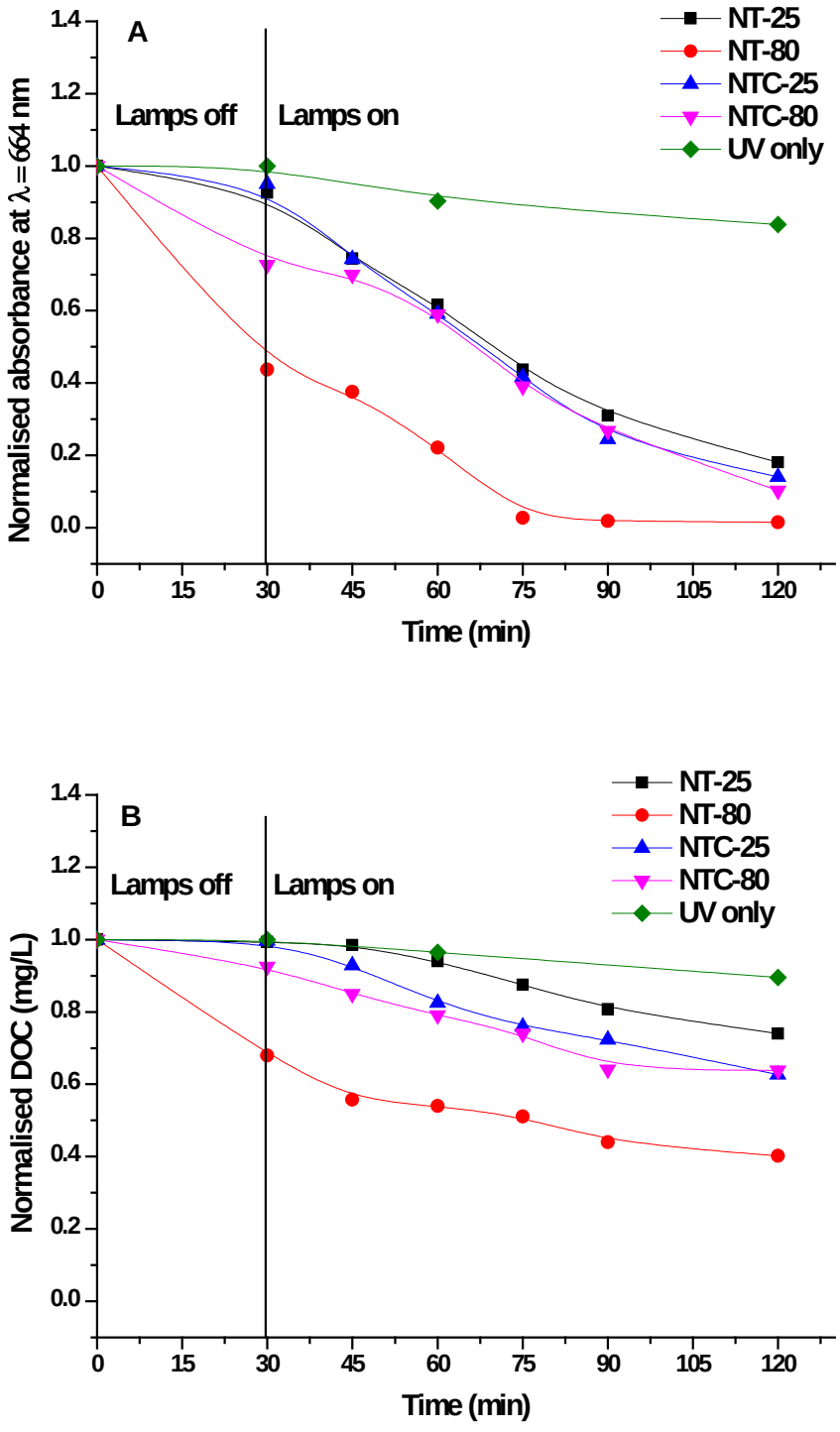

Figure 6.6. Kinetics of (A) decolourisation of MB and (B) DOC photodegradation on NT-80, NTC-80, NT-25 and NTC-25 ([MB] = 10 mg/L, pH 7, photocatalyst loading = 50 mg/L).

6.3.4. Mineralisation of Methylene Blue

The initial step of MB degradation is due to the cleavage of the bonds of the C-S^+=C functional group in MB. This will result in the formation of sulphate ions probably via the formation of a sulfoxide as an intermediate compound as reported by Houas et al. (2001). In the photocatalytic degradation of MB over titania, two oxidative agents can be considered: i) photo-produced holes h^+ and ii) the strongly active $OH^\bullet$ radicals. In MB degradation, h^+ is not involved in the initial step (cleavage of the bonds of the C-S^+=C) of degradation since MB is a cationic dye (not an electron donor). Therefore, $OH^\bullet$ radicals are essential for the initiation of the MB degradation, which proceeds through a set of chemical reactions. The end of the mineralisation is attained when the sulphur reaches its final maximum oxidation degree (+6) and SO_4^{2-} is produced after a 4th attack from $OH^\bullet$ radicals on the final by-product: R-C_6H_4-SO_3H (Houas et al. 2001).

$$R\text{-}C_6H_4\text{-}SO_3H + OH^\bullet \rightarrow R\text{-}C_6H_4 + SO_4^{2-} + 2H^+$$

Thus, the increase in sulphate concentration in the solution indicates the mineralisation of MB. The evolution of sulphate ions was monitored and is presented in Figure 6.7.

In these experiments NT-25 showed higher mineralisation rates than NTC-25, NT-80, and NTC-80. The suppressed mineralisation observed for NT-80 and NTC-80 might be due to their high adsorption capacity. The adsorbed MB might have saturated most of the active sites of the photocatalysts and shaded them from the incident photons. This implies that the degradation process was concurrent with the adsorption process, indicating that the DOC removal and decolourisation of MB was due to sorption and photooxidation at the same time. NT-80 was a strong adsorbent of MB, but showed the lowest mineralisation implying that new MB molecules were adsorbed on the powders after others have been decomposed. In contrast, NT-25 was a weaker adsorbent but had the highest degree of mineralisation, indicating its better photocatalytic properties.

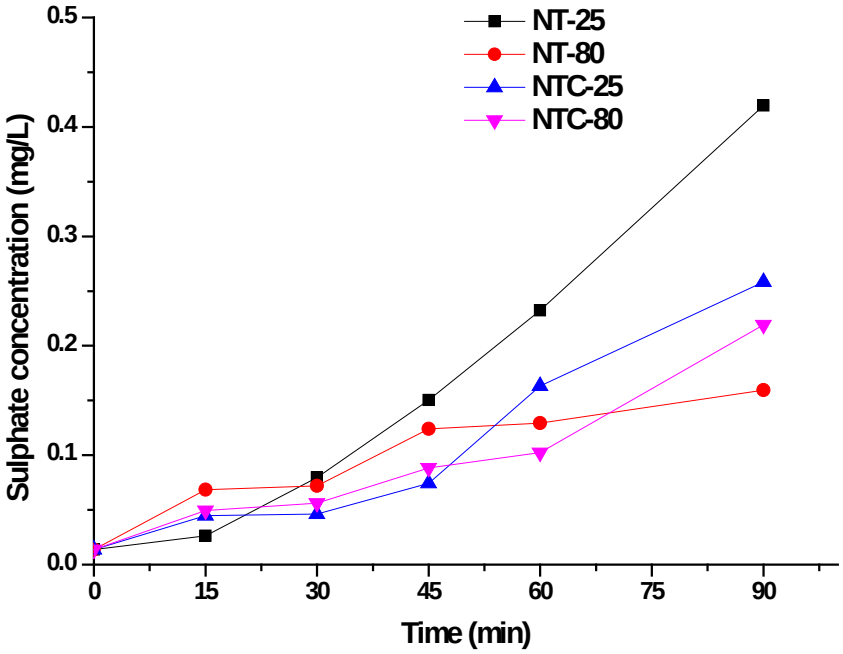

Figure 6.7. Evolution of sulphate ions during the photocatalytic degradation of MB over NT-25, NTC-25, NT-80 and NTC-80 ([MB] = 10 mg/L, pH 7, photocatalyst loading = 50 mg/L).

6.3.5. Photocatalytic stability

The life cycle of microspheres was monitored over five consecutive photodegradation cycles of MB solution (10 mg/L) at 50 mg/L photocatalyst loading (Figures 6.8 and 6.9). The photocatalyst was recovered after each cycle by sedimentation, washed, separated by centrifugation, and dried at 80 °C before being used again in the next cycle. All tested photocatalysts showed stability in performance after 5 complete cycles of MB decomposition. The overall reduction of photocatalytic activity was less than 5% according to absorbance results at λ = 664 nm. Thus, no significant catalyst poisoning was observed, and the microspheres showed robust photocatalytic performance.

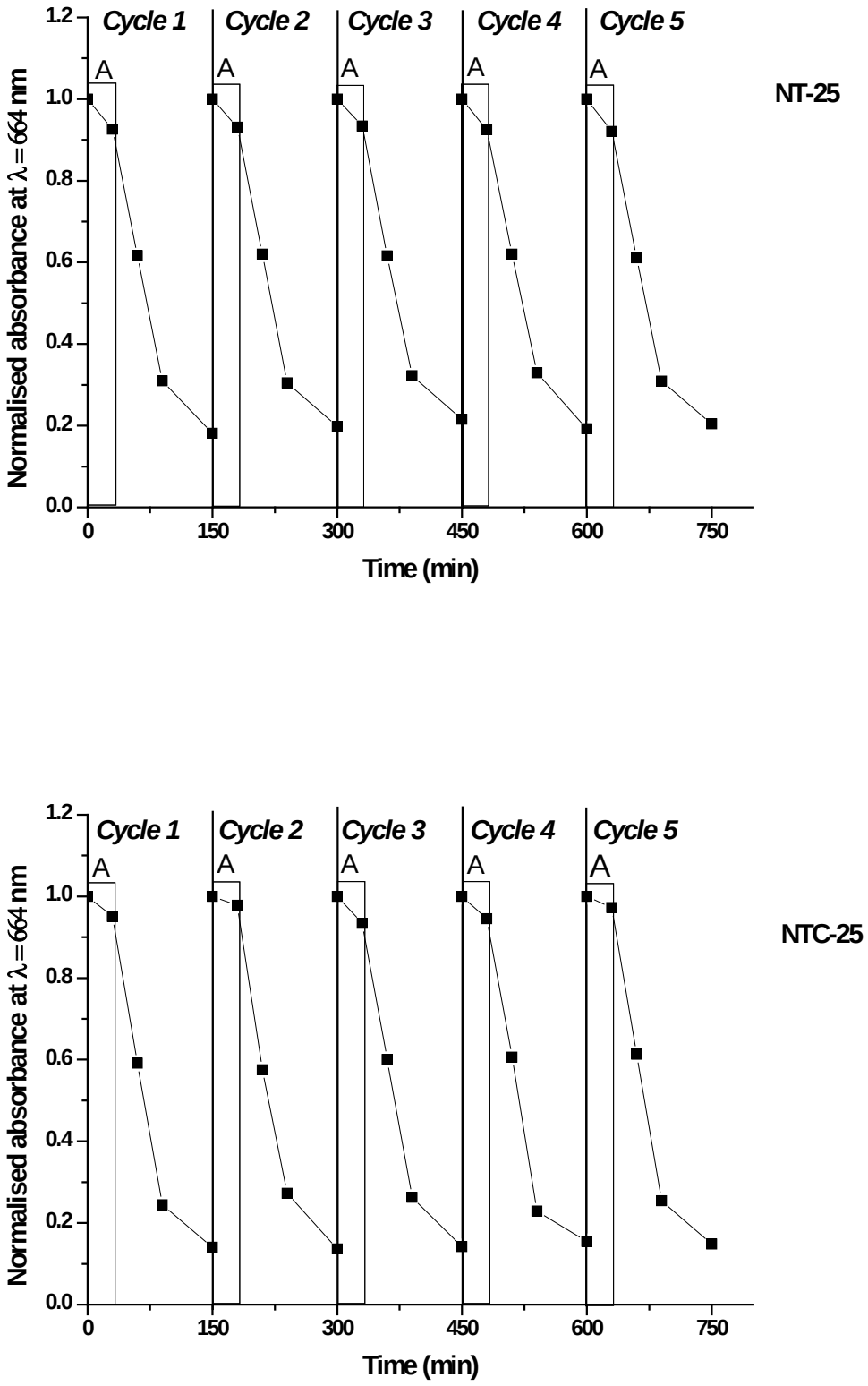

Figure 6.8. Lifetime cycles of NT-25, NTC-25 for the decolourisation of MB ([MB] = 10 mg/L, pH 7, photocatalyst loading = 50 mg/L, (A) dark adsorption).

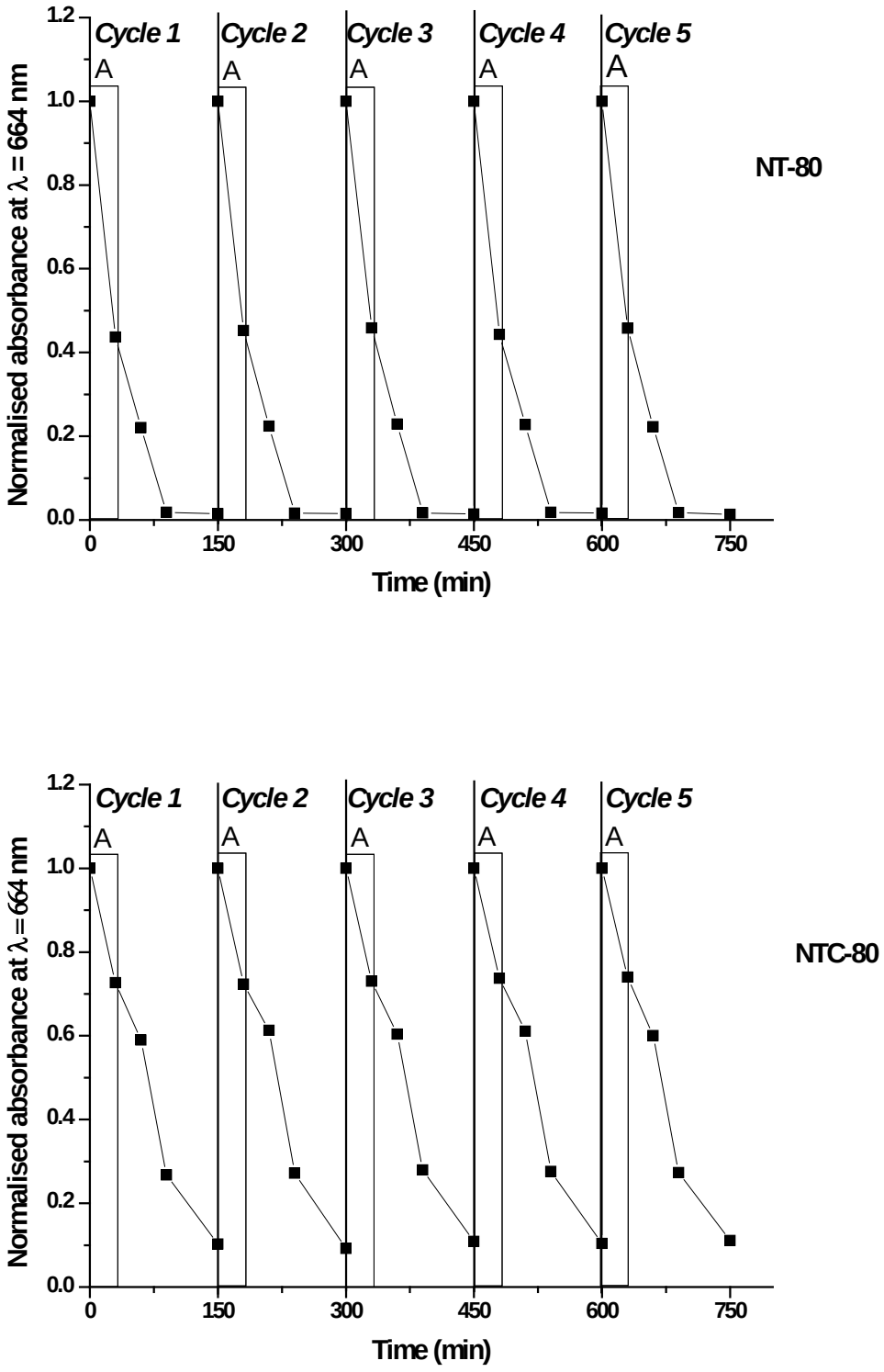

Figure 6.9. Lifetime cycles of NT-80 and NTC-80 for the decolourisation of MB ([MB] = 10 mg/L, pH 7, photocatalyst loading = 50 mg/L, (A) dark adsorption).

6.3.6. Supernatant Turbidity

Post-treatment separation of photocatalysts is a difficult problem in photocatalytic water treatment processes. In this study, the synthesised photocatalysts were tested for their ability to separate from the solution using simple and cost-effective sedimentation. Turbidity measurement, which is used to assess the amount of suspended particles in solution, was used to monitor the sedimentation of photocatalysts at 50 mg/L loading. The decrease in solution turbidity over time indicates an increase in the sedimentation rate of suspended particles. Normalised turbidity figures were plotted to compare different photocatalysts (Figure 6.10). After 2 h at static conditions, the decrease in solution turbidity was about 95% for NT-80 and NTC-80, although it was only 20% and 25% for NT-25 and NTC-25, respectively. In contrast, the turbidity of the water/P25 suspension remained relatively unchanged with only a 5% decrease in turbidity after 2 h settling time. These results show that nanofibrous microspheres can be quickly and easily separated from the solution by sedimentation, even without the use of coagulants and flocculants, which is due to their larger particle sizes.

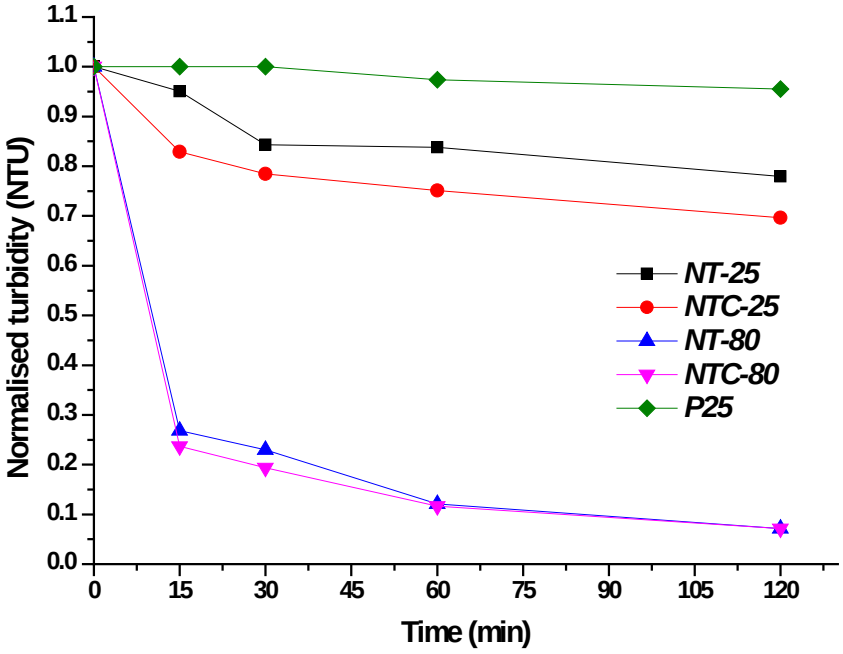

Figure 6.10. Normalised decrease in supernatant turbidity using NT-25, NTC-25, NT-80, NTC-80 and P-25 (pH 7, photocatalyst loading = 50 mg/L).

6.4. Conclusions

Novel Na-titanate nanostructures were synthesised using a simple and facile method at low temperatures. Mesoporous microspheres having smooth surface and average diameter of 700 nm were produced by the simple treatment of P25 precursor with NaOH and H_2O_2 at room temperature. Larger size fibrous microspheres resulted from the same treatment at 80 °C.

The microspheres showed high affinity in adsorbing MB, which was mainly due to the high surface area of NT-80. The binding of Na^+ and peroxo groups had detrimental effect on the adsorption of the cationic dye MB because of surface saturation, which decreased the number of available adsorption sites. Dye decolourisation and DOC removal showed that the microspheres possess photocatalytic activity under UV light irradiation.

The mineralisation of MB was studied for sulphate evolution, which confirmed the photo-oxidative degradation of the pollutant, and therefore the photocatalytic activity of the microspheres. These novel mesoporous microspheres are considered as effective adsorbents of MB, and also capable of its photocatalytic degradation.

The photocatalytic activity of the microspeheres showed negligible decrease after 5 photocatalytic treatment cycles and the particles (NT-80 and NTC-80) could be easily separated from treated solutions by settling.

UNIVERSITY OF TECHNOLOGY, SYDNEY
FACULTY OF ENGINEERING AND INFORMATION TECHNOLOGY

CHAPTER 7

ADSORPTION AND PHOTOCATALYTIC DECOMPOSITION OF METHYLENE BLUE OVER H-TITANATE NANOFIBRES

7.1. Introduction

The use of titania nanoassemblies in the treatment of contaminated water have provided a solution to the problem encountered during the separation of nanoparticles from water. Even though "traditional" nanoparticles showed better apparent photocatalytic activity, their separation from the suspension remains the major challenge for process up-scaling. Therefore, the use of relatively large titanate nanoassemblies has become more popular because they can be easily removed from the solution.

The production of titanate nanostructures using a peroxo-titanate solution has been discussed in details in Chapter 4, and the application of Na-titanates in the adsorption and photocatalytic removal of MB was presented in Chapter 6. Titanate nanostructures can effectively adsorb dye molecules due to their high surface area and special characteristics (Lee et al. 2007; Baiju et al. 2009; Xiong et al. 2010). The effect of synthesis temperature (Lee et al. 2008a), and sodium content (Lee et al. 2008b) on the cation exchange capacity of titanate nanotubes were reported. It was found that the increase of sodium content in the nanotubes increases the adsorption of dye through cationic exchange. Na^+ can be replaced by H^+ in the nanostructure framework by washing the Na-titanates in an HCl solution (Wei et al. 2004; Zhu et al. 2004; Mao et al. 2006; Bela et al. 2010). Bela et al. (2010) reported that the ion exchange in the titanate nanobelts was highly dependent on the duration of acid wash. The authors found that the acid wash of titanate nanobelts in a 0.1 M HCl solution for 72 h was enough to completely exchange Na^+ for H^+.

The adsorption of MB on TiO_2 from aqueous solution was studied by Fetterolf et al. (2003). The authors found that the Langmuir adsorption model is adequate for representing the adsorption of MB, which was attributed to electrostatic attractions. Similarly, Xiong et al. (2010) studied the adsorption of MB on titanate nanotubes and reported that the Langmuir model was appropriate for describing the monolayer adsorption mechanism.

The photocatalytic decomposition of MB over TiO_2 was discussed in Chapter 2 (Section 2.4.2). However, in a recent study, MB adsorption on titanate nanostructures has been found to significantly affect the degradation of the dye under UV light (Xiong et al. 2011). Better photocatalytic decomposition was achieved in the adsorption/photocatalysis system compared to the adsorption followed by photocatalysis system under UV irradiation. The adsorption of dye molecules onto titanate nanostructures can be of significant importance in terms of initiating the dye sensitization mechanism. This can be used in solar light treatment systems that treat dye contaminated wastewater. Thus, the objectives of this Chapter were to:

- Study the effect of exchanging Na^+ for H^+ on the morphology and physico-chemical characteristics of nanofibrous microspheres prepared in Chapter 6.
- Investigate the kinetics of MB adsorption on the nanofibres.
- Carry out photocatalytic degradation of MB under simulated solar light.
- Test the photocatalytic stability and the ease of separation of the produced nanofibres.

7.2. Experimental Investigations

7.2.1. Synthesis

H-titanate nanofibres were fabricated by the same method used for making Na-titanates fibrous microspheres that was described in Chapter 6. Here again, 2 g of P25 powder was dispersed in 12 mL of H_2O_2 (50%) under alkaline conditions by adding 4 g of NaOH (final pH 13). Later on, the mixture was placed in a Teflon cell at 80 °C for 24 h. After hydrothermal treatment, the pH of the Na-titanates suspension was decreased to pH 2 by using 1 N HCl, at which ion exchange (Na^+ and H^+) was carried out for 60 min under magnetic stirring. This was followed by washing with Milli Q water until a pH of 7. The as-prepared nanofibres were dried in oven at 100 °C for 12 h and annealed at 550 °C for 6 h to obtain anatase nanofibres. H-titanate nanofibres will be named hereafter as HTNF.

7.2.2. HTNF Characterisation

Morphology and elemental composition analyses were carried out using the Zeiss Supra 55VP SEM/EDS operating at 20 kV. X-ray diffraction (XRD) patterns were generated on MDI Jade 5.0 X-ray diffractometer. Brunauer, Emmet and Teller (BET) surface area analyses were performed on an automated surface area analyser (Micromeritics Gemini 2360, USA) by means of nitrogen adsorption-desorption. The zeta potential of as-prepared powders was determined by dispersing the nanofibres in MQ water under variable pH (adjusted by HCl and NaOH) and measured using the Malvern nano-series ZS equipment.

7.2.3. MB Adsorption Experiments

MB powder was dissolved in pure water to prepare a stock solution of 1 g/L concentration. All experimental MB solutions were prepared from the stock solution by dilution.

7.2.3.1. Effect of HTNF Loading

In this experiment, five different powder loadings (0.1, 0.2, 0.5, 1 and 2 g/L) were selected to study the adsorption of MB molecules onto HTNF. The experimental conditions were: MB concentration 10 mg/L, pH = 9 (after adding the powder no pH adjustment was done), T = 25 °C and shaking speed 150 rpm.

7.2.3.2. Effect of MB Concentration

After optimising the HTNF loading, three MB concentrations (5, 10 and 20 mg/L) were selected to study the kinetics of adsorption. The experiment was performed under the following conditions: HTNF = 0.5 g/L, pH = 9, T = 25 °C and shaking speed 150 rpm.

7.2.3.3. Effect of pH

The pH of the solution is known to affect the surface charge of the nanofibres, and consequently the adsorption of dye molecules. The experiments were conducted at the pH values of 3, 5, 7 and 9. All other factors were kept constant: HTNF = 0.5 g/L, MB = 20 mg/L, T = 25 °C and shaking speed 150 rpm.

7.2.3.4. Effect of Solution Temperature

The temperature of the solution was changed to study its effect on the adsorption process. In these experiments the selected temperatures were 25, 35, and 45 °C. The experimental conditions were: HTNF = 0.5 g/L, MB = 20 mg/L, pH = 9 and shaking speed 150 rpm.

7.2.3.5. Adsorption Equilibrium and Isotherms

The amount of dye adsorbed at equilibrium was calculated from the following formula:

$$q_e = (C_0 - C_e)\frac{V}{m} \quad \text{(Eq. 7.1)}$$

where, C_0 and C_e (mg/L) are the initial and equilibrium concentration of MB in solution, V (L) is the solution volume and m (g) is the mass of the HTNF.

Adsorption data was analysed by fitting them to the commonly used Langmuir isotherm. The Langmuir isotherm can be expressed by the following equation (Langmuir 1918):

$$\frac{C_e}{q_e} = \frac{1}{kq_m} + \frac{1}{q_m}C_e \quad \text{(Eq. 7.2)}$$

where, C_e is the equilibrium concentration, q_e (mg/g) is the amount of adsorbate adsorbed on unit mass of adsorbent, q_m (mg/g) and k (L/mg) are the Langmuir adsorption constants related to adsorption capacity and rate of adsorption, respectively. The q_m and k values were calculated from the slope and intercept of the straight line obtained after plotting C_e/q_e against C_e, respectively.

7.2.4. Photocatalytic Degradation under Simulated Solar Light

The photocatalytic activity of HTNF (0.5 g/L) was assessed using 200 mL volume of MB solution (20 mg/L) as model pollutant. The HTNF loading and MB concentration were selected based on the results obtained in the adsorption experiments. The effect of solution pH (3, 5, 7 and 9) and solar light intensity (5 000, 15 000 and 28 000 lx; measured by a digital power meter AR 823) on the removal of MB were studied. MB molecules were adsorbed on HTNF in dark after mixing at 450 rpm for 30 min. The solution was then placed in the Solar Simulator (Chapter 3, Section 3.4.3) and photocatalysis was carried out for 180 min at a stable temperature of 26 ºC. Air sparging was adjusted at 0.6 L/min to provide adequate dissolved oxygen to the reaction. MB degradation was monitored by collecting samples (filtered by 0.45 µm PTFE filters) at fixed time intervals and analysed for colour removal at λ = 664 nm using a Shimadzu UV-Vis1700 spectrophotometer. Samples were also analysed for DOC removal (Multi N/C 3100, Analytik Jena). The kinetics

of the photocatalytic degradation reactions were obtained by fitting to the nonlinear equation:

$$C_t = C_0 \cdot e^{-k_a \cdot t} \quad \text{(Eq. 7.3)}$$

where, C_t (mg/L) is the concentration of MB at time t, C_0 (mg/L) is the initial concentration of MB, t is time, and k_a is the apparent pseudo first order constant.

7.2.5. Photocatalytic Stability

The photocatalytic stability of HTNF (0.5 g/L) was examined over three successive cycles using 200 mL volume of MB solution (20 mg/L). The pH of the solution was 9 and air sparging was adjusted to a rate of 0.6 L/min at a light intensity of 28 000 lx. At the end of each cycle (for 8 h to ensure complete regeneration), HTNF were recovered and washed with Milli Q water before being used in the next degradation cycle. Samples were also analysed for changes in absorbance at 254 nm and 664 nm wavelengths, and for DOC removal.

7.2.6. Photocatalyst Separation by Settling

The separation of HTNF in Milli Q water by gravity settling was studied by collecting samples from 5 cm below the water surface (HTNF = 0.5 g/L, pH = 9). Sample turbidity was logged over time and measured using the Hach HI 93414 turbidity and chlorine meter.

7.3. Results and Discussion

7.3.1. Characteristics of H-titanate Nanofibres

Figure 7.1 shows the zeta potential of the as-prepared and calcined HTNF. The calcination shifted the PZC towards higher pH due to the evaporation of peroxo groups. While the properties of the as-prepared titanate will not be discussed in this Chapter, its zeta potential characteristics are useful to elucidate the noticed shift of pH, and to help understanding the process detailed in Chapter 8.

SEM pictures of HTNF revealed fibrous nanostructures of randomly dispersed nanofibres with an average diameter of 40-70 nm and few hundred nanometers in length (Figure 7.2). It has been discussed in Chapter 6 that the Na-titanate nanofibres were arranged in microspheres of few micrometres in diameter. In contrast, the acid wash at low pH (ion exchange) affected the aggregation of nanofibres but the nanofibres conserved their typical morphology, which has also been observed by several researchers (Wei et al. 2004; Zhu et al. 2004; Bela et al. 2010).

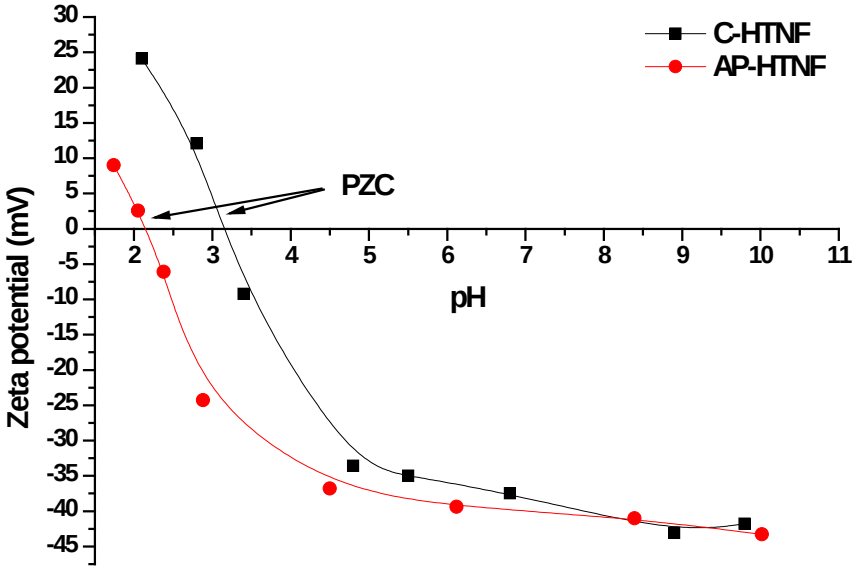

Figure 7.1. Zeta potential of 1 g/L suspension of as-prepared (AP-HTNF) and calcined HTNF (C-HTNF).

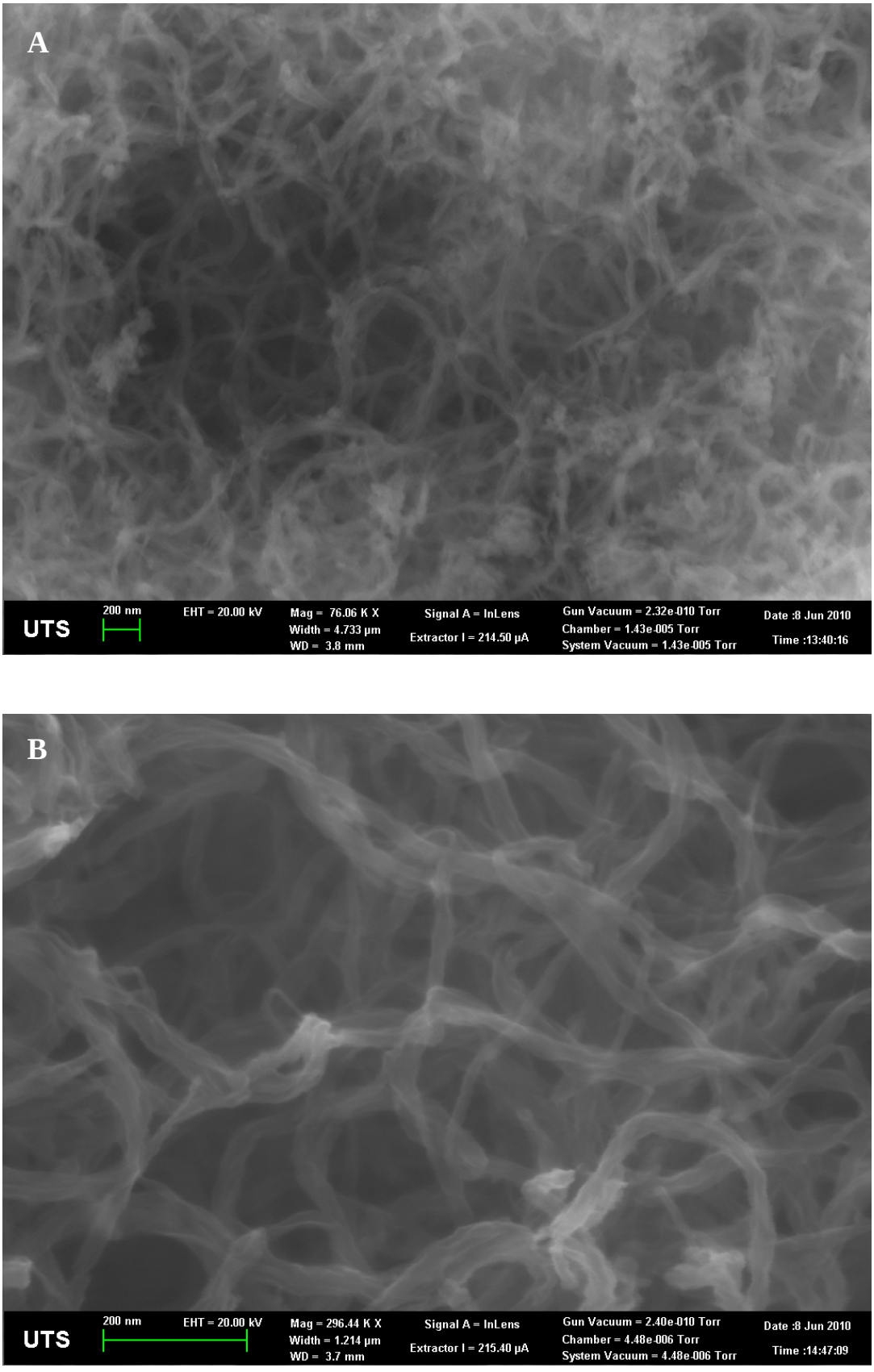

Figure 7.2. SEM images of H titanate nanofibres (A and B).

The exchange of Na^+ with H^+ was checked by EDS measurements (Figure 7.3). The XRD analysis showed that the nanofibres were mainly anatase (data not shown). The calculated surface area of nanofibres was 31.5 m^2/g, the average pore volume 0.10 cm^3/g and average pore size 50 Å.

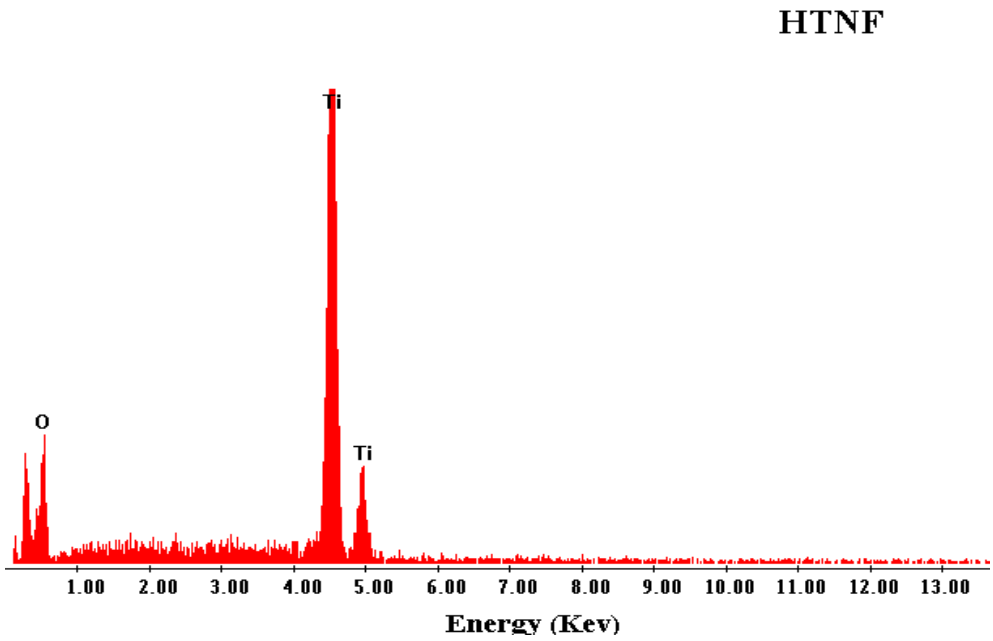

Figure 7.3. EDS plot showing the elemental composition of HTNF.

7.3.2. Effect of Operating Conditions on MB Adsorption

7.3.2.1. Effect of HTNF Loading

The effect of HTNF loading on the removal of MB from the solution was studied using photocatalyst loadings of 0.1, 0.2, 0.5, 1 and 2 g/L. The results of experiments carried out at 25 °C and 10 mg/L of MB are shown in Figure 7.4. The adsorption of MB increased with photocatalyst loading until equilibrium was reached after 30 min. An increase in HTNF dosage from 0.1 to 0.5 g/L increased the adsorption of MB from 11% to a remarkably high 90%. The increase in the adsorption efficiency can be explained by the increase in the surface area available for adsorption. However, no significant increase in adsorption was recorded after increasing the loading to 1 and 2 g/L (92% and 93%, respectively). This could be attributed to the attainment of adsorption equilibrium between MB and HTNF, or reaching the adsorption

saturation point. The photocatalyst loading of 0.5 g/L was considered optimum and was adopted for the next optimisation process.

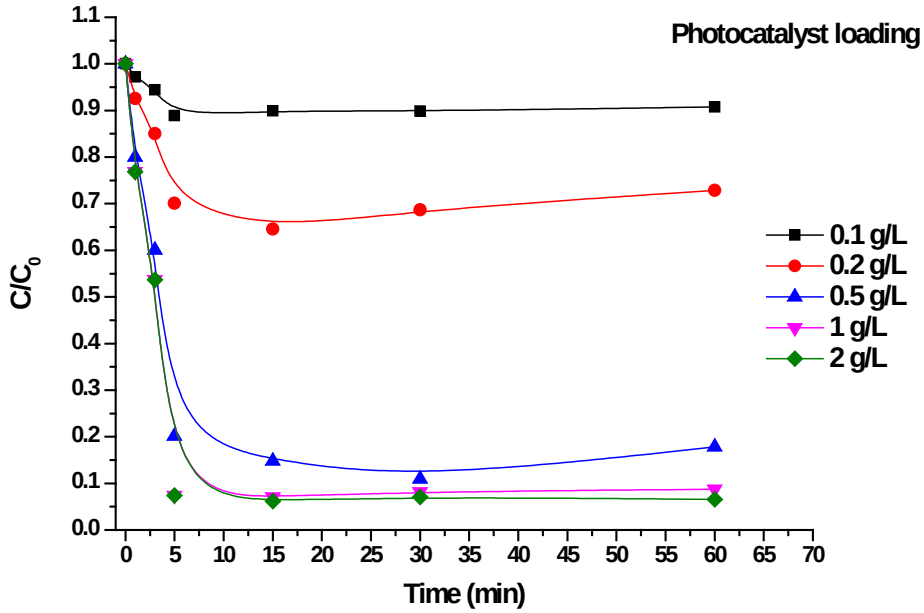

Figure 7.4. Effect of HTNF loading on the adsorption of MB from solution. (Experimental conditions: MB = 10 mg/L, T = 25 °C, shaking speed = 150 rpm, pH = 9).

7.3.2.2. Effect of Initial MB Concentration

Figure 7.5 shows the adsorption of MB onto HTNF using initial MB concentrations of 5, 10 and 20 mg/L. It is evident that the initial MB concentration played a significant role in the adsorption process, where 97%, 89% and 42% of MB were removed at MB concentrations equal to 5, 10 and 20 mg/L, respectively. The HTNF removed almost all the dye at relatively low initial concentration. In industrial applications, high MB removal at low concentrations is considered to be of a great importance. The amount of MB adsorbed increased with time until the equilibrium was attained at 30 min for high MB concentrations (10 and 20 mg/L), while almost all MB molecules were adsorbed within 5 min at 5 mg/L of MB. The initial uptake (first few minutes) for MB was high because a large number of adsorption sites were available for adsorption. Later on, the adsorption decreased as the repulsive forces

between the adsorbed MB molecules (on HTNF) and the MB molecules in the solution increased (Fetterolf et al. 2003; Xiong et al. 2010). In order to study the effect of other parameters in the adsorption process such as pH and temperature, 20 mg/L MB concentration was selected and will be discussed in the following sections.

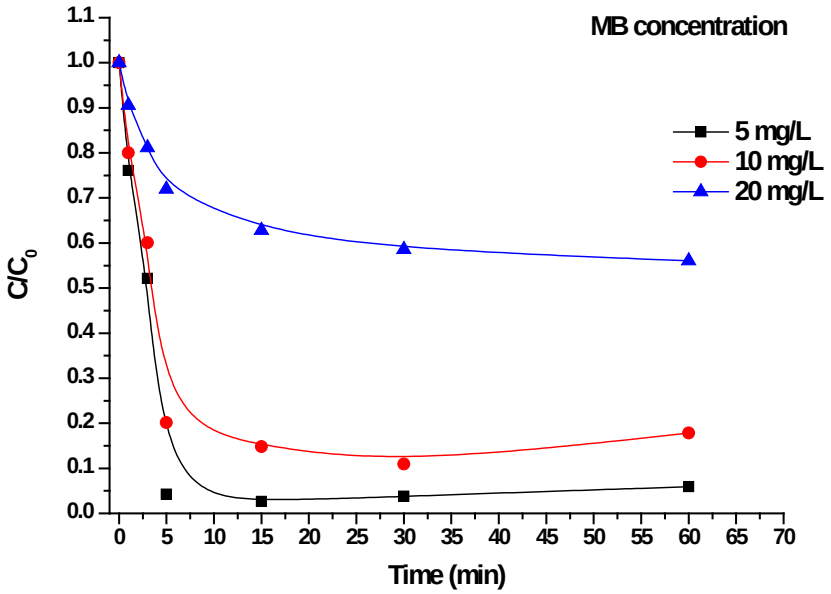

Figure 7.5. Effect of initial MB concentration on the adsorption of MB onto HTNF. (Experimental conditions: HTNF = 0.5 g/L, T = 25 °C, shaking speed = 150 rpm, pH = 9).

7.3.2.3. Effect of Solution pH

The adsorption of MB was studied in a suspension of 0.5 g/L of HTNF and 20 mg/L of MB using different pH values (3, 5, 7 and 9). The results of adsorption are shown in Figure 7.6. MB is a cationic dye which is favourably adsorbed on negatively charged surfaces (Feetrolf et al. 2003). The zeta potential measurements of HTNF revealed that the surface charge of the nanofibres was negative over a wide pH range, and that the PZC was around pH 3.2. At pH 3, the repulsive forces between the HTNF and MB molecules dominated the adsorption process, leading to a low overall adsorption (7% after 30 min). In contrast, when the pH was increased to 5, 7, and 9, MB adsorption increased to 28%, 32% and 42%, respectively. This was

mainly due to electrostatic attraction between the HTNF surface and MB molecules. This finding was in agreement with previous studies on the adsorption of MB onto titania (Fetterolf et al. 2003), titanate nanotubes (Xiong et al. 2010) and different organic and inorganic adsorbent (Ai et al. 2011).

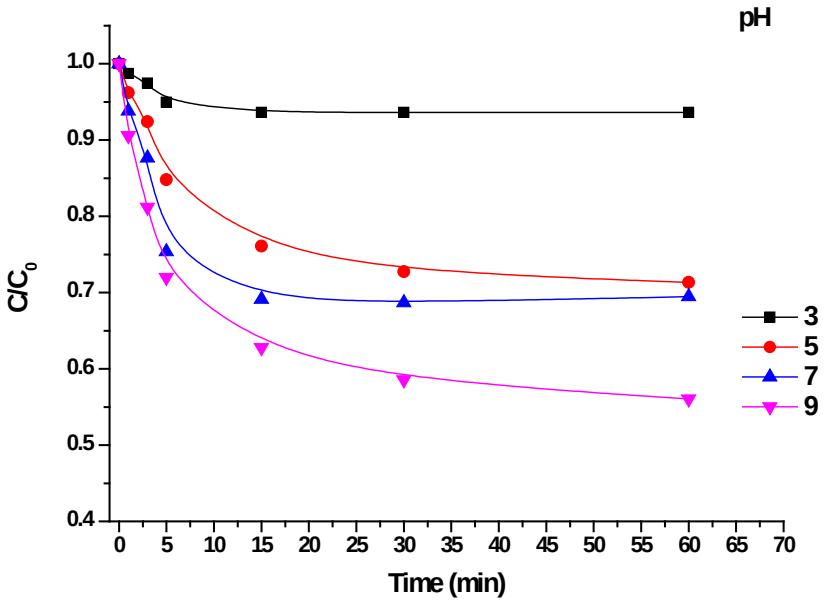

Figure 7.6. Effect of solution pH on the adsorption of MB onto HTNF. (Experimental conditions: HTNF = 0.5 g/L, MB = 20 mg/L, T = 25 °C, shaking speed = 150 rpm).

7.3.2.4. Effect of Solution Temperature

The effect of different solution temperature on the adsorption is shown in Figure 7.7. The adsorption of MB increased with temperature increase, indicating an endothermic adsorption process (Bulut and Aydin 2006; Hong et al. 2009). The total adsorption at equilibrium (30 min) was found to slightly increase from 42% to 48% for an increase in the solution temperatures from 25 to 35 °C. Similar findings were reported by Hong et al. (2009) who attributed this to the stronger bonds formed at higher temperatures between the dye and the adsorbent.

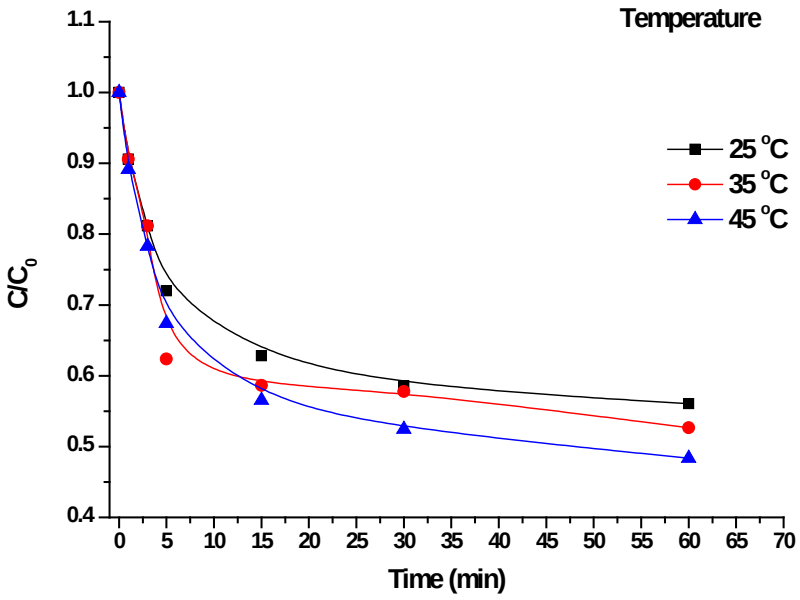

Figure 7.7. Effect of solution temperature on the adsorption of MB onto HTNF. (Experimental conditions: HTNF = 0.5 g/L, MB = 20 mg/L, shaking speed = 150 rpm, pH = 9).

7.3.2.5. Adsorption Equilibrium and Isotherms

Figures 7.8A and 7.8B show the amount of MB adsorbed at equilibrium (30 min) using different HTNF loading and MB concentrations, respectively. The adsorption of dye increased with HTNF loading to a maximum of 17.8 mg/g at 0.5 g/L and then decreased to 9.18 and 4.64 mg/g at 1 and 2 g/L, respectively. The increase in the adsorption capacity (q_e) reached a maximum at 0.5 g/L of HTNF loading while further increase in the mass of HTNF (denominator in Eq.7.1) with $(C_0\text{-}C_e)*V$ (Eq. 7.1) remaining constant caused the decrease in q_e. The effect of initial MB concentration revealed that the increase of MB concentration at a constant HTNF loading increased the adsorption mainly because of high driving force for mass transfer (Bulut and Aydin 2006). The data shown in Figure 7.8B showed some decrease in q_e after increasing the concentration of MB from 10 to 20 mg/L (data collected after 30 min of contact). However, the experiments were continued for 3 h and no significant difference in q_e at MB concentrations of 10 mg/L and 20 mg/L was found (q_e for both concentrations varied from 16.5 to 17.8 mg/g).

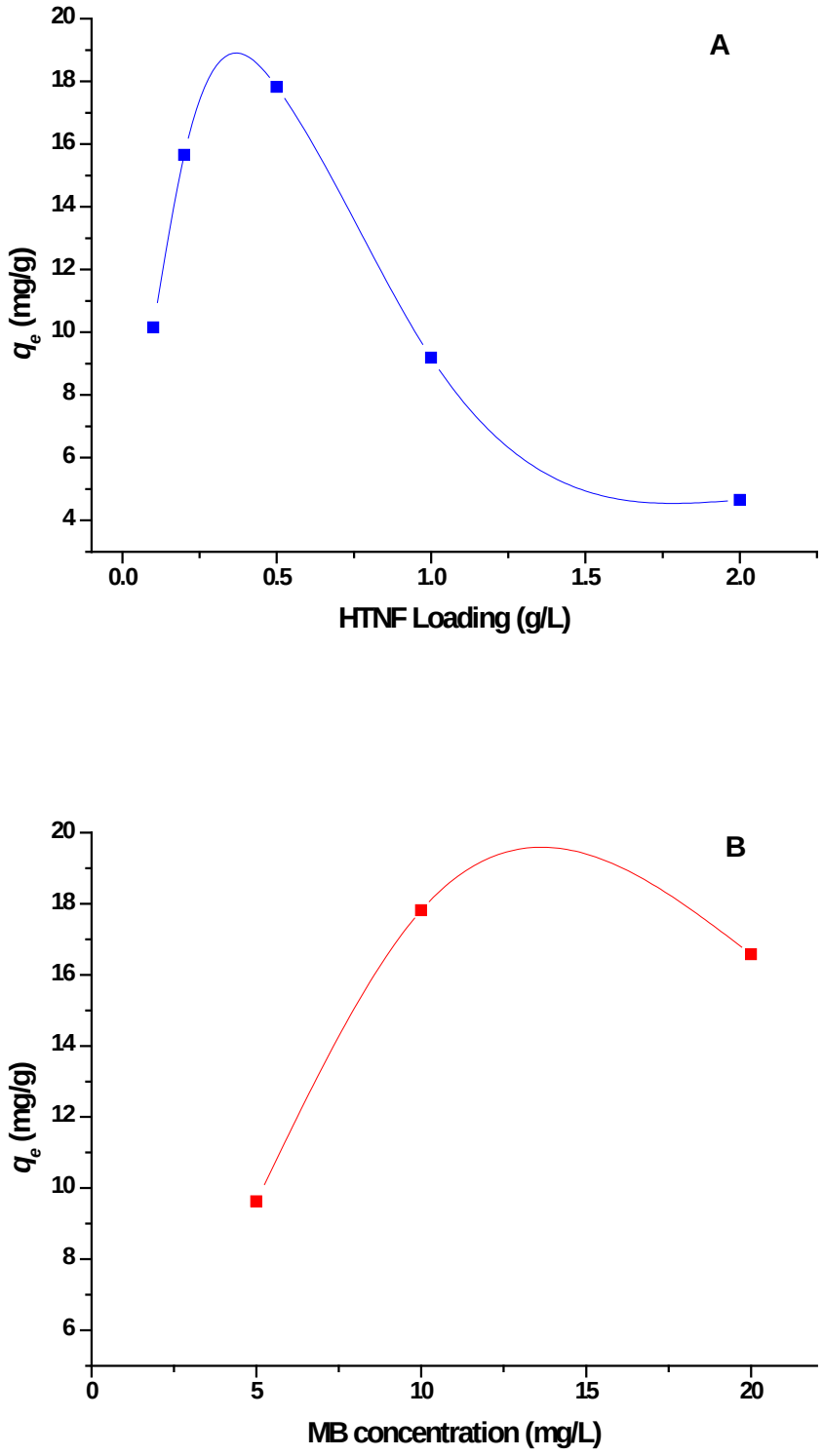

Figure 7.8. (A) Effect of HTNF loading and (B) MB concentration on the amount of dye adsorbed at equilibrium (q_e, mg/g).

During adsorption, the adsorption capacity is highly influenced by the pH variations of the solution (Wang et al. 2005a). The plot of pH variation against the adsorption capacity is shown in Figure 7.9A. The adsorption capacity increased from 2.55 mg/g at pH 3 to 16.57 mg/g at pH 9 after 30 min of contact. As discussed earlier, the surface charge of HTNF changed from positive to negative at pH 3 and 9, respectively. This played an important role in adsorbing more cationic MB molecule at high pH.

Increasing the temperature of the solution enhanced the adsorption of MB molecules onto HTNF (Figure 7.9B). The adsorption capacity increased from 16.57 mg/g at 25 °C to 19 mg/g at 45 °C. It has been discussed earlier in this Chapter that the process of adsorption is endothermic. Some authors have suggested that the heat of adsorption can only describe the physical or chemical adsorption of gas molecules into solid surfaces. Nevertheless, the use of endothermic and exothermic adsorption terminologies to explain adsorption in water has been widely accepted.

To further describe the equilibrium of adsorption, the most commonly used adsorption models (Langmuir) has been used to fit the data obtained under different operating conditions. The data was fitted using Eqs. 7.2 and the results are shown in Table 7.1. Our data fitted well the Langmuir model. The goodness of fit was shown with R^2 equal to 0.99, 0.91, 0.89 and 0.99 for experiments on HTNF loading, MB concentration, pH and temperature, respectively. These findings indicated that the monolayer adsorption of MB on HTNF was the dominant mechanism of adsorption. The Langmuir model has fitted well the adsorption data of MB onto titanate nanotubes (Xiong et al. 2010). It has been reported that uniform nanotubular structure and homogenous distribution of active sites on the walls favoured this adsorption mechanism.

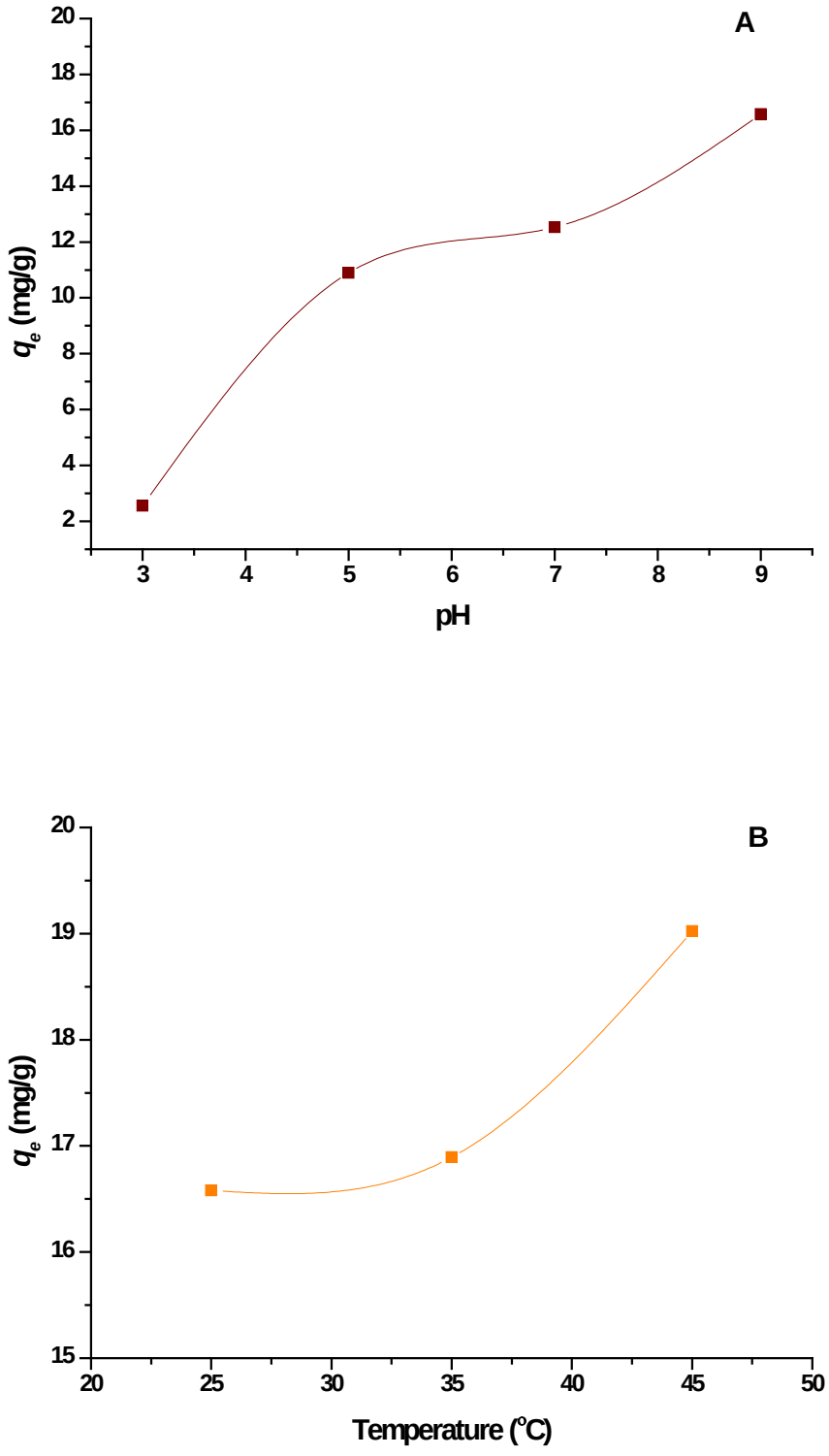

Figure 7.9. (A) Effect of solution's pH and (B) temperature on the amount of dye adsorbed at equilibrium (q_e, mg/g).

Table 7.1. Langmuir isotherm constants for MB adsorption onto HTNF under different operating conditions

Isotherms	**Parameters**	**Operational conditions**			
		HTNF Loading	**MB concentration**	**pH**	**Temperature**
Langmuir	q_m (mg/g)	12	16.7	1.1	8.84
	k (L/mg)	5.5	30	0.08	0.17
	$\boldsymbol{R^2}$	**0.91**	**0.99**	**0.89**	**0.99**

The Langmuir isotherm was further evaluated by the dimensionless constant separation factor R_L (Hall et al. 1966; Weber and Chakravorti 1974):

$$R_L = \frac{1}{1+kC_0} \quad \text{(Eq. 7.4)}$$

with k Langmuir constant (L/mg) and C_0 initial MB concentration (mg/L). The value of R_L indicates the shape of the adsorption isotherm and values between 0 and 1 indicate favourable adsorption (McKay et al. 1989). The calculated R_L from our data showed values between 0 and 1 suggesting that the adsorption between MB and HTNF was favourable (Table 7.2). Moreover, low R_L values (<0.04) indicated that the interaction between MB and HTNF was relatively strong (Xiong et al. 2010).

Table 7.2. R_L values for different operational conditions

Operational conditions	**HTNF loading (g/L)**	**MB concentration (mg/L)**			**pH**	**Temp (°C)**
		5	**10**	**20**		
R_L	0.018	0.00002	0.028	0.001	0.37	0.22

7.3.3. Photocatalytic Decolourisation and DOC Removal of MB

7.3.3.1. Effect of Solution pH

It was discussed in Section 7.3.2.3 that the variation of solution pH directly influenced the adsorption of MB molecules onto HTNF through electrostatic interactions. The adsorption was favoured at high pH between different surface charges and decreased with pH decrease. Figure 7.10 shows the discolouration and the DOC removal of MB solution after 30 min adsorption and 180 min of light irradiation. The discolouration of the solution was almost complete after 90 min for pH values of 5, 7 and 9. In contrast, only 89% of MB was removed after 180 min of light irradiation at pH 3. The decrease in DOC was slower being 48%, 75%, 78% and 78% for pHs of 3, 5, 7 and 9. The results of regression analysis between MB discolouration and DOC removal are presented in Table 7.3.

The effect of solution pH on the discolouration of MB solution was reported in the literature (Shimizu et al. 2007; Tayade et al. 2009). Shimizu et al. (2007) found that the change of pH between 3 and 10 did not influence the solution colour in the absence of the photocatalyst. However, significant decrease in colour was reported at pH above 10. In this study, the pH range was between 3 and 9, thus it can be assumed that the initial concentration of MB was constant. Moreover, photodegradation data collected in different experiments were normalised to the initial MB absorbance measured at pH values of 3, 5, 7 and 9. Lachheb et al. (2002) studied the adsorption of several dyes, including MB, onto TiO_2 under different pH values ranging from 3 to 9. In agreement with the present findings, they also reported low MB adsorption at low pH but little influence of pH variations upon the kinetics of colour disappearance under UV light. In another study on MB photodegradation, Wu and Chern (2006) showed that increasing the pH above the PZC of TiO_2 (PZC $\approx$ 4.5 according to authors' measurements) has dramatically impacted the dispersion of particles in solution, leading to coagulation and sedimentation. Consequently, the decomposition of MB was decreased because of the decrease in TiO_2 surface area. In this study, no coagulation of HTNF was observed but the decrease of adsorption (at pH 3) retarded the discolouration. This observation indicates that the decomposition of MB molecules was due to the attack by the $OH^{\bullet}$ radicals under these conditions.

In contrast, surface degradation was the dominating degradation mechanism at high solution pH.

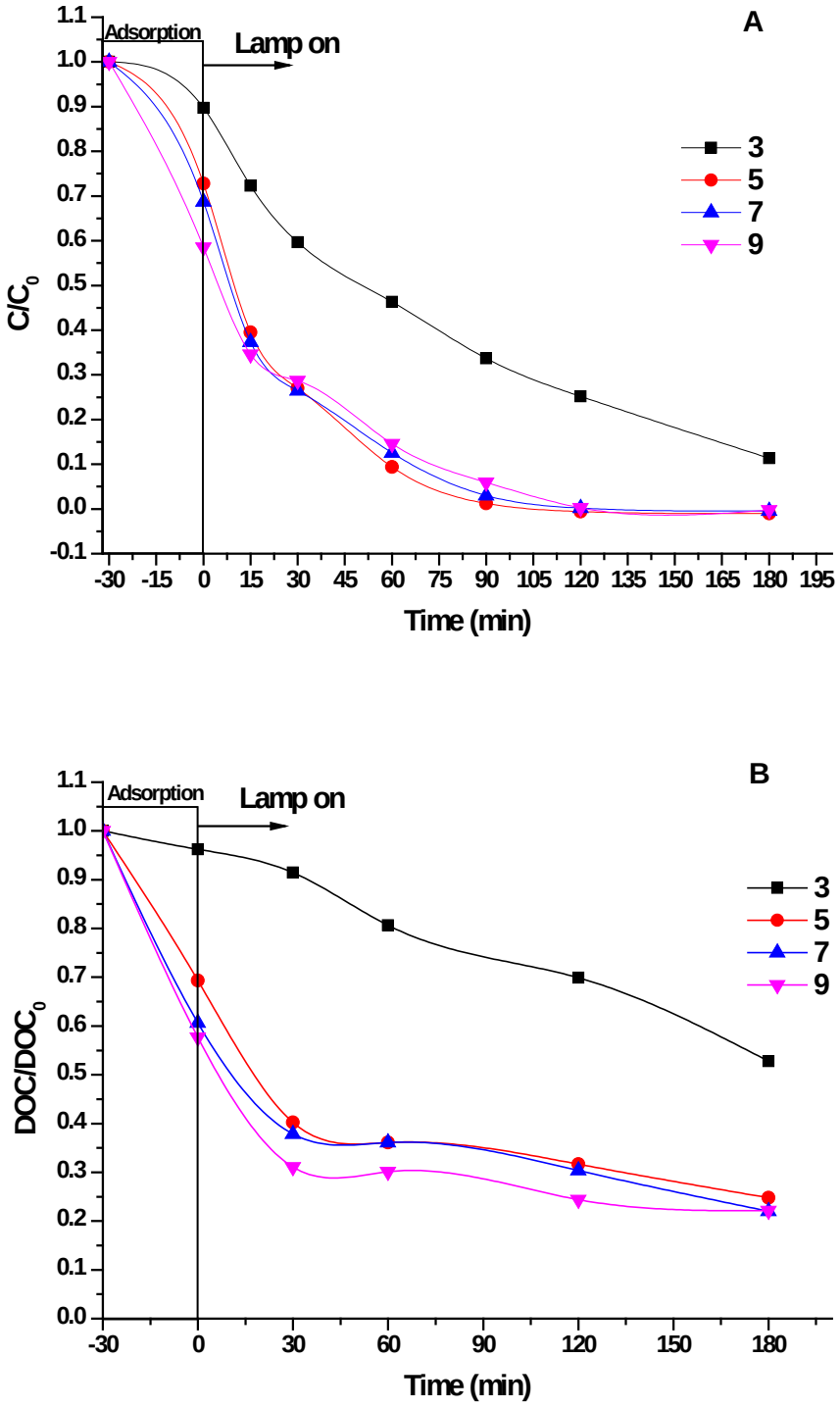

Figure 7.10. (A) Effect of solution pH on the discolouration and (B) DOC removal of MB solution using HTNF. (Experimental conditions: HTNF = 0.5 g/L, MB = 20 mg/L, T = 26 °C, air flow = 0.6 L/min, light intensity = 28 000 lx).

Table 7.3. Regression equation and R^2 for MB discolouration against DOC removal

Parameter	**Solution pH**			
	3	**5**	**7**	**9**
Linear Regression equation	$y^{\S} = 0.489x^* + 0.547$	$y^{\S} = 0.668x^* + 0.272$	$y^{\S} = 0.677x^* + 0.244$	$y^{\S} = 0.753x^* + 0.188$
R^2	0.906	0.966	0.942	0.958

§y represents normalised DOC

*x represents normalised absorbance

7.3.3.2. Effect of Light Intensity

The effect of light intensity on the photodegradation of MB was studied and the results are shown in Figure 7.11. It has been discussed in Chapter 2 (Section 2.2.4.5) that the light intensity of the system will affect the electron/hole formation, their separation and recombination rate. However, this can also be affected by the emitted wavelength of the lamp and the type of photocatalyst. In the reactor used in the present experiments, the decrease of light intensity from 28 000 lx to 15 000 lx did not significantly decrease the degradation rate of MB after 180 min of light irradiation. However, a further reduction in light intensity to 5 000 lx resulted in 25% decrease in discolouration efficiency of the system (adsorption + photodegradation). DOC removal of the system was high (78%) for the maximum intensity (28 000 lx), decreasing to 73% at 15 000 lx and to 64% at 5 000 lx.

The pseudo-first order apparent constants are shown in Table 7.4. These were calculated by using the decrease in MB concentration (k^1_a) and the decrease of solution DOC (k^2_a) over time. k^1_a values increased from 0.011 min^{-1} at pH 3 to 0.034 min^{-1} at pH 9. Similarly, k^1_a increased from 0.0037 min^{-1} to 0.034 min^{-1} with the increase in light intensity. The photodiscolouration of MB over HTNF followed the pseudo-first order reaction kinetics, noting that similar finding was reported by Houas et al. (2001) for photodegrading MB over Degussa P25.

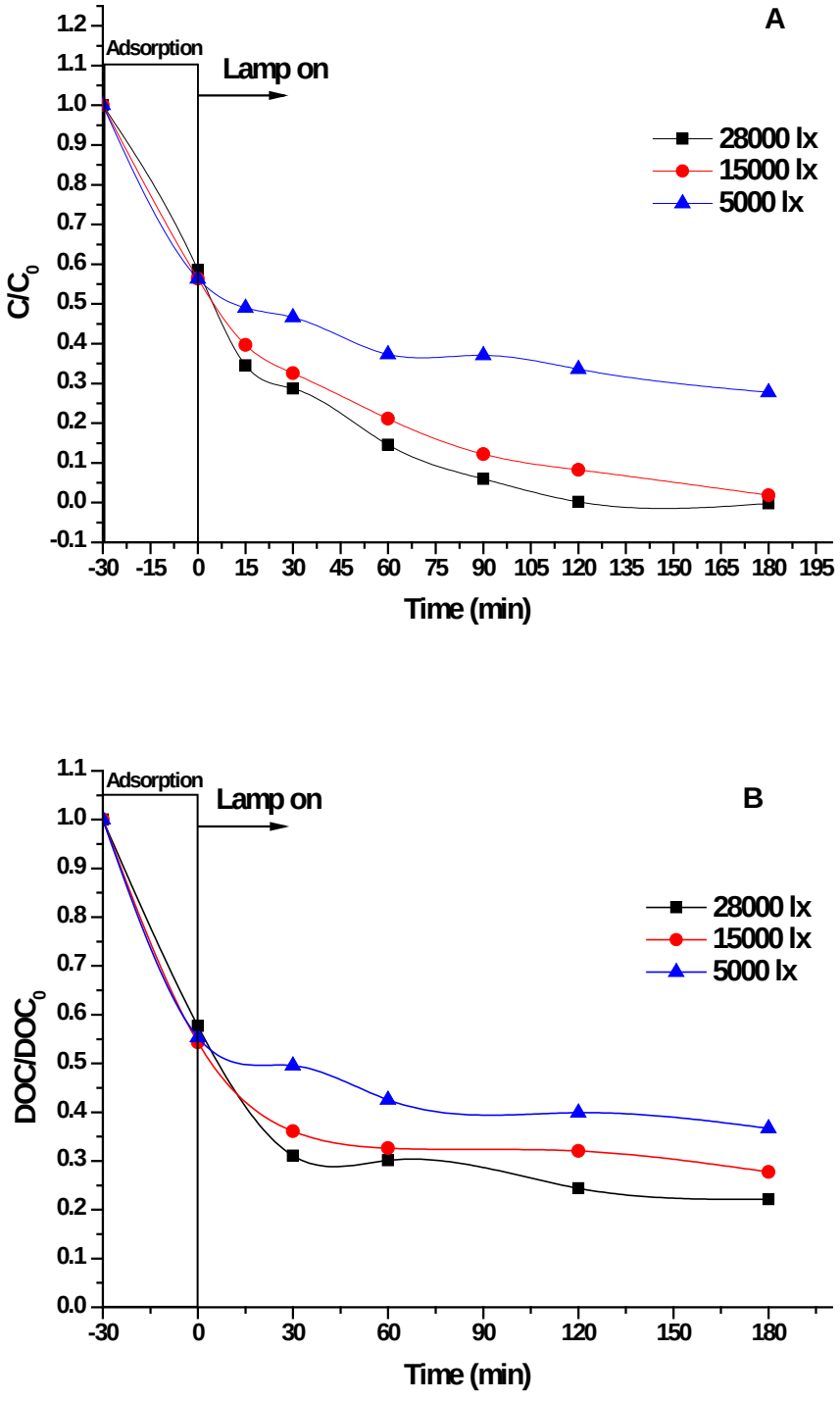

Figure 7.11. Effect of light intensity on the discolouration (A) and DOC removal (B) of MB solution using HTNF. (Experimental conditions: HTNF = 0.5 g/L, MB = 20 mg/L, T = 26 °C, air flow = 0.6 L/min, pH = 9).

k^2_a was calculated from the DOC concentration decrease over time (Table 7.4). DOC removal kinetics were slower than those observed for MB discolouration and this could be attributed to the formation of photodegradation intermediates (Herrmann 1999; Houas et al. 2001; Lachheb et al. 2002). The apparent rate constant increased with pH and light intensity increase. The adsorption of MB onto HTNF favoured its photocatalytic removal from the solution at basic pH (Houas et al. 2001).

Table 7.4. Apparent pseudo-first order kinetics for the photocatalytic degradation of MB over HTNF under different operating conditions

Parameter	**Operational conditions**						
	pH				**Light Intensity**		
	3	**5**	**7**	**9**	**28000**	**15000**	**5000**
k^1_a (min^{-1})§	0.011	0.025	0.037	0.034	same as pH 9	0.018	0.0037
R^2	0.994	0.828	0.915	0.893	same as pH 9	0.986	0.9440
k^2_a (min^{-1})*	0.003	0.004	0.004	0.004	same as pH 9	0.003	0.002
R^2	0.979	0.820	0.888	0.735	same as pH 9	0.708	0.906

§Constants were calculated from the MB concentration degradation curves.

*Constants were calculated from the DOC degradation curves to include the degradation of intermediate compounds.

7.3.4. Photocatalytic Stability of HTNF

The photocatalytic stability of HTNF was also tested by adopting the model of Xiong et al. (2011). The experiments consisted of running photocatalytic degradation reactions without the dark adsorption of MB onto HTNF. A 200 mL beaker containing 0.1 g of HTNF suspended in 20 mg/L MB solution was placed in the solar simulator at 28 000 lx and at a temperature of 26 °C.

Figures 7.12 and 7.13 show the normalised photocatalytic degradation data obtained from the absorbances at λ = 254 nm and 664 nm. The MB solution changed to colourless after 2 h of photoreaction, than turned to humic-like water colour between 2 h to 6 h before becoming colourless at the end (after almost 8 h). These findings suggest that the photocatalytic degradation of MB in this system has occurred in three stages:

- Stage 1: Concurrent adsorption of MB and photocatalytic degradation to positively charged intermediates (surface reaction) (Houas et al. 2001; Orendorz et al. 2008).
- Stage 2: Desorption of intermediate compounds, (mainly negatively charged phenolic or aromatic organics) from HTNF surface (Houas et al. 2001).
- Stage 3: Degradation of aromatic intermediates by $OH^{\bullet}$ attacks.

The experiments were repeated using the recycled photocatalyst over three degradation cycles, with no significant changes in photocatalytic activity (Figure 7.14).

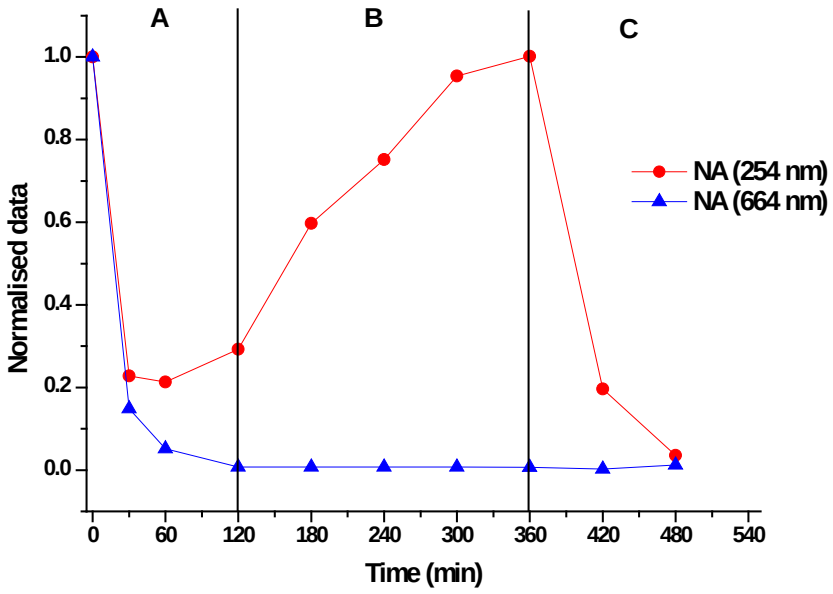

Figure 7.12. (A) Photocatalytic degradation of MB, (B) desorption of intermediate products and (C) Photocatalytic decomposition of intermediates ("NA" stands for normalised absorbance).

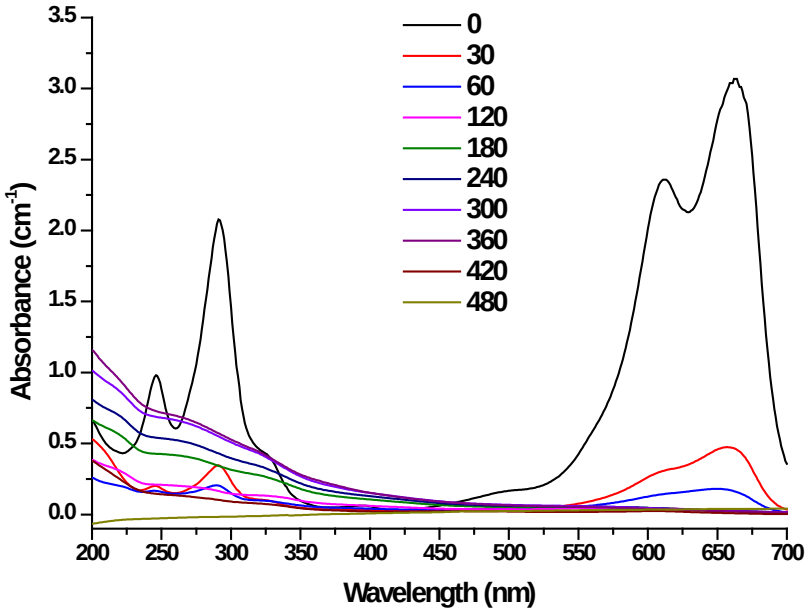

Figure 7.13. UV-vis spectrum for the photocatalytic degradation of MB showing three stages (stage 1: 0 to 120 min; stage 2: 121 to 360 min; stage 3: 361 to 480 min).

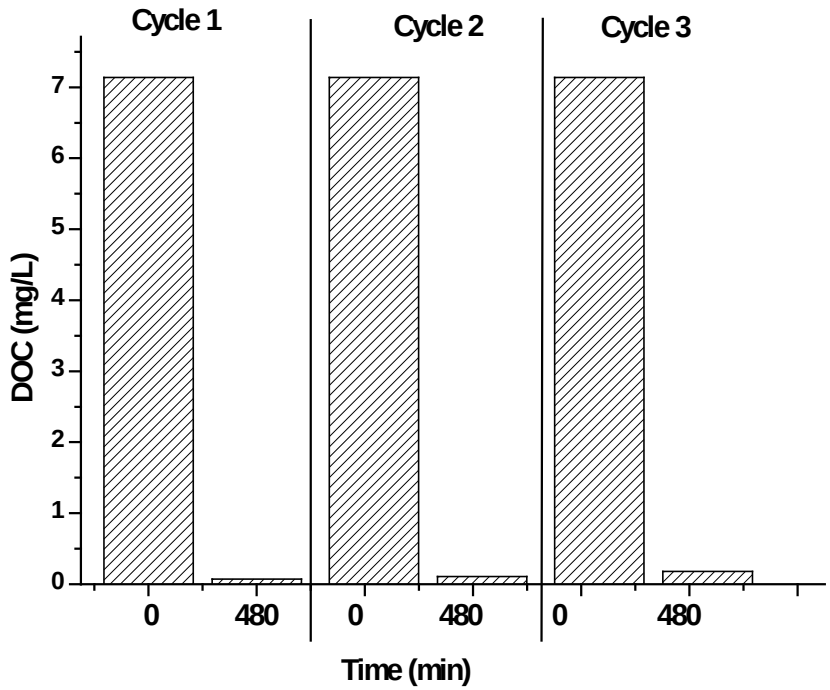

Figure 7.14. Photocatalytic stability of HTNF over three degradation cycles.

7.3.5. Settling Characteristic of HTNF

The high cost associated with the separation of titania at commercial scale has seriously retarded the use of industrial photocatalysis. At the end of photocatalysis, the facile recovery of the photocatalyst is very important for its reuse. A low cost catalyst separation process can be achieved by settling of particles. Accordingly, the settling characteristics of HTNF were also evaluated by comparing the sedimentation of HTNF to Degussa P25 in aqueous suspensions (Figure 7.15). The catalyst concentration was 0.5 g/L at a pH of 9. Rapid HTNF sedimentation was recorded by measuring the turbidity of decanted solution at fixed time intervals. About 80% turbidity removal was achieved after 30 min of settling that increased up to 90% after 2 h settling time. In contrast, the turbidity of P25 suspension did not change significantly. In a similar study, Xiong et al. (2011) reported 72% decrease in turbidity within 180 min settling time for titanate nanotubes. The rapid sedimentation of HTNF is another advantage for their industrial application in wastewater photocatalysis.

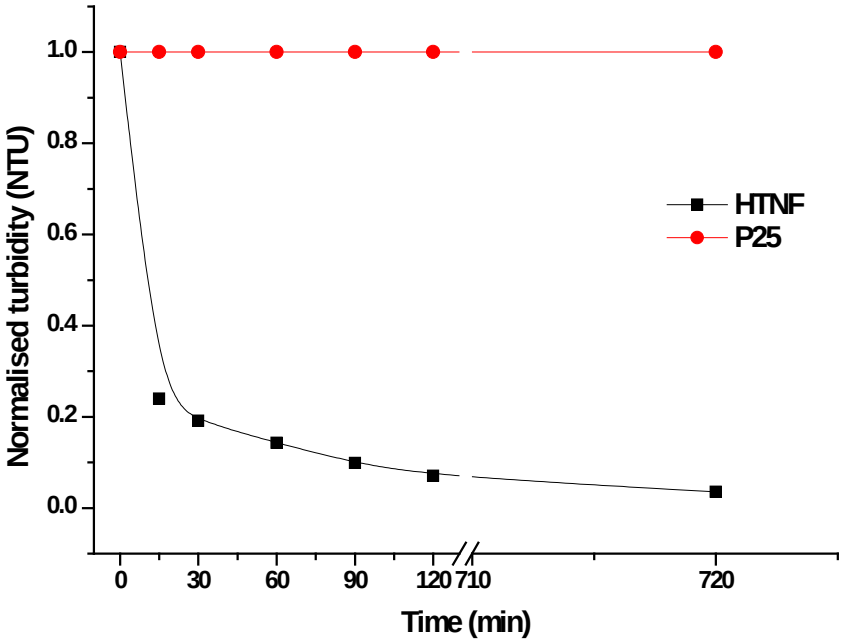

Figure 7.15. Normalised turbidity decrease in function of sedimentation time for HTNF and Degussa P25.

7.4. Conclusions

H-titanate nanofibres were synthesised by washing the Na-titanates (Chapter 6) in HCl solution at pH 2 for 60 min. The HTNF were characterised for changes in morphology by observing SEM pictures which revealed randomly dispersed nanofibres with an average diameter of 40-70 nm and few hundred nanometers in length. The nanofibres were negatively charged over a wide pH range and their PZC was found at pH 3.2. H^+ successfully replaced Na^+ in the nanofibres by ion exchange as confirmed by EDS measurements. The HTNF were mainly anatase with a surface area of 31.54 m^2/g, average pore volume of 0.10 cm^3/g and average pore size of 50 Å.

The adsorption of MB onto HTNF was examined by investigating the effect of HTNF loading, MB concentration, solution pH, and temperature on the adsorption capacity. The results showed that the adsorption of MB was promoted by high catalyst loadings, high pH (greater than the PZC) and temperature. The adsorption capacity increased from 2.55 mg/g at pH 3 to 16.57 mg/g at pH 9 after 30 min of contact, and from 16.57 mg/g at 25 °C to 19 mg/g at 45 °C. The adsorption data fitted well the Langmuir model for all operational conditions. In contrast, the Freundlich model only fitted the data obtained after varying the solution pH and temperature. The optimum operational conditions for the adsorption of MB onto HTNF were found at 0.5 g/L of photocatalyst, 10 mg/L MB, pH 9 and temperature of 45 °C.

The photocatalytic degradation of MB was studied under simulated solar light to study the effect of pH and light intensity. No significant differences were found for the discolouration of MB at pHs greater than the PZC. However, at pH 3, the decrease in MB adsorption significantly reduced its consecutive photocatalytic degradation. The increase in light intensity from 5 000 lx to 28 000 lx was found to increase 10 folds the discolouration of MB, according to the apparent degradation constant (k^1_a) obtained from the L-H model. In contrast, the DOC removal at the highest light intensity was only twice as good as the DOC removal found at the lowest light intensity (k^2_a).

The photocatalytic activity of the nanofibres was found stable after 3 degradation cycles using the adsorption/photocatalysis model. Moreover, the fibres were easily separated from the solution by settling at room temperature.

UNIVERSITY OF TECHNOLOGY, SYDNEY
FACULTY OF ENGINEERING AND INFORMATION TECHNOLOGY

CHAPTER 8

SYNTHESIS, CHARACTERISATION AND SEPARATION OF H-TITANATE NANOFIBROUS CHANNEL

8.1. Introduction

The fabrication of metal oxide nanostructures is getting more popular because of their unique features and their importance in many applications (Morgan et al. 2008). Titanium dioxide (TiO_2) is the far most widely used semiconductor/metal-oxide, which has been well studied for its potential use in several fields, mainly photocatalysis (Nahar et al. 2006; Chong et al. 2009). The production of titanate nanostructures has started with the pioneering work of Kasuga et al. (1999) with the hydrothermal treatment of nanoparticles in alkaline conditions. Since then, the hydrothermal process has been well investigated and the factors influencing the shape and phase of nanostructure formations are well known. The treatment of TiO_2 nanoparticles at temperatures between 100-200 °C in concentrated NaOH (10 N) induced morphology transfer to nanotubes, nanofibres and nanoribbons (Morgan et al. 2008). Yada et al. (2006) successfully produced titanate nanofibers by treating peroxo-titanic acid (titania and hydrogen peroxide) with NaOH, at lower temperatures (100 to 120 °C).

Generally, nanofibres synthesised by the hydrothermal route are randomly dispersed when examined under scanning electron microscope. Templates can be used to allow the arrangement of these fibres in organised manners and desired shapes. Template synthesis of semi-conductor material has been reported through the induced aggregation of nanoparticles on template surface (Lakshmi et al. 1997; Xiong et al. 2006). Lakshmi et al. (1997) have combined the concepts of sol-gel (using titanium isopropoxide) and template synthesis of nanomaterials to produce micro and nanostructures of inorganic oxide such as TiO_2. Xiong et al. (2006) synthesised TiO_2 nanofibres by controlled hydrolysis of titanium tetrachloride ($TiCl_4$) on mesoporous silica spheres. The diameter of nanofibres was highly correlated to the mesopore size of the molecular sieve and the hydrolysis rate. Biological structures found in nature are a rich source of neatly organised macro, micro and nanodesigns, which have been an inspiration for the development of novel materials with special features. The morphology of bioresources is diverse and multidimensional that has been acquired through a number of complex phenomena incorporating external physical and chemical adaptation of living organisms. In general, it is not easy to reach a uniform

and perfect replication of biotemplates. Therefore, the imitation of these structures has become a challenging task to scientists in the past few years. Since the successful work of Davis et al. (1997) in synthesising silica and zeolite from bacterial thread templates, many advances have been integrated into the fabrication process. Recently, the production of hierarchical nanomaterials was reported through the morphology transcription of various biospecies. A series of biological structures, such as green-leaf (Li et al. 2009a), eggshell (Su et al. 2008), cotton (Imai et al. 2002; Aminian et al. 2007), plant seeds (Han et al. 2010), and bamboo membrane (Li et al. 2007a) were successfully copied through morphology transcription.

Aminian et al. (2007) prepared titania nanofibres by adsorbing titania nanoparticles on cellulose fibres, followed by thermal removal of the cellulose template. The chain aggregation of nanoparticles on the cellulose fibres ensured the imitation of the cellulose nanomorphology. The morphology transcription of various templates including cotton was investigated by Imai et al. (2002). Hollow fibres (a few μm in diameter) were prepared by depositing TiO_2 on cotton fibres. The thickness of the deposition was kept above 500 nm to ensure the stability of the structure, and to prevent a subsequent collapsing of the fibre during calcination. These examples show that the organised titania nanofibres in desired shapes could be produced using simple methods. Moreover, the application of such photocatalytic structures in water treatment is promising since it might help in reducing the cost of photocatalyst separation process.

Humic acids (HA) are a group of complex natural organic compounds formed after the decay of dead plant and animal tissues and cells (Corin et al. 1996). They are undesirable products in water and considered as precursors of mutagenic products when water is chlorinated (Wiszniowski et al. 2002). Chlorine and Hypochlorites are commonly used biocides in water treatment to ensure disinfection. HAs bind with chlorine to form trihalomethanes, haloacetic acids and other chlorinated by-products, which are suspected to be carcinogenic (Al-Rasheed and Cardin 2003). Therefore, removing HAs from water is essential and can be achieved through heterogenous photocatalysis over TiO_2.

In this chapter, the possibility of using Australian merino wool microfibres as a natural biotemplate to produce novel titania micro channel was investigated. A simple method for producing nanofibrous channel by combining the production of nanofibres through the hydrothermal route and their deposition on wool microfibres as biotemplates was adopted. The synthesised photocatalysts were characterised for morphology, porosity, structure phase and chemical composition. The photocatalytic activity of the photocatalysts was assessed through the decomposition of humic acid under UV light, and its separation from the solution by sedimentation was also assessed.

8.2. Materials and Methods

8.2.1. Materials and Synthesis of Nanofibrous Channel

Merino clean wool fleeces (ultrafine fibres, 11.5 µm in diameter) were purchased from Virginia farm woolworks (Annangrove, NSW, Australia). The wool fleeces were used without any further treatment as biotemplates to produce the titanate micro-channel.

The typical synthesis of H-titanate nanofibres was described in details in Chapter 7. The as-prepared nanofibres were dispersed in pure water at a ratio of 1:50 (w/v) to get a colloidal H-titanate aqueous solution. The PZC of obtained fibres was previously found (Chapter 7) to be about pH 2.2. Nanofibrous channel was obtained by adsorption of H-titanate nanofibres on wool fibres by a simple impregnation method at room temperature. In a typical synthesis, 5 g of clean merino wool fleece were soaked in 100 ml of colloidal H-titanate solution (pH 3-4) for 2 h. After that, the impregnated fibres were dried in oven at 100 °C and heat-treated at 600 °C for 60 min to remove the organic template (Figures 8.1 and 8.2). The obtained powder will be denoted hereafter as NC-TiO_2.

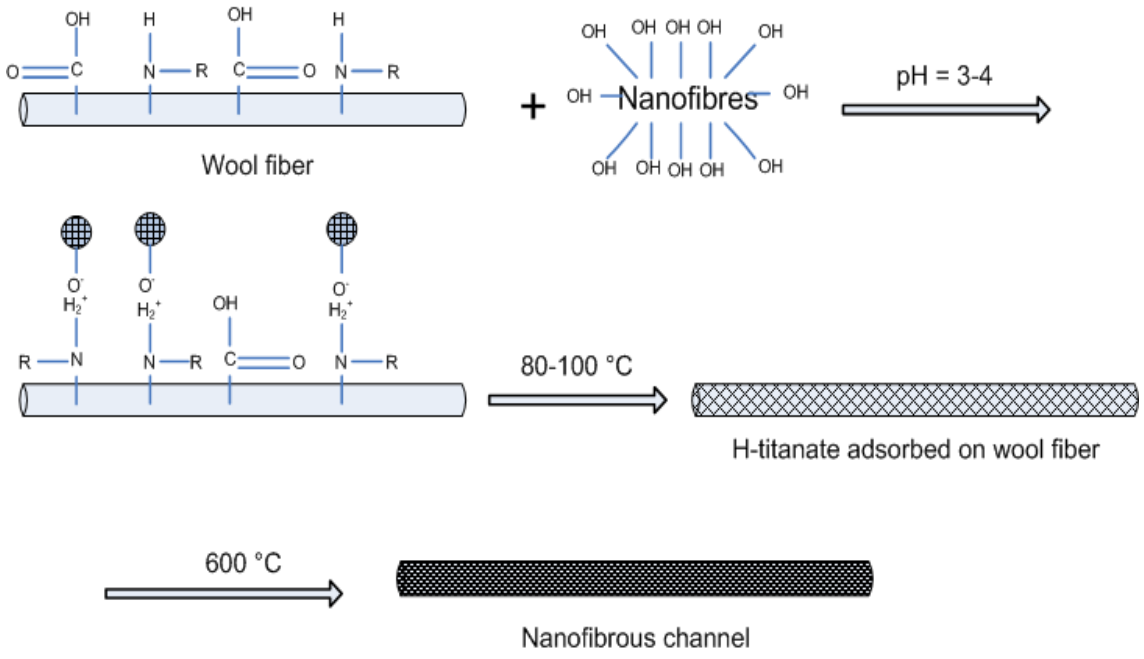

Figure 8.1. A proposed mechanism for NC-TiO_2 synthesis.

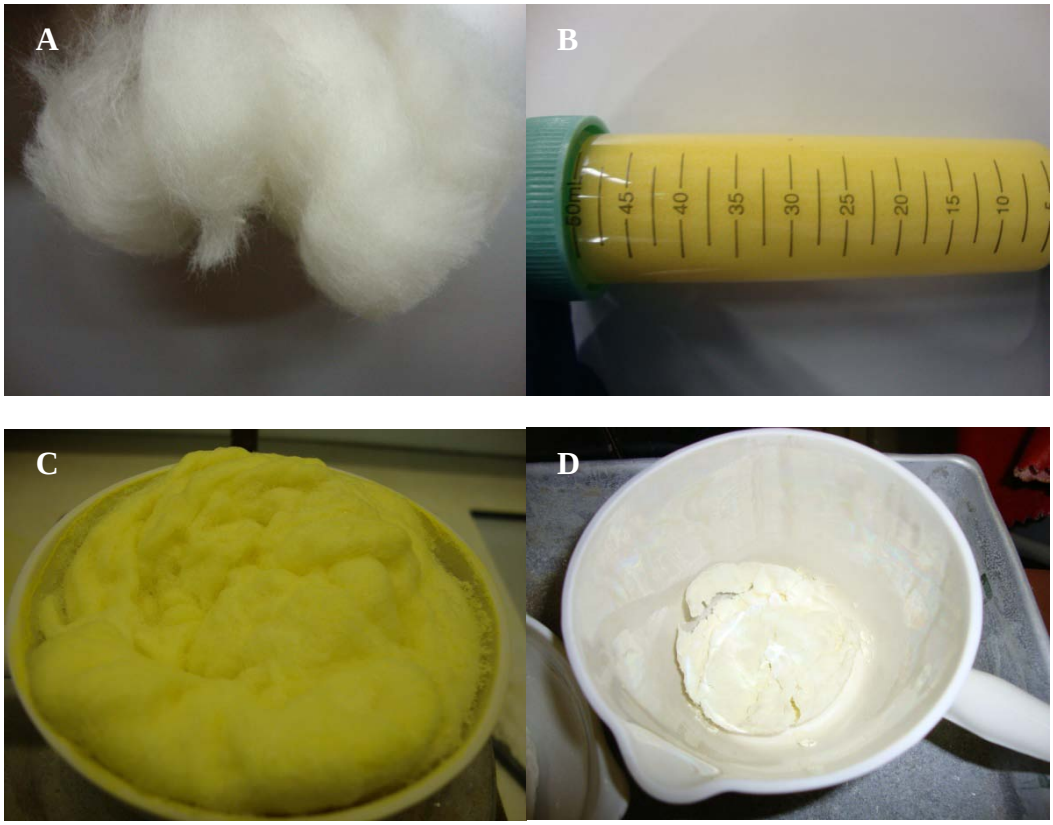

Figure 8.2. NC-TiO_2 synthesis steps. (A) wool fleeces, (B) H-titanate suspension, (C) adsorption of H-titanate on wool fibres, (D) NC-TiO_2 after calcination.

8.2.2. Characterisation of NC-TiO_2

Morphology and elemental composition analyses were carried out using a scanning electron microscope (SEM) equipped with an energy dispersive X-ray (EDX) detector (Zeiss Supra 55VP SEM) operating at 15-20 kV. X-ray diffraction (XRD) patterns were generated on a MDI Jade 5.0 (MaterialsData Inc., USA) X-ray diffractometer with Cu Kα radiation source. Data were measured within the range of scattering angle 2θ of 20-85º. Brunauer, Emmet and Teller (BET) surface area analyses were performed on an automated surface area analyser (Micromeritics Gemini 2360, USA) by means of nitrogen (N_2) adsorption-desorption. The BET surface area was determined by a multipoint BET method using the adsorption data in the relative pressure (P/P_0) range of 0.05-0.18. The mean pore diameter and the total pore volume of samples was determined from the desorption isotherm via the Barret-Joyner-Halender (BJH) model. X-ray photoelectron spectra were performed on a Multilab2000 (VG, UK) XPS instrument with a non-monochromatic Mg Kα

radiation at a residual gas pressure of below 10^{-9} Pa. Zeta potential was measured using the method previously described in Chapter 5.

8.2.3. Study of Photocatalytic Activity

A mass of 1 g HA powder was first dissolved in 62.5 ml of 0.1 N NaOH for 1 h under magnetic stirring and then the volume was topped to 1 L volume with MQ water to prepare a stock solution of 1 g/L (Doulia et al. 2009). The stock solution had a pH of 11.5 and was used for the preparation of 5, 10 and 20 mg/L HA solutions.

The photocatalytic activity of NC-TiO_2 was assessed in Photoreactor 2 (Chapter 3) using 2 L of 10 mg/L HA solution. After the addition of the desired amount of photocatalyst (0.5, 1, 1.5, 2 g/L), the slurry was mixed with a magnetic stirrer at 450 rpm for 30 min to ensure dark adsorption. Photocatalysis was carried out for 3 h at a stable temperature of 26 ºC. Slurry samples were collected at fixed time intervals, filtered through 0.45 µm (Whatman, regenerated cellulose) syringe membrane and analysed for HA decomposition for the UV absorbance at λ = 254 nm using a Shimadzu UV-Vis 1700 spectrophotometer. Dissolved organic carbon (DOC) removal in collected samples was monitored using a Multi N/C 3100 (Analytik Jena) DOC analyser. The effects of solution pH (4, 7 and 10) and HA concentration (5, 10 and 20 mg/L) were also carried out under the same experimental conditions described earlier and at 1g/L NC-TiO_2 loading.

The photocatalytic stability of NC-TiO_2 was studied by repeating the photodecomposition of HA for 4 cycles. The circled degradation was monitored by collecting samples at 0, 60, 120 and 180 min of photoreaction and analysed for the decrease of absorbance at UV_{254} and the removal of DOC. After each cycle, the clear supernatant was removed from the reactor vessel and the photocatalyst was recovered by centrifugation at 3000 rpm for 5 min. The used photocatalyst was washed with MQ water, separated by centrifugation and dried at 80 °C for the next degradation cycle.

8.2.4. Sedimentation Experiments

The sedimentation rate of the photocatalyst was assessed by monitoring the turbidity of the supernatant as a function of time. The experiments were carried out at 22 °C in conical shape 50 ml centrifuge tubes (11 x 2.5 cm, Axygen Sci.) at different powder loadings. The catalyst (0.5, 1, 1.5 and 2 g/L) was initially mixed with 50 ml of MQ water (pH 6.8) and left to settle at static conditions. Samples were collected at specific time intervals at 4 cm depth from the water surface. Turbidity was measured using a combined turbidity and chlorine meter (HI 93414, Hanna instruments, USA), which was calibrated using standard turbidity solutions.

8.3. Results and Discussion

8.3.1. NC-TiO_2 Characteristics

The zeta potential of NC-TiO_2 was monitored after changing the pH of the suspension from 2 to 10. First, 0.1 g of powder was suspended in 100 mL of MQ water under continuous magnetic stirring. The solution pH was adjusted by 0.1 N NaOH and 0.1 N HCl in order to monitor the changes in surface charges. Results are shown in Figure 8.3 and reveal that the point of zero charge slightly shifted towards higher pH compared to the H-titanate plot. This can be due to the evaporation of surface adsorbed peroxo complexes under calcination conditions leading to reduced proton requirement for surface neutralisation.

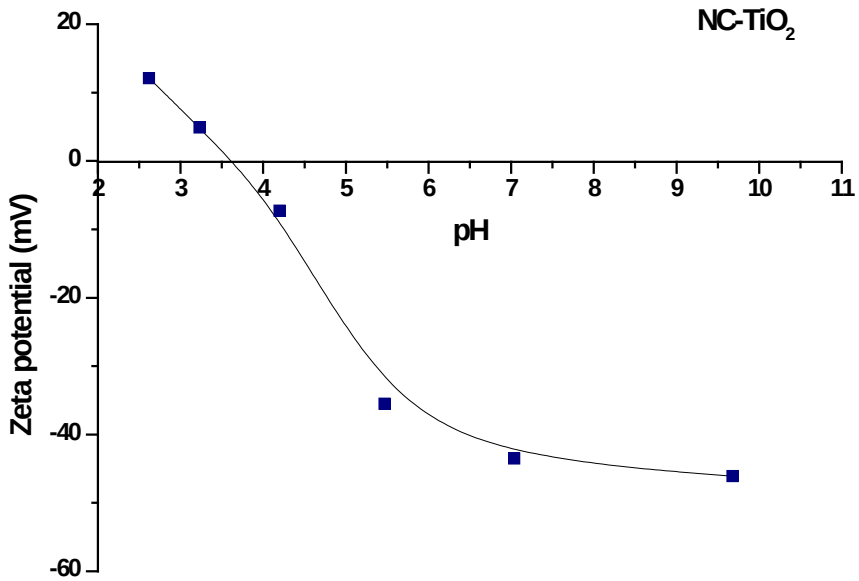

Figure 8.3. Zeta potential of NC-TiO_2 solution (1g/L).

Figure 8.4 shows the SEM micrographs of NC-TiO_2 obtained by the direct deposition of H-titanate nanofibres on wool microfibres. The negatively charged H-titanate nanofibers were adsorbed on the positively charged wool fibres before the latter was removed by calcination. The nanofibres were arranged in a micro-channel shape by morphology transcription of the wool fibre. Moreover, the colour change

from yellow to white (Figure 8.2) indicated the loss of adsorbed peroxo species during the calcination process as it has been mentioned before.

The micro-channels had lengths in the range of 50-70 µm (Figure 8.4A), inner diameters about 9.5 µm (Figure 8.4B), and wall thicknesses in the range of 1-2.6 µm (Figure 8.4C). The H-titanate nanofibres were of few hundred nanometres in length and had an average diameter of about 60 nm (Figure 8.4D). The inner diameter of the channel was equal to or less than the outer diameter of the wool fibres used as template. This was due to shrinkage of the deposited material during heat-treatment at 600 °C. Shrinkage and deformation were the main cause of morphology deformation reported by Imai et al. (2002) in preparing hollow microfibres using cotton as an organic template. Increasing the deposition thickness (wall thickness) to more than 500 nm reduced significantly the shrinkage and deformation associated with thin metal oxide deposition. In this study, the deposition was greater than the minimum recommended thickness. Therefore, no deformation was observed and the shrinkage could be due to the compression of nanofibres during calcination.

EDX measurements revealed that NC-TiO_2 was composed of carbon, titanium, oxygen and sulphur with atomic percentages of 2.81%, 28.75%, 68.25% and 0.19%, respectively. Sulphur and carbon are residual combustion compounds from burning wool biotemplate (Hodgkin et al. 1983; Hearle et al. 2001).

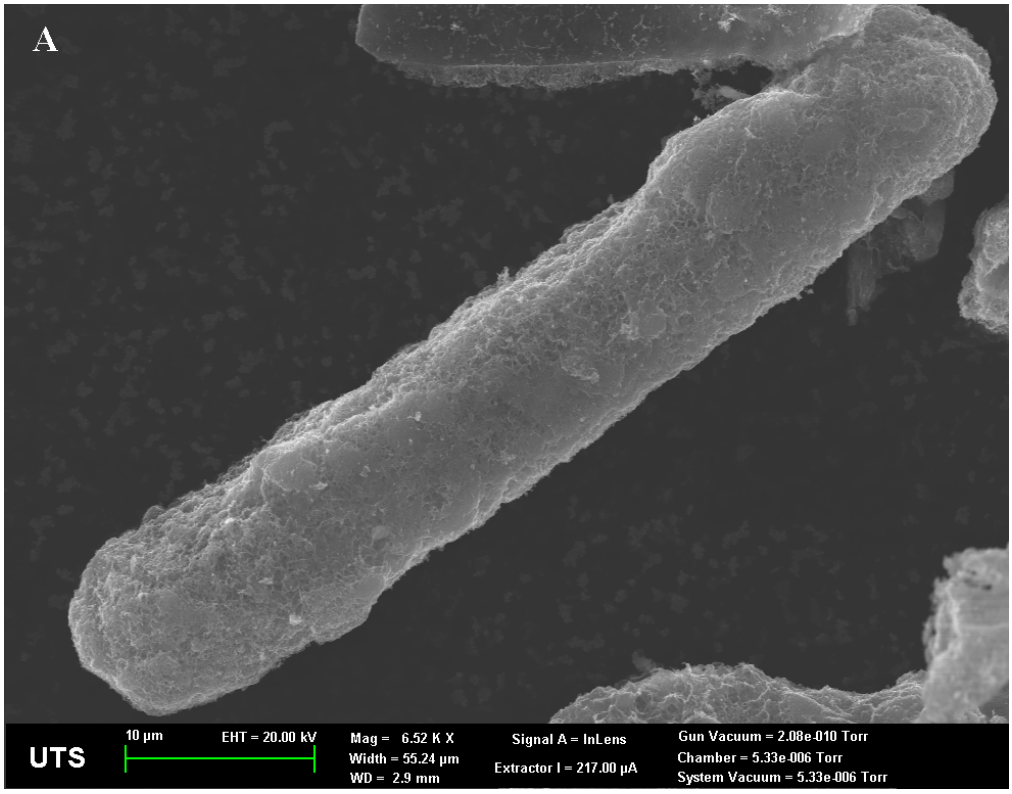
A
UTS
10 µm
EHT = 20.00 kV
Mag = 6.52 K X
Width = 55.24 µm
WD = 2.9 mm
Signal A = InLens
Extractor I = 217.00 µA
Gun Vacuum = 2.08e-010 Torr
Chamber = 5.33e-006 Torr
System Vacuum = 5.33e-006 Torr

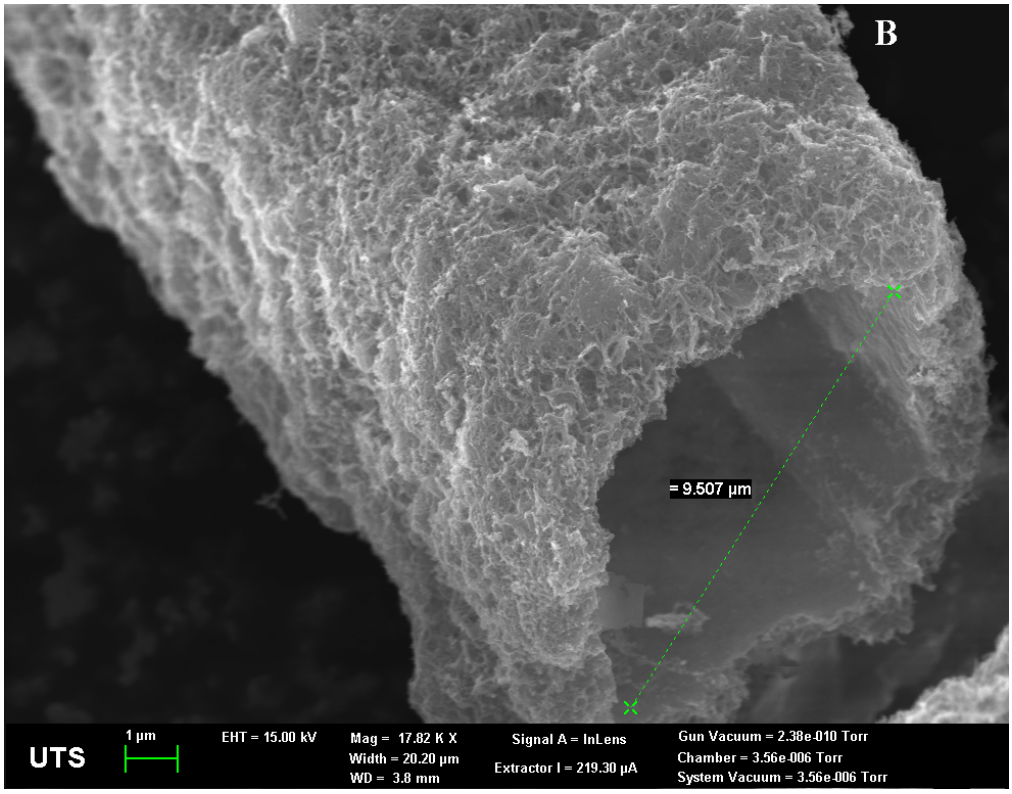
B
= 9.507 µm
UTS
1 µm
EHT = 15.00 kV
Mag = 17.82 K X
Width = 20.20 µm
WD = 3.8 mm
Signal A = InLens
Extractor I = 219.30 µA
Gun Vacuum = 2.38e-010 Torr
Chamber = 3.56e-006 Torr
System Vacuum = 3.56e-006 Torr

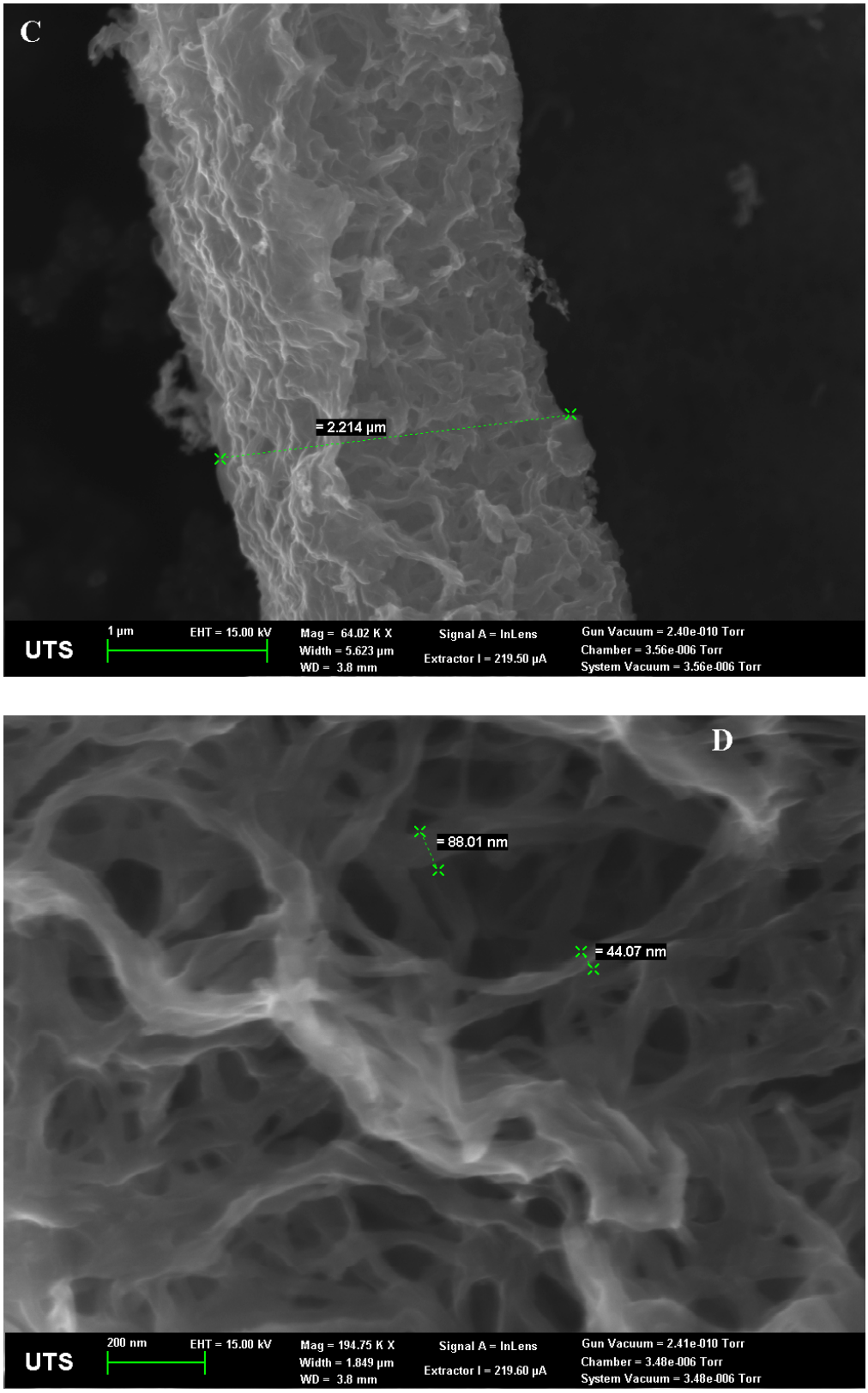

Figure 8.4. SEM micrographs of NC-TiO_2 at different magnifications; (A) full size, (B) internal diameter of the channel, (C) maximum wall thickness, (D) nanofibres dimensions.

XRD pattern of NC-TiO_2 was determined within the range of scattering angle 2θ of 20º-85º. Five primary peaks of anatase phase at 25.2°, 38°, 48.2° and 55° were identified indicating the crystal phase of NC-TiO_2. Small crystal size was observed due to the short calcination time of the as-prepared sample that could be increased by prolonging the calcination period (Figure 8.5).

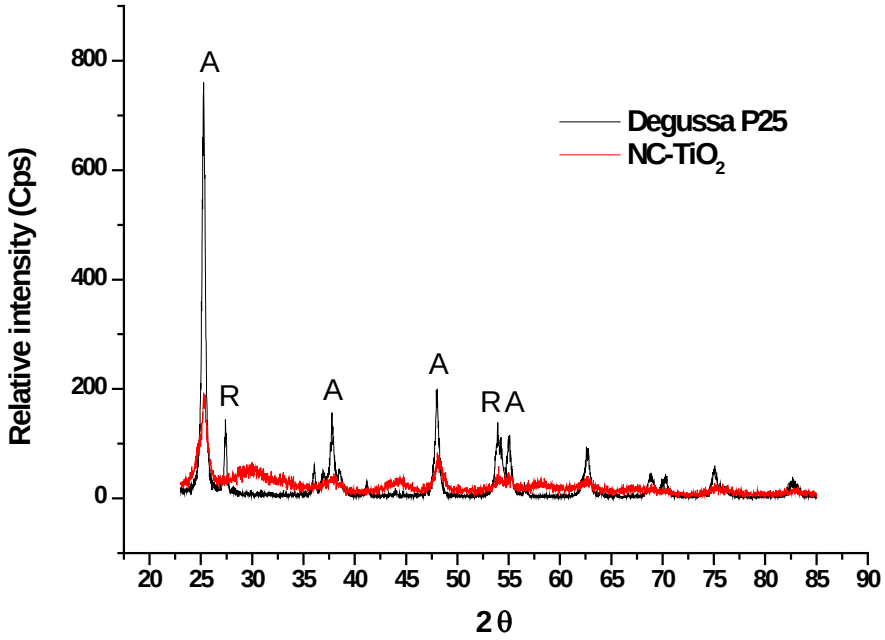

Figure 8.5. X-ray diffraction patterns showing NC-TiO_2 and Degussa P25. (A) anatase and (R) rutile.

The porous structure of NC-TiO_2 was characterised by N_2 adsorption-desorption measurements. At low relative pressure (P/P_0 below 0.2), the adsorption of N_2 was very low in the micropores indicating their small number. At high pressure (P/P_0 above 0.8), the isotherms exhibit a hysteresis loop of type H3, indicating the presence of mesopores (type IV isotherms). The shape of these isotherms suggested the presence and dominance of slit-shaped pores (Figure 8.6) (Bordère et al. 1998). The pore sizes at nanoscale were distributed between 2 nm and 45 nm with an average pore width of 9.6 nm. The BET specific surface area was 24.0 m^2/g and the total pore volume was 0.21 cm^3/g. The mesoporous structure of NC-TiO_2 could offer

more reaction sites for the photocatalytic decomposition of organic compounds, promote the diffusion of various reactants and enhance the overall photocatalytic reaction rate (Zhou et al. 2009; Han et al. 2010).

Wool fibres contain more than 170 different proteins composed of amino acids. Nitrogen atom is present in the amino group of amino acids while sulphur plays an important role in the intermolecular bonding through the disulfide crosslink. XPS measurements identified the presence of titanium, oxygen and sulphur in NC-TiO_2 (Figure 8.7). Two peaks located at 457.8 and 463.5 eV could be attributed to the Ti2p3 and Ti2p1 states, respectively (Sun et al. 2008). Two peaks at 529.4 and 531.2 eV in the O1s spectrum can be assigned to the lattice oxygen in TiO_2 and the adsorbed oxygen species (CO_2, SO_2, etc.), respectively (Lv et al. 2009; Han et al. 2010). S2p analysis indicated the presence of sulphur in the form of adsorbed SO_2 on the H-titanate surface based on the location of the S2p peak at 168.9 eV (Onishi et al. 1988; Zhang et al. 2004). No other peaks were detected to indicate the success of sulphur doping (peaks $\approx$ 161-163 eV). Moreover, the high resolution scanning of the elements indicated that no nitrogen doping was possible in the H-titanate network, suggesting that the nitrogen was lost during heat-treatment at 600 °C. Generally, TiO_2 is a stable compound and it is difficult to achieve successful non-metal doping when dealing with large size atoms without employing a mechanochemical process (Zhang et al. 2004).

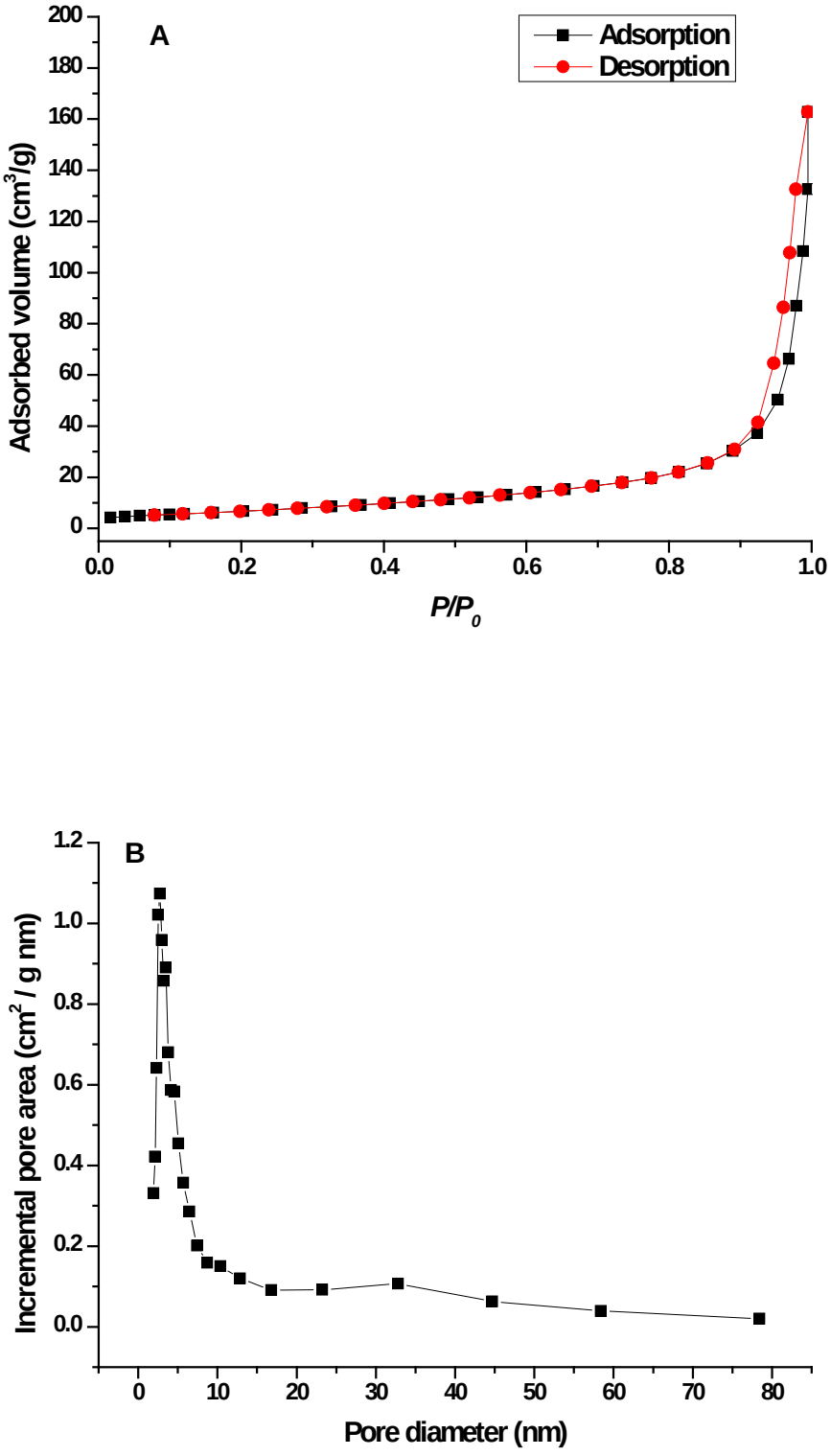

Figure 8.6. Nitrogen adsorption results of nanofibrous channels. (A) adsorption-desorption isotherms and (B) pore size distribution curve

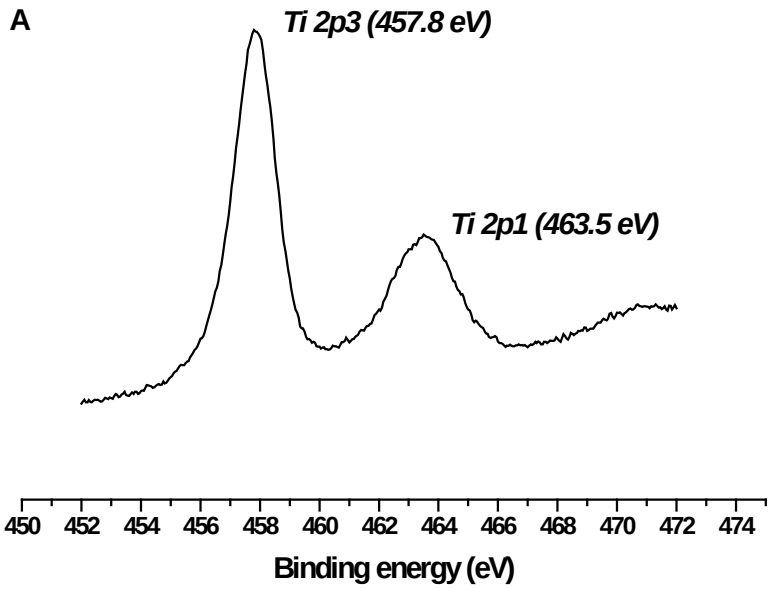
A
Ti 2p3 (457.8 eV)
Ti 2p1 (463.5 eV)
450 452 454 456 458 460 462 464 466 468 470 472 474
Binding energy (eV)

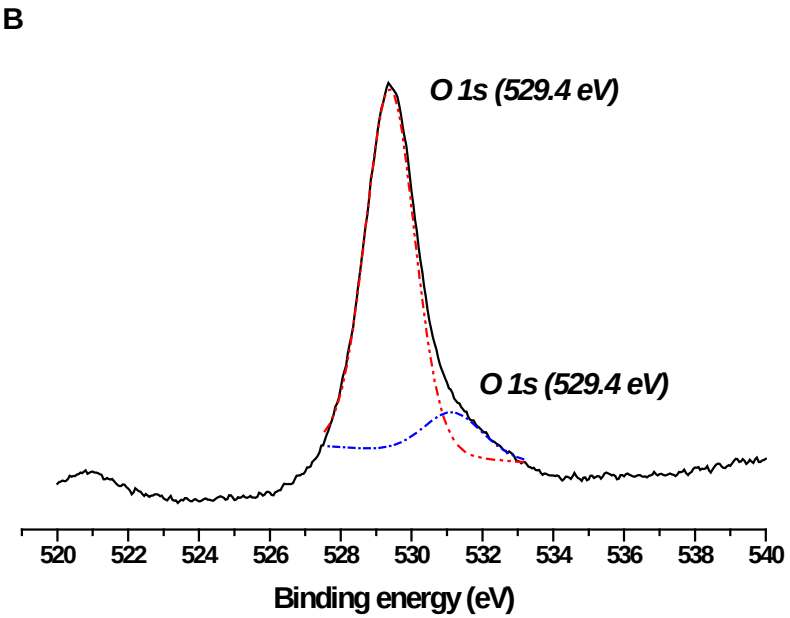
B
O 1s (529.4 eV)
O 1s (529.4 eV)
520 522 524 526 528 530 532 534 536 538 540
Binding energy (eV)

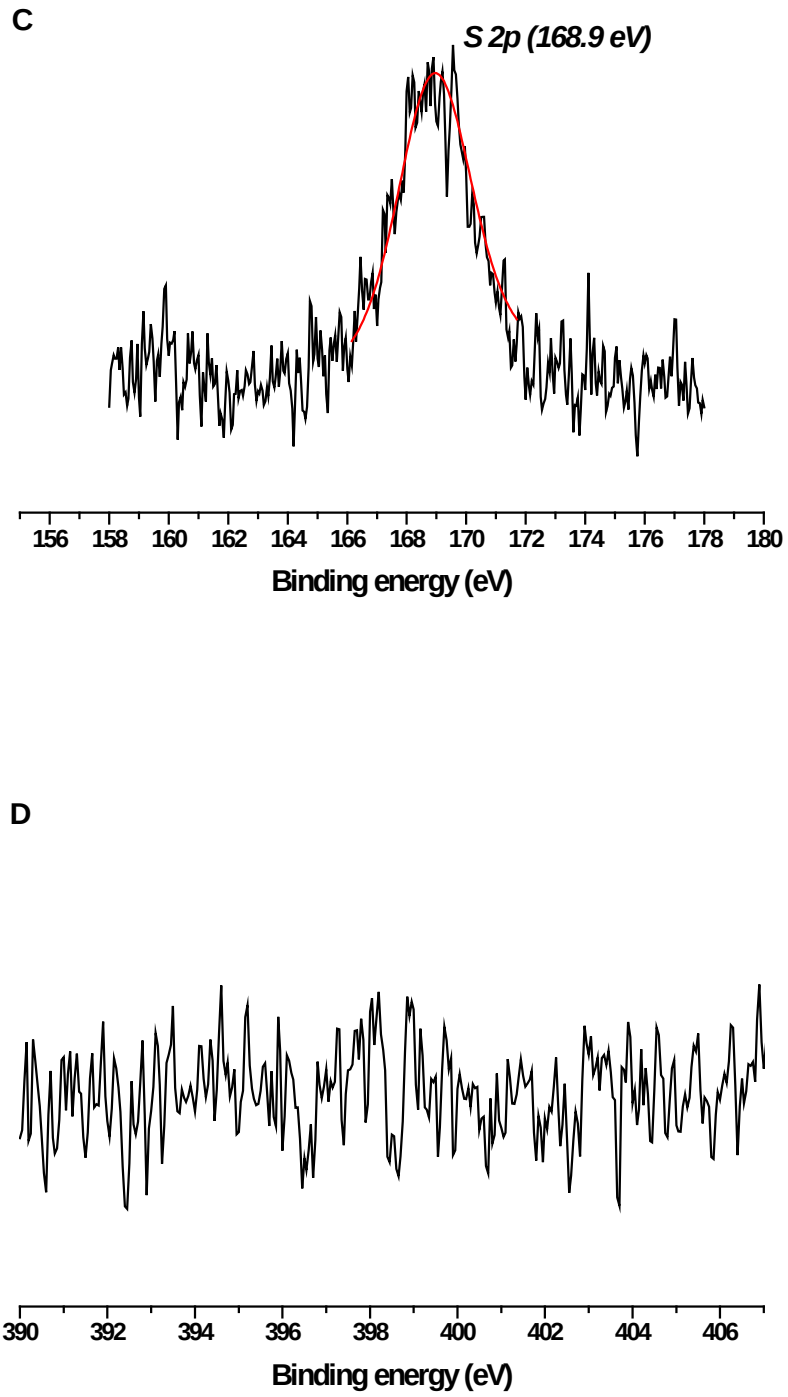

Figure 8.7. XPS patterns of nanofibrous channels. (A) high-resolution spectra of Ti2p; (B) high-resolution spectra of O1s; (C) high-resolution spectra of S2p and (D) high-resolution spectra of N1s.

8.3.2. Photocatalytic properties

8.3.2.1. NC-TiO_2 loading

The photocatalytic properties of NC-TiO_2 were initially studied for the removal of 10 mg/L of HA in an aerobic batch reactor under UVC irradiation. The removal of HA was monitored for the decrease in DOC and UV_{254} absorbance using different quantities of NC-TiO_2 catalyst (Figure 8.8). HA photolysis was carried out to detect the removal rate during UV irradiation of humic acid water. In the absence of NC-TiO_2, a total of 18% of aromatic moieties were removed after 3 h of UV-irradiation (photolysis) in the reactor setup used in this study, while DOC decreased by 11%. The difference between UV_{254} absorbance and DOC results can be attributed to the organic carbon content of photodegradation by-products resulting from the decomposition of aromatic moieties and colour adsorbing moieties under UV light irradiation (Corin et al. 1996; Wiszniowski et al. 2002; Al-Rasheed et al. 2003).

HA was allowed to adsorb on the surface of the catalyst for 30 min in dark that was sufficient to achieve adsorption equilibrium. DOC results showed 2.5, 6.5, 9 and 9.9% dark adsorptions at 0.5, 1, 1.5 and 2 g/L photocatalyst loadings, respectively. In contrast, NC-TiO_2 adsorbed 6.5, 9.4, 13 and 13.8% of aromatic moieties at 0.5, 1, 1.5 and 2 g/L photocatalyst loading, respectively.

Photocatalytic treatment was carried out under UV-irradiation for 3 h. Following UV irradiation, NC-TiO_2 (0.5 g/L) removed 74% of aromatic organic compounds after 3 h. At 1 g/L photocatalyst loading, the decrease in UV_{254} was 82%, improving to 83%, and 88 % for 1.5 and 2 g/L loadings, respectively. The DOC normalised reduction rates were 10-15% lower than the UV_{254} decrease rates. Based on the data presented in Figure 8.8, the linear relationship between DOC and UV_{254} can be expressed by the following equation (1 g/L NC-TiO_2):

UV_{254} (cm^{-1}) = 0.01 (DOC (mg/L)) – 0.006.
(R^2 = 0.974)

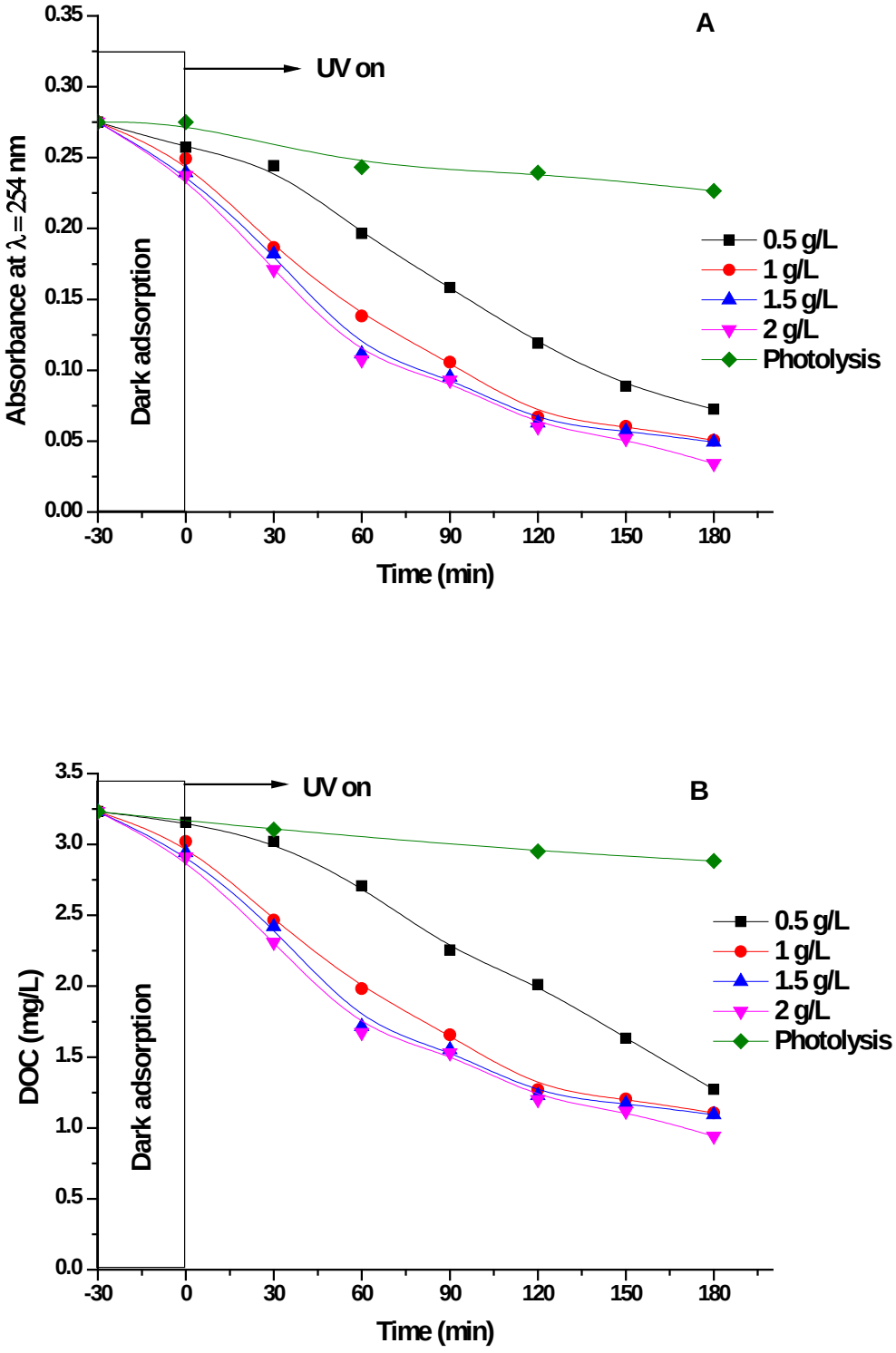

Figure 8.8. Photocatalytic removal of HA over different NC-TiO_2 loads (0.5, 1, 1.5 and 2 g/L) as revealed by absorbance at λ = 254 nm (**A**) and DOC measurement (**B**). Experimental conditions: pH 7; Air flow 0.6 L/min; temperature 26 °C; 3x15W UVC lamps.

The decomposition of HA on the surface of the photocatalyst is achieved after UV-irradiation through the heterogeneous photocatalysis phenomenon. The ultra-band gap illumination of TiO_2 produces hole pairs, h^+ and e^-, which can recombine to generate heat or migrate to the photocatalyst surface to initiate redox reactions. The degradation of HA can happen in two ways: i) dissolved oxygen (electron acceptor) combines with generated electron on the photocatalyst surface resulting in the generation of $OH^\bullet$ radicals, which attack free HA molecules; or ii) the positive hole (h^+) directly reacts with adsorbed HA acid molecules to generate oxidised products (Mills and Lee 2004). The advantage of using this process relies on the fact that the HA is mineralised to harmless by-products, minimal waste is generated compared to other chemical processes, and the photocatalyst can be recovered for reuse over many treatment cycles. A 1 g/L of NC-TiO_2 loading was used in the subsequent experiments as the experimental optimum value.

8.3.2.2. Effect of Initial HA Concentration

The concentration of organics may affect the decomposition rate through surface saturation, which becomes a barrier to the absorption of photons by TiO_2 (Arana et al. 2004). The selected HA concentrations were based on the concentration of HA usually found in natural waters. It was found that organics with complex molecular formula such as HA degrade to several intermediate/interim products before complete mineralisation (Corin et al. 1996). Therefore, at high initial HA concentrations, the decomposition of excessive intermediate products will be reducing the overall reaction rate.

The experiments were designed with an initial HA concentrations of 5, 10 and 20 mg/L. The adsorption equilibrium of HA onto NC-TiO_2 was reached after mixing the adsorbent and the adsorbate in dark for 30 min. A total of 8.5%, 9% and 4% of HA were adsorbed onto NC-TiO_2 for 5, 10 and 20 mg/L of initial HA concentrations, respectively. The relatively low adsorption could be mainly due to the like negative surface charges of HA and NC-TiO_2 at pH 7 (Figure 8.9).

The photocatalytic degradation of HA showed that the increase in the initial concentration did not have a significant effect on the performance of NC-TiO_2. UV_{254} absorbance results revealed that 87.2, 81.6 and 82% of HA were removed from the water at 5, 10 and 20 mg/L of HA concentrations, respectively. At 20 mg/L of HA, the initial degradation was fast (0-90 min) and became slower toward the end of the photoreaction (91-180 min). Similarly, at 5 and 10 mg/L of HA, the removal rate showed an expected exponential decrease. This was mainly due to the formation of degradation by-products which reduced the photocatalytic degradation of HA. The performance of NC-TiO_2 was stable at different initial organic loadings and showed similar removal rates. NC-TiO_2 can be successfully used for treating natural waters contaminated with HA of up to 20 mg/L.

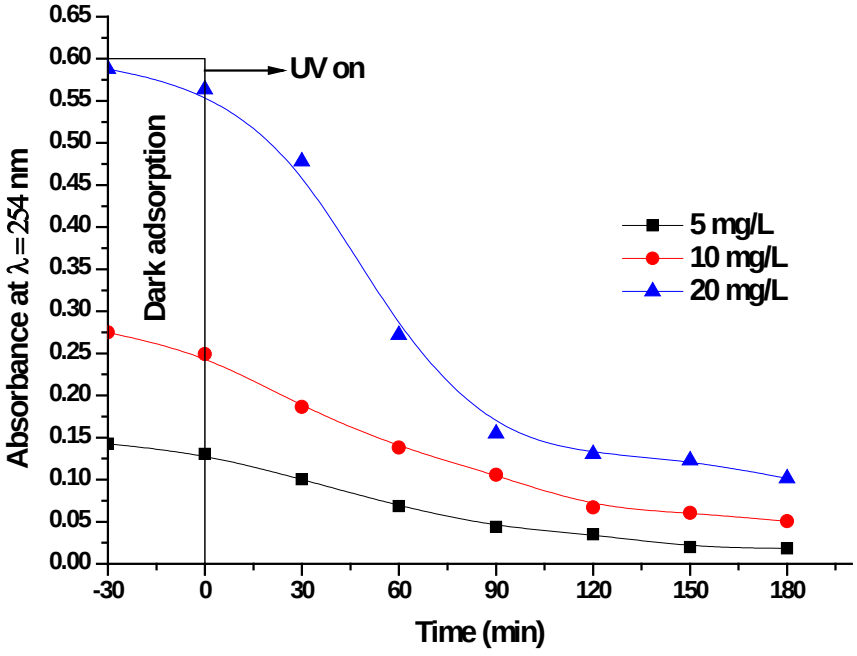

Figure 8.9. Photocatalytic removal of HA (5, 10 and 20 mg/L) over NC-TiO_2 as revealed by absorbance at λ = 254 nm. Experimental conditions: pH 7; Air flow 0.6 L/min; temperature 26 °C; 3x15W UVC lamps; NC-TiO_2 = 1g/L.

8.3.2.3. Effect of process pH

As expected, the pH of the water solution had a great impact on the surface charge of the photocatalyst and HA (Figure 8.10). The PZC of NC-TiO_2 was found to be around pH 3.8-4. We have measured the zeta potential of HA solution (10 mg/L) to determine the changes in surface charges. The surface charge of HA was found to be negative over a wide acidic pH range (1 to 6.5) and remained negative as expected in the alkaline region.

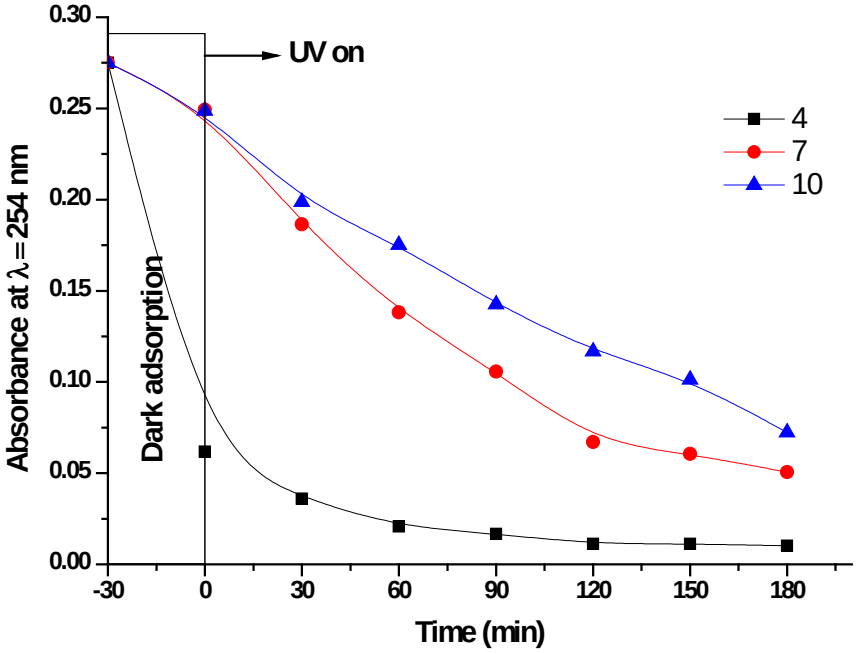

Figure 8.10. Photocatalytic removal of HA over NC-TiO_2 in different pH as revealed by absorbance at λ = 254 nm. Experimental conditions: HA = 10 mg/L, Air flow 0.6 L/min; temperature 26 °C; 3x15W UVC lamps; NC-TiO_2 = 1g/L.

The low adsorption at high pH was due to the repulsive forces among similarly charged particles of NC-TiO_2 and HA (carboxyl and phenolic hydroxyl groups). A decrease in pH from 10 to 7 has not significantly affected the adsorption (9.3% and 9.5% at pH 7 and 10, respectively) but enhanced the overall photodecomposition of HA. Usually, at high pH more hydroxyl ions are available in solution and the formation of hydroxyl radicals is promoted by the reaction of hydroxyl ions and a positive hole (Konstantinou and Albanis 2004). However, the repulsion of NC-TiO_2

and HA particles made the photodegradation at the photocatalyst surface difficult, while the active radicals could only attack the HA particles present at a very short distance from the photocatalyst surface. The increase in photocatalytic activity after pH decrease therefore was due to weaker repulsive forces which reduced the gaps between HA and NC-TiO_2 particles. This was confirmed by the results, whereby the further decrease in the pH till 4 resulted in a significant removal of HA by adsorption onto NC-TiO_2 (77%) due to the factors listed by Konstantinou and Albanis (2004), and also described earlier in Chapter 2. The neutralisation of surface charges on the NC-TiO_2 surface or the change in the ionisation state of NC-TiO_2 increased the affinity of adsorbing negatively charged particles. At lower pH values, the formation of reactive radical species by the reaction between H^+ ions and e^- played a major role in the photodegradation process.

8.3.3. Lifetime Cycle of NC-TiO_2

The photocatalytic stability of NC-TiO_2 was examined over four complete consecutive photodegradation cycles of HA (10 mg/L) solutions at 1 g/L photocatalyst loading (Figure 8.11). The photocatalyst was recovered after each cycle by sedimentation, washed with pure water, separated by centrifugation and dried at 80 °C before being used in the next cycle. NC-TiO_2 remained photoactive after the fourth cycle and the overall decrease of photocatalytic activity was less than 10% according to both UV_{254} and DOC data analysis results. Thus, the repeated use of NC-TiO_2 did not affect significantly its photocatalytic activity, and this product could be considered stable (Figure 8.12).

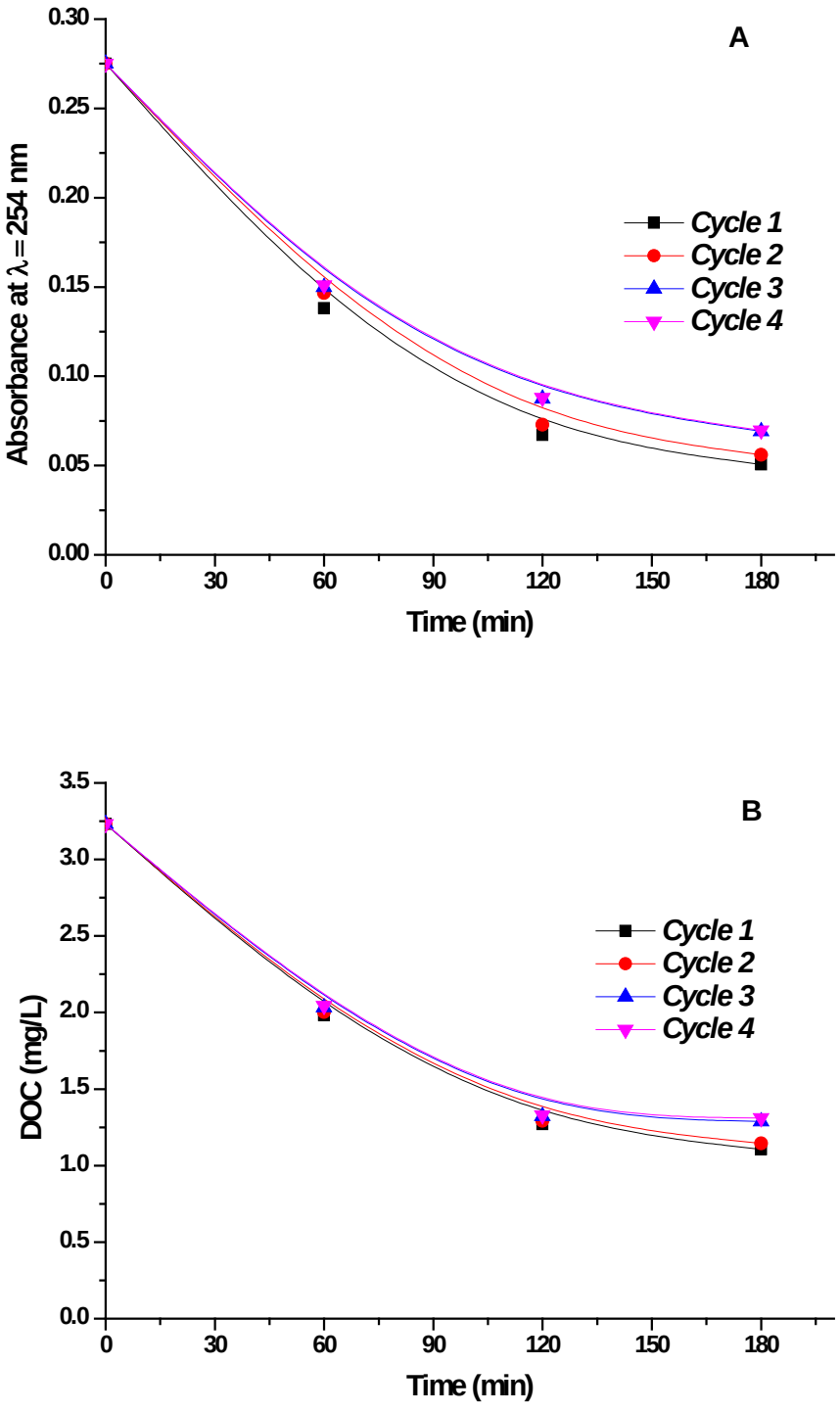

Figure 8.11. Photocatalytic lifecycle of NC-TiO_2 for the degradation of HA as shown by UV absorbance (A) at λ = 254 nm and DOC (B). Photodegradation reaction conditions: NC-TiO_2 load (1 g/L); pH 7; Air flow 0.6 L/min; temperature 26 °C; 3x15W UVC lamps.

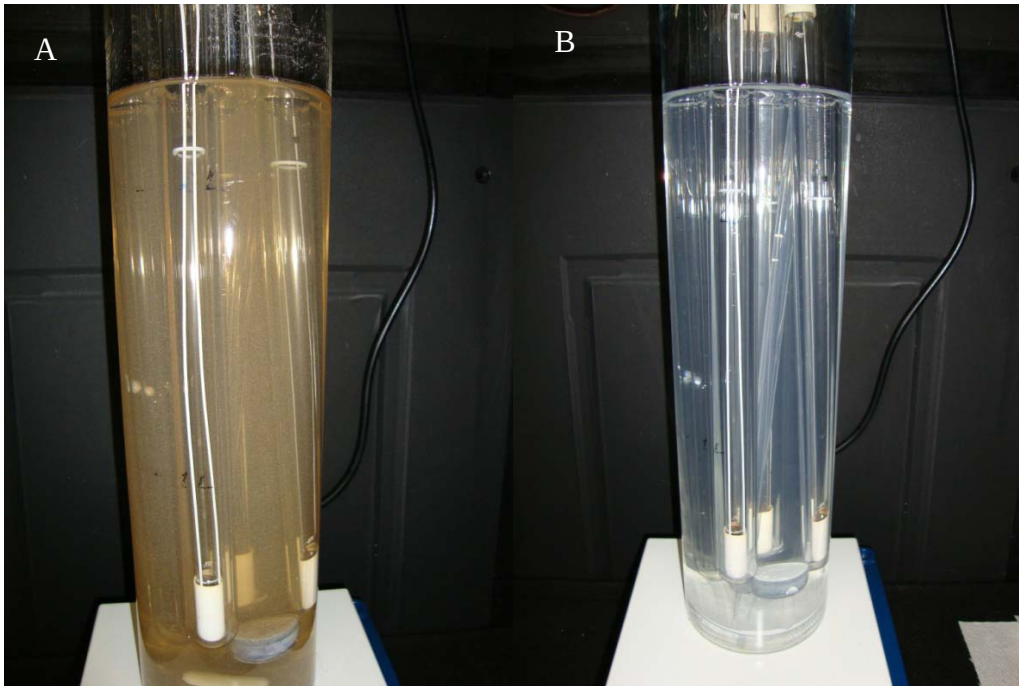

Figure 8.12. Initial (A, 10 mg/L) and treated (B) HA solutions after the fourth treatment cycle using 1 g/L NC-TiO_2 loading.

8.3.4. Settleability of NC-TiO_2

The separation of the fine photocatalyst particles from the treated solution is one of the drawbacks of slurry reactors that hinder industrial use. Although many scientists have suggested different methods to achieve effective separation, such as coagulation (Kagaya et al. 1999), ultrasonic irradiation (Suzuki et al. 2000), and cross-flow microfiltration (Xi and Geissen 2001); conventional sedimentation is the simplest and most favoured process (Vamanu et al. 2008; Allouni et al. 2009).

Several methods are being used to assess the efficiency of separation, such as measuring the interface level of the sediment (Chong et al. 2009), or the transmittance of the supernatant (Nahar et al. 2006). In this study turbidity measurement, which is used to assess the amount of suspended particles in solution, was used to monitor the sedimentation of NC-TiO_2 at different loadings (Figure 8.13). The decrease in solution turbidity indicated the better setteability of suspended particles. The initial turbidities were about 1000, 727, 496, and 294 NTU at 2, 1.5, 1, and 0.5 g/L photocatalyst loadings, respectively. The turbidity was decreased by 84

to 89% after 15 min in static conditions. As expected, the residual turbidity value increased with photocatalyst loading, due to increasing collision among particles and zone settling effects. Normalised values were calculated to identify the best loading/separation combination; and it was found that the 1 g/L loading optimum for photocatalysis also provided very effective solid separation.

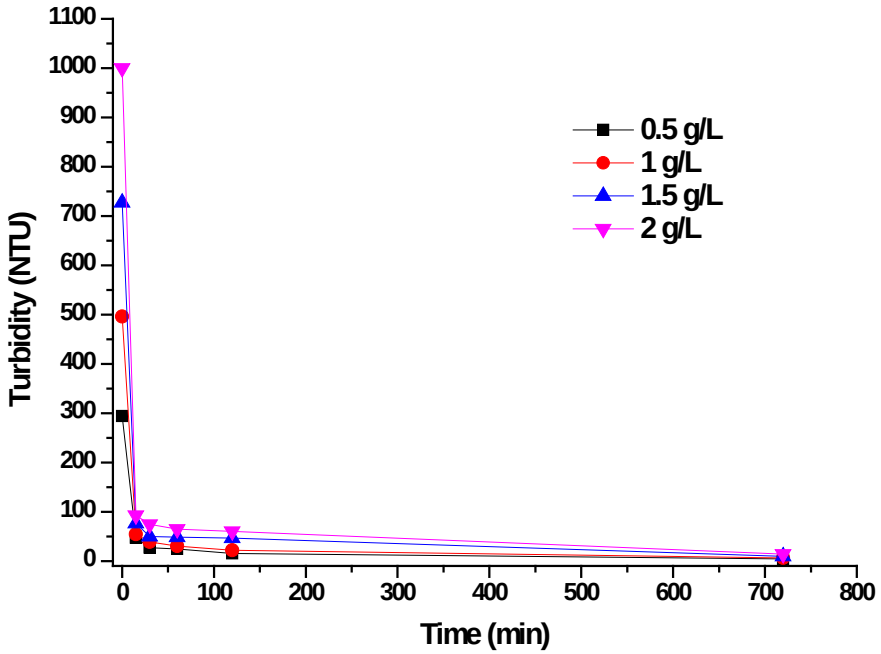

Figure 8.13. Decrease of the supernatant turbidity in function of time at different NC-TiO_2 loads.

8.4. Conclusions

The use of wool fibres as biotemplate for synthesising an easily separable photocatalyst was investigated in this chapter. NC-TiO_2 was successfully synthesised by depositing H-titanate nanofibres on wool fibres as biotemplate. The adsorption of nanofibers was assisted by surface charge differences between the H-titanate colloidal solution and the wool fibres.

The produced photocatalyst exhibited an anatase crystal phase and nanofibrous morphology of about 50 µm length and 9.5 µm in diameter. EDX analyses showed that sulphur and carbon as residual combustion products were present in the powder. Doping with non-metal elements, such as N and S, was not possible as revealed by XPS analysis. The specific surface area of NC-TiO_2 was about one half of P-25 (24.0` m^2/g) and the pore size distribution indicated a mesoporous porosity.

NC-TiO_2 was photoactive under UV-irradiation and removed 82% of aromatic organic compounds and 66% of DOC from HA aqueous solution using an aerobic batch reactor system at 1 g/L photocatalyst loading. The increase of NC-TIO_2 loading above 1 g/L had no significant effect on the photocatalytic performance. Similarly, the increase in HA concentration up to 20 mg/L did not show any negative effect on photocatalytic degradation in terms of overall removal rate.

The stability of the photocatalyst was monitored through the degradation of 10 mg/L of HA over four complete treatment cycles. At 1g/L of photocatalyst loading and a pH of 7, NC-TiO_2 showed photocatalytic stability as revealed by UV_{254} absorbance data analysis. The end cycle measurements found a very small (less than 10%) decrease of photocatalytic activity.

Solution turbidity measurements were used as a simple indicator to assess the settleability of suspended particles. NC-TiO_2 could be easily separated from the treated solution by sedimentation with very low supernatant turbidity.

UNIVERSITY OF TECHNOLOGY, SYDNEY
FACULTY OF ENGINEERING AND INFORMATION TECHNOLOGY

CHAPTER 9

CONCLUSIONS AND RECOMMENDATIONS

9.1. Conclusions

This research study presented the fabrication of novel titania-based nanomaterials, and examined their use in water purification. Material synthesis was achieved through the adoption of a modified peroxide method, to produce nano-assemblies of titanium oxide with some remarkable properties. The physico-chemical characterisation of these novel nanomaterials have been carried out to study changes in morphology, surface area and chemical composition. Finally, their use in water treatment applications was investigated using lab-scale photocatalytic systems.

9.1.1. The Synthesis of Nanomaterials from Peroxo-Titanium Complex

The use of peroxo-titanium complex (PTC) for advanced titanate nanomaterials synthesis showed that interesting nano-assemblies can be obtained at low hydrothermal temperatures, without using templates and surfactants as required in current methods. Several promising PTC routes have been explored to produce effective photocatalysts.

The dissolution of P25 at high pH (adjusted by NaOH or NH_4OH) was studied by measuring absorbance at 410 nm. In the case of NaOH base, both partial and full dissolution can be attained at high pH (12-13). In contrast, full dissolution was achieved at lower pH (>10) alkaline conditions using NH_4OH base. The full dissolution of titania was not affected by the type of base at very high pH. The morphology of nanomaterials was not affected by the dissolution rate of P25. Microspheres composed of many nanoparticles were observed in both conditions. XRD analyses showed that the partially dissolved Na^{12} has an anatase structure while Na^{18}, A^{8}, and A^{20} were amorphous. The use of NaOH base facilitated the synthesis of sodium-titanate microspheres, while nitrogen doped photocatalysts were obtained through the same method, simply by using ammonium hydroxide base.

9.1.2. Nitrogen-doped and Silver Co-doped photocatalysts for Visible and Solar Light Photocatalysis

The synthesis of nitrogen-doped (TiO_2-N) and silver co-doped (TiO_2-N-Ag) photocatalysts was achieved by adopting a modified version of the method described in Chapter 4. To minimise the loss of N due to annealing, crystallised powders were obtained by ageing the

PTC solution at remarkably low (75 °C) temperature for 24 h. The measured points of zero charge (PZC) were around 3.6 and 4.2 for TiO_2-N and TiO_2-N-Ag, respectively. The obtained nanomaterials were characterised by relatively high BET surface areas, 144.6 and 92.9 m^2g^{-1} for TiO_2-N and TiO_2-N-Ag, respectively, twice and thrice larger than that of the P25 precursor (50 m^2/g). Structural changes regarding the shapes and sizes of nano-assemblies were detected by SEM and TEM. The ageing of samples resulted in anatase crystals with elongated rod and needle-like forms. The doped photocatalysts had a mean mesopore sizes of 6.5 nm and 5.4 nm for TiO_2-N-Ag and TiO_2-N, respectively. Nitrogen doping and nitrogen-silver co-doping were successfully detected by XPS. According to binding energy results, these photocatalysts have O–Ti–N bonds and silver in ionic state (Ag^{3+} or AgO).

Batch experiments were carried out to assess the photocatalytic activity of both photocatalysts under visible light irradiation, using MB as a model pollutant. The visible light responsive photocatalysts were effective in adsorbing a large portion of MB (40% for TiO_2-N and 67% for TiO_2-N-Ag) and also capable of its destruction by photo-oxidation. Silver co-doped nanoneedles showed better apparent photocatalytic activity due to the role of Ag that acted as electron sink (promoting electron-hole separation). The photocatalysts were also tested under simulated solar light spectra. Both photocatalysts fully decolourised MB within 2 h of irradiation, and the co-doped product matched the performance of P25 in terms of demineralisation efficiency.

9.1.3. Adsorption of Methylene Blue and its Photodecomposition using Na-Titanate Microspheres under UV Light

Na-titanate mesoporous microspheres (NT-25), which were described in Chapter 4, showed smooth surface and average diameter of 700 nm. In contrast, larger size nanofibrous microspheres resulted from the hydrothermal treatment of the solution at 80 °C for 24 h (NT-80). The nanofibrous microspheres were formed from the curling and interconnection of nanofibres. The nanofibres were a few hundred nanometres long and had diameters in the range of 40-70 nm. The zeta potential measurements of photocatalysts revealed that the point of zero charge (PZC) was not affected by hydrothermal treatment at 80 °C but increased after the calcination of powders. This was caused by the liberation of peroxo complexes adsorbed on the surface of the photocatalysts. The surface area of NT-25 and NT-80 was 24.4 m^2/g and

64.8 m^2/g, respectively. The samples showed an expected decrease in BET surface areas after calcination.

The microspheres showed high affinity for adsorbing MB. In a short 30 min adsorption time, complete decolourisation was achieved both for NT-80 and NTC-80 at 0.5 g/L catalyst loading. This finding was mainly due to their higher surface area compared to the NT-25 and NTC-25 products. The binding of Na^+ and peroxo groups in NT-25 and NTC-25 had detrimental effect on the adsorption of the cationic dye MB through surface saturation, which decreased the number of available adsorption sites.

The photocatalytic activity of microspheres was tested in a batch reactor irradiated by UV light. Dye decolourisation and DOC removal showed that the microspheres were photoactive. The increase of sulphate concentration was studied to assess the mineralisation of the pollutant, confirming that the removal was due to photo-oxidative degradation. The microspeheres showed photocatalytic stability after five complete treatment cycles with insignificant decrease in performance. NT-80 and NTC-80 were easily separated from the solution by settling, with a 90% decrease in solution turbidity. In contrast, NT-25 and NTC-25 were difficult to separate, showing high residual solution turbidity after 2 h of settling.

9.1.4. Kinetics of Adsorption of Methylene Blue over Hydrogen-Titanate Nanofibres and its Photodecomposition under Solar Light

The Na-titanates microspheres (Chapter 6) were washed in HCl solution at pH 2 for 60 min to produce hydrogen-titanate nanofibres (HTNF). The nanofibres were randomly dispersed (not grouped in microspheres) and conserved their typical fibrous morphology. They were negatively charged over a wide pH range (PZC at pH 3.2), and were comprised mainly of crystalline anatase with a surface area of 31.5 m^2/g, average pore volume of 0.10 cm^3/g and average pore size of 50 Å.

The adsorption of MB onto HTNF was promoted by high catalyst loadings, high pH (greater than the PZC) and temperature. The adsorption capacity increased from 2.55 mg/g at pH 3 to 16.57 mg/g at pH 9 after 30 min of contact, and from 16.57 mg/g at 25 °C to 19 mg/g at 45 °C. The Langmuir model was adequate for fitting the adsorption data for all operational

conditions. The optimum operational conditions for the adsorption of MB onto HTNF were found at 0.5 g/L of photocatalyst, 10 mg/L MB, pH 9 and temperature of 45 °C.

No significant differences were found for the photocatalytic discolouration of MB at pH values greater than the PZC under simulated solar light irradiation. In contrast, the decrease of pH below the PZC decreased MB adsorption and significantly reduced its photocatalytic degradation. The increase in light intensity from 5 000 lx to 28 000 lx was found to increase 10 folds the discolouration rate of MB, according to the apparent degradation constant (k^1_a) obtained from the L-H model. In contrast, DOC removal at the highest light intensity was only twice as high as DOC removal at the lowest light intensity (k^2_a). The photocatalytic stability of HTNF was tested over three complete degradation cycles using the dark adsorption/photocatalysis procedure. No reduction in activity was recorded when this process was adopted. Finally, the effective separation of nanofibres was achieved by gravity settling with low residual solution turbidity.

9.1.5. Degradation of Humic Acid over Nanofibrous Channel under UV light

Wool microfibres were used as biotemplate for synthesising an easily separable photocatalyst. NC-TiO_2 was successfully synthesised by depositing H-titanate nanofibres (Chapter 7) on wool fibres. The adsorption of nanofibres was assisted by surface charge differences between the H-titanate colloidal solution and the wool fibres.

The produced photocatalyst exhibited an anatase crystal phase and nanofibrous morphology of about 50 μm length and 9.5 μm in diameter. EDX analyses showed that sulphur and carbon (residual combustion products) also were present in the powder. Doping with non-metal elements, such as N and S, was not possible as indicated by XPS analysis. The specific surface area of NC-TiO_2 was about one half of P-25 (24.0 m^2/g) and the pore size distribution indicated a mesoporous porosity.

The degradation of HA solution was achieved in an aqueous solution using an aerobic batch reactor system at 1 g/L photocatalyst (optimum) loading irradiated by UV lamps. A total of 82% of aromatic organic compounds and 66% of DOC were removed after 3 h of photocatalysis. The increase in HA concentration up to 20 mg/L did not show any negative effect on the photocatalytic degradation in terms of overall removal rate. The decrease of HA

solution pH increased the adsorption of HA onto NC-TiO_2 from 9.3% at pH 7 to 77% at pH 4. This finding indicated that the adsorption was dominated by electrostatic attractions.

The stability of the photocatalyst was tested over three complete degradation cycles (NC-TiO_2 = 1g/L, pH 7, HA = 10 mg/L). Less than 10% decrease of photocatalytic activity was recorded after the third cycle. Finally, NC-TiO_2 could be easily separated from the treated solution by sedimentation with very low supernatant turbidity.

9.2. Recommendations

The fabrication of advanced nanomaterials using the peroxide method was successful. However, some aspects such as the type of base and the hydrothermal treatment temperatures and calcination temperatures could not be explored in this study, and should be further investigated. Additionally, the nanomaterials produced in this research study should be tested in different operating systems and under different conditions such as the use of different type of pollutants, different reactor designs and natural solar light. Below are some recommendations for further studies:

- The dissolution of tungsten (W) in H_2O_2 can be used to produce co-doped photocatalysts by following the procedure detailed in Chapter 4 and 5. N/W co-doped TiO_2 may be especially suitable for indoor pollutant degradation under visible light.
- Preliminary investigations indicated that the novel photocatalysts produced in this study are suitable for the complete degradation of some PPCP (Pharmaceutical and Personal Care Products). However, further investigations are required for process optimisation and improvement.
- The results showed that the photocatalysts are negatively charged over a wide pH range, therefore very effective in removing cationic dyes from industrial effluent at lower pH values. Moreover, they can be easily regenerated by simple exposure to solar light, and then reused in consecutive treatment cycles.

UNIVERSITY OF TECHNOLOGY, SYDNEY

FACULTY OF ENGINEERING AND INFORMATION TECHNOLOGY

APPENDICES

Appendix A

List of publications

- **Chapter 2:**

El Saliby I., Shon H.K., McDonagh A., Visible-light active doped titania for water purification: nitrogen and silver doping, In: Nanotechnology for water and wastewater treatment, IWA Publishing, (In Press) 2012.

El Saliby I., Shon H.K., Erdei L. (2012) Water reclamation by heterogeneous photocatalysis (In preparation).

El Saliby I., Shon H.K., Kandasamy J. and Vigneswaran S., Nanotechnology for wastewater treatment: in brief, In: Waste Water Treatment Technologies, Encyclopedia of Life Support Systems (EOLSS), Eolss Publishers, Oxford, UK 2008.

- **Chapter 4:**

El Saliby I., Shon H.K., Erdei L., Kim J.-B. and Kim J.-H. (2011) Co-doped Photocatalyst Nanomaterials for Effective Utilisation of Solar Radiation. The 8th Asia Pacific Conference on Sustainable Energy & Environmental Technologies (APCSEET 2011), University of Adelaide, Adelaide, South Australia, AUSTRALIA.

- **Chapter 5:**

El Saliby, I., Erdei, L., Shon, H.K. and Kim, J.-H. (2011) Development of visible light sensitive titania photocatalysts by combined nitrogen and silver doping. Journal of Industrial and Engineering Chemistry 17(2), 358-363.

El Saliby I., Erdei L., Shon H.K., Kim J.-H. (2009) Development of visible light sensitive titania photocatalysts by combined nitrogen and silver doping. The

7th Asia Pacific Congress on Sustainable Energy and Environmental Technologies (APCSEET 2009), Qingdao, CHINA.

- **Chapter 6:**

El Saliby, I., Erdei, L., Shon, H.K., Kim, J.B. and Kim, J.-H. (2011) Preparation and characterisation of mesoporous photoactive Na-titanate microspheres. Catalysis Today 164(1), 370-376.

El Saliby I., Erdei L., Shon H.K., Kim J.B., Kim J.-H. (2010) Photoactive Na-Titanate nanospheres. Sixth Tokyo Conference on Advanced Catalytic Science and Technology & Fifth Asia Pacific Congress on Catalysis (TOCAT6/APCAT5 2010), Sapporo, JAPAN.

- **Chapter 7:**

El Saliby I., Erdei L., Kim J.-H., Shon H.K. (2012) Adsorption and photocatalytic degradation of Methylene Blue over Hydrogen-titanate nanofibres produced by a peroxide method (Submitted to Water Research).

- **Chapter 8:**

El Saliby, I., Shon, H.K., Kandasamy, J. and Kim, J.-H. (2011) Synthesis, characterisation and separation of photoreactive Hydrogen-titanate nanofibrous channel. Separation and Purification Technology 77(2), 202-207.

El Saliby I., Shon H.K., Kandasamy J., Kim J.-H. (2010) Synthesis and photoactivity of titania nanofibers produced by morphology transcription of wool. Challenges in Environmental Science and Engineering (CESE 2010), Cairns, Queensland, AUSTRALIA.

Appendix B

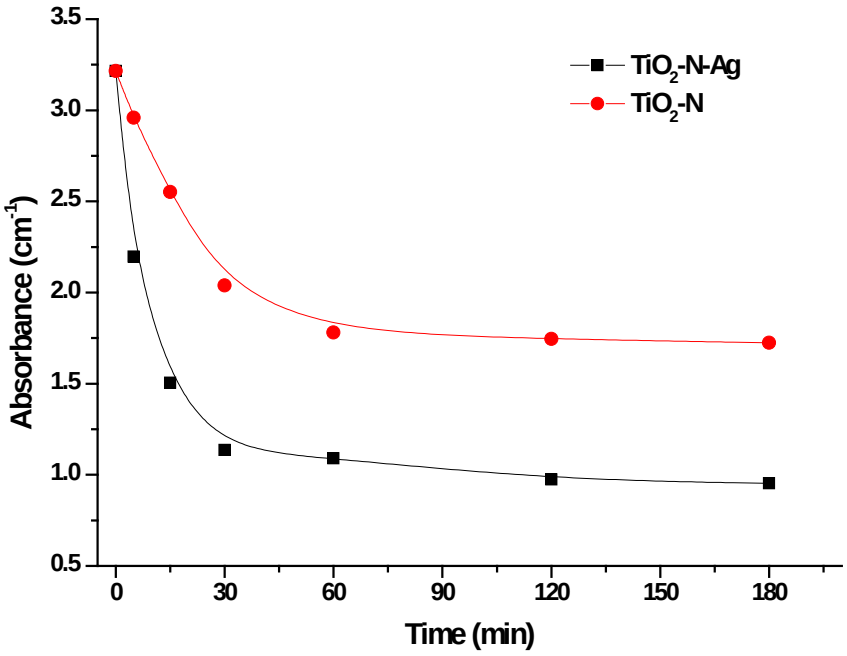

Figure B.1. Adsorption of MB onto TiO_2-N and TiO_2-N-Ag.

Appendix C

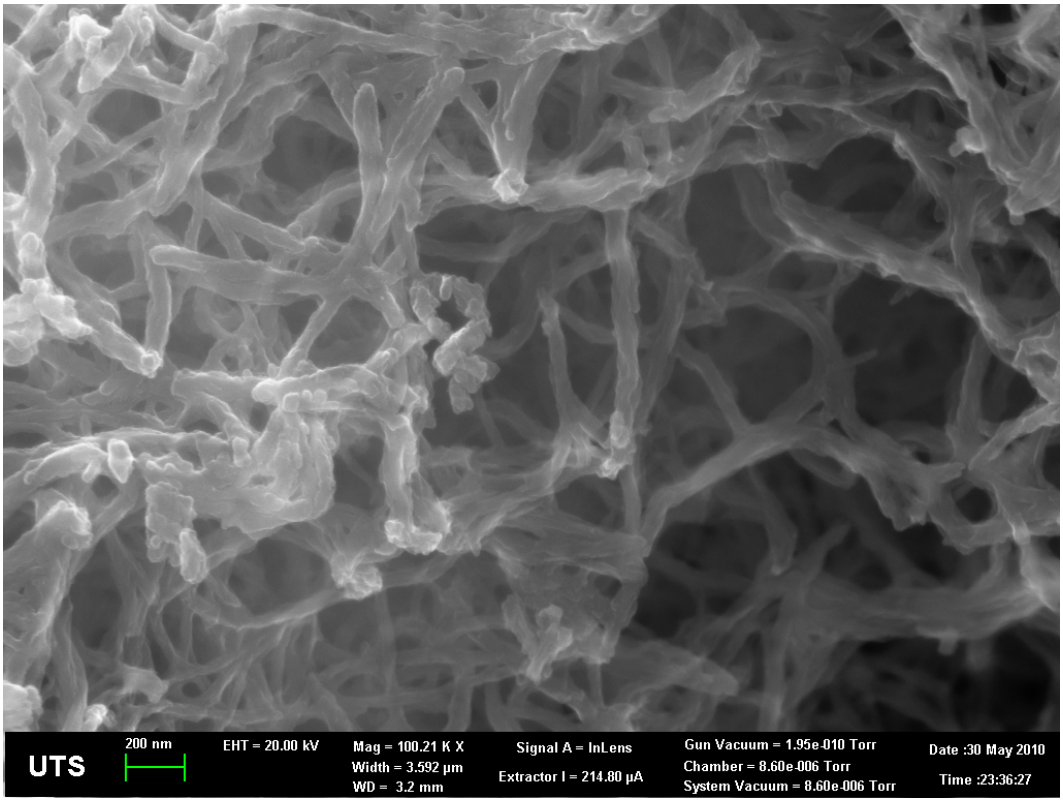

Figure C.1. High magnification image of NT-80.

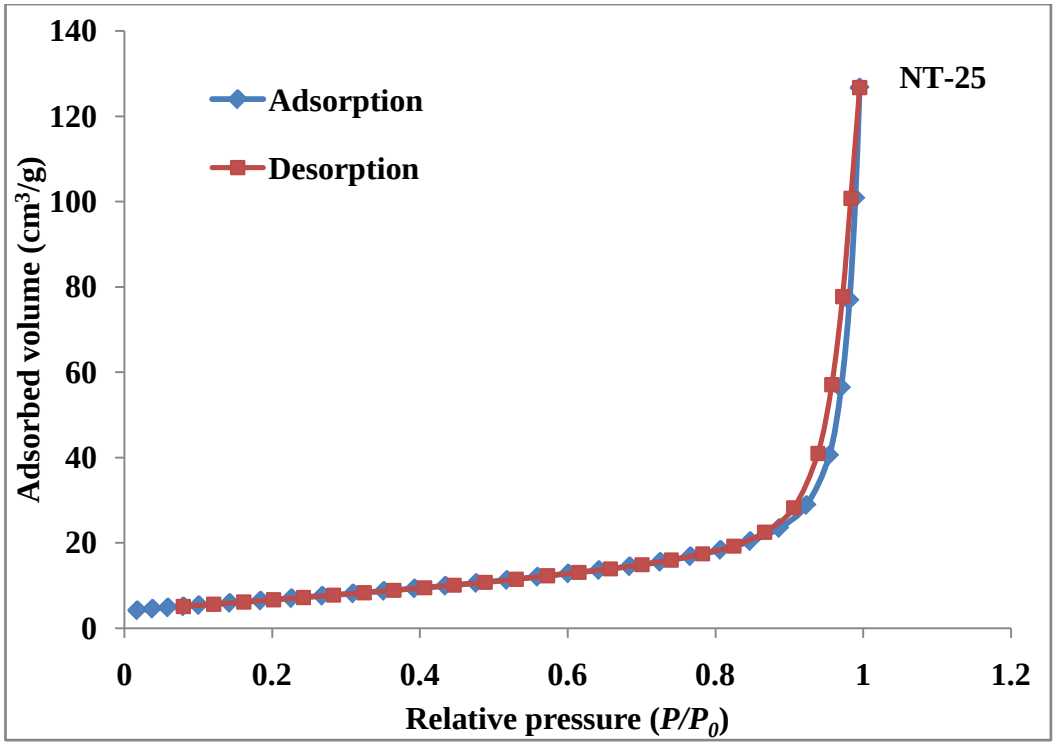

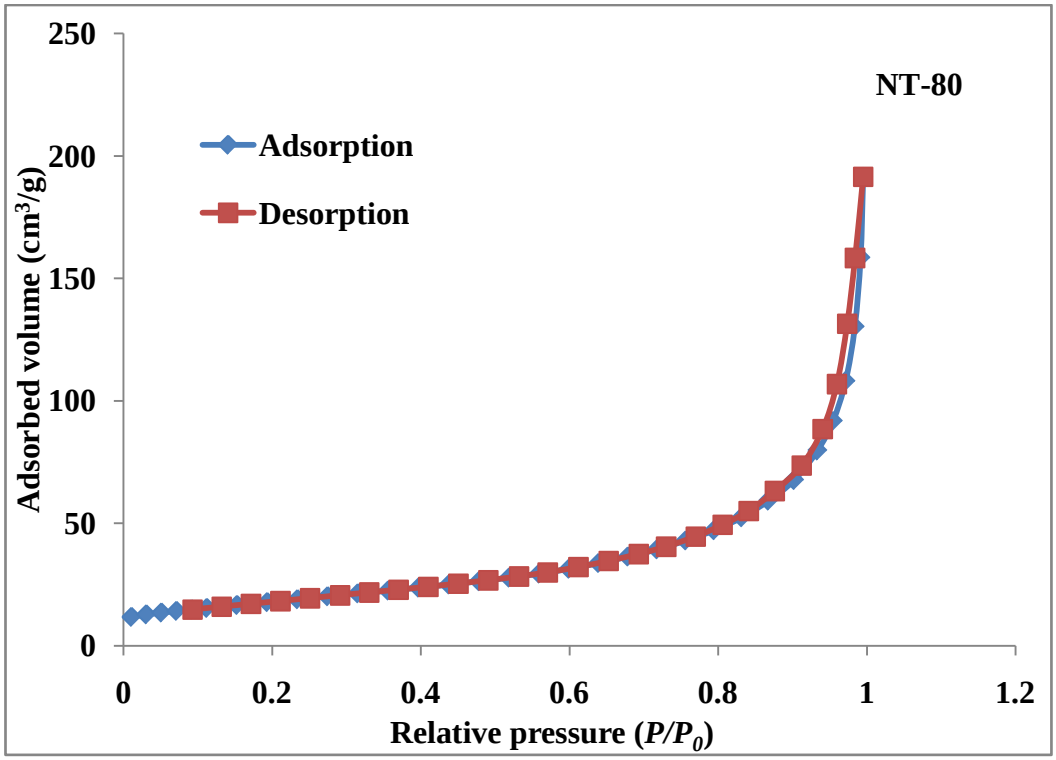

Figure C.2. Adsorption/Desorption isotherms of NT-25 and NT-80.

UNIVERSITY OF TECHNOLOGY, SYDNEY

FACULTY OF ENGINEERING AND INFORMATION TECHNOLOGY

BIBLIOGRAPHY

Abramovic B.F., Sojic D.V., Anderluh V.B., Abazovic N.D., Comor M.I. (2009) Nitrogen-doped TiO_2 suspensions in photocatalytic degradation of mecoprop and (4-chloro-2-methylphenoxy)acetic acid herbicides using various light sources. Desalination 244(1-3), 293-302.

Ai L., Li M., Li L. (2011) Adsorption of methylene blue from aqueous solution with activated carbon/cobalt ferrite/alginate composite beads: kinetics, isotherms, and thermodynamics. Journal of Chemical and Engineering Data 56(8), 3475-3483.

Alexandrescu R., Scarisoreanu M., Morjan I., Birjega R., Fleaca C., Luculescu C., Soare I., Cretu O., Negrila C.C., Lazarescu N., Ciupina V. (2009) Preparation and characterization of nitrogen-doped TiO_2 nanoparticles by the laser pyrolysis of N_2O-containing gas mixtures. Applied Surface Science 255(10), 5373-5377.

Allouni Z.E., Cimpan M.R., Høl P.J., Skodvin T., Gjerdet N.R. (2009) Agglomeration and sedimentation of TiO_2 nanoparticles in cell culture medium. Colloids and Surfaces B: Biointerfaces 68(1), 83-87.

Al-Rasheed R., Cardin D.J. (2003) Photocatalytic degradation of humic acid in saline waters. Part 1. Artificial seawater: influence of TiO_2, temperature, pH, and air-flow. Chemosphere 51(9), 925-933.

Aminian M.K., Taghavinia N., Zad A.I., Mahdavi S.M., Chavoshi M. (2007) Synthesis of titania nanofibers for photocatalytic applications. Synthesis and Reactivity in Inorganic, Metal-Organic, and Nano-Metal Chemistry 37(6), 457 - 460.

Ananpattarachai J., Kajitvichyanukul P., Seraphin S. (2009) Visible light absorption ability and photocatalytic oxidation activity of various interstitial N-doped TiO_2 prepared from different nitrogen dopants. Journal of Hazardous Materials 168(1), 253-261.

Anpo M. (1997) Photocatalysis on titanium oxide catalysts Approaches in achieving highly efficient reactions and realizing the use of visible light. Catalysis Surveys from Japan 1, 169-179.

Aoki A., Nogami G. (1996) Fabrication of anatase thin films from peroxo-polytitanic acid by spray pyrolysis. Journal of The Electrochemical Society 143(9), L191-L193.

Arabatzis I.M., Falaras P. (2002) Synthesis of porous nanocrystalline tio_2 foam. Nano Letters 3(2), 249-251.

Arana J., Martinez Nieto, J.L., Herrera Melian J.A., Dona Rodriguez J.M., Gonzalez Diaz O., Perez Pena J., Bergasa O., Alvarez C., Mendez J. (2004) Photocatalytic degradation of formaldehyde containing wastewater from veterinarian laboratories. Chemosphere 55(6), 893-904.

Arana J., Nieto J.L.M., Melian J.A.H., Rodriguez J.M.D., Diaz O.G., Perna J.P., Bergasa C.A., Alvarez C., Mendez J. (2004) Photocatalytic degradation of formaldehyde containing wastewater from veterinarian laboratories. Chemosphere 55(6), 893-904.

Asahi R., Morikawa T., Ohwaki T., Aoki K., Taga Y. (2001) Visible-light photocatalysis in nitrogen-doped titanium oxides. Science 293(5528), 269-271.

Asahi R., Morikawa, T. (2007) Nitrogen complex species and its chemical nature in TiO_2 for visible-light sensitized photocatalysis. Chemical Physics 339(1-3), 57-63.

Ashkarran A.A. (2011) Antibacterial properties of silver-doped TiO_2 nanoparticles under solar simulated light. Journal of Theoretical and Applied Physics 4(4), 1-8.

Augugliaro V., Loddo V., Pagliaro M., Palmisano G., Palmisano L. (2010) Clean by light irradiation: practical applications of supported TiO_2, Royal Society of Chemistry, Cambridge, UK.

Ayuso E.A., Sanchez A.G., Querol X. (2003) Purification of metal electroplating waste waters using zeolites. Water Research 37, 4855–4862.

Bach U., Lupo D., Comte P., Moser J.E., Weissortel F., Salbeck J., Spreitzer H., Gratzel M. (1998) Solid-state dye-sensitized mesoporous TiO_2 solar cells with high photon-to-electron conversion efficiencies. Nature 395, 583-585.

Bae E., Choi W. (2002) Highly Enhanced photoreductive degradation of perchlorinated compounds on dye-sensitized metal/TiO_2 under visible light. Environmental Science and Technology 37(1), 147-152.

Bahnemann D. (2004) Photocatalytic water treatment: solar energy applications. Solar Energy 77(5), 445-459.

Baiju K.V., Shukla S., Biju S., Reddy M.L.P., Warrier K.G.K. (2009) Hydrothermal processing of dye-adsorbing one-dimensional hydrogen titanate. Materials Letters 63(11), 923-926.

Barrett E.P., Joyner L.G., Halenda P.P. (1951) The determination of pore volume and area distributions in porous substances. I. Computations from nitrogen isotherms. Journal of the American Chemical Society 73, 373–380.

Behnajady M.A., Modirshahla N., Shokri M., Rad B. (2008) Enhancement of photocatalytic activity of TiO_2 nanoparticles by silver doping: photodeposition versus liquid impregnation methods. Global NEST Journal 10(1), 1-7.

Bekbolet M., Ozkosemen G. (1996) A preliminary investigation on the photocatalytic degradation of a model humic acid. Water Science and Technology 33(6), 189-194.

Bekbolet M., Suphandag A.S., Uyguner C.S. (2002) An investigation of the photocatalytic efficiencies of TiO_2 powders on the decolourisation of humic acids. Journal of Photochemistry and Photobiology A: Chemistry 148, 121-128.

Bela S., Wong A.S.W., Ho G.W. (2010) Hydrolysis and ion exchange of titania nanoparticles towards large-scale titania and titanate nanobelts for gas sensing applications. Journal of Physics D: Applied Physics 43(3), 035401.

Bellona C., Drewes J.E. (2007) Viability of a low-pressure nanofilter in treating recycled water for water reuse applications: A pilot-scale study. Water Research, 41, 3948-3958.

Bessekhouad Y., Robert D., Weber J. V. (2003) Preparation of TiO_2 nanoparticles by sol-gel route. International Journal of Photoenergy 5, 154-158.

Bianchi C.L., Cappelletti G., Ardizzone S., Gialanella S., Naldoni A., Oliva C., Pirola, C. (2009) N-doped TiO_2 from $TiCl_3$ for photodegradation of air pollutants. Catalysis Today 144(1-2), 31-36.

Binitha N.N., Yaakob Z., Reshmi M.R., Sugunan S., Ambili V.K., Zetty A.A. (2009) Preparation and characterization of nano silver-doped mesoporous titania photocatalysts for dye degradation. Catalysis Today 147(1), S76-S80.

Binks P. (2007) Nanotechnology & water: opportunities and challenges. Victorian Water Sustainability Seminar, May 15 2007.

Bordère S., Llewellyn P.L., Rouquerol F., Rouquerol J. (1998) Multiple features of a porous structure as assessed from the hysteresis of nitrogen

adsorption/desorption: case study of the formation of UO_3 from $UO_2(NO_3)_2 \cdot 6H_2O$. Langmuir 14(15), 4217-4221.

Borgarello E., Kiwi J., Graetzel M., Pelizzetti E., Visca M. (1982) Visible light induced water cleavage in colloidal solutions of chromium-doped titanium dioxide particles. Journal of the American Chemical Society 104(11), 2996-3002.

Bradley R.H., Mathieson I., Byrne K.M. (1997) Spectroscopic studies of modified wool fibre surfaces. Journal of Materials Chemistry 7(12), 2477–2482.

Bulut Y., Aydin H. (2006) A kinetics and thermodynamics study of methylene blue adsorption on wheat shells. Desalination 194, 259-267.

Burda C., Lou Y., Chen X., Samia A.C.S., Stout J., Gole J.L. (2003) Enhanced nitrogen doping in TiO_2 nanoparticles. Nano Letters 3(8), 1049-1051.

Byrappa K., Adschiri T. (2007) Hydrothermal technology for nanotechnology. Progress in Crystal Growth and Characterization of Materials 53(2), 117-166.

Cai R., Itoh K., Sun C.Q. (2005) pH effect on the optical properties of peroxo-titanium complex. Materials Research Society Symposium Proceedings 900, 476-483.

Calvert J.G., Pitts, J.N. (1966) Photochemistry, Wiley, New York.

Chang J.A., Vithal M., Baek I.C., Seok S.I. (2009) Morphological and phase evolution of TiO_2 nanocrystals prepared from peroxotitanate complex aqueous solution: Influence of acetic acid. Journal of Solid State Chemistry 182(4), 749-756.

Chatterjee D., Dasgupta S. (2005) Visible light induced photocatalytic degradation of organic pollutants. Journal of Photochemistry and Photobiology C: Photochemistry reviews 6(2-3), 186-205.

Chen D., Sivakumar M., Ray A.K. (2000) Heterogeneous photocatalysis in environmental remediation, pp. 505-550, Wiley Subscription Services, Inc., A Wiley Company.

Chen H.W., Ku Y., Kuo Y.L. (2007) Photodegradation of o-Cresol with Ag deposited on TiO_2 under visible and UV light irradiation. Chemical Engineering and Technology 30(9), 1242-1247.

Chen R., Jiang H., Jin W., Xu N. (2009) Model study on a submerged catalysis/membrane filtration system for phenol hydroxylation catalyzed by TS-1. Chinese Journal of Chemical Engineering 17(4), 648-653.

Chen W., Cai W., Zhang L., Wang G., Zhang L. (2001) Sonochemical processes and formation of gold nanoparticles within pores of mesoporous silica. Journal of Colloid Interface Science, 238, 291-295.

Chen X., Burda C. (2004) Photoelectron spectroscopic investigation of nitrogen-doped titania nanoparticles. The Journal of Physical Chemistry B 108(40), 15446-15449.

Chen X., Burda C. (2008) The electronic origin of the visible-light absorption properties of C-, N- and S-Doped TiO_2 nanomaterials. Journal of the American Chemical Society 130(15), 5018-5019.

Cheng S.F., Wu S.C. (2001) Feasibility of using metals to remediate water containing TCE. Chemosphere, 43, 1023-1028.

Cho M., Chung H., Choi W., Yoon J. (2005) Different inactivation behaviours of MS-2 phage and Escherichia coli in TiO_2 photocatalytic disinfection. Applied

and Environmental Microbiology, 71, 270-275.

Cho I.-H., Park J.-H., Kim Y.-G. (2005a) Oxidative degradation and toxicity reduction of trichloroethylene (TCE) in water using TiO_2/solar light, comparative study of TiO_2 slurry and immobilized systems. Journal of Environmental Science and Health A, 40, 1033-1044.

Choi I.-H., Lee S.-m., Kim I.-C., Min B.-R., Lee K.-H. (2007) Effect of new photocatalytic coagulant on NF membrane fouling. Industrial and Engineering Chemistry Research 46(8), 2280-2285.

Chong M.N., Jin B., Zhu H.Y., Chow C.W.K., Saint C. (2009) Application of H-titanate nanofibers for degradation of Congo Red in an annular slurry photoreactor. Chemical Engineering Journal 150(1), 49-54.

Chong M.N., Vimonses V., Lei S., Jin B., Chow C., Saint C. (2009) Synthesis and characterization of novel titania impregnated kaolinite nano-photocatalyst. Microporous and Mesoporous Materials, 117, 223-242.

Chong M.N., Jin B., Chow C.W.K., Saint C. (2010) Recent developments in photocatalytic water treatment technology: A review. Water Research 44(10), 2997-3027.

Cohen Y. (2006) Membrane surface nano-structuring: Selective enhancement, fouling reduction and mineral scale formation. In US-Israeli Nanotechnology for Water Purification Workshop, Arlington, Virginia, USA, March 13-15, 2006.

Cong Y., Zhang J., Chen F., Anpo M., He D. (2007) Preparation, photocatalytic activity, and mechanism of nano-TiO_2 co-doped with nitrogen and iron (III). Journal of Physical Chemistry C 111(28), 10618-10623.

Corin N., Backlund P., Kulovaara M. (1996) Degradation products formed during UV-irradiation of humic waters. Chemosphere 33(2), 245-255.

Crist B.V. (Ed) (1999) Handbook of monochromatic XPS spectra “the elements and native oxides”, XPS international, LLC.

Crites R., Tchobanoglous G. (1998) Small and decentralized wastewater management systems. McGraw Hill, NY, USA.

Davies J.C. (2006) Managing the effects of Nanotechnology. Woodrow Wilson International Center for Scholars, National Institutes of Health, Washington, D.C., USA.

Davis S.A., Burkett S.L., Mendelson N.H., Mann S. (1997) Bacterial templating of ordered macrostructures in silica and silica-surfactant mesophases. Nature 385(6615), 420-423.

Deng N., Luo F., Wu F., Xiao M. (2000) Discoloration of aqueous reactive dye solution in the UV/Fe^0 system. Water Research, 34, 2408–2411.

Deorsola F.A., Vallauri D. (2009) Study of the process parameters in the synthesis of TiO_2 nanospheres through reactive microemulsion precipitation. Powder Technology 190(3), 304-309.

Derjaguin, B.V. (1954) Investigations of the forces of interaction of surfaces in different media and their application to the problem of colloid stability**.** Discussion of the Faraday Society, 18, 24-27.

Doll T.E., Frimmel F.H. (2005) Cross-flow microfiltration with periodical back-washing for photocatalytic degradation of pharmaceutical and diagnostic residues evaluation of the long-term stability of the photocatalytic activity of TiO_2. Water Research 39(5), 847-854.

Dotzauer D.M., Dai J., Sun L., Bruening M.L. (2006) Catalytic membranes prepared using layer-by-layer adsorption of polyelectrolyte/metal nanoparticle films in porous supports. Nano Letters, 6, 2268-2272.

Doulia D., Leodopoulos C., Gimouhopoulos K., Rigas F. (2009) Adsorption of humic acid on acid-activated Greek bentonite. Journal of Colloid and Interface Science 340(2), 131-141.

Dubinin M.M. (1960) The potential theory of adsorption of gases and vapors for adsorbents with energetically non-uniform surfaces. Chemical Reviews 60(2), 235-241.

Dupont L., Guillon E. (2003) Removal of hexavalent chromium with a lignocellusic substrate extracted from wheat bran. Environmental Science and Technology, 37, 4235–4241.

Dvoranova D., Brezova V., Malati M.A. (2002) Investigations of metal doped titanium dioxide photocatalysts. Applied Catalysis B Environmental, 37, 91-105.

Eggins B.R., Palmer F.L., Byrne J.A. (1997) Photocatalytic treatment of humic substances in drinking water. Water Research 31(5), 1223-1226.

Ellis T.G. (2004) Chemistry of wastewater. Encyclopedia of Life Support System (EOLSS), Developed under the Auspices of the UNESCO, Eolss Publishers, Oxford, UK, http://www.eolss.net**.**

Emeline A.V., Kuznetsov V.N., Rybchuk V.K., Serpone N. (2008) Visible-light-active titania photocatalysts: the case of N-doped TiO_2s—properties and some fundamental issues. International Journal of Photoenergy. Volume 2008, Article ID 258394, 19 pages.

EPA (1979) Contaminants regulated under the safe drinking water act. http://water.epa.gov/drink/contaminants/upload/2003_05_27_contaminants_contam_timeline.pdf

Eriksson P. (1988) Nanofiltration extends the range of membrane filtration. Environmental Progress, 7(1), 58–62.

Everett D.H. (1972) Definitions, terminology and symbols in colloid and surface chemistry. Pure Applied Chemistry 31(4), 579-638.

Falaras P., Arabatzis I.M., Stergiopoulos T., Bernard M.C. (2003) Enhanced activity of silver modified thin-film TiO_2 photocatalysts. International Journal of Photoenergy 5(3), 123-130.

Fetterolf M.L., Patel H.V., Jennings J.M. (2003) Adsorption of methylene blue and acid blue 40 on titania from aqueous solution. Journal of Chemical & Engineering Data 48(4), 831-835.

Fleischer T., Grunwald A. (2008) Making nanotechnology developments sustainable, A role for technology assessment. Journal of Cleaner Production, 16, 889-898.

Freundlich H.M.F. (1906) über die adsorption in lösungen. Zeitschrift für Physikalische Chemie 57, 385-470.

Fu J., Ji M., Wang Z., Jin L., An D. (2006) A new submerged membrane photocatalysis reactor (SMPR) for fulvic acid removal using a nano-structured photocatalyst. Journal of Hazardous Materials 131(1-3), 238-242.

Fujishima A., Honda K. (1972) Electrochemical photolysis of water at a semiconductor electrode. Nature 238(5358), 37-38.

Fujishima A., Rao T.N., Tryk D.A. (2000) Titanium dioxide photocatalysis. Journal of Photochemistry and Photobiology C: Photochemistry Reviews 1(1), 1-21.

Fujishima A., Zhang X., Tryk D.A. (2007) Heterogeneous photocatalysis: From water photolysis to applications in environmental cleanup. International Journal of Hydrogen Energy 32(14), 2664-2672.

Fujishima A., Zhang X., Tryk D.A. (2008) TiO_2 photocatalysis and related surface phenomena. Surface Science Reports 63(12), 515-582.

Gao H., Zhou J., Dai D., Qu Y. (2009) Photocatalytic activity and electronic structure analysis of N-doped anatase TiO_2: A combined experimental and theoretical study. Chemical Engineering and Technology 32(6), 867-872.

Gao Y., Masuda Y., Peng Z., Yonezawa T., Koumoto K. (2003) Room temperature deposition of a TiO_2 thin film from aqueous peroxotitanate solution. Journal of Materials Chemistry 13(3), 608-613.

Gao Y., Masuda Y., Seo W.-S., Ohta H., Koumoto K. (2004) TiO_2 nanoparticles prepared using an aqueous peroxotitanate solution. Ceramics International 30(7), 1365-1368.

Gaya U.I., Abdullah A.H. (2008) Heterogeneous photocatalytic degradation of organic contaminants over titanium dioxide: A review of fundamentals, progress and problems. Journal of Photochemistry and Photobiology C: Photochemistry Reviews 9(1), 1-12.

Ge L., Xu M.X., Sun M. (2006) Synthesis and characterization of TiO_2 photocatalytic thin films prepared from refluxed PTA sols. Materials Letters 60(2), 287-290.

Ge L., Xu M., Fang H. (2006a) Photo-catalytic degradation of methyl orange and formaldehyde by Ag/$InVO_4$-TiO_2 thin films under visible-light irradiation. Journal of Molecular Catalysis A: Chemical 258(1-2), 68-76.

Geng J., Yang D., Zhu J., Chen D., Jiang Z. (2009) Nitrogen-doped TiO_2 nanotubes with enhanced photocatalytic activity synthesized by a facile wet chemistry method. Materials Research Bulletin 44(1), 146-150.

Ghosh A.K., Maruska H.P. (1977) Photoelectrolysis of water in sunlight with sensitized semiconductor electrodes. Journal of the Electrochemical Society 124(10), 1516-1522.

Graciani J., Alvarez L.J., Rodriguez J.A., Sanz J.F. (2008) N doping of rutile TiO_2 (110) surface. A theoretical DFT study. Journal of Physical Chemistry C 112(7), 2624-2631.

Gribbin J. (1997) Richard Feynman: A Life in Science. Dutton, pg 170.

Gu D.-E., Yang B.-C., Hu Y.-D. (2008) V and N co-doped nanocrystal anatase TiO_2 photocatalysts with enhanced photocatalytic activity under visible light irradiation. Catalysis Communication 9(6), 1472-1476.

Gupta A.K., Pal A., Sahoo C. (2006) Photocatalytic degradation of a mixture of Crystal Violet (Basic Violet 3) and Methyl Red dye in aqueous suspensions using Ag^+ doped TiO_2. Dyes Pigments 69(3), 224-232.

Gyliene O., Vengris T., Stoncius A., Nivinskiene O. (2008) Decontamination of solutions containing EDTA using metallic iron. Journal of Hazardous Materials, 159, 446-451.

Hall K.R., Eagleton L.C., Acrivos A., Vermeulen T. (1966) Pore- and solid-diffusion kinetics in fixed-bed adsorption under constant-pattern conditions. Industrial and Engineering Chemistry Fundamentals 5(2), 212-223.

Hamal D.B., Klabunde K.J.J. (2007) Synthesis, characterization, and visible light activity of new nanoparticle photocatalysts based on silver, carbon, and sulfur-doped TiO_2. Journal of Colloid Interface Science, 311(2), 514-522.

Han T., Fan T., Chow S.-K., Zhang D. (2010) Biogenic N-P-codoped TiO_2: Synthesis, characterization and photocatalytic properties. Bioresource Technology 101(17), 6829-6835.

Hearle J.W.S., Buschow K.H.J., Robert W.C., Merton C.F., Bernard I., Edward J.K., Subhash M., Patrick V. (2001) Encyclopedia of materials: science and technology, pp. 9100-9116, Elsevier, Oxford.

Herrmann J.M., Disdier J., Pichat P. (1986) Photoassisted platinum deposition on TiO_2 powder using various platinum complexes. Journal of Physical Chemistry 90(22), 6028-6034.

Herrmann J.M., Guillard C., Pichat P. (1993) Heterogeneous photocatalysis: an emerging technology for water treatment. Catalysis Today 17(1-2), 7-20.

Herrmann J.M., Tahiri H., Ait-Ichou Y., Lassaletta G., Gonzalez-Elipe A.R., Fernandez A. (1997) Characterization and photocatalytic activity in aqueous medium of TiO_2 and Ag-TiO_2 coatings on quartz. Applied Catalysis B: Environmental 13(3-4), 219-228.

Herrmann J.-M. (1999) Heterogeneous photocatalysis: fundamentals and applications to the removal of various types of aqueous pollutants. Catalysis Today 53(1), 115-129.

Hilderbrand H., Machenzie K., Kopinke F.D. (2008) Novel nano-catalysts for wastewater treatment. Global NEST Journal, 10(1), 47-53.

Hillie T., Munasinghe M., Hlope M., Deraniyagala Y. (2006) Nanotechnology, water and development. Global Dialogue on Nanotechnology and the Poor:

Opportunities and Risks, Meridian Institute.

Hitchman M.L., Alexandrov S.E. (2001) New approaches to titania and silica via CVD. The Electrochemical Society Interface 10, 40-45.

Hodgkin J.H., Galbraith M.N., Chong Y.K. (1983) Combustion products from burning wool fabric. Fire and Materials 7(4), 210-215.

Hollman A.M., Bhattacharyya D. (2004) Pore assembled multilayers of charged polypeptides in microporous membranes for ion separation. Langmuir, 20, 5418-5424.

Hong S., Wen C., He J., Gan F., Ho Y.-S. (2009) Adsorption thermodynamics of methylene blue onto bentonite. Journal of Hazardous Materials 167, 630-633.

Houas A., Lachheb H., Ksibi M., Elaloui E., Guillard C., Herrmann J.-M. (2001) Photocatalytic degradation pathway of methylene blue in water. Applied Catalysis B: Environmental 31(2), 145-157.

Hoyt V.W., Mason E. (2008) Nanotechnology emerging health issues. Journal of Chemical Health and Safety, March/April, 10-15.

Hu E.L., Shaw D.T. (1998) Synthesis and assembly In: Nanostructure science and technology, eds. R.W. Siegel, E. Hu, M.C. Roco. Kluwer academic publishers, Dordrecht, The Netherlands.

Hu J., Chen G., Lo I.M.C. (2005) Removal and recovery of Cr(VI) from wastewater by maghemite nanoparticles. Water Research, 39, 4528-4536.

Hung W.C., Chen Y.C., Chu H., Tseng T.K. (2008) Synthesis and characterization of TiO_2 and Fe/TiO_2 nanoparticles and their performance for photocatalytic degradation of 1,2-dichloroethane. Applied Surface Science, 255, 2205-2213.

Huo Y., Bian Z., Zhang X., Jin Y., Zhu J., Li H. (2008) Highly active $TiO_{2-x}N_x$ visible photocatalyst prepared by N-doping in Et_3N/EtOH fluid under supercritical conditions. The Journal of Physical Chemistry C 112(16), 6546-6550.

I.H.S.S. (2007) What are humic substances? http://www.humicsubstances.org/whatarehs.html

Ichinose H., Terasaki M., H. Katsuki (1996) Synthesis of peroxo-modified anatase sol from peroxo titanic acid solution Journal of the Ceramic Society of Japan 104(8), 715-718.

Ichinose H., Taira M., Furuta S., Katsuki H. (2003) Anatase sol prepared from peroxotitanium complex aqueous solution containing Niobium or Vanadium. Journal of the American Ceramic Society 86(9), 1605-1608.

Ichinose H., Terasaki M., Katsuki H. (2001) Properties of peroxotitanium acid solution and peroxo-modified anatase sol derived from peroxotitanium hydrate. Journal of Sol-Gel Science and Technology 22(1), 33-40.

Ihara T., Miyoshi M., Ando M., Sugihara S., Iriyama Y. (2001) Preparation of a visible-light-active TiO_2 photocatalyst by RF plasma treatment. Journal of Materials Science 36(17), 4201-4207.

Ihara T., Miyoshi M., Iriyama Y., Matsumoto O., Sugihara S. (2003) Visible-light-active titanium oxide photocatalyst realized by an oxygen-deficient structure and by nitrogen doping. Applied Catalysis B: Environmental 42(4), 403-409.

Imai H., Matsuta M., Shimizu K., Hirashima H., Negishi N. (2002) Morphology transcription with TiO_2 using chemical solution growth and its application for photocatalysts. Solid State Ionics 151(1-4), 183-187.

Iorio M., Pan B., Capasso R., Xing B. (2008) Sorption of phenanthrene by dissolved

organic matter and its complex with aluminium oxide nanoparticles. Environmental Pollution, 156, 1021-1029.

Janus M., Choina J., Morawski A.W. (2009) Azo dyes decomposition on new nitrogen-modified anatase TiO_2 with high adsorptivity. Journal of Hazardous Materials 166(1), 1-5.

Jensen M., Fuierer P. (2006) Low-temperature preparation of nanocrystalline anatase films through a sol-gel route. Journal of Sol-Gel Science and Technology 39(3), 229-233.

Jiang L., Zhong Y., Li G. (2009) A simple H_2O_2-assisted route to hollow TiO_2 structures with different crystal structures and morphologies. Materials Research Bulletin 44(5), 999-1002.

Jiuhui Q. (2008) Research progress of novel adsorption processes in water purification: A review. Journal of Environmental Sciences, 20, 1-13.

Kagaya S., Shimizu K., Arai R., Hasegawa K. (1999) Separation of titanium dioxide photocatalyst in its aqueous suspensions by coagulation with basic aluminium chloride. Water Research 33(7), 1753-1755.

Kaneco S., Rahman M.A., Suzuki T., Katsumata H., Ohta K. (2004) Optimization of solar photocatalytic degradation conditions of bisphenol A in water using titanium dioxide. Journal of Photochemistry and Photobiology A: Chemistry 163(3), 419-424.

Kartsonakis I.A., Liatsi P., Danilidis I., Bouzarelou D., Kordas G. (2008) Synthesis, characterization and antibacterial action of hollow titania spheres. Journal of Physics and Chemistry of Solids 69(1), 214-221.

Kasuga T., Hiramatsu M., Hoson A., Sekino T., Niihara K. (1999) Titania nanotubes prepared by chemical processing. Advanced Materials 11(15), 1307-1311.

Khalyavka T.A., Shimanovskaya V.V., Strelko V.V., Kapinus E.I. (2001) Photocatalytic activity of titanium dioxide in the degradation of methylene blue and tetrachlorofluorescein in aqueous solutions. Theoretical and Experimental Chemistry 37(1), 58-62.

Kikuchi Y., Sunada K., Iyoda T., Hashimoto K., Fujishima A. (1997) Photocatalytic bactericidal effect of TiO_2 thin films: dynamic view of the active oxygen species responsible for the effect. Journal of Photochemistry and Photobiology A: Chemistry 106(1-3), 51-56.

Kim T.H., Lee K.H., Kwon Y.K. (2006) Monodisperse hollow titania nanospheres prepared using a cationic colloidal template. Journal of Colloid and Interface Science 304(2), 370-377.

Kisch H. (1989) What is photocatalysis? In: Photocatalysis Fundamentals and Applications, Serpone N. and Pelizzetti E. (eds), Wiley, New York.

Kobayakawa K., Murakami Y., Sato Y. (2005) Visible-light active N-doped TiO_2 prepared by heating of titanium hydroxide and urea. Journal of Photochemistry and Photobiology A 170(2), 177-179.

Konstantinou I.K., Albanis T.A. (2004) TiO_2-assisted photocatalytic degradation of azo dyes in aqueous solution: kinetic and mechanistic investigations: A review. Applied Catalysis B: Environmental 49(1), 1-14.

Kuchibhatla S.V.N.T., Karakoti A.S., Bera D., Seal S. (2007) One dimensional nanostructured materials. Progress in Materials Science 52(5), 699-913.

Kudo T. (1984) A new heteropolyacid with carbon as a heteroatom in a Keggin-like structure. Nature 312(5994), 537-538.

Kumar P.S.S., Sivakumar R., Anandan S., Madhavan J., Maruthamuthu P.,

Ashokkumar M. (2008) Photocatalytic degradation of Acid Red 88 using Au-TiO_2 nanoparticles in aqueous solutions. Water Research, 42, 4878-4884.

Kurusu Y. (1981) Thermal behavior of a new type of molybdenum oxide obtained by oxidation of molybdenum powder or molybdenum trioxide with hydrogen peroxide Bulletin of the Chemical Society of Japan 54, 293-294.

Lachheb H., Puzenat E., Houas A., Ksibi M., Elaloui E., Guillard C., Herrmann J.-M. (2002) Photocatalytic degradation of various types of dyes (Alizarin S, Crocein Orange G, Methyl Red, Congo Red, Methylene Blue) in water by UV-irradiated titania. Applied Catalysis B: Environmental 39(1), 75-90.

Lakshmi B.B., Patrissi C.J., Martin C.R. (1997) Sol-gel template synthesis of semiconductor oxide micro- and nanostructures. Chemistry of Materials 9(11), 2544-2550.

Lakshmi S., Renganathan R., Fujita S. (1995) Study on TiO_2-mediated photocatalytic degradation of methylene blue. Journal of Photochemistry and Photobiology A: Chemistry 88, 163-167.

Langmuir I. (1918) The adsorption of gases on plane surfaces of glass, mica and platinum. Journal of the American Chemical Society 40(9), 1361-1403.

Lee C.-K., Liu S.-S., Juang L.-C., Wang C.-C., Lyu M.-D., Hung S.-H. (2007) Application of titanate nanotubes for dyes adsorptive removal from aqueous solution. Journal of Hazardous Materials 148(3), 756-760.

Lee P.F., Zhang X., Sun D.D., Du J., Leckie J.O. (2008) Synthesis of bimodal porous structured TiO_2 microsphere with high photocatalytic activity for water treatment. Colloids and Surfaces A: Physicochemical and Engineering Aspects 324(1-3), 202-207.

Lee C.-K., Lin K.-S., Wu C.-F., Lyu M.-D., Lo C.-C. (2008a) Effects of synthesis temperature on the microstructures and basic dyes adsorption of titanate nanotubes. Journal of Hazardous Materials 150(3), 494-503.

Lee C.-K., Wang C.-C., Juang L.-C., Lyu M.-D., Hung S.-H., Liu S.-S. (2008b) Effects of sodium content on the microstructures and basic dye cation exchange of titanate nanotubes. Colloids and Surfaces A: Physicochemical and Engineering Aspects 317, 164-173.

Lee D.-K., Kim S.-C., Cho I.-C., Kim S.-J., Kim S.-W. (2004) Photocatalytic oxidation of microcystin-LR in a fluidized bed reactor having TiO_2-coated activated carbon. Separation and Purification Technology 34(1-3), 59-66.

Lee C.K., Kim D.K., Lee J.H., Sung J.H., Kim I., Lee K.H., Park J.W., Lee Y.K. (2004a) Preparation and Characterization of Peroxo Titanic Acid Solution Using $TiCl_3$. Journal of Sol-Gel Science and Technology 31(1), 67-72.

Lee S., Cho I.-S., Lee D.K., Kim D.W., Noh T.H., Kwak C.H., Park S., Hong K.S., Lee J.-K., Jung H.S. (2010) Influence of nitrogen chemical states on photocatalytic activities of nitrogen-doped TiO_2 nanoparticles under visible light. Journal of Photochemistry and Photobiology A 213(2-3), 129-135.

Leone J. (1973) Collaborative study of the quantitative determination of titanium dioxide in cheese. Journal of the Association of Official Analytical Chemists 56, 535-558.

Lepape H., Solano-Serena F., Contini P., Maftah A., Leprat P. (2002) Evaluation of the anti-microbial properties of an activated carbon fibre supporting silver using a dynamic method. Carbon, 40(15), 2947-2954.

Li D., Haneda H., Hishita S., Ohashi N. (2005) Visible-light-driven nitrogen-doped TiO_2 photocatalysts: effect of nitrogen precursors on their photocatalysis for

decomposition of gas-phase organic pollutants. Materials Science and Engineering: B 117(1), 67-75.

Li F.B., Li X.Z., Hou M.F. (2004) Photocatalytic degradation of 2-mercaptobenzothiazole in aqueous La^{3+}-TiO_2 suspension for odour control. Applied Catalysis B: Environmental 48(3), 185-194.

Li G., Pang S., Jiang L., Guo Z., Zhang Z. (2006) Environmentally friendly chemical route to vanadium oxide single-crystalline nanobelts as a cathode material for lithium-ion batteries. The Journal of Physical Chemistry B 110(19), 9383-9386.

Li Q., Xie R., Mintz E.A., Shang J.K. (2007) Enhanced visible-light photocatalytic degradation of humic acid by palladium-modified nitrogen-doped titanium oxide. Journal of the American Ceramic Society 90(12), 3863-3868.

Li J., Shi X., Wang L., Liu F. (2007a) Synthesis of biomorphological mesoporous TiO_2 templated by mimicking bamboo membrane in supercritical CO_2. Journal of Colloid and Interface Science 315(1), 230-236.

Li X., Fan T., Zhou H., Chow S.-K., Zhang W., Zhang D., Guo Q., Ogawa H. (2009) Enhanced light-harvesting and photocatalytic properties in *Morph*-TiO_2 from green-leaf biotemplates. Advanced Functional Materials 19(1), 45-56.

Li X., Fan T., Zhou H., Chow S.-K., Zhang W., Zhang D., Guo Q., Ogawa H. (2009a) Enhanced light-harvesting and photocatalytic properties in *Morph*-TiO_2 from green-leaf biotemplates. Advanced Functional Materials 19(1), 45-56.

Li X.S., Fryxell G.E., Wang C., Engelhard M.H. (2008) The synthesis of Ag-doped mesoporous TiO_2. Microporous and Mesoporous Materials 111(1-3), 639-642.

Linder C., Oren Y. (2006) Relationships between materials parameters of nanofiltration membranes and the resultant membrane performance. In US-Israeli Nanotechnology for Water Purification Workshop, Arlington, Virginia, USA, March 13-15, 2006.

Linsebigler A.L., Lu G., Yates J.T. (1995) Photocatalysis on TiO_2 Surfaces: principles, mechanisms, and selected results. Chemical Reviews 95(3), 735-758.

Liu S., Lim M., Fabris R., Chow C., Chiang K., Drikas M., Amal R. (2008) Removal of humic acid using TiO_2 photocatalytic process fractionation and molecular weight characterisation studies. Chemosphere 72(2), 263-271.

Liu C., Tang X., Mo C., Qiang Z. (2008a) Characterization and activity of visible-light-driven TiO_2 photocatalyst codoped with nitrogen and cerium. Journal of Solid State Chemistry 181(4), 913-919.

Liu G., Wang X., Chen Z., Cheng H.-M., Lu G.Q. (2009a) The role of crystal phase in determining photocatalytic activity of nitrogen doped TiO_2. Journal of Colloid Interface Science 329(2), 331-338.

Liu G., Wang X., Wang L., Chen Z., Li F., Lu G.Q., Cheng H.-M. (2009b) Drastically enhanced photocatalytic activity in nitrogen doped mesoporous TiO_2 with abundant surface states. Journal of Colloid Interface Science 334(2), 171-175.

Liu H., Yang T. (2003) Photocatalytic inactivation of Escherichia coli and Lactobacillus helveticus by ZnO and TiO_2 activated with ultraviolet light. Process Biochemistry, 39, 475-481.

Liu Y., Li J., Qiu X., Burda C. (2006) Novel TiO_2 nanocatalysts for wastewater purification: tapping energy from the sun. Water Science and Technology 54(8), 47-54.

Liu Y., Liu C.-y., Rong Q.-h., Zhang Z. (2003) Characteristics of the silver-doped TiO_2 nanoparticles. Applied Surface Science 220(1-4), 7-11.

Liu Z., Wang Y., Chu W., Li Z., Ge C. (2010) Characteristics of doped TiO_2 photocatalysts for the degradation of methylene blue waste water under visible light. Journal of Alloys Compounds 501(1), 54-59.

Livraghi S., Czoska A.M., Paganini M.C., Giamello E. (2009) Preparation and spectroscopic characterization of visible light sensitized N doped TiO_2 (rutile). Journal of Solid State Chemistry 182(1), 160-164.

Lopez A., Acosta D., I. Martinez A., Santiago, J. (2010) Nanostructured low crystallized titanium dioxide thin films with good photocatalytic activity. Powder Technology 202(1-3), 111-117.

Lützenkirchen-Hecht D., Strehblow H.-H. (2009) Anodic silver (II) oxides investigated by combined electrochemistry, ex situ XPS and in situ X-ray absorption spectroscopy. Surface and Interface Analysis 41(10), 820-829.

Lu J.G., Chang P., Fan Z. (2006) Quasi-one-dimensional metal oxide materials Synthesis, properties and applications. Materials Science and Engineering: R: Reports 52(1-3), 49-91.

Lv Y., Ding Y., Zhou J., Xiao W., Feng Y. (2009) Preparation, characterization, and photocatalytic activity of N, S-codoped TiO_2 nanoparticles. Journal of the American Ceramic Society 92(4), 938-941.

Makhluf S., Dror R., Nitzan Y., Abramovich A., Jelinek R., Gedanken A. (2005) Microwave-assisted synthesis of nanocrystalline MgO and its use as a

bactericide. Advanced Functional Materials, 15, 1708-1715.

Malato S., Fernandez-Ibaez P., Maldonado M.I., Blanco J., Gernjak W. (2009) Decontamination and disinfection of water by solar photocatalysis: Recent overview and trends. Catalysis Today 147(1), 1-59.

Manttari M., Viitikko K., Nystrom M. (2006) Nanofiltration of biologically treated effluents from the pulp and paper industry. Journal of Membrane Science, 272, 152-160.

Mao Y., Kanungo M., Hemraj-Benny T., Wong S.S. (2006) Synthesis and growth mechanism of titanate and titania one-dimensional nanostructures self-assembled into hollow micrometer-scale spherical aggregates. The Journal of Physical Chemistry B 110(2), 702-710.

Mardare D., Luca D., Teodorescu C.M., Macovei, D. (2007) On the hydrophilicity of nitrogen-doped TiO_2 thin films. Surface Science 601(18), 4515-4520.

Martyanov I.N., Berger T., Diwald O., Rodrigues S., Klabunde K.J. (2010) Enhancement of TiO_2 visible light photoactivity through accumulation of defects during reduction-oxidation treatment. Journal of Photochemistry and Photobiology A: Chemistry 212(2-3), 135-141.

Matthews R.W. (1989) Photocatalytic oxidation and adsorption of methylene blue on thin films of near-ultraviolet-illuminated TiO_2. Journal of the Chemical Society, Faraday Transactions 1: Physical Chemistry in Condensed Phases 85(6), 1291-1302.

Matthews R.W. (1991) Photooxidative degradation of coloured organics in water using supported catalysts TiO_2 on sand. Water Research 25(10), 1169-1176.

McAleer J.F., Peter L.M. (1980) Photocurrent spectroscopy of anodic oxide films on titanium. Faraday Discussions of the Chemical Society 70, 67-80.

McCullagh C., Skillen N., Adams M., Robertson P.K.J. (2011) Photocatalytic reactors for environmental remediation: a review. Journal of Chemical Technology and Biotechnology 86(8), 1002-1017.

McKay G., Blair H.S., Gardner, J.R. (1982) Adsorption of dyes on chitin. I. Equilibrium studies. Journal of Applied Polymer Science 27(8), 3043-3057.

Michalow K.A., Logvinovich D., Weidenkaff A., Amberg M., Fortunato G., Heel A., Graule T., Rekas, M. (2009) Synthesis, characterization and electronic structure of nitrogen-doped TiO_2 nanopowder. Catalysis Today 144(1-2), 7-12.

Mills A., Lee S.-K. (2004) Semiconductor photocatalysis In: Advanced oxidation processes for water and wastewater treatment. Parsons S. (Ed.), pp. 137-166, IWA publishing, Cornwall, UK.

Minabe T., Tryk D.A., Sawunyama P., Kikuchi Y., Hashimoto K., Fujishima A. (2000) TiO_2-mediated photodegradation of liquid and solid organic compounds. Journal of Photochemistry and Photobiology A: Chemistry 137(1), 53-62.

Mohan D., Pittman Jr.C.U. (2007) Arsenic removal from water/wastewater using adsorbents-A critical review. Journal of Hazardous Materials, 142, 1-53.

Molinari R., Mungari M., Drioli E., Di Paola A., Loddo V., Palmisano L., Schiavello M. (2000) Study on a photocatalytic membrane reactor for water purification. Catalysis Today 55(1-2), 71-78.

Morgada M.E., Levy I.K., Salomone V., Farias S.S., Lopez G., Litter M.I. (2008) Arsenic (V) removal with nanoparticulate zerovalent iron: Effect of UV light and humic acids. Catalysis Today, 143(3-4), 261-268.

Morgan D.L., Zhu H.-Y., Frost R.L., Waclawik E.R. (2008) Determination of a morphological phase diagram of titania/titanate nanostructures from alkaline hydrothermal treatment of Degussa P25. Chemistry of Materials 20(12), 3800-3802.

Moriguchi I., Honda M., Ohkubo T., Mawatari Y., Teraoka Y. (2004) Adsorption and photocatalytic decomposition of methylene blue on mesoporous metallosilicates. Catalysis Today 90(3-4), 297-303.

Mozia S. (2010) Photocatalytic membrane reactors (PMRs) in water and wastewater treatment. A review. Separation and Purification Technology 73(2), 71-91.

Muhlebach J. Mueller K., Schwarzenbach G. (1970) Peroxo complexes of titanium. Inorganic Chemistry 9(11), 2381-2390.

Mulder G.J. (1840) Untersuchungen über die Humussubstanzen (English). Journal für Praktische Chemie 21(1), 203-240.

Murau P.C. (1961) Dissolution of tungsten by hydrogen peroxide. Analytical Chemistry 33(8), 1125-1126.

Myers W.D., Ludden P.A., Nayigihugu V., Hess B.W. (2004) Technical Note: A procedure for the preparation and quantitative analysis of samples for titanium dioxide. Journal of Animal Science 82(1), 179-183.

Nahar M.S., Hasegawa K., Kagaya S. (2006) Photocatalytic degradation of phenol by visible light-responsive iron-doped TiO_2 and spontaneous sedimentation of the TiO_2 particles. Chemosphere 65(11), 1976-1982.

Nasr-Esfahani M., Habibi M.H. (2008) Silver doped TiO_2 nanostructure composite photocatalyst film synthesized by sol-gel spin and dip coating technique on glass. International Journal of Photoenergy 2008, 11.

Nouri S., Haghseresht F., Lu M. (2002) Adsorption of aromatic compounds by activated carbon: effects of functional groups and molecular size. Adsorption Science and Technology, 20(1), 1-15.

Nutt M.O., Hughes J.B., Wong M.S. (2005) Designing Pd-on-Au bimetallic nanoparticle catalysts for trichloroethene hydrodechlorination. Environmental Science and Technology, 39, 1346-1353.

Obata K., Irie H., Hashimoto K. (2007) Enhanced photocatalytic activities of Ta, N co-doped TiO_2 thin films under visible light. Chemical Physics 339(1-3), 124-132.

Ogawa S., Tanigawa M., Fujioka M., Hanasaki Y. (1995) Photocatalyzed destruction of humic acid in aqueous semiconductor suspension and diminution of its trihalomethane producibility. Japanese Journal of Toxicology and Environmental Health 41, 7.

Ogino C., Dadjour M.F., Iida Y., Shimizu N. (2008) Decolorization of methylene blue in aqueous suspensions of titanium peroxide. Journal of Hazardous Materials 153(1-2), 551-556.

Oh S.W., Kang M.N., Cho C.W., Lee M.W. (1997) Detection of carcinogenic amines from dyestuffs or dyed substrates. Dyes Pigments 33(2), 119-135.

Ohko Y., Hashimoto K., Fujishima A. (1997) Kinetics of photocatalytic reactions under extremely low-intensity UV illumination on titanium dioxide thin films. Journal of Physical Chemistry A 101(43), 8057-8062.

Ohko Y., Iuchi K.-i., Niwa C., Tatsuma T., Nakashima T., Iguchi T., Kubota Y., Fujishima A. (2002) 17β-Estradiol degradation by TiO_2 photocatalysis as a means of reducing estrogenic activity. Environmental Science and Technology 36(19), 4175-4181.

Ohtani B., Azuma Y., Li D., Ihara T., Abe R. (2007) Isolation of anatase crystallites from anatase-rutile mixed particles by dissolution with aqueous hydrogen peroxide and ammonia. Transactions of the Materials Research Society of Japan 32(2), 401-404.

Ohtani B., Prieto-Mahaney O.O., Li D., Abe R. (2010) What is Degussa (Evonic) P25? Crystalline composition analysis, reconstruction from isolated pure particles and photocatalytic activity test. Journal of Photochemistry and Photobiology A: Chemistry 216(2-3), 179-182.

Ollis D.F. (1985) Contaminant degradation in water. Environmental Science and Technology 19(6), 480-484.

Ollis D.F., Pelizzetti E., Serpone N. (1989) Heterogeneous Photocatalysis in the Environment: Application to Water Purification In: Photocatalysis Fundamentals and Applications. Serpone, N. and Pelizzetti, E. (Eds.), pp. 603-637, Wiley, New York.

Ollis D.F., Pelizzetti E., Serpone N. (1991) Photocatalyzed destruction of water contaminants. Environmental Science and Technology 25(9), 1522-1529.

Onishi H., Aruga T., Egawa C., Iwasawa Y. (1988) Adsorption of CH_3OH, HCOOH and SO_2 on TiO_2(110) and stepped TiO_2(441) surfaces. Surface Science 193(1-2), 33-46.

Orendorz A., Ziegler C., Gnaser H. (2008) Photocatalytic decomposition of methylene blue and 4-chlorophenol on nanocrystalline TiO_2 films under UV illumination: A ToF-SIMS study. Applied Surface Science 255(4), 1011-1014.

Palmer F.L., Eggins B.R., Coleman H.M. (2002) The effect of operational parameters on the photocatalytic degradation of humic acid. Journal of Photochemistry and Photobiology A: Chemistry 148, 137-143.

Palmisano G., Addamo M., Augugliaro V., Caronna T., Di Paola A., Lopez E.G., Loddo V., Marco G., Palmisano L., Schiavello M. (2007) Selectivity of hydroxyl radical in the partial oxidation of aromatic compounds in heterogeneous photocatalysis. Catalysis Today 122(1-2), 118-127.

Park M.-S., Kang M. (2008) The preparation of the anatase and rutile forms of Ag-TiO_2 and hydrogen production from methanol/water decomposition. Materials Letters 62(2), 183-187.

Pereira W.S., Freire R.S. (2006) Azo dye degradation by recycled waste zero-valent iron powder. Journal of the Brazilian Chemical Society, 17(5), 832-838.

Pingxiao W., Jianwen T., Zhi D. (2007) Preparation and photocatalysis of TiO_2 nanoparticles doped with nitrogen and cadmium. Materials Chemistry and Physics 103(2-3), 264-269.

Powell R.M., Puls R.W., Hightower S.K., Sabatini D.A. (1995) Coupled iron corrosion and chromate reduction: mechanisms for subsurface remediation. Environmental Science and Technology, 29, 1913-1922.

Qamar M., Muneer M., Bahnemann D. (2006) Heterogeneous photocatalysed degradation of two selected pesticide derivatives, triclopyr and daminozid in aqueous suspensions of titanium dioxide. Journal of Environmental Management 80(2), 99-106.

Qi B., Wu L., Zhang Y., Zeng Q., Zhi J. (2010) Low-temperature and one-step synthesis of rutile TiO_2 aqueous sol by heterogeneous nucleation method. Journal of Colloid and Interface Science 345(2), 181-186.

Qian Y., Chen Q., Chen Z., Fan C., Zhou G. (1993) Preparation of ultrafine powders of TiO_2 by hydrothermal H_2O_2 oxidation starting from metallic Ti. Journal of Materials Chemistry 3(2), 203-205.

Qiu X., Zhao Y., Burda C. (2007) Synthesis and characterization of nitrogen-doped group IVB visible-light-photoactive metal oxide nanoparticles. Advanced Materials 19(22), 3995-3999.

Rajeshwar K., Chenthamarakshan C.R., Goeringer S., Djukic M. (2001) Titania-based heterogeneous photocatalysis. Materials, mechanistic issues, and implications for environmental remediation. Pure and Applied Chemistry 73(12), 1849-1860.

Rao K.V.S., Lavédrine B., Boule P. (2003) Influence of metallic species on TiO_2 for the photocatalytic degradation of dyes and dye intermediates. Journal of Photochemistry and Photobiology A: Chemistry 154(2-3), 189-193.

Rehman S., Ullah R., Butt A.M., Gohar N.D. (2009) Strategies of making TiO_2 and ZnO visible light active. Journal of Hazardous Materials 170(2-3), 560-569.

Rengaraj S., Li X.Z. (2006) Enhanced photocatalytic activity of TiO_2 by doping with Ag for degradation of 2,4,6-trichlorophenol in aqueous suspension. Journal of Molecular Catalysis A: Chemical 243(1), 60-67.

Roco M.C. (1999) Nanotechnology, shaping the world atom by atom. National Science and Technology Council, Committee on Technology, The Interagency Working Group on Nanoscience, Engineering and Technology, September 1999, Washington D.C., USA.

Rouquerol J., Avnir D., Fairbridge C.W., Everett D.H., Haynes J.M., Pernicone N., Ramsay J.D.F., Sing K.S.W., Unger A.K.K. (1994) Recommendations for the characterization of porous solids (Technical Report). Pure and Applied Chemistry 66(8), 1739-1758.

Ruiz V.S.O., Airoldi C. (2005) Intercalation and thermochemistry of amines in lamellar titanium phenylarsonate. Journal of Brazilian Chemical Society 16(5), 1030-1037.

Ryu J., Choi W., Choo K.-H. (2005) A pilot-scale photocatalyst-membrane hybrid reactor: performance and characterization. Water Science and Technology 51(6-7), 491-497.

Ryu Y.B., Lee M.S., Jeong E.D., Kim H.G., Jung W.Y., Baek S.H., Lee G.-D., Park S.S., Hong S.-S. (2007) Hydrothermal synthesis of titanium dioxides from peroxotitanate solution using different amine group-containing organics and their photocatalytic activity. Catalysis Today 124(3-4), 88-93.

Ryu Y.B., Jung W.Y., Lee M.S., Jeong E.D., Kim H.G., Yang J.S., Lee G.-D., Park S.S., Hong S.-S. (2008) Hydrothermal synthesis of titanium dioxides from peroxotitanate solution using basic additive and their photocatalytic activity on the decomposition of orange II. Journal of Physics and Chemistry of Solids 69(5-6), 1457-1460.

Sakata T. (1989) Heterogeneous catalysis at solid-liquid interface In: Photocatalysis Fundamentals and Applications. Serpone, N. and Pelizzetti E. (Eds.), pp. 1-8, Wiley New York.

Saquib M., Muneer M. (2003) TiO_2-mediated photocatalytic degradation of a triphenylmethane dye (gentian violet), in aqueous suspensions. Dyes and Pigments 56(1), 37-49.

Sathish M., Viswanathan B., Viswanath R.P., Gopinath C.S. (2005) Synthesis, characterization, electronic structure, and photocatalytic activity of nitrogen-doped TiO_2 nanocatalyst. Chemistry of Materials 17(25), 6349-6353.

Sato S. (1986) Photocatalytic activity of NO_x-doped TiO_2 in the visible light region. Chemical Physics Letters 123(1-2), 126-128.

Sato S., Nakamura R., Abe S. (2005) Visible-light sensitization of TiO_2 photocatalysts by wet-method N doping. Applied Catalysis A: General 284(1-2), 131-137.

Satterfield C.N. (1970) Mass transfer in heterogeneous catalysis, M.I.T. Press, Cambridge, Massachusetts.

Satyawali Y., Balakrishnan M. (2008) Wastewater treatment in molasses-based alcohol distilleries for COD and color removal: A review. Journal of Environmental Management, 86, 481-497.

Savage N., Wentsel R. (2008) Draft nanomaterial research strategy (NRS). Environmental Protection Agency, United States, 1-2.

Schiavello M. (1998) Photocatalysis and Environment. Kluwer, Dordecht, The Netherlands.

Schmidt K.F. (2007) Nanofrontiers, visions for the future of nanotechnology. Project on Emerging Technologies, Woodrow Wilson International Center for Scholars, National Institutes of Health, Washington, D.C., USA.

Schonn, G. (1870) Ueber das Verhalten des Wasserstoffsuperoxyds zu Molybdän- und Titansäure (II) Zeitschrift fur analytische Chemie 9(1), 330.

Schulten H.-R. (1993) A state of the art structural concept for humic substances. Naturwissenschaften 80, 29-30.

Schulten H.-R., Plage B. (1991) A chemical structure of humic substances. Naturwissenschaften 78, 311-312.

Seery M.K., George R., Floris P., Pillai S.C. (2007) Silver doped titanium dioxide nanomaterials for enhanced visible light photocatalysis. Journal of Photochemistry and Photobiology A: Chemistry 189(2-3), 258-263.

Senthilkumaar S, Porkodi K., Gomathi R., Maheswari A.G., Manonmani N. (2006) Sol-gel derived silver doped nanocrystalline titania catalysed photodegradation of methylene blue from aqueous solution. Dyes and Pigments 69(1-2), 22-30.

Serpone N. (1997) Relative photonic efficiencies and quantum yields in heterogeneous photocatalysis. Journal of Photochemistry and Photobiology A: Chemistry 104(1-3), 1-12.

Seok S.I., Ahn B.Y., Pramanik N.C., Kim H., Hong S.-I. (2006) Preparation of nanosized rutile TiO_2 from an aqueous peroxotitanate solution. Journal of the American Ceramic Society 89(3), 1147-1149.

Shankar M.V., Kako T., Wang D., Ye J. (2009) One-pot synthesis of peroxo-titania nanopowder and dual photochemical oxidation in aqueous methanol solution. Journal of Colloid and Interface Science 331(1), 132-137.

Sharma V.K., Yngard R.A., Lin Y. (2009) Silver nanoparticles: Green synthesis and their antimicrobial activities. Advances in Colloid and Interface Science, 145, 83-96.

Shelley S.A. (2005) Nanotechnology: Turning basic science into reality In: Nanotechnology Environmental Implications and Solutions, Theodore L. and Kunz R.G. (Eds.), John Wiley & Sons, Inc, 61-107.

Shen Y., Xiong T., Li T., Yang, K. (2008) Tungsten and nitrogen co-doped TiO_2 nano-powders with strong visible light response. Applied Catalysis B: Environmental 83(3-4), 177-185.

Shifu C., Lei C., Shen G., Gengyu C. (2005) The preparation of nitrogen-doped photocatalyst $TiO_{2-x}N_x$ by ball milling. Chemical Physics Letters 413(4-6), 404-409.

Shih Y.H., Chen Y.C., Chen M.Y., Tai Y.T., Tso C.P. (2009) Dechlorination of hexachlorobenzene by using nanoscale Fe and nanoscale Pd/Fe bimetallic particles. Colloids and Surfaces A: Physicochemical and Engineering Aspects, 332, 84-89.

Shimizu N., Ogino C., Dadjour M.F., Murata T. (2007) Sonocatalytic degradation of methylene blue with TiO_2 pellets in water. Ultrasonics Sonochemistry 14(2), 184-190.

Shirayama H., Tohezo Y., Taguchi S. (2001) Photodegradation of chlorinated hydrocarbons in the presence and absence of dissolved oxygen in water. Water Research 35(8), 1941-1950.

Smith A. (2006) Nanotech – the way forward for clean water? Filtration and Separation, 43(8), 32-33.

Smith A.D. (1997) Oxford Dictionary of Biochemistry and Molecular Biology. Oxford University Press, North Carolina, USA.

Srivastava A., Srivastava O.N, Talapatra S., Vajtai R., Ajayan P.M. (2004) Carbon nanotube filters. Nature Materials, 3, 610-614.

Stathatos E., Petrova T., Lianos P. (2001) Study of the efficiency of visible-light photocatalytic degradation of Basic Blue adsorbed on pure and doped mesoporous titania films. Langmuir 17(16), 5025-5030.

Steelink C. (1999) What is humic acid? A perspective of the past forty years In: Understanding humic substances: advanced methods, properties and applications. Ghabbour E.A. and Davies G. (Eds.), pp. 1-8, RSC, UK.

Štengl V., Houšková V., Bakardjieva S., Murafa N., Bezdička P. (2010) Niobium and tantalum doped titania particles. Journal of Materials Research 25, 2015-2024.

Stevenson F.J. (1994) Humic chemistry: genesis, composition, reactions. Wiley, New York.

Strathmann H. (2001) Membrane separation processes: current relevance and future opportunities. American Institute of Chemical Engineers Journal, 47(5), 1077-1087.

Su H., Dong Q., Han J., Zhang D., Guo Q. (2008) Biogenic synthesis and photocatalysis of Pd-PdO nanoclusters reinforced hierarchical TiO_2 films with interwoven and tubular conformations. Biomacromolecules 9(2), 499-504.

Sun H., Bai Y., Jin W., Xu N. (2008) Visible-light-driven TiO_2 catalysts doped with low-concentration nitrogen species. Solar Energy Materials and Solar Cells 92(1), 76-83.

Sun H., Bai Y., Liu H., Jin W., Xu N. (2009) Photocatalytic decomposition of 4-chlorophenol over an efficient N-doped TiO_2 under sunlight irradiation. Journal of Photochemistry and Photobiology A: Chemistry 201(1), 15-22.

Sun J., Qiao L., Sun S., Wang G. (2008) Photocatalytic degradation of Orange G on nitrogen-doped TiO_2 catalysts under visible light and sunlight irradiation. Journal of Hazardous Materials 155(1-2), 312-319.

Sung-Suh H.M., Choi J.R., Hah H.J., Koo S.M., Bae Y.C. (2004) Comparison of Ag deposition effects on the photocatalytic activity of nanoparticulate TiO_2

under visible and UV light irradiation. Journal of Photochemistry and Photobiology A: Chemistry 163(1-2), 37-44.

Sutherland K. (2008) What is nanofiltration? Filtration and Separation 45(8), 32-35.

Sutton R., Sposito G. (2005) Molecular structure in soil humic substances: The new view. Environmental Science & Technology 39(23), 9009-9015.

Suzuki Y., Warsito, Maezawa A., Uchida S. (2000) Liquid-solid separation of photo-catalyst suspension induced by ultrasound. Chemistry Letters 29(2), 130-131.

Tang Y., Yang L., Chen J., Qiu Z. (2010) Facile fabrication of hierarchical hollow microspheres assembled by titanate nanotubes. Langmuir 26(12), 10111-10114.

Taniguchi N. (1974) On the Basic Concept of 'Nano-Technology', Proceeding of the International Conference on Precision Engineering, Tokyo, Part II, Japan Society of Precision Engineering, 1974.

Tatsuma T., Tachibana S.-i., Fujishima A. (2001) Remote oxidation of organic compounds by UV-irradiated TiO_2 via the gas phase. Journal of Physical Chemistry B 105(29), 6987-6992.

Tayade R.J., Natarajan T.S., Bajaj H.C. (2009) Photocatalytic degradation of methylene blue dye using ultraviolet light emitting diodes. Industrial and Engineering Chemistry Research 48(23), 10262-10267.

Theron J., Walker J.A., Cloete T.E. (2008) Nanotechnology and water treatment: applications and emerging opportunities. Critical Reviews in Microbiology, 34, 43-69.

Thompson T.L., Yates, J.T. (2006) Surface science studies of the photoactivation of TiO_2 new photochemical processes. Chemical Reviews 106(10), 4428-4453.

Thorsen T., Flogstad H. (2006) Nanofiltration in drinking water treatment, Literature review, Techneau, European Commission.

Tian F., Sun J., Yang J., Wu P., Wang H.-L., Du X.-W. (2009) Preparation and photocatalytic properties of mixed-phase titania nanospheres by laser ablation. Materials Letters 63(27), 2384-2386.

Tsai S.-J., Cheng S. (1997) Effect of TiO_2 crystalline structure in photocatalytic degradation of phenolic contaminants. Catalysis Today 33(1-3), 227-237.

Ullah R., Dutta J. (2008) Photocatalytic degradation of organic dyes with manganese-doped ZnO nanoparticles. Journal of Hazardous Materials, 156, 194-200.

Umwelt Bundes Amt (UBA), (2006) Nanotechnoogy: Opportunities and risks for humans and the environment, http://www.umweltbundesamt.de/uba-info-presse-e/hintergrund/nanotechnology.pdf

Uyguner C.S., Bekbolet M. (2005) Evaluation of humic acid photocatalytic degradation by UV-vis and fluorescence spectroscopy. Catalysis Today 101, 267-274.

Uyguner C.S., Bekbolet M. (2011) Significance of analytical parameters for the understanding of natural organic matter in relation to photocatalytic oxidation. Chemosphere 84(8), 1009-1031.

Vamanu C.I., Høl P.J., Allouni Z.E., Elsayed S., Gjerdet N.R. (2008) Formation of potential titanium antigens based on protein binding to titanium dioxide nanoparticles. International Journal Nanomedicine 3(1), 69-74.

Vautier M., Guillard C., Herrmann J.-M. (2001) Photocatalytic degradation of dyes in water: case study of indigo and of indigo carmine. Journal of Catalysis 201(1), 46-59.

Ventresque C., Gisclon V., Bablon G., Chagneau G. (2000) An outstanding feat of modern technology: the Mery-sur-Oise Nanofiltration Plant. Desalination, 131, 1-16.

Vinu R., Madras G. (2009) Photocatalytic activity of Ag-substituted and impregnated nano-TiO_2. Applied Catalysis A: General 366(1), 130-140.

Wang P., Garcia A., Ivovich C., Smith D. (2010) Photocatalysis for water treatment, http://ebookbrowse.com/ense350-gp-vegoil-pdf-d182345206**.**

Wang S., Boyjoo Y., Choueib A. (2005a) A comparative study of dye removal using fly ash treated by different methods. Chemosphere 60(10), 1401-1407.

Wang X., Chen C., Chang Y., Liu H. (2009) Dechlorination of chlorinated methanes by Pd/Fe bimetallic nanoparticles. Journal of Hazardous Materials, 161, 815-823.

Wang X., Hu Z., Chen Y., Zhao G., Liu Y., Wen Z. (2009a) A novel approach towards high-performance composite photocatalyst of TiO_2 deposited on activated carbon. Applied Surface Science 255(7), 3953-3958.

Wang Y., Doren D.J. (2005) First-principles calculations on TiO_2 doped by N, Nd, and vacancy. Solid State Communications 136(3), 186-189.

Wang Y., Hong C.-S. (2000) TiO_2-mediated photomineralization of 2-chlorobiphenyl: the role of O_2. Water Research 34(10), 2791-2797.

Wang Z., Hu X. (1999) Fabrication and electrochromic properties of spin-coated TiO_2 thin films from peroxo-polytitanic acid. Thin Solid Films 352(1-2), 62-65.

Wang Y.Q., Yu X.J., Sun D.Z. (2007) Synthesis, characterization, and photocatalytic activity of $TiO_{2-x}N_x$ nanocatalyst. Journal of Hazardous Materials 144(1-2), 328-333.

Wang Z., Cai W., Hong X., Zhao X., Xu F., Cai C. (2005) Photocatalytic degradation of phenol in aqueous nitrogen-doped TiO_2 suspensions with various light sources. Applied Catalysis B: Environmental 57(3), 223-231.

Weber T.W., Chakravorti R.K. (1974) Pore and solid diffusion models for fixed-bed adsorbers AIChE Journal 20(2), 228-238.

Wegmann M., Michen B., Graule T. (2008) Nanostructured surface modification of microporous ceramics for efficient virus filtration. Journal of the European Ceramic Society, 28, 1603-1612.

Wei F., Zeng H., Cui P., Peng S., Cheng T. (2008) Various TiO_2 microcrystals: Controlled synthesis and enhanced photocatalytic activities. Chemical Engineering Journal, 144, 119-123.

Wei M., Konishi Y., Zhou H., Sugihara H., Arakawa H. (2004) A simple method to synthesize nanowires titanium dioxide from layered titanate particles. Chemical Physics Letters 400, 231-234.

Wiszniowski J., Robert D., Surmacz-Gorska J., Miksch K., Weber J.-V. (2002) Photocatalytic decomposition of humic acids on TiO_2: Part I: Discussion of adsorption and mechanism. Journal of Photochemistry and Photobiology A: Chemistry 152(1-3), 267-273.

World Health Organization (WHO), (2004) Drinking water quality.

http://www.who.int/water_sanitation_health/dwq/en/

Wu C.-H., Chern J.-M. (2006) Kinetics of photocatalytic decomposition of methylene blue. Industrial and Engineering Chemistry Research 45(19), 6450-6457.

Wu D., Liu J., Zhao X., Li A., Chen Y., Ming N. (2006) Sequence of events for the formation of titanate nanotubes, nanofibers, nanowires, and nanobelts. Chemistry of Materials 18(2), 547-553.

Wu M.K., Windeler R.S., Steiner C.K., Bros T., Friedlander S.K. (1993) Controlled synthesis of nanosized particles by aerosol processes. Aerosol Science and Technology 19, 527-548.

Wu P., Xie R., Imlay K., Shang J.K. (2010) Visible-light-induced bactericidal activity of titanium dioxide codoped with nitrogen and silver. Environmental Science and Technology 44(18), 6992-6997.

Xi W., Geissen S.-u. (2001) Separation of titanium dioxide from photocatalytically treated water by cross-flow microfiltration. Water Research 35(5), 1256-1262.

Xiao L., Erdei L., McDonagh A., Cortie M. (2008) Photocatalytic nanofibres. ICONN, 2008. International Conference on Nanoscience and Nanotechnology, Melbourne, Vic, Australia.

Xin B., Jing L., Ren Z., Wang,B., Fu H. (2005) Effects of simultaneously doped and deposited Ag on the photocatalytic activity and surface states of TiO_2. Journal of Physical Chemistry B 109(7), 2805-2809.

Xing M., Zhang J., Chen F. (2009) New approaches to prepare nitrogen-doped TiO_2 photocatalysts and study on their photocatalytic activities in visible light. Applied Catalysis B: Environmental 89(3-4), 563-569.

Xiong C., Kim M.J., Balkus K.J. (2006) TiO_2 Nanofibers and core-shell structures prepared using mesoporous molecular sieves as templates13. Small 2(1), 52-55.

Xiong L., Sun W., Yang Y., Chen C., Ni J. (2011) Heterogeneous photocatalysis of methylene blue over titanate nanotubes: Effect of adsorption. Journal of Colloid and Interface Science 356(1), 211-216.

Xiong L., Yang Y., Mai J., Sun W., Zhang C., Wei D., Chen Q., Ni J. (2010) Adsorption behavior of methylene blue onto titanate nanotubes. Chemical Engineering Journal 156(2), 313-320.

Xu J., Ao Y., Fu D., Yuan C. (2008) A simple route for the preparation of Eu, N-codoped TiO_2 nanoparticles with enhanced visible light-induced photocatalytic activity. Journal of Colloid and Interface Science 328(2), 447-451.

Xu Z., Gan L. , Jia Y., Hao Z. , Liu M., Chen L. (2007) Preparation and characterization of silica-titania aerogel-like balls by ambient pressure drying. Journal of Sol-Gel Science and Technology, 41(3), 203-207.

Yada M., Goto Y., Uota M., Torikai T., Watari T. (2006) Layered sodium titanate nanofiber and microsphere synthesized from peroxotitanic acid solution. Journal of the European Ceramic Society 26(4-5), 673-678.

Yamashita H., Harada M., Misaka J., Takeuchi M., Ikeue K., Anpo M. (2002) Degradation of propanol diluted in water under visible light irradiation using metal ion-implanted titanium dioxide photocatalysts. Journal of Photochemistry and Photobiology A: Chemistry 148(1-3), 257-261.

Yang G.C.C., Li C.J. (2008) Tubular TiO_2/Al_2O_3 composite membranes: preparation, characterization, and performance in electrofiltration of oxide-CMP

wastewater. Desalination, 234, 354-361.

Yang G.-J., Li C.-J., Huang X.-C., Li C.-X., Wang Y.-Y. (2007) Influence of silver doping on photocatalytic activity of liquid-flame-sprayed-nanostructured TiO_2 coating. Journal of Thermal Spray Technology 16(5), 881-885.

Yang S., Gao L. (2008) Photocatalytic activity of nitrogen doped rutile TiO_2 nanoparticles under visible light irradiation. Materials Research Bulletin 43(7), 1872-1876.

Yang X., Xu L., Yu X., Guo Y. (2008a) One-step preparation of silver and indium oxide co-doped TiO_2 photocatalyst for the degradation of rhodamine B. Catalysis Communications 9(6), 1224-1229.

Yu J., Liu S., Zhou M. (2008) Enhanced photocalytic activity of hollow anatase microspheres by Sn^{4+} incorporation. The Journal of Physical Chemistry C 112(6), 2050-2057.

Yuan J., Chen M., Shi J., Shangguan W. (2006) Preparations and photocatalytic hydrogen evolution of N-doped TiO_2 from urea and titanium tetrachloride. International Journal of Hydrogen Energy 31(10), 1326-1331.

Yuan Y., Ding J., Xu J., Deng J., and Guo A.J. (2010) TiO_2 nanoparticles co-doped with silver and nitrogen for antibacterial application. Journal of Nanoscience and Nanotechnology 10, 1-7.

Yuan Z.-Y., Su B.-L. (2004) Titanium oxide nanotubes, nanofibers and nanowires. Colloids and Surfaces A: Physicochemical and Engineering Aspects 241(1-3), 173-183.

Zaleska A. (2008) Doped-TiO_2: A Review. Recent Patents in Engineering 2, 157-164.

Zdravkov B.D., Cermak J.J., Sefara M., Janku J. (2007) Pore classification in the characterization of porous materials: A perspective. Central European Journal of Chemistry 5(2), 385-395.

Zhang F., Pi Y., Cui J., Yang Y., Zhang X., Guan N. (2007) Unexpected selective photocatalytic reduction of nitrite to nitrogen on silver-doped titanium dioxide. The Journal of Physical Chemistry C 111(9), 3756-3761.

Zhang H., Quan X., Chen S., Zhao H., Zhao Y. (2006) Fabrication of photocatalytic membrane and evaluation its efficiency in removal of organic pollutants from water. Separation and Purification Technology, 50, 147-155.

Zhang Q., Wang J., Yin S., Sato T., Saito F. (2004) Synthesis of a visible-light active $TiO_{2-x}S_x$ photocatalyst by means of mechanochemical doping. Journal of the American Ceramic Society 87(6), 1161-1163.

Zhang T., Oyama T.k., Horikoshi S., Hidaka H., Zhao J., Serpone N. (2002) Photocatalyzed N-demethylation and degradation of methylene blue in titania dispersions exposed to concentrated sunlight. Solar Energy Materials and Solar Cells 73(3), 287-303

Zhang X., Du A.J., Lee P., Sun D.D., Leckie J.O. (2008) TiO_2 nanowire membrane for concurrent filtration and photocatalytic oxidation for humic acid in water. Journal of Membrane Science 313, 44-51.

Zhang X., Pan J.H., Du A.J., Fu W., Sun D.D., Leckie J.O. (2009) Combination of one-dimensional TiO_2 nanowire photocatalytic oxidation with microfiltration for water treatment. Water Research 43(5), 1179-1186.

Zhang X., Pan J.H., Du A.J., Ng J., Sun D.D., Leckie J.O. (2009a) Fabrication and photocatalytic activity of porous TiO_2 nanowire microspheres by surfactant-mediated spray drying process. Materials Research Bulletin 44(5), 1070-1076.

Zhang, W.-X., (2005) Nanotechnology for water purification and waste treatment. Frontiers in Nanotechnology, US EPA Millennium Lecture Series, July 18 2005, Washington, D.C., USA.

Zhao G.J., Stevens S.E. (1998) Multiple parameters for the comprehensive evaluation of the susceptibility of Escherichia coli to the silver iron. Biometals, 11, 27-32.

Zhou M., Yu J., Liu S., Zhai P., Huang B. (2009) Spray-hydrolytic synthesis of highly photoactive mesoporous anatase nanospheres for the photocatalytic degradation of toluene in air. Applied Catalysis B: Environmental 89(1-2), 160-166.

Zhu A.M., Nie L.H., Wu Q.H., Zhang X.L., Yang X.F., Xu Y., Shi C. (2007) Crystalline, uniform-sized TiO_2 nanosphere films by a novel plasma CVD process at atmospheric pressure and room temperature. Chemical Vapor Deposition 13(4), 141-144.

Zhu H., Gao X., Lan Y., Song D., Xi Y., Zhao J. (2004) Hydrogen titanate nanofibers covered with anatase nanocrystals: A delicate structure achieved by the wet chemistry reaction of the titanate nanofibers. Journal of the American Chemical Society 126(27), 8380-8381.

Zodrow K., Brunet L., Mahendra S., Li D., Zhang A., Li Q., Alvarez P.J.J. (2009) Polysulfone ultrafiltration membranes impregnated with silver nanoparticles show improved biofouling resistance and virus removal. Water Research, 43(3), 715-723.

Zsigmondy, R. (1914) Colloids and the Ultramicroscope. John Wiley and Sons, NY, USA.